SYNTHESIS AND PHOTOTHERMAL APPLICATION OF PLASMONIC TRANSITION METAL CARBIDE NANOPARTICLES

by

Matthew J. Margeson

Submitted in partial fulfillment of the requirements
for the degree of Doctor of Philosophy

at

Dalhousie University
Halifax, Nova Scotia
July 2024

"A scientist is just a kid who never grew up. So even as you grow older, never stop being a kid. This guarantees that the world will become and remain your playgrounds of curiosity."

This thesis is dedicated to the memory of my grandfather, Cliff Stanworth.

TABLE OF CONTENTS

LIST OF TABLES

LIST OF FIGURES

ABSTRACT

Plasmonic materials have been a topic of increasing interest for a growing number of applications such as chemical sensing, energy harvesting, photothermal therapy, catalysis, and communications. These all stem from the unique optical interaction they have with light, causing a drastic energy enhancement leading to strong light absorption or scattering, enhanced electromagnetic field, and heat generation. Certain nanomaterials, such as Au and Ag have historically been the focus of plasmonic research, with their optical properties making them particularly suitable for sensing. Harnessing the heat generated by plasmonic nanomaterials has recently become a topic of importance, leading to the discovery of new materials. Refractory nanostructures have the potential to be low-cost and chemically and thermally robust plasmonic materials. While the past decade has seen immense attention on transition metal nitrides (TMN), there has been much less emphasis on their closely related transition metal carbide (TMC) counterparts. While select research groups have shown promising initial results for two-dimensional plasmonic TMCs, three-dimensional TMC nanoparticles have predominantly been studied theoretically. This could be due in part to the high synthesis temperatures needed to form TMCs. This often destroys the nanostructure, causing them to lose any plasmonic characteristics.

To alleviate this, and provide experimental data for promising 3D TMC nanomaterials, a magnesium reduction reaction was developed and explored for the formation of group 4 (Ti, Zr, and Hf), and group 5 (V, Nb, and Ta) TMCs. These reactions were performed at reduced temperatures compared to traditional carbothermal reduction, thus preserving the nanoscale structure. The project included the first instance of in-depth characterization of both the physical and optical properties of the resulting TMCs. Subsequent studies assessed how the magnesium reduction reaction could be tuned to influence the plasmonic behaviour of the product TMCs and allow for scaling up of the process. This involved incorporating a variety of waste products into the reaction scheme, decreasing the overall environmental footprint. Assessing the plasmonic heating capability of the group 4 TMCs, TiC, ZrC, and HfC was done via solar-driven water evaporation and desalination of Atlantic Ocean water experiments. Ease of increasing the process scale was highlighted by developing a floating solar still, which further displayed the plasmonic TMC potential by generating electricity in tandem with freshwater. This work attempts to showcase TMCs as promising plasmonic materials from both a physical and optical property standpoint and provide a roadmap towards informed synthesis of other TMCs.

List of Abbreviations and Symbols Used

Abbreviations	Description
BET	Brunauer-Emmet-Teller
BW	Birch Woof
CCD	Charge Coupled Device
CG	Coffee Ground
cm^{-1}	Wavenumber
CT	Commuted Tomography
DLS	Dynamic Light Scattering
EDS	Energy-Dispersive Spectroscopy
EELS	Electron Energy-Loss Spectroscopy
eV	Electronvolts
FEM	Finite Element Method
FJH	Flash Joule Heating
FO	Forward Osmosis
FSS	Floating Solar Still
HAADF	High-Angle Annular Dark Field
HRTEM	High-Resolution Transmission Electron Microscopy
IR	Infrared
keV	Kiloelectronvolt
KW	Japanese Knotweed
LED	Light Emitting Diode
LS	Lobster Shell
LSPR	Localized Surface Plasmon Resonance
LSS	Land Solar Still
MB	Methylene Blue
ME	Multiple Effect
min	Minute
mL	Milliliter
µL	Microliter

Abbreviations	Description
mm	Millimeter
MOF	Metal Organic Framework
ms	Millisecond
MSF	Multi-Stage Flash
NIR	Near Infrared
nm	Nanometer
NP	Nanoparticle
PML	Perfectly Matched Layer
ppm	Parts per Million
ppb	Parts per Billion
PXRD	Powder X-ray Diffraction Spectroscopy
QGA	QuenchGone™ Aqueous
RO	Reverse Osmosis
SEM	Scanning Electron Microscopy
SEF	Surface Enhanced Fluorescence
SERS	Surface Enhanced Raman Spectroscopy
SPR	Surface Plasmon Resonance
SSM	Solid State Metathesis
SVG	Solar-Vapor Generation
TD	Thermal Distillation
TEM	Transmission Electron Microscopy
TMC	Transition Metal Carbide
TMN	Transition Metal Nitride
TR	Tire Rubber
UV	Ultraviolet
XPS	X-ray Photoelectron Spectroscopy
WHO	World Health Organization

Symbol	Description
Å	Angstrom
K_α	X-ray Wavelength
λ	Wavelength
g	Grams
h	Hours
2θ	Bragg Angle
d	Inter Plant Distance
s	Seconds

ACKNOWLEDGEMENTS

Completing a thesis is rarely a single person job, and my time at Dalhousie was absolutely no exception to the rule. I'm extremely happy to be able to acknowledge all of the people who helped me get through to the end of my time at Dalhousie. First, a supervisor that any graduate student would be lucky to have, Dr. Mita Dasog has been a constant support throughout my entire time at Dalhousie. Both in the lab and outside of the lab, she has been a strong support and an inspiring role model. This includes but is definitely not limited to keeping passion for research going over the course of a (very) lengthy pandemic, and by giving back to the community while encouraging countless young minds. I have grown as both a researcher and person over my time here and couldn't have gotten through it all without Mita.

My supervisory committee, including Dr. Heather Andreas, Dr. Michael Freund, and Dr. Peng Zhang have given me some of the most helpful feedback when parts of my research stalled out. I appreciate all of the time you have committed to pushing me forward. An additional thank you to Dr. Pramod Pillai for being my external examiner. There has also been a world-class group of technicians who have supported the project and have been a pleasure to work with over the years. Dr. Carmen Andrei at the Canadian Center for Microscopy, and the Electron Microscopy Core Facility at Dalhousie are thanked for TEM assistance. The Clean Technologies Research Institute is thanked for SEM access. Dr. Andrew George and Dr. Carlie Charron are thanked for XPS and lyophilizer experiments, respectively. Dr. Graham Gagnon is thanked for access to ICP-MS and ATP assays. A massive thanks goes to Lea Gawne, who has been able to sort out any situation I have approached her with, including winning a rule-following argument with a German University before I even arrived at Dalhousie. Funding from various sources including NSERC, CFI, OFI, and Sumner Foundation is greatly appreciated to facilitate this research.

One of the biggest thanks I can send out goes to the entire Dasog lab group, past and present and includes the fantastic undergraduate researchers I have had the pleasure of working with. A special shoutout to Mark Atwood and Dr. Yashar

Monfared who were backbones of certain projects throughout this thesis. The office chatter has always been a welcome addition to the workday and has led to some of the most important research brain-clicks when things weren't running smoothly in the lab. Getting to know and becoming friends with all of you has made coming to campus an absolute treat. For the times not in the lab, I'd like to thank all of my friends on the outside to help refresh the battery and partake in some pretty amazing trips together.

My endless thanks goes out to my family (Elaine, Mike, Blair, Kim, Chris, Emily, Ellen, Claire, and Jacob), plus grandparents (Marilyn and Sheila), and all those by extension who have been supportive of my still being in school after 25+ years and always show interest in my research. You have made a huge impact on getting me to the point I am at today. Finally, to Katie (and the boys Mowgli, Linus, and little yet to be named Margeson), it's hard to overstate how thankful I am to have you going along on this wild ride with me. It's set to be one of the craziest summers of our lives and I am looking forward to every minute of it.

CHAPTER 1

INTRODUCTION

Part of this chapter is adapted from Margeson, M. J.; Dasog, M. Plasmonic Metal Nitrides for Solar-Driven Water Evaporation. *Environ. Sci.: Water Res. Technol.* **2020**, *6*, 3169-3177. Copyright 2020. Royal Society of Chemistry.

1.1 Introduction to Plasmonics

The field of light-material interactions has been an area of great interest in chemistry and physics since their inception[1] and the theories and concepts are under constant development and modification.[2–5] Many modern technologies, such as photovoltaic solar cells, or energy efficient LEDs stem from the study of these fundamental interactions.[6,7] Plasmonics is one such area of focus which was unknowingly exploited over a thousand years ago by Roman glassmakers.[8] Stained glass window artisans of European Cathedrals employed similar techniques in the centuries that followed.[9,10] It wasn't until 1902 that this phenomenon was examined scientifically by R. W. Wood while studying the spectrum of reflected light from metallic gratings.[11] The actual term plasmon was first used in the 1950s to describe the unique excitation of conduction electrons of these materials.[12] Over a century later, plasmonics has now drawn considerable research attention, becoming an integral part of the field of photonics.[13,14]

Fundamentally, plasmonics interests itself in examining the interaction between electromagnetic radiation and free electrons in a nanoscale material.[15,16] Research

includes theoretical and computational studies, synthesis and property evaluation, and application of the corresponding materials, with noble metals historically being of particular interest for reasons that will become apparent later in this chapter. Recent advances in fabrication and characterization techniques have led to remarkable progress in exploring plasmonic nanomaterials for a wide variety of applications[17] such as sensing for environmental and medicinal purposes,[18] catalytic processes,[19] and energy harvesting.[20,21] This section will introduce the key concepts underlying the mechanism of action for plasmonic materials and how these lead to the physical properties of interest for plasmonic applications.

1.1.1 Optical Properties of Plasmonic Materials

Certain metals have long been known to have unique optical properties compared to their non-metallic counterparts.[22] For example, they are very efficient at reflecting visible light making them a good material choice for mirrors, except perhaps for their cost in many cases.[23] Such optical properties, as well as physical properties like heat and electric conductivity all have the same origin: the presence of free conduction electrons.[24,25] While the relationship between conduction electrons and heat or electric conductivity is quite intuitive, their connection with optical responses can be much less obvious. The movement of these negatively charged electrons is constantly counteracting a background of positive charge, working to maintain an overall neutral state.[26] The overall electron flow can be defined as being a *free-electron plasma*.[27] The response of this plasma to an external electromagnetic field will dictate the optical properties of the metal for the wavelength of light used.[28,29] How the electron plasma will behave under electromagnetic irradiation is dependent on the dielectric function (ε) of the metal itself. The dielectric function expresses the metal's dielectric constant as a function of light wavelength, with the dielectric constant being a measure of a materials ability to store electrical energy.[30,31] The dielectric function contains much of the information required to model metals and can be split into a *real* (ε_i) and an *imaginary* (ε_r) part, as shown in equation 1.1.[32]

$$\varepsilon(\lambda) = \varepsilon_r(\lambda) + i\varepsilon_i \tag{1.1}$$

The real part describes all the electric energy stored from interaction of the free electron plasma as well as every other electron in the material with an electromagnetic field, while the negative part represents potential losses of this energy.[33] Often, these losses are from electronic transitions of electrons that are not in the plasma.

This brings us now to how a plasmonic material differs from a non-plasmonic material. The criteria of a plasmonic material is to have a negative value for the real part of the dielectric function, and a very small imaginary part for a given wavelength of light.[34] Most transition metals meet the first criteria within the visible light spectrum, meaning the free-electron plasma is able to store the electromagnetic energy.[35] Unfortunately, many metals suffer from a larger number of losses, resulting in a large imaginary dielectric part (Figure 1.1).[36] This is the reason why the majority of plasmonic research has focused on noble metals like gold (Au) and silver (Ag), as will be discussed further in subsequent sections. For a material that does meet the above criteria, the wavelength at which overlap of the negative real and small imaginary dielectric parts occurs will yield a plasmonic response.[37] For example, compared to Ag (Figure 1.1A), the imaginary dielectric function for Pd increases quickly above ~250 nm (Figure 1.1B), resulting in poor or no plasmonic response above those wavelengths. This plasmonic response will establish itself as an oscillation of the free-electron plasma. In other words, the oscillation of the free electron plasma can be thought of simply as an excitation of every free electron of the material simultaneously.[38] It is important to note that this oscillation will occur at a frequency matching the wavelength of the incoming light. This can occur either along a planar interface or on the surface of a nanoparticle (NP), termed surface plasmon resonance (SPR) and localized surface plasmon resonance (LSPR), respectively (Figure 1.2).[39] For this thesis, LSPR will be the relevant plasmonic term used.

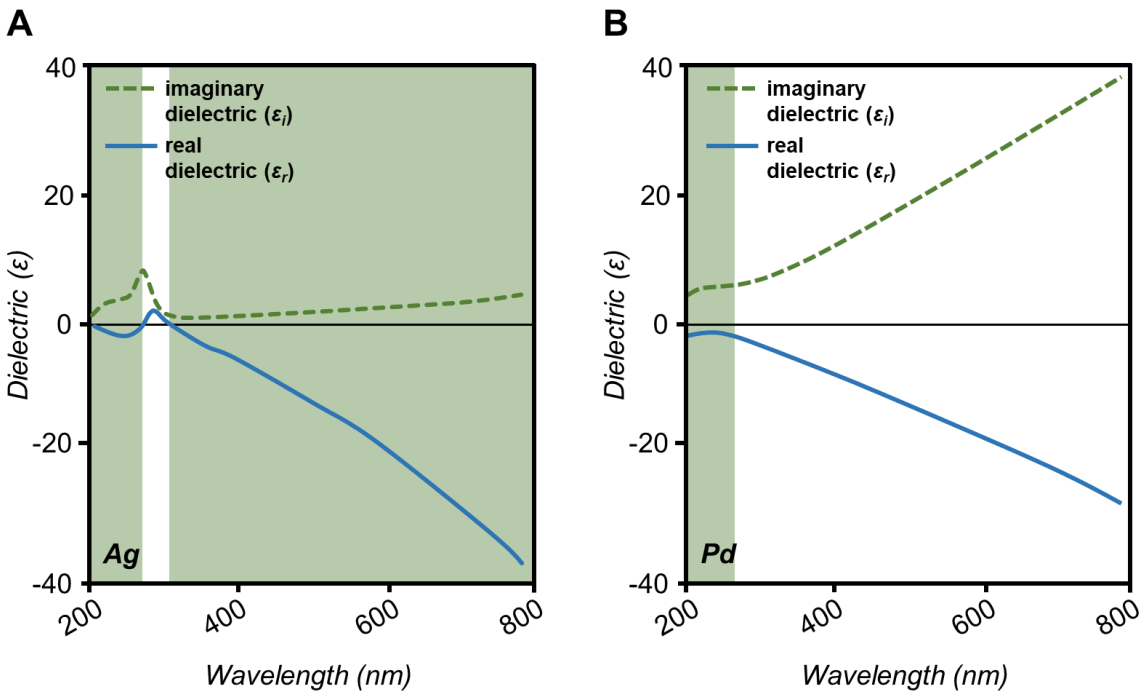

Figure 1.1. Real (solid blue) and imaginary (dashed green) dielectric functions for (A) Ag and (B) Pd. Green and white regions represent locations where LSPR formation could and could not occur, respectively. Adapted from reference (34).

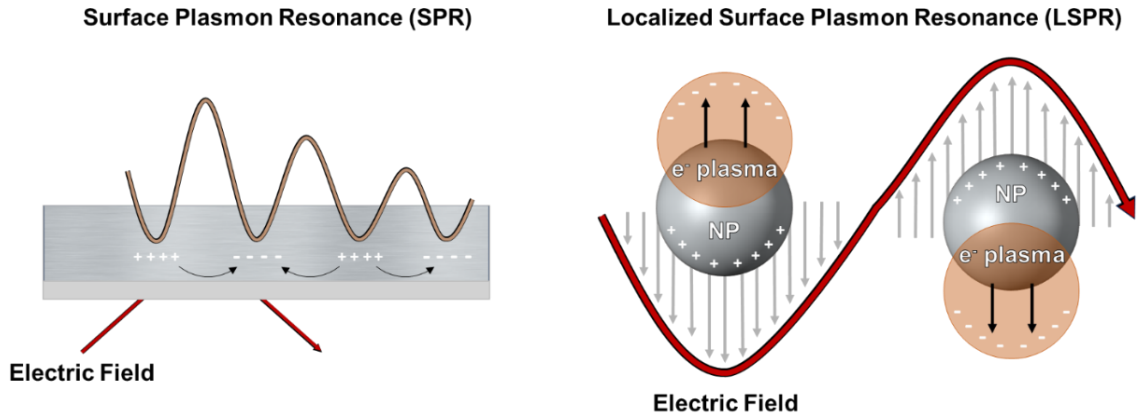

Figure 1.2. Schematic of electron wave oscillation by SPR (left) and by LSPR (right). Adapted from reference (37).

Digging further into the formation of plasmonic responses, we can start to identify the physical manifestation of this phenomenon. The overall light-matter interaction consists of both an *absorbing* and *scattering* component, which together comprise what's known as the *extinction*.[40,41] It is important to note here that the

frequencies at which the absorbance and scattering will occur, is material dependent.[42] Not only that, but the ratio of absorbance vs scattering is also highly material dependent as well.[42] Herein lies one of the most useful characteristics of plasmonic nanomaterials, which is the tuneability of the response depending on the desired application.[43] This inherent material dependence is in part what allowed for the creation of such brilliant stained-glass colors in the past. In the simplest case, we consider a small (<50 nm) spherical Au NP, the corresponding LSPR will be a symmetric oscillation across the particle like that shown in Figure 1. The oscillation can be visualized as a weight on a spring. The spring is working to restore the weight back to the central position, in this case the center of the particle. Since it is symmetric, this is seen as a single peak when using absorbance spectroscopy. The main way that an LSPR is modified works on the basis of introducing new oscillations or altering the restorative force of the particle, i.e. the strength of the spring. Keeping this restoration action in mind, if the size of this spherical particle is increased, the restoring force will become more dispersed and weaker across the particle.[44] This in turn will decrease the frequency of the plasmonic oscillation, causing the extinction to shift to longer wavelength, or *red-shift*.[45] As the size continues to increase the overall extinction shifts away from absorbance to increased light scattering.[46] Building from this, in a sample containing multiple different nanoparticle sizes, or a polydisperse sample, a broadening of the LSPR absorbance peak will be observed. This is due to the plasmonic contribution of each particle size occurring at a slightly different wavelength.[47] Broadening of LSPR peaks can be either desirable or undesirable, depending on the intended application, as will be discussed in upcoming sections.

The shape of the particle in question can also influence the frequency and number of LSPRs. To understand this, it must be stated that the oscillation of the free-electron plasma will occur in an orientation matching the incoming electromagnetic field. For a spherical particle, no matter which direction the nanoparticle is facing it will be the same due to the symmetry but particle shapes like cubes, rods, pyramids, etc., can support additional LSPRs.[48,49] For example, nanorods form LSPR with both their long axis (longitudinal) and short axis (transverse) aligned with the incoming light, showing absorbance at two distinct locations. This can be seen using absorbance spectroscopy, where multiple peaks will be observed (Figure 1.3A).[50] It has also been well reported that the LSPR can

be unique when two or more plasmonic materials are combined, for example as an alloy. A particle consisting of pure Au will have different optical properties to that of a 50:50 Au:Ag particle, which again will be different than a pure Ag particle with all other parameters the same (Figure 1.3B).[51,52]

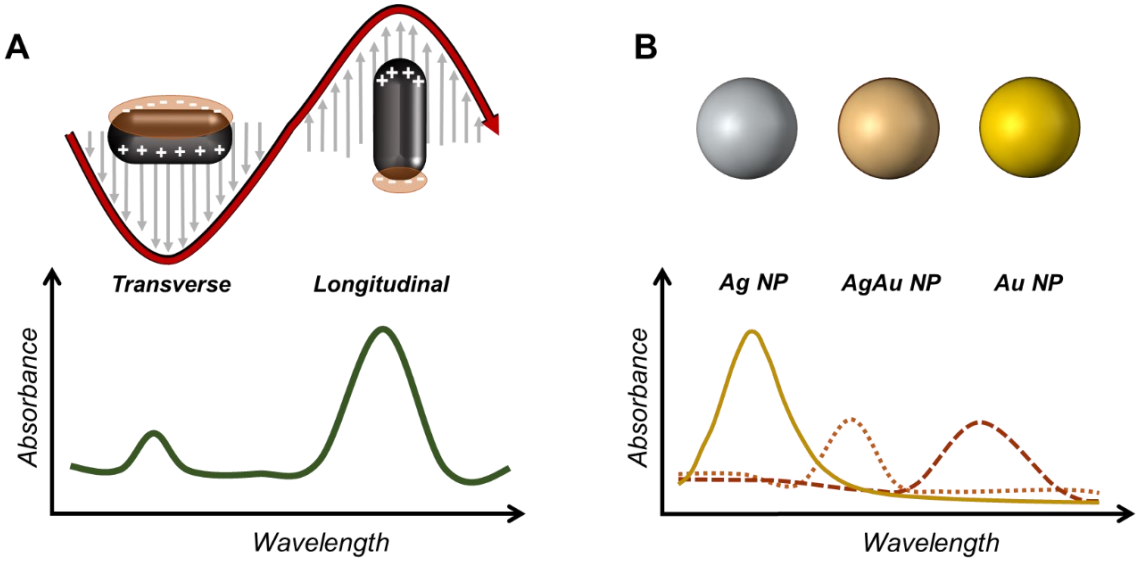

Figure 1.3. Schematic of electron wave oscillation by SPR (left) and by LSPR (right). Adapted from references (50) and (51).

Finally, a trait that feeds some of the current most interesting research avenues of plasmonic nanomaterials and one that is important for the current thesis report is a plasmonic NPs interaction with its surrounding environment. Plasmonic oscillations work in part due to the free electron plasma being at the interface and interacting with another dielectric material, such as water, air, ceramics, etc.[53,54] By simply changing the characteristics (dielectric constant or refractive index) of the environment surrounding the plasmonic NPs, the frequency of LSPR can be shifted.[55] This most importantly includes other plasmonic NPs in the vicinity of the particle in question. The LSPR of one particle can couple with one or more nearby particles, creating a secondary oscillation occurring at a different frequency. This leads to absorbance at a new wavelength of light due to the additional interaction.[56–58] Each of these traits has been explored to further the field of plasmonics, but as previously mentioned, the inherent optical properties of certain materials will ultimately determine their success for a given application. The

absorbance versus scattering of light, which part of the electromagnetic spectrum the LSPR lies, how the excited LSPR dissipates the energy, and even the physical properties of a material must be considered. The following section will seek to provide a road map in the decision-making process for plasmonic nanomaterials.

1.1.2 Application of Plasmonic Materials

It has become abundantly clear in the past decade how versatile plasmonic materials can be.[59] Interestingly, as the field has matured, certain traits of plasmonic nanomaterials that were once thought to hinder their use have found unexpected and exciting application.[60] This highlights the importance of fully understanding the optical properties discussed above for both old and new plasmonic materials alike to unlock their full potential. In general, there are four main mechanisms of interest that occur during the excitation and relaxation of the free electron plasma (Figure 1.4).[61–63] These are enhancement of the local electromagnetic field, light scattering, formation of high energy electrons, known as hot electrons, and finally local heating near the NP surface known as the photothermal effect. Multiple, if not all the mentioned mechanisms can be ongoing simultaneously after formation of an LSPR. Again, modelling of the NPs using the methods mentioned previously can provide a good approximation of how the material will behave.[64,65] For this project, the photothermal effect will be the focus, but each of the mechanisms will be briefly explored here with real world examples to show the diversity of ongoing plasmonic research.

The enhancement of the electric field directly surrounding a plasmonic NP occurs because the formation of an LSPR is effectively confining the energy from light of a certain wavelength to the surface of a NP. The diameter of plasmonic NPs in most cases are much smaller than the wavelength of light and therefore there is an increase in the amount of energy per unit volume.[66] This is known as a near-field enhancement. When molecules are placed within the amplified near-field, their fluorescence or Raman scattering can be dramatically enhanced. Surface enhanced Raman scattering (SERS) and surface enhanced fluorescence (SEF) utilize this effect and have become widespread techniques for characterization and detection of molecules at very low concentrations.[67–70] These have shown to increase sensitivity for their respective technique by six orders of magnitude in many cases,

and up to 10^{14} in specific cases.[71] Groups continue to work towards single molecule detection with high specificity in more ambitious cases for medical diagnostic applications.[72,73]

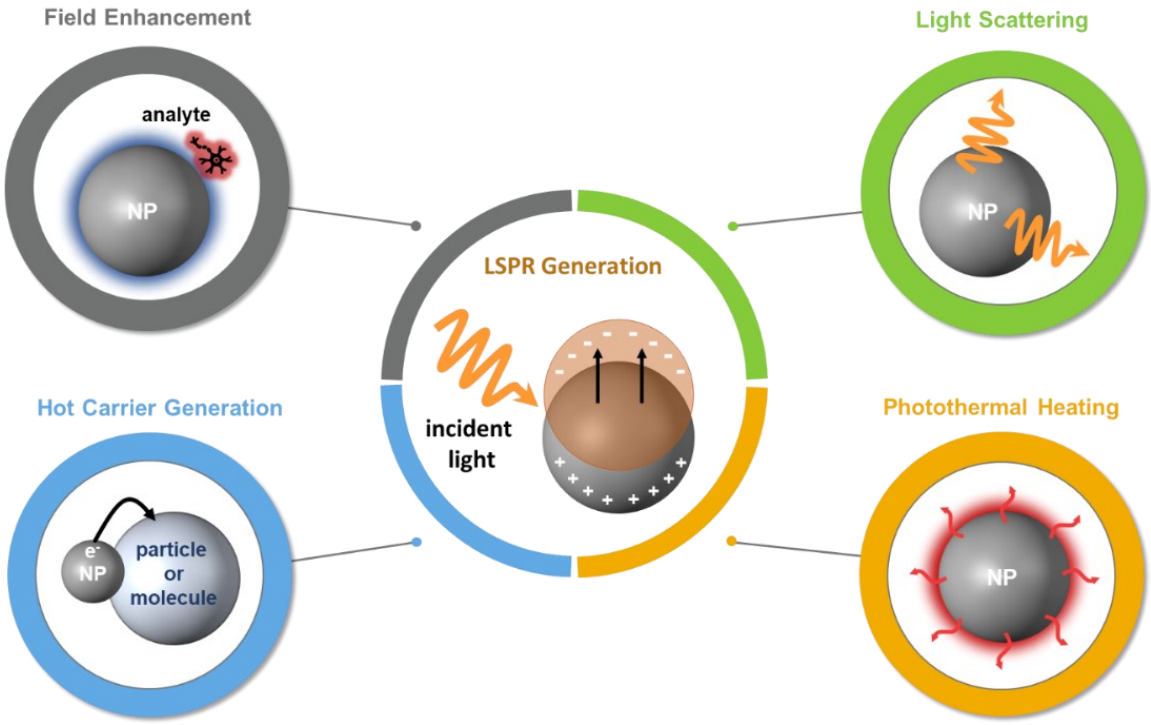

Figure 1.4. Depiction of four possible mechanisms of LSPR relaxation: (A) Enhancement of local electric field. (B) Scattering of incident light. (C) Generation of high energy ″hot″ electrons. (D) Localized heating by the photothermal effect. Adapted from reference (61).

The use of plasmonic light scattering has predominantly been used throughout biology and medicine.[74,75] Bioimaging is possibly the most promising application and works similarly to SERS mentioned above. The major difference is that focus will now be directly on the light scattered by the plasmonic nanostructure. The frequency of the LSPR, and therefore the light re-emitted, is highly sensitive to the direct environment of the NP. Introducing a biomolecule or cell close to the plasmonic NP will cause a change in the scattered light energy and can be monitored using microscopy, or as a contrast agent in commuted tomography (CT) scans.[76,77] This is useful for analysis of molecules that don't produce strong fluorescence or Raman scattering patterns themselves. More recently, the scattering

of light by plasmonic NPs has been incorporated into solar cells to increase electricity generation efficiency. The constant scattering of light works to trap the light within the solar cell, giving the active photovoltaic material additional time to absorb it.[78–80]

In the past, non-radiative dissipation of LSPR energy was seen as detrimental to the utility of a given plasmonic material but have flourished now for many unique and exciting applications.[81,82] The absorbed light energy can be used to excite electron above the material Fermi level, to generate what is known as ″hot electrons″. These can then be directly donated to a neighbouring molecule or material. Most notably, when plasmonic NPs are used in conjunction with a semiconductor catalyst, the donation of the hot electrons to the conduction band of the semiconductor can increase photochemical process efficiency.[83,84] This has been explored to aid environmentally relevant catalytic processes such as pollutant degradation[85], reduction of CO_2,[86] and even H_2 generation by water splitting.[87] The choice of plasmonic material and catalyst is very important in such applications to allow efficient transfer of the formed hot electrons.[88] Though less commonly explored, it has been shown that certain plasmonic NPs can facilitate these transformations themselves by directly injecting the hot electrons to species like CO_2 and H_2O without the need for an additional catalyst.[89] For medicinal purposes, certain plasmonic NPs show antibacterial properties as the hot electrons can be used to make reactive species upon reaction with O_2.[90] These reactive species can then damage proteins, DNA and cell walls of certain bacteria.[91]

Lastly, after generation of an LSPR, the absorbed light can be converted to localized heat through a series of non-radiative processes (Figure 1.5). The LSPR decays to generate hot electrons which in this scenario will not be separated from the NP and will instead redistribute the energy to other electrons within the particle.[92] A process known as electron-phonon coupling will finally occur which results in the dissipation of that energy as heat.[93] This entire process happens on a nanosecond timescale, and a rapid surface temperature increase of several hundred degrees can be achieved.[94] The field of medicinal chemistry has used this mechanism for treatment of cancerous cells in a process known as photothermal therapy.[95] By bringing plasmonic NPs to a tumor, followed by selectively radiating the area of concern with a light or laser the heat generation can induce cell death.[96,97] This heat could also be used for any number of other applications,

ranging from heat-driven catalysis[98,99] to sterilization processes[100] and even de-icing.[101] Notably, the heat can be used for distillation of water to purify using just light.[102] This concept will be explored next to review the interest in the research area, the state of the art, and opportunity of plasmonics within the water purification field.

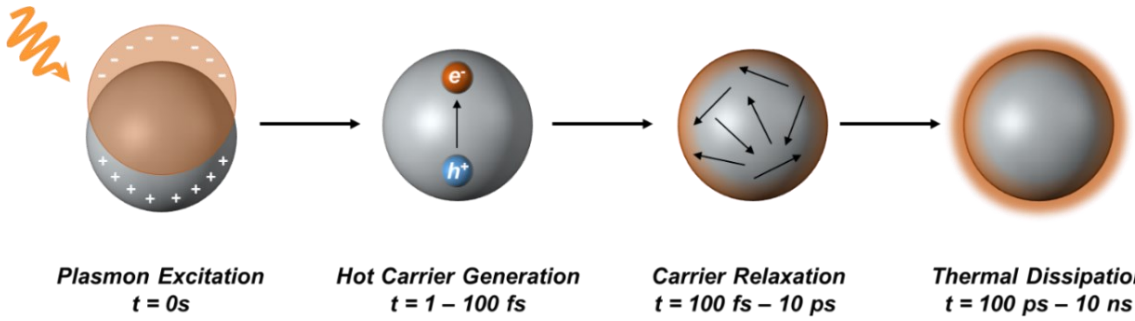

Figure 1.5. Schematic of plasmon excitation at t = 0, with subsequent generation of hot electron-hole pairs, then thermal relaxation by electron-phonon coupling with final thermal dissipation to environment. Adapted from reference (92).

1.2 Solar Desalination

Tackling freshwater shortage worldwide has emerged as one of the most pressing humanitarian issues of our generation.[103] Currently, 2.7 billion humans live under times of severe water scarcity for at least one month of each year.[104] Close to 1 billion of these people lack access to a clean water throughout the year. Ongoing events such as population growth, climate change, and further industrialization are increasing demand while causing contamination of freshwater reserves.[105] It is therefore crucial to expand access to clean water through traditional and modern approaches. One attractive method to boost clean water production is by using alternative water sources.[106,107] The most readily available sources of water worldwide are saline, which includes oceans, inland seas, and brackish groundwater. Direct consumption of water from these sources is not possible, so removal of dissolved solids by desalination is required. Major innovations over the past 50 years in desalination technology has made it a viable option in certain areas, though limitations exist preventing widespread use.[108,109] More recently, researchers have switched focus to desalination using only sunlight energy as the input potentially

reducing their cost and carbon footprint.[110,111] Solar desalination can be both direct and indirect. Indirect solar desalination compounds solar collection, using photovoltaics or thermal collectors with traditional desalination technology.[112] Direct on the other hand aims to mimic Earth's natural water cycle, which is effectively a planet wide open distillation plant in perpetual operation.[113] We can once again look back thousands of years ago when ancient Greek mariners practiced a rudimentary form of solar desalination for water treatment.[114] The following section will introduce the working mechanisms of standard desalination methods, as well as their shortcomings and future use. This is followed by an introduction to the development of photothermal water purification methods where the state of the art will be examined as well as the current shortcomings and opportunities for material design and engineering towards sustainable and reliable solar desalination.

1.2.1 Traditional Desalination Methods

As mentioned, it is difficult to dispute the potential of desalination to provide clean drinking water for an ever-demanding planet. However, standard desalination techniques are generally much more expensive to produce clean water. The principal methods to accomplish this on a larger scale are thermal distillation (TD) and membrane-based filtrations.[115] Within these main methods are many subcategories, and new options are being discovered rapidly. Solar desalination falls under another wing and comprises any process where the major energy contribution comes from sunlight and will be discussed at length in the following sections. A summary of select techniques is given in Figure 1.6. While a complete description of every technique is out of the scope of this thesis, the state of the art for the most popular options will be discussed to discover where improvement lies within each technique.

The practical utility of TD as a means of freshwater generation from seawater has been limited by the high energy consumption causing large amounts of emissions.[116,117] TD however is quite a mature technology, and unique ways of recycling heat within a system have been developed.[118–120] Most modern TD systems work below atmospheric pressures to decrease the temperatures needed for steam generation.[121] Multi-stage flash (MSF) is the most popular among distillation techniques which involves cycling preheated saltwater through a series of tanks where each tank rapidly evaporates the water, producing steam.[122,123] The steam

will recondense on pipes containing incoming source saltwater and transfer the heat released from condensation to it, thus recycling the energy. This occurs at each stage and the condensed water will drop onto drip trays for removal from the system.[124,125] A similar route, known as multiple effect (ME) distillation doesn't require preheating before introduction into the system, instead pumping in ambient temperature water. Once introduced though, the salt water is rapidly heated, and flash evaporated under reduced pressure before being sent to the next chamber which is under lower pressure than the first. This allows the saltwater to be evaporated again without re-heating it, and this process can be repeated many times.[126,127] The energy consumption of ME plants can be much lower than MSF for these reasons.[128,129] Finally, vapor compression (VC) desalination works on the principal of generating steam which is rapidly compressed into a chamber. This compression step will increase the temperature of the steam before it recondenses on pipes with feedwater flowing through.[130–133] All three of these methods are quite similar, as is expected for such a mature technology.

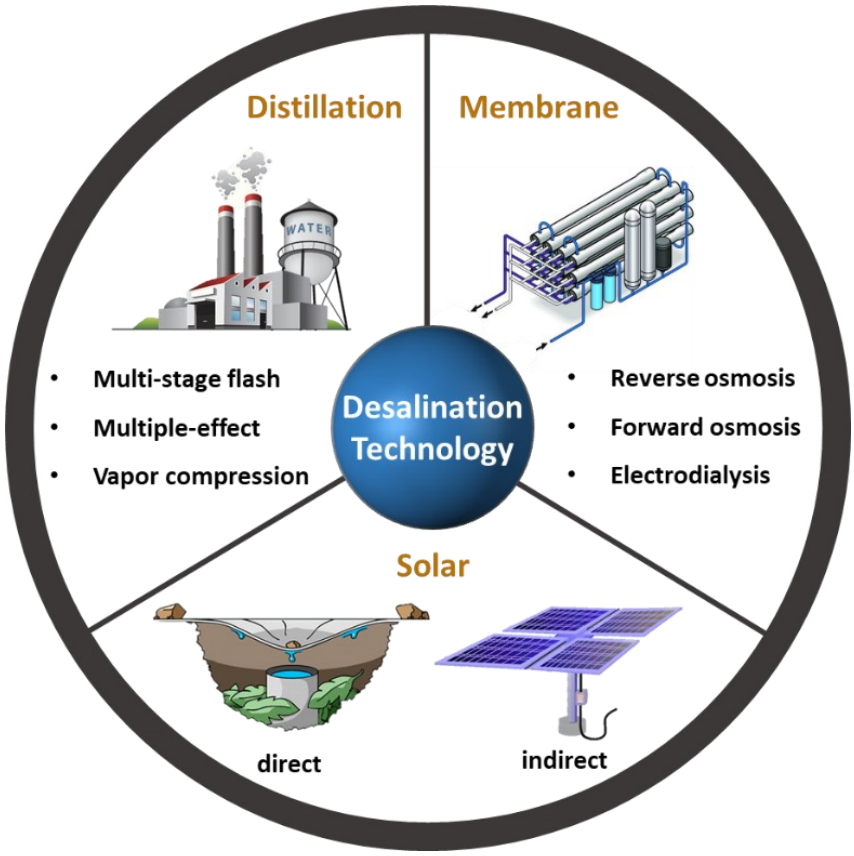

Figure 1.6. Select seawater desalination techniques.

Unfortunately, heating steps in TD methods generally use fossil fuel-based energy input. The high specific heat of water makes for large energy input requirement, making TD much less efficient than other methods. Ongoing efforts in this field are working to couple water treatment with waste industrial heat for the heating steps.[134] Often, this waste heat is quite diffuse and difficult to use effectively but has been proven economical in certain situations.[135,136] The high energy input cost compared to membrane methods which will be discussed makes it less ideal to spend renewable energy for TD desalination.[137] Finally, a major downfall here is that up to 60% of the feed water isn't evaporated and the brine must be dealt with.[138,139] This creates environmental concerns as simply pumping it back into the ocean can cause local salinity increases, killing marine life. Additional toxicity concerns from chemicals used in pretreatment steps have been flagged recently.[140]

Attempting to alleviate some of these issues, reverse osmosis (RO) has become the gold standard for desalination.[141,142] Source saltwater is forced through a semi-permeable membrane which allows water molecules to pass through while salt ions remain in the feed water stream.[143,144] This goes against natural diffusion behaviour though, and water transport from high to low concentration is not spontaneous. For this reason, energy is used to apply substantial amounts of pressure to force the water across the membrane.[145] While being the most promising desalination technique in many ways, there are still major deficiencies that prevent global RO implementation. Practically, the intensive infrastructure and capital cost required for the method make it inaccessible for many developing nations where it's needed most.[146] While the past couple decades have seen progress in membrane technology, high operational costs to replace membranes periodically can put RO further out of reach.[147] Once again, environmental concerns behind the use of fossil fuels to generate the needed energy and brine discharge are at the forefront of RO research, which have been well reviewed.[148,149] RO membrane development is working towards increasing the flow of water across membranes without sacrificing the salt ion rejection capabilities, with success by doping various materials like NPs, carbon materials, metal organic frameworks (MOF), among others.[150–152]

As opposed to RO where pressure is used to counteract the natural osmosis flow, forward osmosis (FO) uses it to its advantage. A generic FO system looks very

similar to RO, with a membrane separating source water (in this case ocean water) and what's called draw water.[153] Historically, this draw water contains a much higher concentration of a certain solute compared to the saltwater concentration, that can be removed in a second step.[154] The high concentration differential causes water to cross the membrane from the saltwater side to the draw water side. This diluted draw water is sent to a second step where the solute is separated from the water to be reused, affording the freshwater product. The two major advantages to FO are that no external energy is required to force the water across the membrane and because of this membrane fouling is much less of an issue for extended use.[155] Of course, the major downfall is that an FO system must be used in tandem with another water purification technique.[156] The state of the art for FO has moved in two main directions with one focusing on the solute for draw water and the other on membrane development.[157] Perhaps most interestingly, coated magnetic particles have been used as a draw solute which can easily be isolated afterwards by passing over a strong magnet.[158] The potential power in forward osmosis could be in capturing water from waste streams, for example high concentration brines and mining water waste that TD and RO systems can't deal with.[159] Still, finding suitable draw solutions remains incredibly challenging and must be addressed moving forward.

Electrodialysis is the final technique which will be briefly discussed here. The method works by applying an electric field to saltwater passing along a membrane.[160] This membrane is different from RO in that it selectively allows ions, not water to cross. This way, positive and negative ions will cross over the corresponding membrane arranged in a way to completely remove them from the main flow of water.[161] This affords pure water at the outlet of the dialysis cell, albeit in relatively low flux compared to other desalination techniques. The technology is still in its infancy, suffering from membrane fouling and high energy cost, but could become more important as research addresses these issues.[162]

Most conventional desalination processes share the same drawbacks, which are high energy demand, intensive infrastructure increasing freshwater production costs, and generation of brine which can be further contaminated by pretreatment chemicals. The most apparent solution to the first issue would be using renewable energy sources to run processes.[163] No doubt this will be a key factor in the near future and brings up the concept of solar-based desalination mentioned at the start

of the section.[164] Driving desalination via TD or membrane-filtration using energy input from solar panels, wind turbines, or other green sources is known as indirect solar desalination.[165] This helps decrease emissions, but can exacerbate the accessibility side, and doesn't solve the waste brine stream problem.[166] For the entire process, the extra conversion from light to electricity back to heat or mechanical energy can decrease the overall efficiency of freshwater generation. A light to heat transformation occurring directly at the site of desalination to facilitate evaporation is known as direct solar desalination.[167] Broadly, the class of materials capable of doing this transformation are known as photothermal materials and desalination employing them will be discussed below.

1.2.2 Photothermal Desalination

There remain countless opportunities in the desalination space and interest has been revitalized recently with strides made in direct solar desalination. Of course, the limiting factors behind evaporation using sunlight is the limited light absorption by bare water and low evaporation rates.[168] Generally, an additional material, known as a photothermal material, is needed to increase the efficiency of this process.[169] This brings up the major points of interest for unlocking the full potential of solar desalination, which are: (1) capture and use as much incoming light as possible; (2) effectively use any generated heat solely for the evaporation process and prevent losses via other mechanisms; and (3) efficiently recapture the generated steam.[170,171] The first is predominantly a material consideration and will be discussed first. The second and third are heavily influenced by the design of a solar desalination system, termed solar still from here on out.

The photothermal process is broadly defined as the excitation of a material by incident light, followed by heat release when relaxing to its initial state. As above, solar desalination concepts tend to come in strings of three ideas. The three prominent photothermal material classifications are: (1) carbonaceous and polymeric materials,[172,173] (2) metal-oxide semiconductors,[174] and (3) plasmonic NPs[175,176] which are classified based on the principle of one of the heat generation mechanisms (Figure 1.7). Carbonaceous and polymeric materials will generally be black in appearance when they are strong broadband absorbers. In these cases, the absorbed light energy causes excitation of electrons from π to π^* orbitals.[177] The

relaxation can occur by energy transfer to vibrational modes, resulting in temperature increase. Semiconductors can similarly be excited, but in this case generates an electron-hole pair if the incoming energy is larger than the bandgap of the semiconductor.[177] The excited electrons that were excited above the bandgap will relax to the band edges and non-radiatively across the bandgap thus converting absorbed light energy into heat. Finally, plasmonic NPs will generate heat through the decay of hot electrons, as described in section 1.1. Traditionally, carbon-based materials have been well explored based on their abundance (i.e. from biomass sources) and ease of conversion to strong solar absorbers by carbonization.[172] Plasmonic NPs are considered the most promising photothermal materials as the plasmonic generation and photothermal relaxation process can reach much higher efficiencies. This means that more of the absorbed energy can be converted into thermal energy compared to other materials. The main bottleneck of plasmonics for photothermal processes has been the high cost and limited scale of fabrication, which will be further discussed in the coming section.[178]

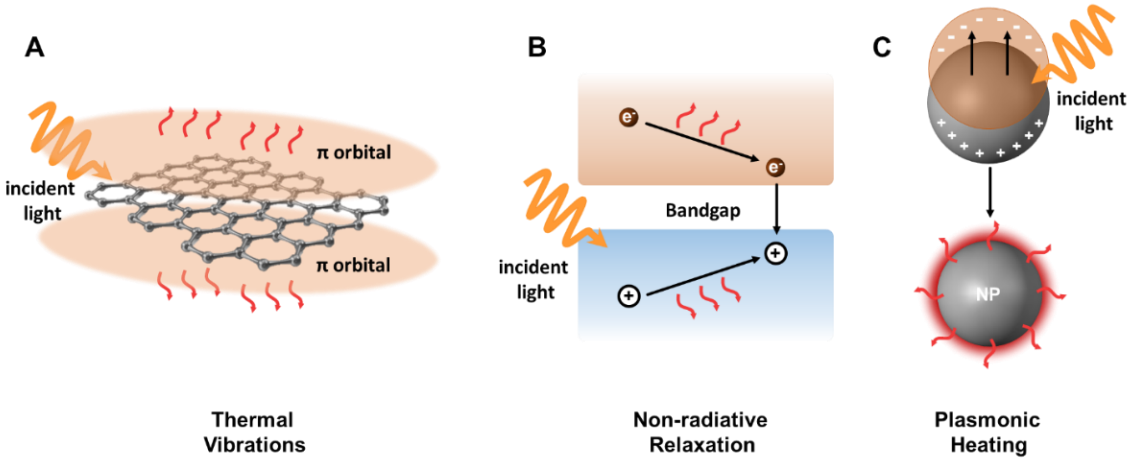

Figure 1.7. Mechanism of photothermal heating by (A) thermal vibrations, (B) non-radiative electron-hole pair relaxation, and (C) plasmonic localized heating. Adapted from reference (172).

Apart from choosing the right photothermal materials, its placement within an evaporation system is important, and several common layouts are presented in Figure 1.8.[179] Early solar stills, the photothermal material was placed at the bottom but most of the generated heat is lost to the bulk saltwater, with only small

amounts of steam bubbles reaching the surface. A second method requires dispersing the solar absorbing material throughout a sample of water which will heat up after being illuminated. This heats the container more effectively, but still suffers from energy being lost below the surface. The third and currently most explored configuration is known as interfacial heating.[180] Here, the photothermal material is confined to the water surface, where most of the heat generated can be used towards evaporating water with minimal thermal losses. The effectiveness of a photothermal material for the evaporation process is known as the solar-to-vapor generation efficiency.[181] This encompasses the entire process of light absorption, conversion to heat, evaporation of water, and finally release of the steam. It can be used to track new materials and systems and will be used throughout this thesis. Without using solar concentrators, bottom heated systems can generally reach efficiencies of up to 10%.[182] Bulk system fare slightly better, with top contenders peaking at around 30% efficiency.[183] Interfacial systems consistently perform with efficiencies above 80% and will be the focus in this thesis.

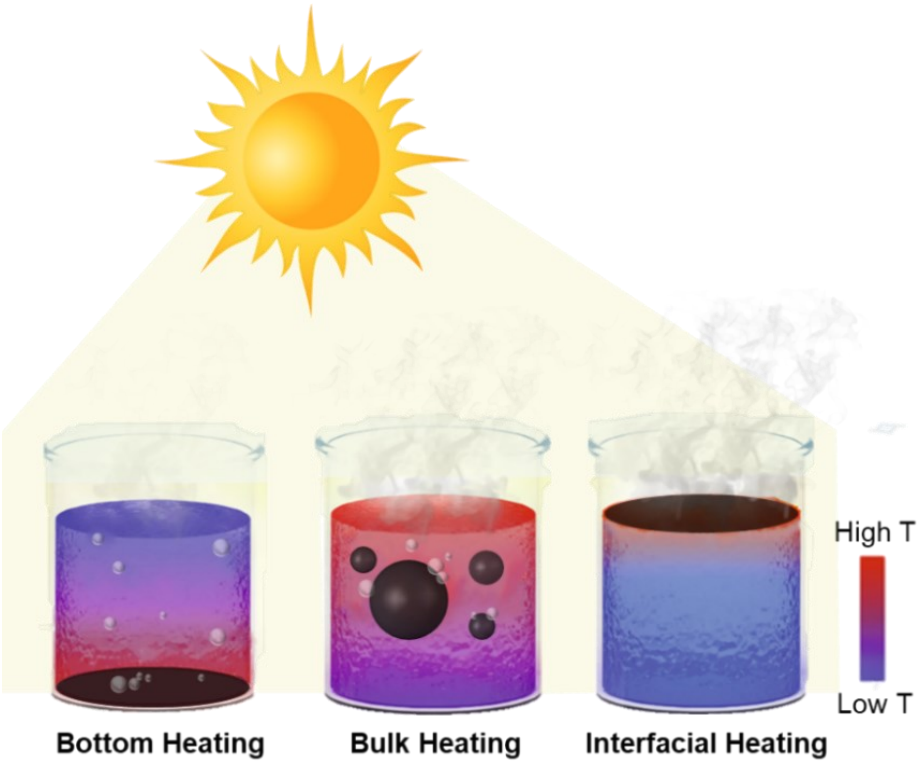

Figure 1.8. Schematic of interfacial solar evaporation methods showing heating processes. Adapted from reference (180).

Within the realm of interfacial evaporation there has been countless advances in the past decade. Three key characteristics have surfaced proving essential for interfacial solar evaporation.[184] They are: (1) increase insulation between the bulk water and the evaporation surface, often accomplished by layering foam or other insulating materials beneath the photothermal interface. (2) Enable sufficient water replenishment to the evaporation surface, typically ensured by incorporating wicking materials. (3) Have an evaporation interface with a porous structure, which increases the surface area in contact with water and facilitates efficient release of steam. The initial concept of interfacial evaporation consisted of photothermal interfaces floating directly on water. These evaporators lose heat more readily to the bulk water, but nevertheless remains a strong area of research. This is due to the ease of fabrication of such devices, and carbon materials are most at home in this category.[185] The carbonization process can most often lead to solar absorbance over 90%, and porous networks retained from the parent biomass allows for water transport across the materials. This type of structure is termed monolithic can be fully comparable to expensive synthetic materials such as graphene.[186] For example, a two-dimensional (2D) carbonized bamboo shoot recorded a solar evaporation efficiency of 80% when floated directly on water under 1 sun irradiation.[187] Meanwhile, another report showed that a floatable graphene membrane reached rates just slightly above the bamboo evaporator under the same conditions, corresponding to an efficiency of 82%.[188] While structures such as these partly satisfy the three characteristics above, newer structures can provide more insulation to the evaporation surface without sacrificing ease of device fabrication. The idea here is to place the photothermal layer on top of a substrate which provides insulation, buoyancy, and water transport (Figure 1.9).[179] These can be considered 2D for very thin substrates or three-dimensional (3D) for thicker substrates. For example, our group reported group 4 transition metal nitrides TiN, ZrN, and HfN as an efficient 2D interfacial evaporation platform when coated on a floating porous aluminium oxide interface.[189] The evaporation and desalination rates were the fastest reported at the time due to the inherent material efficiency. Since then, relatively simple evaporation devices using various foam supports have shown the importance of the maximized insulation, achieving even higher efficiencies.[190] As a universal trend, thicker foam leads to decreased thermal losses but must be balanced with water transport to the surface. Not only is this

important to keep the photothermal interfaces properly wetted during evaporation, but for desalination water flow to and from the interface resists salt buildup.[191] This is perhaps the most important aspect of interfacial solar desalination engineering. If salt is allowed to concentrate near the surface, crystallization can occur which blocks water vapor from escaping, increases reflection of incoming light, impeding the process. Taking all the above-mentioned material and design aspects into consideration, research groups have achieved impressive solar desalination results.[192–194]

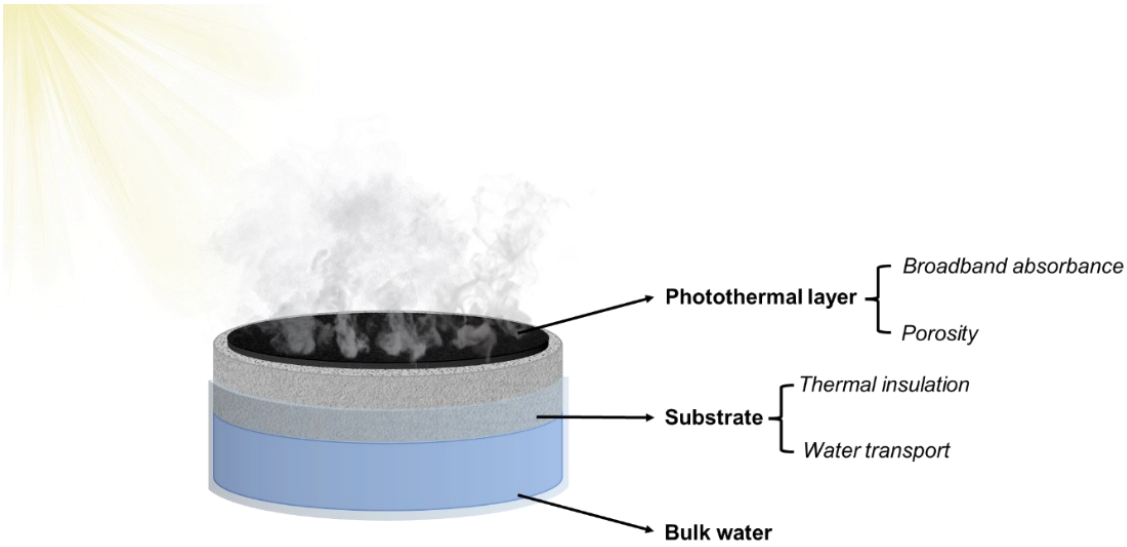

Figure 1.9. Generic schematic of layered interfacial desalination support. Adapted from reference (184).

The evaporation process for a photothermal material on a 2D interface is fundamentally limited by the amount of energy required to convert water from a liquid state to a vapor state. This is seen in the following equation describing the overall solar-to-vapor generation efficiency (η):

$$\eta = \nu \frac{C\Delta T + \Delta_{vap} H_m}{C_{opt} q_i} \tag{1.2}$$

where ν is the evaporation rate, C is the specific heat capacity of water (4.18 kJ kg^{-1} K^{-1}), ΔT is the change in temperature, $\Delta_{vap}H_m$ is the liquid to vapor phase

change enthalpy of water, C_{opt} is the optical concentration, and q_i is the illumination intensity of the light in kW m^{-2}. The equation states that the rate of water evaporation and therefore the efficiency depends on how much of the incoming light energy (bottom term) is used to facilitate the transition of liquid water to vapor (top term).[195] This isn't surprising as a description for water evaporation, but interestingly if the value of the evaporation rate is too high the efficiency will be larger than 100%. This is of course impossible and therefore means that there is a thermodynamic limit on the rate due to the enthalpy of vaporization.[196] In other words, at 100% efficiency every bit of light energy is being used for the phase transition from liquid to gas. This is known as the thermal evaporation limit, and research focus has shifted towards unique ways of altering it for increased water generation rates.[197] The evaporation rates can be enhanced by increasing the intensity of incoming light. This can be done by concentrating light using mirrors and lenses,[198–200] but unfortunately, can be expensive and difficult to employ, particularly for floating desalination where evaporation devices are prone to moving.[201–203] 3D photothermal interfaces with large aspect ratios can take advantage of both surface evaporation and lateral, or side, evaporation. Here, the increased water generation rates arise from calculations based on the projected ground area and not the entire surface area.204–206 In effect, these are just larger surface areas within the same footprint.

The only other way to raise the thermal evaporation limit is to decrease the enthalpy of vaporization of water. While seemingly counter-intuitive, this is a recently described phenomenon.[207,208] Certain polymeric materials such as hydrogels have been shown to decrease the enthalpy of vaporization of water.[209,210] Hydrogels are networks of cross-linked polymer chains capable of absorbing and trapping large amounts (>70%) of water within the structure.[211] They have been widely studied in the biomedical industry for drug delivery, as medical dressings, and for bone tissue, neural tissue, spinal cord, and cardiac repair.[223-225] Not until quite recently has their interest towards water evaporation come to the forefront. Initial studies into this phenomenon suggested evaporation proceeding via a water cluster theory. Here, water is evaporated in small groups as opposed to as single molecules.[215] The decrease in evaporation enthalpy was thought to arise when the functional groups inside of the hydrogel interact with water and disrupt the hydrogen bonding, though no mechanistic studies were reported. Recently,

researchers have identified the so-called photomolecular effect as the reason for evaporation rates above the thermal limit.[216] Here, water clusters at the hydrogel-air interface can be cleaved directly by incoming photons without going through any heat generation process (Figure 1.10). Chen et al. suggested that this is a very efficient process compared to thermal evaporation and offered several mechanistic studies, also stating this phenomenon could be occurring widely in nature.[217] The photomolecular effect working in tandem with photothermal evaporation is thought to allow evaporation rates higher than the thermal limit.[218]

By incorporating Ag and graphene NPs into a polyacrylamide hydrogel for solar desalination, Li et al. reached evaporation rates of 3.09 kg m^{-2} h^{-1}.[219] The units here simply show the mass of freshwater generated for a normalized evaporation area per unit of time and is the standard for reporting in the field. Using the standard enthalpy of vaporization value for water would lead to an efficiency of 211%, over 2 times the thermodynamic limit. Taking the decreased vaporization enthalpy into consideration as will be discussed in Chapter 6, the efficiency was just over 80%. While, more concrete proof is needed to validate the proposed mechanism, but regardless, hydrogels have already made profound effects for interfacial desalination and will continue to do so in the future.[220,221]

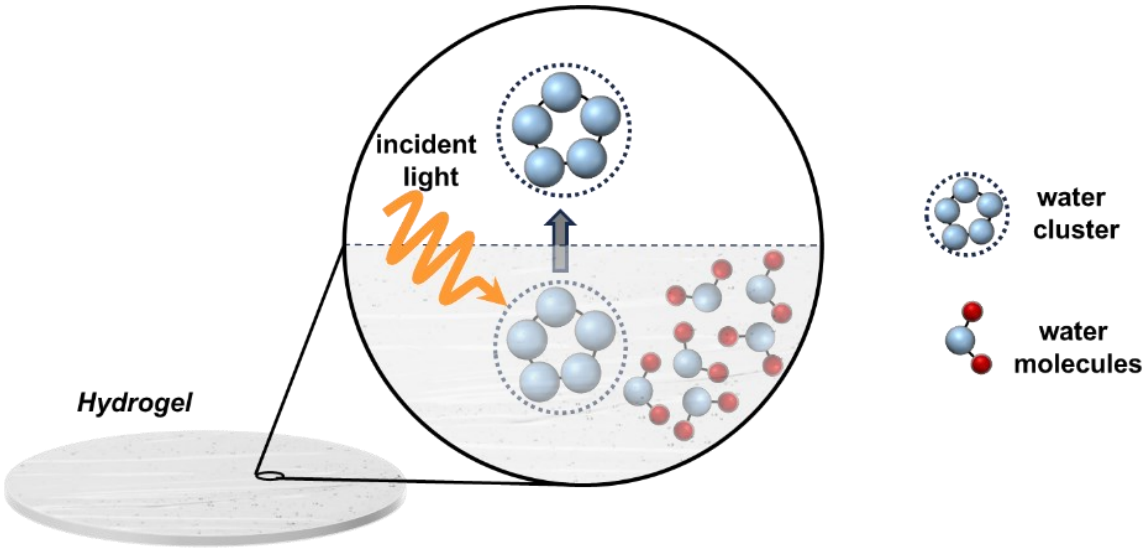

Figure 1.10. Proposed schematic for lowering of water vaporization enthalpy by the photomolecular effect. Adapted from reference (209).

1.2.3 Scalable Floating Desalination

Up to this point, all the discussed photothermal evaporation interfaces have been studied only in a controlled laboratory setting. While the results have been exceedingly promising, it is important to keep in mind that moving from the lab to real world application often brings many new challenges and interfacial solar desalination is no different.[222,223] So far, only few research groups have attempted to increase the scale of evaporators. It is crucial to continue pushing floating solar evaporation as it has the potential to address issues with existing solar still designs. Conventional land solar still (LSS) designs have been used for centuries.[224] Nowadays, a concrete or steel basin with a glass or plastic roof is filled with salt or contaminated water and the heat of the sun is used to form vapor, which recondenses on the roof.[225] This roof is slanted to drip the water backdown to a collection trough (Figure 1.11). Similar to the floating solar evaporation discussed above, many improvements have been made by incorporating photothermal absorbers, evaporation wicks, layered condensation chambers to recycle heat, etc.[226–228] There are two major issues that have yet to be addressed with LSSs.[229] First, the typical performance comes between 20-40% solar efficiency which makes the average water cost very high compared to other methods. This cost includes primarily the materials used and cost of pumping water to the still. Secondly, LSSs have yet to effectively solve the issue of fouling. For desalination this is caused by a buildup of salt which can corrode materials and reduce water generation rates. This makes for more regular cleaning and parts replacement, further increasing the unit cost of water. The additional substantial land use could make project planning difficult.[230]

The losses in the efficiency of solar stills arise mainly from the addition of the cover which impedes light transmission, particularly after water droplets have recondensed on the inside.[231] When considering in the daily and monthly fluctuation in solar intensity this can have a profound effect on the amount of water produced. The closed chamber also decreases air flow and increases operation relative humidity to 100%, both of which supress vapor formation.[232] Each of these works to decrease the effectiveness of solar stills in the real world, and this corresponds to water production costs 10-100 times greater than other desalination methods.[233] Floating solar stills (FSSs) must also contend with these efficiency

drops, perhaps even more so as waves and currents in the cold ocean water below increase thermal loss due to convection.[234] The benefits of floating desalination can easily overcome these issues.[235] FSSs can be made using more affordable materials as they don't have to support the weight of the source water, and replenishing water by pumping it isn't a factor. This can decrease the cost well below traditional TD and RO methods. Addressing the issue of fouling is also possible thanks to the massive amount of water beneath the FSS. By providing a sufficient flow from the ocean water to the evaporation surface and vice versa, the net flux of salt and other contaminants is down towards the bulk water.[236] This is because there is negligible change in the salt concentration of the ocean water during evaporation, and osmosis will work to bring the increased salt concentration on the FSS surface back to the now more dilute water below. This opposes LSSs where the water below is also increasing in salinity. Efficiency loss from salt buildup has been a major drawback of the technology. Various scaffolds that avoid salt buildup in FSSs, known as salt rejection, have been investigated as will be further discussed in Chapter 5.[237,238] While solar evaporation has been used for hundreds of years, the field as a competitive alternative to traditional desalination methods is still in its infancy. New materials and engineering design breakthroughs are seeking to make solar desalination, particularly while floating an attractive source of freshwater.

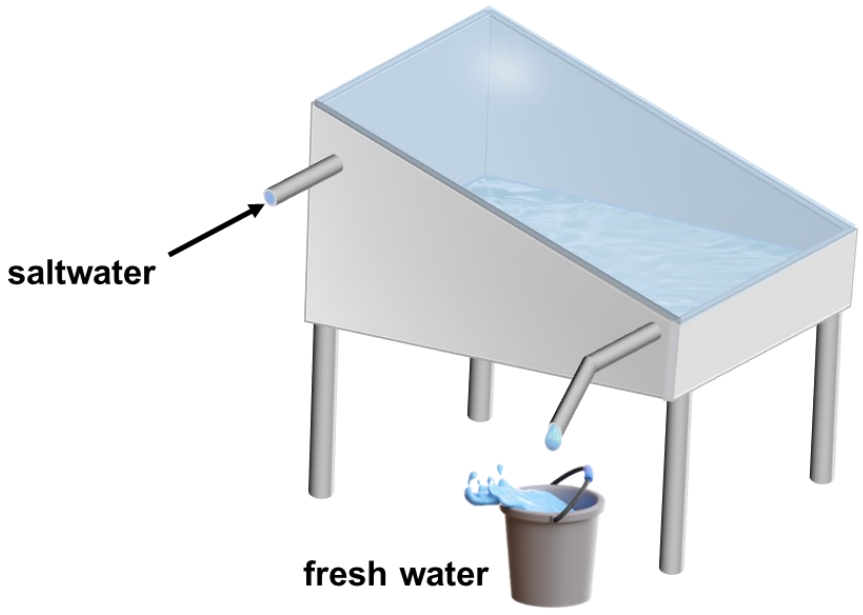

Figure 1.11. Base schematic of an LSS. Adapted from reference (225).

1.3 Alternative Plasmonic Materials

Many of the examples presented so far have predominantly utilized either Au or Ag as the plasmonic material. This isn't just because researchers wanted to follow in the footsteps of the Roman glassmakers of the past. The position of their LSPR is within the visible spectrum, and the metals also tend to exhibit fewer optical losses in this region making them attractive for applications discussed above.[239,240] For the case of Au, interest also lies in the overall chemical stability, even at the nanoscale whereas Ag tends to be more chemically unstable.[241,242] For these reasons, many of the fundamental studies for plasmonic NPs have been conducted using Au and to a slightly lesser extent, Ag.[243] Countless synthetic strategies and methods have been developed in this regard.[244–246] An important consideration when using Au is the economic aspect as Au metal and precursors can be quite expensive. This limits the application when large amounts of material are required.[247] To expand the utility of the field of plasmonics, it has become clear that identifying and researching new materials will be important moving forward. This section will provide a brief overview of some of the emerging classes of plasmonic materials that are being explored to address the issues noble metals have. This new generation of materials includes ceramic, or refractory, NPs which will be the overarching focus. Within this category, previous studies in our lab on transition metal nitrides (TMNs) will be introduced before focusing in on the material used for the current thesis project, transition metal carbides (TMCs). A short overview on the historical importance and synthetic methods for TMCs will be followed by their plasmonic exploration to date.

1.3.1 Frequently Studied Alternative Plasmonic Materials

Plasmonics is entering an explosive new generation of research thanks to the many groups worldwide identifying and studying new classes of materials.[248,249] This has led to exponential growth in the field at a pace not seen before. Spanning large portions of the ultraviolet all the way to the infrared region of the light spectrum, new applications are constantly being described as well.[250] Often, theoretical studies are used to flag potential plasmonic materials as discussed in Section 1.1, followed by experimental studies to verify the predicted properties. The

breadth of materials is out of the scope of this thesis, but some of the most promising alternatives have been summarized in Figure 1.12.[251]

Non-noble metal such as Cu and Al are very attractive option since their LSPR can be tuned between ultraviolet (UV) region all the way to the near-infrared (NIR) region, depending on the NP geometry.[252–254] Their low cost and relative abundance are the big selling points for applications that would require much larger material amounts such as desalination. The major issue with these metals however is the oxidative instability.[255] Research interest continues for Cu and Al, with the focus points being on stabilizing the NPs to avoid oxidation and ultimately destruction of the plasmonic response. Often this is achieved by coating the NPs with more stable chemical species such as polymers, carbon, or SiO_2.[256,257]

The inherent material downfalls of metal plasmonic NPs can be solved by employing materials that behave like metals. The first example of this was through doping of semiconductors to increase their carrier concentrations.[258,259] Depending on the semiconductor, dopant, and extent of doping, LSPRs can be generated. Keep in mind this increase in metallic character corresponds to the real part of the dielectric function becoming negative (section 1.1.1).[260] Choice of semiconductor focuses on the optical bandgap of the material, which correspond to interband transitions. While these transitions are crucial for semiconductors in their performance in photocatalysis for example, but detrimental to their function in plasmonics as they are considered losses. Therefore, the bandgap of the chosen semiconductor must be larger than the light wavelength of interest.[261] These examples tend to fall within the lower energy NIR region and require very high levels of doping to become plasmonic.[262] This is the major limitation of semiconductor based plasmonics as reaching the required dopant levels can lead to phase segregation and introduce crystal defects which destroys any LSPR potential. Nevertheless, semiconductors are still of research interest as they could theoretically have LSPR up to the THz range, making them potentially useful for communications application.[261,263] While this is not an exhaustive list of every alternative material, it is aimed to provide an overview of new materials of interest for plasmonics. Whether an increase in physical and chemical stability, decreased cost, or tuneability is the focus, the ever-growing library of noble metal NP substitutes is opening many new avenues. The materials that are currently witnessing the most impressive coming of age is a family known as refractories.[264]

Broadly, refractory materials are those with unusually high melting points and that maintain structural properties at very high temperatures. They are resistant to chemical degradation and sintering even at elevated temperatures. Refractories as plasmonics will be discussed next, leading to the titular compounds, transition metal carbides.

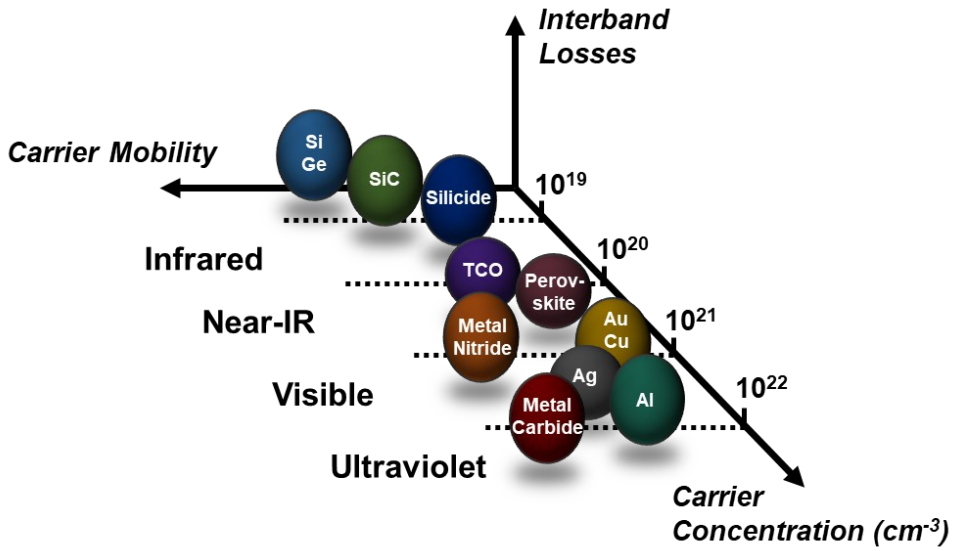

Figure 1.12. Chart of various plasmonic nanomaterials showing carrier concentration (amount of free electron density), carrier mobility (speed of free carrier movement within material), and losses (spheres represent low loss materials, while ovals represent materials with slightly higher losses). Adapted from reference (248)

Semiconductors, as discussed in the previous section can be made plasmonic by doping, provided the dopant introduces enough carriers to induce metal-like behaviour. On the other hand, one can reduce the carrier concentration of a pure metal to achieve similar results. In effect, this is 'diluting' the metal by introducing non-metallic compounds into the lattice.[265] A literature survey shows the optical properties of many such species have been studied. Among these are metal silicides and germanides,[266–269] and ceramics such as borides,[270,271] nitrides,[272] and carbides.[273] In many cases, the introduction of the non-metallic species alters the electronic structure to the point that LSPR damping occurs, essentially increasing the optical losses. Silicides and germanides, which are compounds of metals with silicon or germanium, respectively, are an example of this phenomenon.[266,269]

Heavy altering of the optical properties occurs, and effective LSPR formation has remained elusive. These materials are important technologically as they can be grown or deposited very precisely for ease of fabrication and integration into integrated circuits and microchips. This has kept them in the research spotlight to try and overcome optical loss issues.[274]

Among the discussed noble metal plasmonic alternatives, transition metal nitrides (TMNs) have no doubt received the majority of the focus in the recent years. Nitrides of metals such as Ti, Zr, Hf, Ta, and W are refractory[275,276] and early theoretical studies have showed them to possess LSPR in the UV to NIR regions depending on the transition metal and particle shape and size.[277] This makes them very interesting candidates as direct Au or Ag substitutes. Since these breakout computational analyses, there have been far too many publications surrounding TMNs to properly cover in this thesis, but some highlights will be covered. Studies have seen improvements to the synthesis with emphasis on morphology and composition control, and vast effort showing potential plasmonic applications.[278,279]

Our group was among the first to experimentally study the optical properties of colloidal TMN NPs, preparing TiN, ZrN, HfN, and Cr_2N.[280–282] The resulting TMNs showed LSPRs in the UV (Cr_2N), visible (HfN, ZrN) and NIR (TiN) regions. Initial application sought to take advantage of their theoretically proposed efficiency for photothermal generation, which was expected to exceed Au NPs. The photothermal activity was confirmed experimentally, and our group then exploited it for solar driven evaporation and desalination.[189] Each TMN NP sample was loaded onto a simple porous alumina substrate. Out of the group 4 TMNs, HfN recorded the highest solar to vapor efficiency of 95%, using Equation 1.2. The application of TMNs to desalinate water was reviewed in the early stages of this thesis project.[283] This was to summarize the benefits of TMNs towards desalination, and target shortcomings of those reported. Most studies focus on TiN NPs as the photothermally active material due to the broadness of the observed LSPR, equating to more absorption of the solar spectrum. Ti also tends to be much more economically friendly compared to Zr and Hf. Under 1 sun illumination, TiN NPs on carbonized wood reported by Guo *et al.* showed the highest reported water generation rates so far, which approached 1.4 kg m^{-2} h^{-1},[284] and a corresponding solar-to-vapor generation efficiency of 92%. Despite their superior photothermal

behaviour, certain stability issues have been noted for nanoscale TMNs including decomposition in acidic media, limiting their widespread applicability.[285,286] While TMNs have had massive growth in interest in the past five years or so, a closely related group of refractory materials known as transition metal carbides (TMCs) have yet to be widely studied. TMCs are historically an important class of compounds, and recent theoretical studies have shed light on their potential as efficient plasmonic materials for certain metals. The following section will provide examples of TMC development and use in the past, focusing predominantly on the transition metals of group 4, 5, and 6.

1.3.2 Transition Metal Carbides

The carbides of group 4, 5, and 6 transition metals are generally described as being interstitial compounds.[287] This means that they are derived from relatively large transition metals acting as a host lattice to incorporate small carbon atoms. In such cases, the resulting TMCs are considered refractory and display metallic properties. They also exhibit exceptional hardness, high mechanical and thermal stability, and corrosion resistance.[288] Certain TMCs, including TiC and WC are industrially relevant and are used for coating cutting tools.[289] Transition metal carbides (TMCs) are prepared by introducing carbon atoms into the lattices of transition metals. Electronically, the introduction of carbon atoms leads to an interaction between the s and p orbitals of the carbon and the d orbitals of the metal atoms.[290,291] This causes the metal-metal bond distance to elongate, altering the free electron density (real part of dielectric) because of electron transfer from the metal atom to the carbon atom. The electronic structure of such interstitial carbides has made them of interest for many catalytic processes ranging from ammonia synthesis and decomposition, biomass conversion, and for electrochemical hydrogen production.[292–295] They have been compared catalytically to the Pt-group metals.[296]

A class of 2D TMC nanomaterials known as MXene phase carbides were the first examples of TMCs being studied for their optical properties. This was exciting as carbides up until that point had been mostly overlooked for their promising optical properties, and the strong research foundation on MXenes provides a good starting point.[297,298] In MXene, M represents an early transition metal, and X in

this case is carbon but can also be nitrogen. Like other TMCs, the interest in this class was for their potential use in electrochemical catalysis.[299] So far over 20 MXene phase carbides have been made using etching processes and range from monometallic to bimetallic. Examples of monometallic MXenes that have been reported are shown in Figure 1.13.[300] Those in green have been experimentally reported, and those in black are only theoretically studied so far. In terms of application, promising results have been shown for MXenes as electrical contacts, conductive fillers, and in energy harvesting, photovoltaics, among others.[301] MXenes have also recently been flagged as promising materials for plasmonics.

Like other alternative plasmonic materials, MXenes have metallic character, and similar to nitrides the introduction of carbon into the metal lattice tunes the real part of the dielectric function to produce LSPRs in the NIR region and longer wavelengths.[302] As has been noted, the location in the NIR region has made certain MXenes, such as Ti_2C_3 interesting for photothermal tumor therapy.[303] The potential for precise tuneability is of particular interest here, as incorporating mixtures of metals could help adjust the location and properties of the LSPR. Very recently, Ti_2C_3 was shown to theoretically support plasmonic resonance across the telecommunications wavelength range on optical fibers.[304,305] This presents a tantalizing prospect for highly selective optical fibre communications.[306] Furthermore, because Ti_2C_3 can provide up to 95% transmittance across the UV and visible regions, it has potential to be a lower cost option for transparent conductive electrodes.[307] Nevertheless, there are still some major concerns to address to further the utility of MXene carbide NPs.[308,309] First, the synthesis conditions are intensive, requiring expensive and dangerous chemicals during the exfoliation step. Secondly, controlling the surface termination can be difficult, and uncontrolled surface functionalization can dampen the plasmonic characteristics.

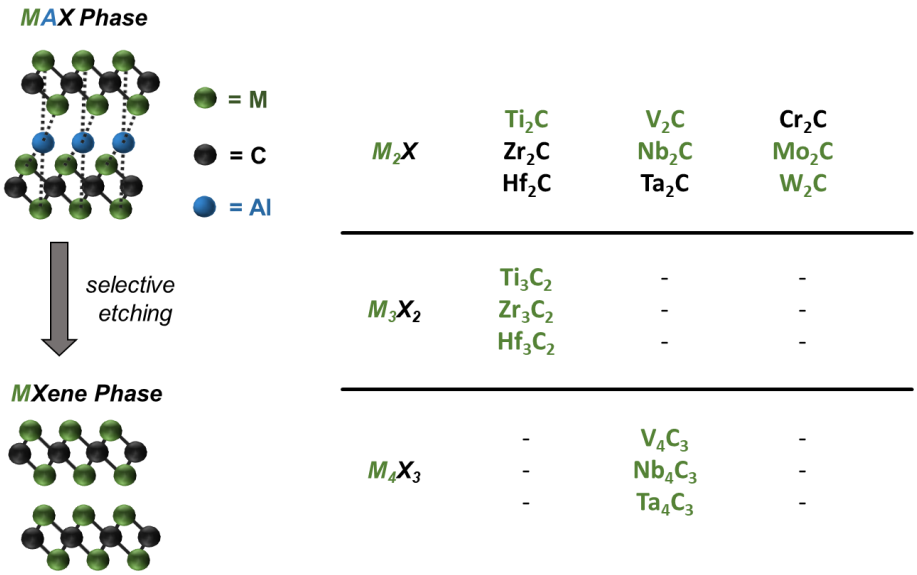

Figure 1.13. Representative reaction scheme for the synthesis of MXene phase carbide NPs (left) with previously synthesized (green) and theoretically studied (black) MXene metals and phases (right).

MXenes were the first instance of TMC nanostructures being explored for plasmonic applications. While there are synthetic challenges to deal with, they have demonstrated versatility across many fields of study already. As the area of 2D plasmonic carbides takes off, another opportunity has presented itself in 3D carbide NPs. Theoretical studies on group IV , V, and VI carbide NPs showed that they should have relatively broad LSPRs located in the UV region, extending into the visible region depending on which metal is present.[277] The authors chalked up the broadness of the LSPR to be from interband transition losses, stating that carbide NPs were not suitable plasmonic materials. It is possible that this paper, being well cited, put up a wall around 3D TMC NPs. Since this article, it has become more obvious that optical losses leading to LSPR broadening isn't necessarily detrimental, particularly for broadband applications, such as sunlight driven processes.[310] Furthermore, the authors only studied very large particles, where losses are known to increase with particle size, particularly as light scattering becomes more prominent (section 1.1).[311,312] The few pioneering works using 3D carbides have already set the precedent that TMC NPs could be much more interesting than claimed in the theoretical paper. For example, TaC NPs synthesized through a solvothermal method were used as a SERS substrate.[313] Again, SERS allows for the enhancement of analyte Raman signals by placing them

within the LSPR field of a NP. Doing this, Xi *et al.* reported signal enhancement of 10^7, putting them on par with the best reported noble metal NPs. In another report, WC NPs were employed by researchers in the groups of Liu, Guo, and Yang for degradation of methylene blue (MB).[314] They proposed that the broadband absorbance was from LSPR formation, and the subsequent hot electron formation facilitated the degradation. The process involved adsorbing the MB onto a carbide sample, followed by illumination of the isolated powder. They suggested that the NP LSPRs were able to couple when in close proximity to one another when dry, causing broadband absorbance into the NIR region. Further studies are needed to verify if this is a hot electron-initiated degradation or simply photothermal degradation of the MB. Either way, the absorbance efficiency makes them interesting organic pollutant candidates. While these studies have provided a small foundation, there is incredible potential for TMC NPs yet to be unlocked.

Synthesis of TMCs can be classified into two main categories: 1) solid-solid reactions and 2) solid-gas reactions.[315,316] The reaction is extremely customizable and requires just carbon or a suitable carbon precursor and the desired metal or metal precursor. The most common way to generate TMCs consists of high temperature carbothermal reaction where solid (graphite, charcoal) or gaseous (CO, CH_4) carbon is reacted with the metal precursor directly.[317,318] Generally, such direct synthesis methods require temperatures in excess of 1800 °C for extended periods of time, sometimes up to a week. This generally boils down to the solid-state diffusion of carbon into the metal. Newly presented methods aim to decrease the energy consumption of formation reactions by using more reactive carbon sources or adding materials that can help the reaction progress faster and at lower temperatures.[319] For this thesis, focus will be on methods of producing TMC NPs as opposed to bulk carbides. Here, heat management becomes very important to avoid sintering of particles during formation. Almost all examples of carbide NP synthesis are for the development of catalysts, but nevertheless provide important information moving towards TMCs as alternative plasmonic materials.

Modifications of the direct reaction of carbon or carbon containing materials with metal precursors (carbothermal reduction) have been made to produce TMC NPs. Often, these products are composite materials with carbon, meaning they are a mixture of TMCs and carbon particles.[315] In a couple examples, metal oxides were reacted with activated carbon to produce TMC NPs.[320,321] For Ti and W this gives

the most consistent results, and the activated carbon reacts at lower temperatures, around 1550 °C. By running the reaction under a reducing H_2 atmosphere, Zhang *et al*. further decreased the formation temperature of TiC NPs to around 1350 °C.[322] Each of these temperature decreases led to less sintering of the resulting product, but still required long reaction times for full carbide formation. Variants of traditional carbothermal reduction use small molecules like urea, or polymers such as chitosan to make a homogeneous gel network which metal precursors can be dispersed in (Figure 1.14A).[323,324] When heated in an inert atmosphere, the gel will decompose to form the reactant carbon. This can greatly increase the homogeneity of the NPs formed while isolating the carbide NPs from one another, so they don't sinter together. Another interesting method to help control the size and shape of carbide particles is by dispersing the metal precursor into a biological template. Xia and coworkers synthesized TiC, NbC, and TaC nanowires and nanotubes by using bamboo as a carbon source and template (Figure 1.14B).[325] Here metal oxide particles were dispersed throughout bamboo powder and reacted at 1300 °C. Similar to the chitosan and urea methods above, the bamboo pyrolyzes, meaning here that it turns to charcoal, and then reacts with the metal oxides.

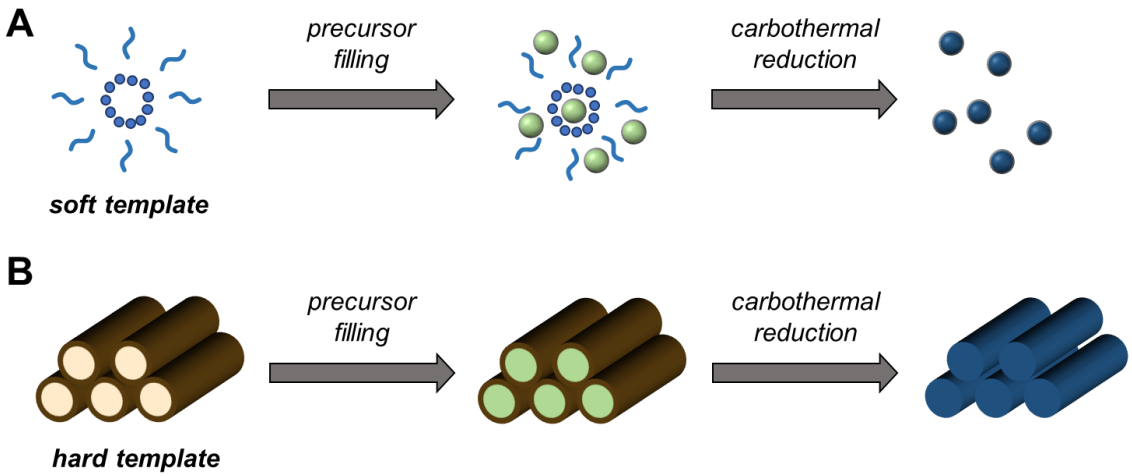

Figure 1.14. (A) Schematic of soft templating with urea, chitosan, etc., and (B) hard templating with biological materials for controlled size and shape during carbothermal reduction synthesis of carbide NPs. Adapted from reference (323) and (325).

For most carbide formation processes, the shorter amount of time the reactants are at high temperatures the better. Using microwaves for rapid heating has been shown to produce a wide range of TMC NPs.[326–328] Wan *et al.* synthesized high-quality W, V, Fe, Nb, Ta, and Mo carbide NPs using a microwave assisted combustion method.[329] Within minutes, the reactions were complete with no detectable sintering. Another low temperature method is high energy ball milling. This is known as a mechanochemical synthesis, where reactants are placed into a mill containing balls. As the balls are rotated, undergo high energy collisions. This energy can be enough to facilitate chemical reactions as has been shown for various TMC NPs, including WC.[330] This has been shown to work on relatively large scales, and due to the high hardness, the balls used in the mill can be made from refractory carbides themselves to avoid sample contamination.[331] Increasing pressure is a third way that the TMC formation reactions can proceed without reaching highly elevated temperatures. These solvothermal syntheses involve reaction with non-aqueous solvent in an autoclave.[332,333] The sealed chamber of the autoclave can be heated, which will surpass the boiling point of the solvent and increase the pressure. Under the nonstandard conditions, reactivity can drastically change and allow the low temperature formation of TMC NPs. In 2007, Ma *et al.* reported on the synthesis of TaC NPs using a solvothermal reaction of $TaCl_5$ and Na_2CO_3 which proceeded at 600 °C.[334] For this example, Mg was added as a reducing agent. One of the reasons for such a low reaction temperature is that the reduction step by Mg is exothermic, meaning it releases heat. This has been shown to facilitate reactions at lower temperatures as the local temperature within the reaction mixture can be hundreds of degrees higher than the set reactor temperature.[335] The large quantities of heat released during magnesiothermic reduction can assist in self-propagation of the reaction. One very interesting example of self-propagating TMC synthesis reported by the groups of Zhao and Tour employed a process known as flash Joule heating (FJH).[336] Here ultrafast current pulses are passed through samples to initiate the reaction, bringing the mixtures to temperatures exceeding 2800 °C. The samples cool rapidly, forming TMC NPs. A range of metal precursors (elemental, oxides, and chlorides) are compatible and form TiC, ZrC, HfC, VC, NbC, TaC, Cr_2C_3, MoC, and W_2C NPs. More interestingly, controlling the electrical pulse voltages, different crystal phases of MoC were formed, which is of interest for catalytic hydrogen generation. The fascination toward TMC NPs for catalytic applications

has led to a surge of synthetic procedures developed. Some examples were discussed above, and other methods such as lithography, chemical vapor deposition, transcription of MO_x, and many sol gel routes exist in the synthetic toolbox.[319]

1.4 Scope of Thesis

This report is composed of eight chapters. Chapter 1 focuses on the theory and introduction of plasmonic materials, diving into the characteristics that lead to unique optical properties. Focusing on the field of solar-driven desalination, with introduction of concepts, the potential of plasmonic NPs towards such processes is highlighted. The chapter ends by introducing alternatives to noble metal plasmonic materials. Chapter 2 provides synthetic details of TMC NPs, all relevant experimental setups for solar vapor generation and desalination, as well as descriptions of the most important characterization techniques used. This is focused on methods less universally known such as X-ray photoelectron spectroscopy (XPS), scanning electron microscopy (SEM) and transmission electron microscopy (TEM) plus the capability for energy dispersive X-ray spectroscopy (EDS), Raman Spectroscopy, and Brunauer-Emmett-Teller (BET) surface area analysis. The sample preparation details for NP analysis and plasmonic characterization is introduced. Chapter 3 discusses the one-step reduction synthesis of group 4 TMC NPs, followed by a broad scope of characterization. This includes evaluation of the photothermal efficiency, a key parameter for further application. Chapter 4 builds from the photothermal efficiency to develop a lab scale floating desalination system employing the group 4 TMCs, TiC, ZrC, and HfC. Each carbide is studied under simulated sunlight with investigations into the longevity of the interfaces. Chapter 5 explores the effect of which carbon source is used in the synthesis of TiC NPs. Characterization of the carbon sources as well as formed carbides is followed by studying the efficacy for floating solar desalination. Chapter 6 discusses scaling up TiC NP based solar desalination via construction of a floating solar still. The still is tested both in a contained rooftop system as well as on the Halifax Harbour. Chapter 7 focuses on the efforts to extend the proposed TMC synthesis to transition metals in Group 5. Chapter 8 discusses conclusions and future work for this project.

CHAPTER 2

EXPERIMENTAL AND CHARACTERIZATION METHODS

The discovery process of new materials requires thorough analysis of both their physical and chemical properties, and therefore many different analytical characterization techniques are needed. This is particularly true for the 3D TMCs focused on for this project as the few reports on their plasmonic ability haven't included full characterizations. Following an overview of their synthesis, this chapter will introduce the various methods used to study the structure, composition, optical properties, and corresponding photothermal characteristics of the TMC NPs. This includes powder X-ray diffraction (PXRD), scanning electron microscopy (SEM), transmission electron microscopy (TEM), X-ray photoelectron spectroscopy (XPS), UV Vis absorbance spectroscopy, Raman spectroscopy, dynamic light scattering (DLS), and N_2 adsorption with Brunauer-Emett-Teller (BET) analysis. The applicability of the TMCs for plasmonic application was tested by analyzing their efficiency of heat generation (photothermal efficiency) and directly for solar-vapor generation (SVG).

2.1 Material Synthesis

2.1.1 Transition Metal Carbides

Titanium dioxide (TiO_2 99.9%, 18 nm), zirconium dioxide (ZrO_2, 99.95%, 20 nm), and hafnium dioxide (HfO_2, 99.95%, 61–80 nm) were purchased from U.S. Research Nanomaterials. Magnesium powder (Mg, 99.8%, 325 mesh) was purchased from

Alfa Aesar. Hydrochloric acid (HCl, ≥99%) and nitric acid (HNO_3, ≥99%), poly(vinyl) alcohol (100% hydrolysed, average M.W. 14 000), glutaraldehyde (50% in H_2O), sodium metavanadate ($NaVO_3$, 99.9%), ammonium chloride (NH_4Cl, ≥99.5%), cetyltrimethylammonium bromide (CTAB, ≥99%), niobium oxide (Nb_2O_5, 99.9%, 325 mesh), and tantalum oxide (Ta_2O_5, 99.9%, 325 mesh) were purchased from Sigma Aldrich. Mixed cellulose ester filters (MCE, 0.45 μm pore size, 25 mm), and polyester filters (PE, 0.50 μm pore size, 25 mm) were purchased from Cole Parmer. Deionized water (DI-water, 18.2 MΩ cm) was obtained from a Sartorius Arium water purification system. All reagents were used as received without further purification. Tires were received from NAPA Southend, Halifax and were shredded and finely ground before use. Knotweed was picked as deadfall from Halifax Peninsula and blended into a fine powder. Spent coffee grounds were purchased from North Mountain Fine Coffees, Berwick and were previously used to make coffee. Lobster shells were received from Fisherman's Market International Inc, Bedford and ground into a fine powder before use.

2.1.2 Synthesis of Waste-Derived Char

The char synthesis was adapted from a previously reported anaerobic pyrolysis process.[337] In a typical reaction, the source waste material was ground into a fine powder and dried in an oven at 110 °C for at least 3 days. The pyrolysis step was carried out in a tube furnace between 400 and 600 °C for 60 min under an Ar atmosphere. Exact pyrolysis temperatures can be found in the respective chapters. After cooling to ~100 °C, the reaction mixture was quenched in cold deionized water. The water was then heated to boiling for 10 minutes. The biochar was collected via filtration and the solid product was washed with water until the filtrate ran clear. The resulting char was dried and finely ground using a mortar and pestle, followed by sieving to ≤250 μm. The sieved product was then added to a beaker equipped with a magnetic stir-bar and reacted with concentrated HNO_3 for 30 minutes. Afterwards, the reaction was filtered, and the acid-treated char was rinsed with deionized water until the filtrate pH was neutral. The biochar was dried in an oven at 100 °C for 2 days.

2.1.3 Group 4 TMC NP Synthesis

All carbide NPs were synthesized using a procedure adapted from a previous report.[280] In a typical reduction reaction, the desired metal oxide NP precursor (MO_2) was mixed with waste-derived char (2 molar equivalents), and Mg powder (4 molar equivalents) inside of a N_2 filled glovebox. Typical reaction masses and conditions are summarized in Table 2.2. The powders were thoroughly mixed using a mortar and pestle until a homogenous powder was obtained. The resulting mixture was transferred to a Coors™ alumina combustion boat and placed into a quartz tube and purged with argon gas for 15 minutes in a Lindberg Blue MTM furnace. After this, the reaction was heated to either 950 °C (TiC, ZrC) or 1050 °C (HfC) at a rate of 10 °C min^{-1} and held at that temperature for 4 h (TiC), 8 h (ZrC) or 12 h (HfC). The tube was then cooled to room temperature, and the reaction product was transferred to a glass vial. Aqueous HCl solution (10 mL, 6.0 M) was added to the product and sonicated for 1 h. Afterward, the solid was collected by centrifugation and washed with distilled water (3 × 10 mL) to remove reaction byproducts. After the third wash, the TMC NPs were filtered and rinsed with acetone, followed by ethanol, then dried in an oven at 110 °C overnight.

Table 2.1. Typical reaction masses and parameters for group 4 TMC NP synthesis.

Sample	Mass MO_2 (mg)	Mass Char (mg)	Mass Mg (mg)	Temperature (°C)	Reaction Time (h)
TiC	250	75	300	950	4
ZrC	250	49	197	950	8
HfC	250	29	115	1100	12

2.1.4 V_2O_5 NP Synthesis

V_2O_5 NPs were synthesized using a modified previously reported synthetic method.[338] First, sodium metavanadate ($NaVO_3$, 99.9%, 1.0 g) was completely dissolved in 250 mL pure water at 22 °C while stirring. Ammonium chloride (NH_4Cl, ≥99.5% 12.0 g) was then added to the solution until dissolve completely. The solution color changed from brown to colorless and became slightly cloudy with further stirring. After 10 min, cetyltrimethylammonium bromide (CTAB, ≥99%, 5.0 g) was added to the solution which was subsequently heated to 80 °C. The color of solution changed from orange to dark brown and after one hour, the color changed to clear yellow. The solvent was evaporated at 110 °C for 12 h, afterwards, the dried reaction product was calcined at 600 °C for 4 h in a muffle furnace.

2.1.5 Group 5 TMC NP Synthesis

All carbide NPs were synthesized using a procedure adapted from a previous report.[280] In a typical reduction reaction, the desired metal oxide NP precursor (M_2O_5) was mixed with birch-derived char, and Mg powder inside of a N_2 glovebox. Reaction masses and conditions providing the best conversion to the corresponding TMC are summarized in Table 2.2. The powders were thoroughly mixed using a mortar and pestle until a homogenous powder was obtained. The resulting mixture was transferred to a Coors™ alumina combustion boat and placed into a quartz tube and purged with argon gas for 15 minutes in a Lindberg Blue MTM furnace. After this, the reaction was heated to the desired temperature at a rate of 10 °C min^{-1} and held at that temperature for the allotted time. The reaction was then cooled to room temperature, and the product was transferred to a glass vial. Aqueous HCl solution (10 mL, 6.0 M) was added to the reaction mixture and sonicated for 1 h. Afterward, the solid was collected by centrifugation and washed with distilled water (3 × 10 mL) to remove reaction byproducts. After the third wash, the TMC NPs were filtered and rinsed with acetone, followed by ethanol, then dried in an oven at 110 °C overnight.

Table 2.2. Typical reaction masses and parameters for group 4 TMC NP synthesis.

Sample	Mass M_2O_5 (mg)	Mass Char (mg)	Mass Mg (mg)	Temperature (°C)	Reaction Time (h)
VC	250	83	200	850	3
NbC	250	45	160	750	6
TaC	250	40	83	950	6

2.2 Computational Studies

All calculations found throughout this thesis were performed by Dr. Yashar Monfared. Simulations were run using a FEM solver for Maxwell's equations in COMSOL Multiphysics. To simulate the optical properties, the dielectric constants as a function of wavelength of each material were used from previously published reports.[277] To ensure the accuracy of results, rigorous convergence analysis and perfectly matched layer (PML) boundary conditions were applied.[339] 3D models were meshed via the built-in meshing algorithm in COMSOL Multiphysics with a maximum element size of $0.1r$, where r is the radius of the nanospheres. In Chapter 3 simulations, particles were modeled as nanospheres suspended in water or embedded in a carbon matrix. To simulate the effects of particle oxidation, metal oxide shells of varying thickness (1, 3, 5, and 10 nm) were placed onto particles so that the total particle diameter matched the average particle size from each sample. In Chapter 4 simulations, absorbance, scattering, and absorption-to-extinction ratio (photothermal efficiency) for TiC, ZrC, and HfC were calculated for nanospheres suspended in water. The trimeric HfC particles were calculated using interparticle distances of 2 nm. The normalized absorption and scattering coefficients (Q_{abs} and Q_{sca}) of TMCs with particle sizes between 10 and 100 nm were derived using the calculated absorption or scattering cross sections of NPs (C_{abs} and C_{sca}) using finite element simulations normalized to the geometrical cross section of NPs. Extinction coefficient of NPs can be then defined as:

$$Q_{ext} = Q_{abs} + Q_{sca} \tag{2.1}$$

The photothermal efficiency (PT_{eff}) of TMC NPs between 50 and 800 nm was calculated using the ratio of absorption and extinction coefficients as shown below:

$$PT_{eff} = \frac{Q_{abs}}{Q_{ext}} \tag{2.2}$$

2.3 Characterization Techniques

2.3.1 Overview

This section of the thesis aims to provide a roadmap for each of the techniques used throughout the project. The focus will be on introducing each technique in the context that they were important to the proposed experiments. To that end, and to avoid redundancy, certain techniques that are generally well introduced throughout Bachelor level studies will not have a full background given. Instead, this overview section will cover how those techniques were employed for the current study. These include UV-Vis-NIR absorbance and reflectance spectroscopy, and mass spectrometry (MS)

As mentioned throughout Chapter 1, the LSPR can be observed using absorbance measurements.[38] For the case of materials in the UV to NIR range, UV-Vis-NIR spectrometers are readily available instruments that provide highly useful optical property information. Throughout this study, the absorbance of any new material was studied and compared to the simulated spectra obtained from the computational studies. This allowed for initial verification of the plasmonic generation from the TMC NPs and shed light on the matrix around the NPs, as will be further discussed in Chapter 3. By using a light source that extends into the NIR region, the technique becomes useful for studying the potential for sunlight driven processes by evaluating the absorbance characteristics across the sunlight spectrum. This will be further discussed in Chapter 4. Absorbance and reflectance spectra were recorded on an Agilent CARY 5000 UV-Vis-NIR spectrometer. For liquid absorbance measurements, dispersions were placed into a quartz cuvette, and the spectrometer was background corrected using deionized water. For film samples, an external diffuse reflectance accessory with a 150 mm integrating sphere

was used. The instrument was used in double beam mode using reduced slit height and was calibrated using a $BaSO_4$. Absorbance values were calculated from reflectance data using the following equation:

$$A = (1 - R)\, x\, 100\% \tag{2.3}$$

where A and R are absorbance and the measured reflectance, respectively. There is no transmission through the interfaces so it can be disregarded.

Inductively-couple plasma (ICP) MS is a type of mass spectrometry that allows for accurate detection of trace elements in a sample.[340] The ICP consists of an Ar plasma torch which ionizes the sample before being sent to the MS for analysis. ICP-MS can be used to detect virtually any element quickly down to the ng L^{-1} range. For this project, ICP-MS was used to detect trace elements, including heavy metals before and after purification by desalination. ICP-MS measurements were performed on a Thermo Scientific X-Series 2 spectrometer and the metal standards were obtained from SCP Science.

2.3.2 Powder X-ray Diffraction (PXRD)

Powder X-ray diffraction (PXRD) has the capability of identifying crystalline materials in a non-destructive manner.[341] PXRD investigations can reveal many characteristics such as crystallite size, phase, stress, strain, and purity. The detection of crystalline materials by XRD starts by irradiating the sample with X-rays. The X-rays will bombard the sample and will "bounce" or diffract off at a given angle from the original beam. The reason X-rays are chosen is because their wavelength is similar to the spacing between atoms in a sample.[342] This causes variations in the angle of diffraction based on the distance between these atoms. Throughout the scan, both the sample and the detector will be rotating to change the effective angle of diffraction.[343] The diffracted beam will then be sent to a detector and analyzed for the output of the final spectrum. Just like ripples in a pond, all of the diffracted X-rays will be interfering with each other either constructively or destructively. Destructive interference will cancel out the X-rays and no output will be recorded, but if they constructively interact a signal will be

recorded by the detector (Figure 2.1). Two waves must be in the same phase to constructively interfere, and this will only happen when the path difference between waves scattered from adjacent planes is an integral multiple of the wavelength. This scenario satisfies what's known as Bragg's Law (equation 2.4).[344] By scanning across an angle range and plotting the intensity of the X-rays that reach the detector, an XRD spectrum is obtained. As different materials have different atomic spacing and arrangement, PXRD can be used as a sort of fingerprint analysis of a given crystalline material.

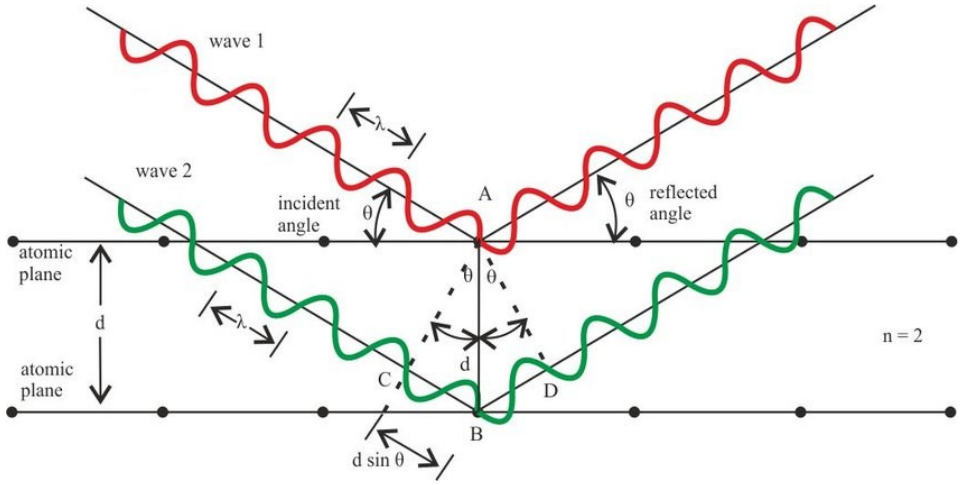

Figure 2.1. Schematic of X-ray interaction with sample crystal planes to satisfy Bragg's Law. Adapted with permission from: Singh, J. X-Ray Diffraction Analysis. Phases in Alloy 625. Springer Nature, New York, 2022; pp 124.Copyright 2022, Springer

Throughout this study, this technique was the first stage of material characterization to provide information about the purity of the obtained compounds as well as targeting of specific phases before moving onto other characterization techniques. Diffraction patterns were collected using a Proto AXRD Benchtop X-ray Diffractometer with Cu K_α radiation (λ = 1.54 Å). Powders were packed into a sample well of a resin holder.

$$n\lambda = 2dsin\theta \tag{2.4}$$

2.3.3 Electron Microscopy Techniques

Electron microscopy encompasses several different techniques that use an electron beam to generate an image of a given sample. The electrons are generated by applying a high voltage normally to a tungsten filament under vacuum, heating it to the point that electrons are emitted. These electrons are then accelerated and focused on the sample. Electron microscopy can provide information about sample morphology, size, and qualitative composition (e.g., contrast).[345] The morphological information can be on the surface for scanning electron microscopy (SEM) or on the inner structure for transmission electron microscopy (TEM), which will be the two methods of focus for the current project. The versatility and high special resolution of electron microscopes has rendered them a very valuable tool for various applications.[346] While there are many different forms of electron microscopy, they all work off the fundamental principle of using a beam of accelerated electrons as the source of illumination. Magnifications of ten million times are achievable because of the short wavelengths of the electrons.[347] To control and shape the electron beam, a series of electromagnetic and electrostatic lenses are used, which mimic the glass lenses used for light microscopy. These, along with the electron source and electron aperture components are housed within a chamber under high vacuum.[348]

Focusing first on SEM, the generated electrons are accelerated by applying a voltage of 5-50 kV and are focused to a spot size of 5 – 50 nm in diameter.[349] This spot will then scan across, or raster, across the sample. The resolution for SEM ranges from 10 – 1000 nm, depending on the instrument, though the instrument used for this study began blurring below the 100 nm scale for the samples run. When the electron beam strikes the sample, various processes occur including electron backscattering, transmission, inelastic and elastic scattering, and X-ray emission (Figure 2.2).[350] Which of these is detected is the major difference between SEM and TEM, and electron spectroscopies in general. SEM can be used in both backscatter and more commonly secondary electron detection mode, which will be the focus here. While backscattered electrons come from the original beam, secondary electrons are ejected from the sample surface atoms when hit with the primary beam.[351] The secondary electrons are primarily used for topographical imaging because they are generated close to the sample surface. Since the energy of the

secondary electrons is quite small, those generated too far into the sample will have a very small chance of making all the way to the surface.

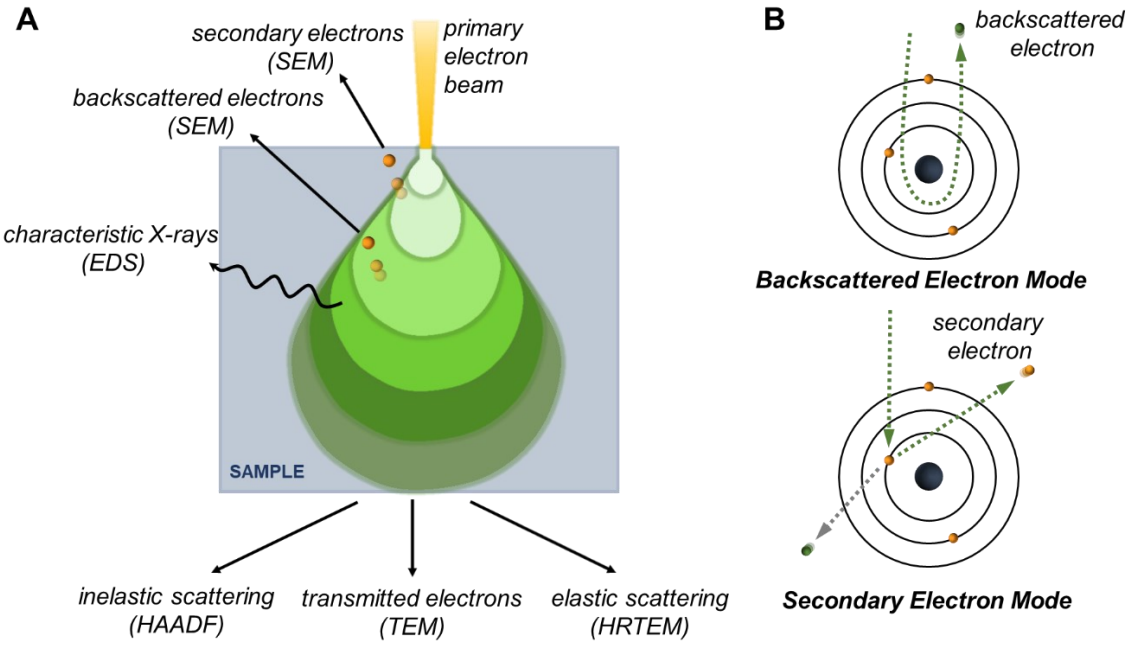

Figure 2.2. (A) Schematic of interaction with an electron beam with a sample with select relevant processes. (B) Processes of interest during backscattering (top) and secondary electron (bottom) mode analysis by SEM. Adapted from reference (350).

TEM, much like SEM uses a focused beam of electrons to image a material. In this instrument though, the electrons are accelerated at a much higher voltage (60 – 300 kV), which results in higher resolution.[352] The main difference is that the detector will collect the electrons that pass through the sample, instead of those scattered like in SEM. It is therefore important to have relatively thin samples (>200 nm) to allow the electrons to pass through effectively.[351] Areas with more material will interact more strongly with the primary electron beam and therefore appear darker in the bright field image. Through this study, all TMC NPs were below 100 nm particle size making TEM a very powerful method for size analysis.

One of the true powers of TEM is that additional imaging modes are possible. High resolution transmission electron microscopy (HRTEM) for example allows for very high resolution to atomic scale level in cases.[353] It uses the transmitted electrons alongside elastically scattered electrons to create an image where the interference of the two beams creates contrast. In this case, ideal samples are 50

nm thick and below to provide clear information of crystalline lattices within the material.[354] In this study, HRTEM allowed identification of crystal lattice planes within the NPs, as well as to identify potential amorphous regions within the sample. A similar method, high-angle annular dark field (HAADF) imaging mode also uses scattered electrons but focuses on those inelastically scattered, i.e. those that have lost energy.[355] The major benefit of HAADF is that it removes any unwanted interference present in HRTEM and each atom can be considered an independent scatterer.[356] Effectively, this provides contrast that is simpler to interpret, particularly for lower atomic number elements. HAADF collects just the scattered electrons to form an image and therefore more material or larger atoms will show up brighter in the resulting image.

The final method of interest is energy dispersive X-ray spectroscopy (EDS) which can be coupled with both SEM and TEM techniques. Here, the incoming primary electron beam can cause an inner-shell electron to be ejected from the sample. This vacancy will quickly be filled by an outer shell electron.[357] The energy difference between these two orbitals will be released as an X-ray with a characteristic energy depending on the element. By scanning the beam over a small area and collecting all the X-rays, the composition of the region can be mapped. This can be shown as an intensity spectrum or as an image with each element color coded like a heat map.

Throughout this thesis all these methods were utilized depending on the information required. SEM was used for analysis of synthesized chars and to gain information on the TMC NPs as a bulk material, for example when studying the thermal stability. SEM images were obtained on a Hitachi S-4700 electron microscope in secondary electron imaging mode with an accelerating voltage of 5 kV. The particles were drop-cast onto a Si wafer which was mounted onto an aluminum stub. TEM was used to study the NPs on an individual or small group scale, and to further study the fine structure with HRTEM. Additional analysis and elemental mapping using EDS and HAADF imaging techniques were done in tandem with the transmission electron microscope. TEM images were collected using a Thermo Fischer Scientific Talos 200X microscope with an accelerating voltage of 200 kV. HAADF imaging was performed with spot size of less than 1 nm and a convergence semi-angle of 10.5 mrad. EDS data were acquired using the Velox

program from Thermo Fischer scientific. The particle size and lattice spacing were analyzed using ImageJ software.[358]

2.3.4 X-ray Photoelectron Spectroscopy (XPS)

X-ray photoelectron spectroscopy (XPS) is perhaps one of the most informative surface techniques available in which X-rays are used to bombard the surface of a sample. The X-rays produced are of sufficient energy (~6 keV) to eject core electrons from surface atoms (~10 nm depth on average) upon interaction.[359] The kinetic energy, from which the binding energy can be derived of the electrons is measured which reveals not only elemental composition of surfaces, but also chemical and electronic states within the sample. This is done using equation 2.5, where BE and KE are the binding and kinetic energy, respectively, and hv is the total energy of the incoming X-rays. Picking up from the moment the x-ray beam strikes the material and ejects an electron, here termed a photoelectron as it was ejected by incident light, it will start its journey towards the detector (Figure 2.3). Before reaching the detector, the photoelectron must travel through a hemispherical analyzer. This analyzer will be under a static electric field established to only allow electrons of a given energy (known as the pass energy) to reach the detector. Important to note is that core electrons which are closer to the nucleus will have a higher binding energy than those in outer orbitals, corresponding to a lower kinetic energy. This is also true for electrons of different subshells (s, p, d, and f). Going even further, the photoelectrons generated from the same subshell, for example the 2p shell, can have slight variance in binding energy. This arises from differences in the chemical environment of atoms and can shed light on the oxidation states present for a given element.[360]

$$BE = hv - K - \phi \tag{2.5}$$

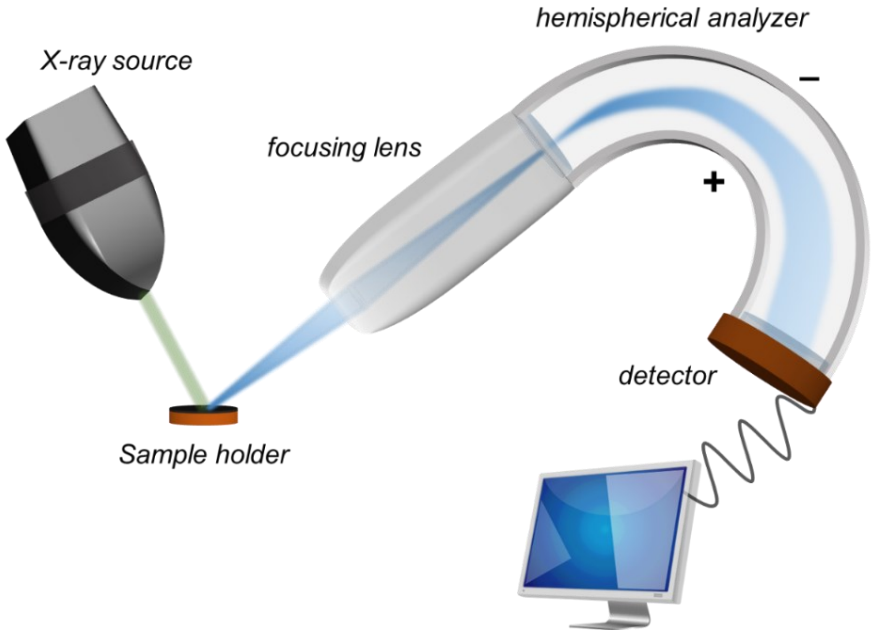

Figure 2.3. Schematic illustration of XPS. The instrumentation is kept under ultrahigh vacuum during acquisition. Adapted from reference (359).

While XPS instrumentation has become much more user friendly, data processing to obtain accurate information from spectra is not trivial.[361] Survey scans spread a wide range of binding energy values for initial identification of elements present. Normally, target signals are then focused in on for a high-resolution scan. When multiple oxidation state species of a given element are present, the peaks often overlap.[362] This requires careful fitting to extract which oxidation states are present and their relative concentrations. Additionally, during XP spectra collection, electrostatic charge can build on the surface which causes shifting of the photoelectron kinetic energy as they interact with the charge while being ejected. The results in peaks being slightly shifted or broadened from their expected position or shape in the output spectrum. Normally, to remedy this, a peak associated with the tiny amount of organic material on samples known as adventitious carbon can be used. By fitting this part of the spectrum and referencing it to the documented binding energy of these photoelectrons the correction can be applied to the entire spectrum. This is known as charge correction.[363] In this study, because the TMC NPs contain their own source of carbon, the adventitious charge correction method is less reliable. To verify the accuracy a calibration based on the Fermi edge location was completed. This

involves fitting the data with a step-down function to estimate the location of the Fermi edge and then correcting it to be exactly 0 eV binding energy.

In this thesis, XPS was chosen to investigate the surface chemistry of the TMC NPs. It helped to reveal the presence of certain chemical species on the surface, which helps to explain some of the observed physical and chemical properties. XPS analysis was performed on a VG Microtech MultiLab ESCA 2000 X-ray Photoelectron Spectrometer. An Al Kα monochromatic X-ray source (1486.6 eV) was used with a system pressure of 10^{-9} Torr. For high-resolution scans, a pass energy of 30 eV, an energy step of 0.1 eV, and a dwell time of 1000 ms were used. XPS binding energy calibration was done using the C 1s peak set to 284.8 eV. This was verified by approximating the location of the Fermi edge using a step-down background type.[364] The position of the Fermi edge, as measured by the intersection of two straight lines computed from the fitted step-down background, was extracted and used to estimate an energy offset required to locate the edge position at 0 eV. Spectra corresponding to the same measurement were calibrated by applying the same offset required to calibrate the Fermi edge.

2.3.5 Raman Spectroscopy

Raman spectroscopy is a non-destructive chemical analysis technique which provides information about chemical structure, phase, crystallinity, and molecular interactions by studying the interaction of light with chemical bonds in a material. It is often used to provide a structural fingerprint for compounds by following the scattering of light incident from a high intensity laser source.[365] Raman is a powerful tool for chemical structure analysis across many fields including pharmaceuticals, geology, life sciences, forensics, and energy technology. During the process, the exchange of energy between the photon and the molecule causes it to be scattered at higher or lower energy than the incoming photon (inelastic scattering). The difference in energy is caused by the rotation or vibration of the molecule, and the resulting spectrum can be used as a fingerprint for a given molecule. Often, transitions which have large Raman intensities have weak IR intensities, which makes it a strong tool for such compounds.

For this project, Raman was used to probe the phases within chars derived from several carbon sources used in the reduction reaction to synthesize the NPs. To

provide context, the pyrolysis of carbon-based materials to make chars produces predominantly amorphous carbon, but small amounts of ordered graphitic carbon are also present. Raman allows investigation of the relative concentration of graphitic carbon for a given sample. There are two Raman responses for amorphous carbon, the D- and G-band. The D-band corresponds to a more disordered structure, while the G-band is more ordered graphite structure vibrations. Throughout Chapter 5, where different carbon sources are used in the NP synthesis this becomes important to explain variations in reactivity and product characteristics. All Raman spectra were acquired using Thermo Fisher Scientific DXR Smart Raman spectrometer equipped with 780 nm excitation wavelength. The spectrometer resolution is 3 cm^{-1}, and it is equipped with an air-cooled charge coupled device (CCD) detector. To acquire the Raman spectrum of a desired solid, a capillary tube or dram vial was filled (at least a quarter of the length) with the solid and then secured in the appropriate sample holder. The sample holder was then placed inside the Raman spectrometer. The spectrometer was previously calibrated using an adenine standard. The acquisition period for each measurement was 30 seconds. A laser power of 100 mW was used to maximize the signal recorded.

2.3.6 Dynamic Light Scattering (DLS) and Zeta Potential

Dynamic light scattering (DLS) is a common technique to analyze the size of emulsion particles, proteins, polymers, and NPs based on their motion when dispersed in solution.[366] The Brownian motion of such particles is determined by irradiating the sample with a laser and collecting the scattered light as the particles move around in solution. Complementary to DLS measurements, the instrument can measure the zeta potential of particles. Zeta potential is the particles electrical potential and provides information on the surface charge of the sample and its stability in solution.[367]

As Figure 2.4 shows, when the light hits particles in solution, it can be scattered in any direction. The amount of scattered light for a given area will fluctuate over time as the particles move due to motion. Smaller particles, which diffuse slightly faster will have more rapid fluctuations in the intensity than larger particles.[368] Crucial to note is that when inferring the particle size from this data it will include any other molecules that travel through solution with the particle. This

measurement is known as the hydrodynamic radius and can include any capping agents on a NP, or even solvent molecules that are interacting with the particle surface. Therefore, the radius measured by DLS is often larger than those measured using microscopy and is a less accurate size description. Nevertheless, it provides useful information for the behaviour of NPs in solution. Zeta potential is a measure of the charge that develops at the location close to the particle surface known as the slipping plane (Figure 2.5). This plane is the interface separating the strongly interacting ions which move through solution with the particle, and ions which only briefly interact with the particle as it moves through the solution. Zeta potential provides important information on the surface charge and colloidal stability of the particles. When considering the stability of bare NP dispersions, anything that is higher or lower than +/- 30 mV, respectively, suggests the particles won't aggregate and precipitate out of solution.[369]

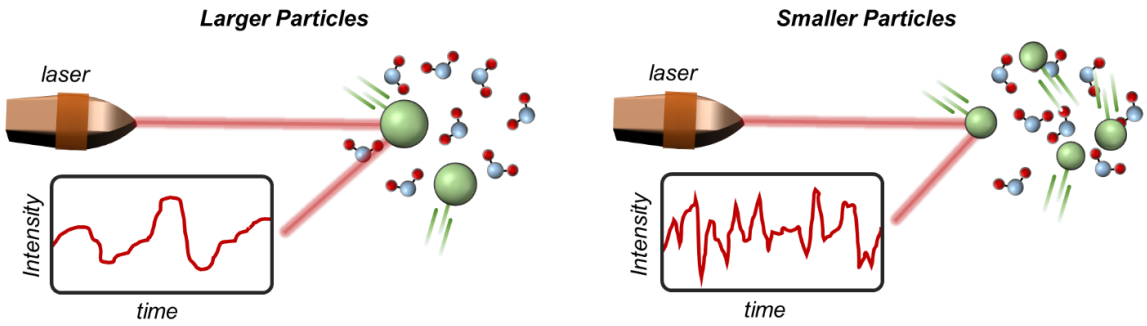

Figure 2.4. Hypothetical dynamic light scattering processes and corresponding output over time for larger particles (left) and smaller particles (right). Adapted from reference (367).

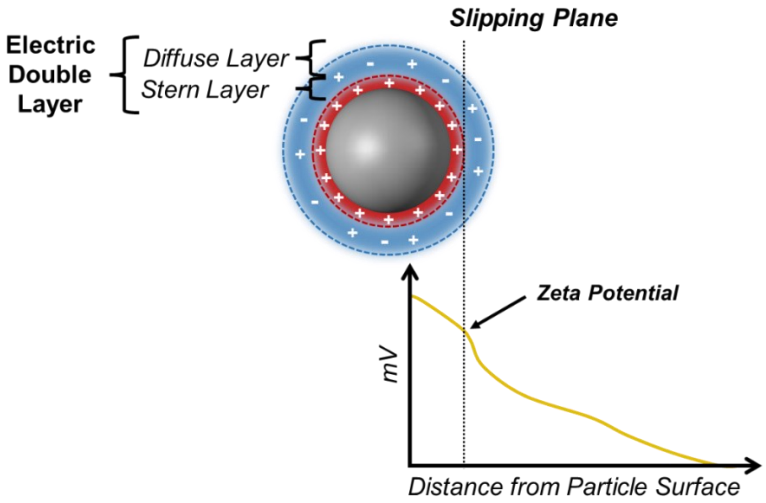

Figure 2.5. Schematic illustration of electric double layer surrounding NPs in solution, showing location of Zeta potential measurement. Adapted from reference (368).

Throughout this study, DLS and zeta potential measurements were used to investigate the surface properties of the TMC NPs while in solution. Zeta potential measurements were conducted using the Zetasizer Nano Series Nano-ZS (Malvern Panalytical) instrument. The NP solutions were placed in a DTS1070 folded capillary cell, and Zetasizer software was used for data analysis.

2.3.7 N_2 Gas Adsorption and Surface Area Analysis

By studying and explaining the physical adsorption of gas molecules on a solid surface, it is possible to measure the surface area of porous materials. The amount of gas adsorbed onto a given surface is affected by the system's temperature and pressure. To simplify gas adsorption measurements, a constant temperature is maintained while the pressure is altered, generating what's known as a gas adsorption isotherm. Many different analyses can be used to gain information about a material from this data. Most commonly, the isotherms are used to determine surface area (BET), pore size distribution and pore morphology.

Prior to the gas adsorption and desorption measurements, samples must be heated under vacuum to remove all moisture present. For standard analysis, N_2 is used as the adsorbent for its strong interaction with a wide range of materials and

availability of very high purity tanks. To enhance the interaction between N_2 and the material, sample holders are placed into liquid N_2. Once fully cooled, He gas is used to purge the pores of the sample, which allows for determination of the total free space within the sample holder. After another evacuation, N_2 is introduced to the system in known amounts until the system reaches a saturation pressure. This is the point where further increasing the pressure doesn't lead to anymore adsorption. Finally, the pressure is incrementally decreased, and the amount of gas removed from the surface, or desorbed, is quantified. This acquired data is the adsorption and desorption isotherm and can be used for further analysis. The BET method is used to calculate the specific surface area of the material. By focusing in on the data points within an area of the isotherm known as the multilayer adsorption region (relative pressure range of 0.05 to 0.3).

This study uses N_2 gas adsorption and desorption isotherms, alongside the BET analysis method to determine specific surface area of samples. N_2 adsorption measurements were made on a Micromeretics 3Flex Adsorption Analyzer. Samples were evacuated at 150 °C for 24 h prior to analysis. He gas was used to determine the free space within the sample and tube prior to analysis. Sample analysis involved an equilibrium interval step of 10 s between N_2 dosing steps. Within the BET region, 10 points were obtained.

2.3.8 Photothermal and Solar Vapor Generation Efficiency

As discussed in Chapter 1, some of the interesting applications of plasmonic NPs involve conversion of light to intense heat for further use.[175] Investigating how efficiently NPs carry out this light-to-heat conversion can shed light on their potential use in such applications. This evaluation is known as photothermal efficiency determination and involves measuring the temperature change of a solution of NPs over time under illumination. A 365 nm LED source (ThorLabs) with a full width at half-maximum of 10 nm was used as the light source. This light source was used as was closest to the LSPR maximum of the group 4 TMC NPs. The illumination power density was calibrated to 1 W cm^{-2} using a silicon photodiode (ThorLabs). The temperature change was monitored using a K-type thermocouple device (EL-USB-TC-LCD, MicroDAQ) with a data logger. A 1.0 cm path length quartz cuvette was used as the container, to which 3.00 mL of the

corresponding TMC suspension was added. The solution was stirred constantly using a Teflon-coated magnetic stirring bar. The cuvette was illuminated from the side with an illumination area of 3.0 cm^2. The thermocouple was placed directly into the middle of the solution. Data were collected at 15 s intervals for 30 minutes of illumination, followed by cooling. The reported efficiency values were averaged over five repetitions.

An experimental procedure published by Roper *et al.* gave a simple and reliable model to fit the heating and cooling cycles of NP dispersions under illumination to calculate their photothermal efficiency.[370] The experiment works off the foundation that a photothermal NP dispersion under illumination will heat up until the point that the generated heat is being dissipated at the same rate as its being generated from light (Figure 2.6). This will lead to a plateau in the solution temperature, which is the energy equilibrium. The maximum temperature achieved can then be directly related to the energy absorbed by the NPs.[371] The full derivation can be found in Appendix A.2, and the photothermal efficiency by the energy balance of thermal heat transfer becomes that shown in equation 2.6. In the equation, η_T is the photothermal transduction efficiency, h is the heat transfer coefficient derived from the heating or cooling data, S is the surface area of illumination (3.0 cm^2), T_{max} and T_{amb} are the maximum temperature of the cell and the ambient temperature, respectively, Q_0 is the energy input by the sample cell, I is the incident light intensity, and A_λ is the optical density of the sample solution at the excitation wavelength. In this case, the optical density of the solution is defined as the average absorbance of the corresponding TMC dispersion over the LED bandwidth.

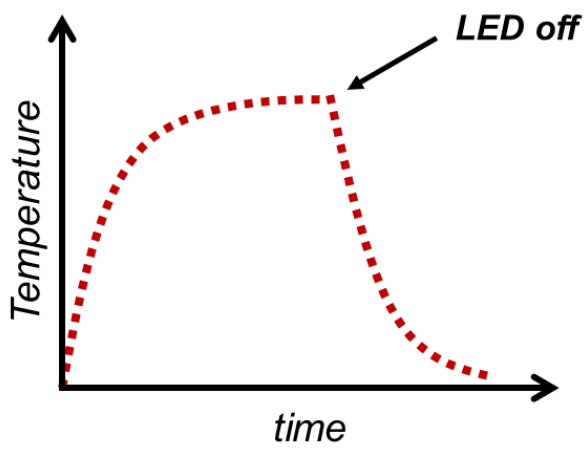

Figure 2.6. Generic schematic of heating curve for NP dispersion under illumination (right) with the photothermal efficiency equation derived from heating curve data (left). Adapted from reference (371).

$$\eta_T = \frac{hS(T_{max}-T_{min})-Q_0}{I(1-10^{-A_\lambda})} \tag{2.6}$$

The data provided from photothermal efficiency measurements provides invaluable information on the plasmonic and photothermal behaviour of NPs. However, to study their potential directly for desalination application, the efficiency of the NPs towards direct water evaporation under sunlight is possible. This was done throughout this study to determine the capability of TMC NPs for solar vapor generation (SVG) and solar desalination, where the efficiency includes the entire solar spectrum of light (broadband source). The various experimental conditions are mentioned above, and this section will just highlight the interpretation of the data. The equations used slightly differ between the lab scale where continuous monitoring of evaporation is possible, and larger scale evaporation where evaporated water is collected each hour.[195] They both describe how efficiently the evaporation interface, consisting of the TMC NPs, can absorb incoming sunlight, convert it to heat, use that heat to evaporate water, and finally release the water vapor. Higher efficiencies mean that more of the incoming energy is being used for evaporation, and not being lost by some other mechanism (Figure 17). For the lab-scale SVG efficiency calculation:

$$\eta_{lab} = v\frac{C\Delta T+\Delta_{vap}H_m}{C_{opt}q_i} \tag{2.7}$$

ν is the evaporation rate, C is the specific heat capacity of water (4.18 kJ kg^{-1} K^{-1}), ΔT is the change in temperature, $\Delta_{vap}H_m$ is the liquid to vapor phase change enthalpy of water, C_{opt} is the optical concentration, and q_i is the illumination intensity of the light in kW m^{-2}.[189] For the large-scale evaporation and desalination equation:

$$\eta_{still} = \frac{m_{H_2O}\Delta_{vap}H_m}{A_{still}\int q_{solar}(t)dt} \tag{2.8}$$

m_{H2O} is the mass of freshwater collected daily, A_{still} is the solar still evaporation area, and q_{solar} is the intensity of solar irradiation incident to the evaporation surface. It is integrated over the course of time that the evaporation process is run.[372] In both cases, the bottom term describes how much total energy there is arriving at the evaporation surface. The top term then describes how much of that energy has effectively been used to facilitate the evaporation and release of water vapor.

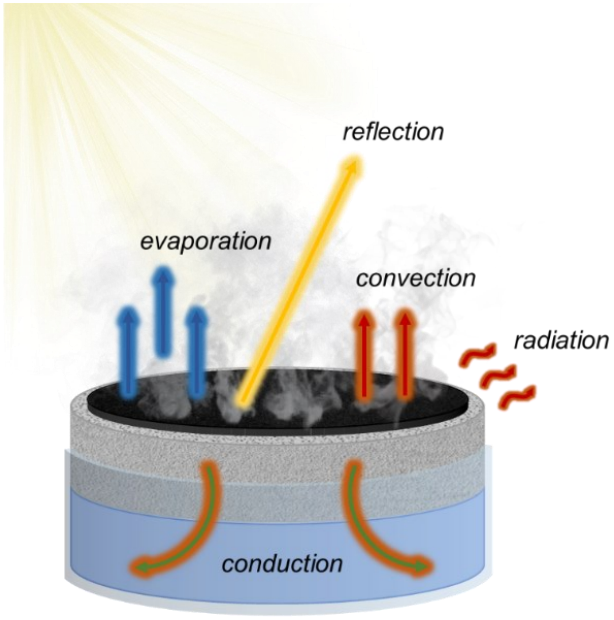

Figure 2.7. Potential energy losses during solar driven evaporation (left).

CHAPTER 3

SYNTHESIS OF GROUP 4 METAL CARBIDE NANOPARTICLES

Part of this chapter is adapted from Margeson, M. J.; Monfared, Y. E.; Dasog, M. Synthesis and Photothermal Properties of UV-Plasmonic Group IV Transition Metal Carbide Nanoparticles. *ACS Appl. Opt. Mater.* **2023**, *1*, 1004-1011. Copyright 2023. American Chemical Society. The synthesis of all Group 4 carbides, material characterization (XRD, UV Vis), and photothermal efficiency measurements were performed by me. TEM and EDS mapping was performed by Dr. Carmen Andrei at the Canadian Center for Electron Microscopy (CCEM). XPS measurements were carried out by Dr. Andrew George, and FEM simulations were conducted by Dr. Yashar Monfared at Dalhousie University. Amorphous carbon generated by birch wood residue pyrolysis was obtained from Dr. S. MacQuarrie at Cape Breton University.

3.1 Introduction

As researchers continue to demand more from plasmonics, there has been an increased interest in exploring new materials that have both strong optical and physical properties.[43,250] Refractory plasmonics, particularly transition metal nitrides (TMNs) have gained traction in a variety of applications such as photothermal therapy,[373] sensing,[374] and in photovoltaic cells.[375] Refractory nanomaterials are envisioned to be suitable for a much larger variety of applications as they can form LSPRs from the UV to near-IR regimes, depending

on the composition and morphology.[261,262,276,277] This, matched with the known physical characteristics of refractory materials such as high melting point, extreme hardness, and metallic conductivity has caused an explosion in their exploration.[273,285,286] One class of materials that has the potential to expand the range of LSPR frequencies are transition metal carbides (TMCs).[274] The 2D carbides known as MXene phase TMCs have a graphene-like structure and have been both theoretically and experimentally explored as NIR plasmonic materials recently.[296,298,300–303] The demanding synthetic conditions using dangerous chemicals like hydrofluoric acid are the most important point to be addressed for MXene carbides to reach their future potential.[294,306,388]

On the other hand, 3D TMCs are expected to display LSPRs throughout the UV and visible regions of the electromagnetic spectrum.[275] Based on preliminary theoretical studies, the location and broadness of the LSPR will change for different metals providing the potential for tunability. While this initial report was for larger particles where the authors found scattering could lead to less efficient plasmonic capability,[275] experimental reports since then have been very promising. In one instance, Fan *et al.* used TaC NPs for SERS application to enhance the detection of organic pollutant, rhodamine 6G at concentrations below 10^{-8} M.[379] This is on par with some of the top performing SERS materials. Shortly after, the group of Gao *et al.* reported WC NPs to successfully degrade methylene blue (MB) under NIR illumination.[311] Finally, a ZrC NP interface by Liu *et al.* was used successfully as a broadband solar absorber in water evaporation and desalination.[380]

Based on these promising results, and interest in defining new plasmonic materials in our lab,[277] we sought to synthesize group 4 TMC NPs and understand their plasmonic behaviour. To facilitate the reaction, a magnesium reduction reaction was developed using transition metal oxide NP precursors in the presence of birch-derived char. The char was used as the carbon source to make TMCs via magnesiothermic reduction reaction. Following this, full characterization of the corresponding metal (Ti, Zr, and Hf) carbide nanostructures was performed which included investigating both physical and optical properties. The particles were exposed to several harsh chemical and thermal conditions to test the proposed stability of such a refractory material, even on the nanoscale. To further verify the LSPR characteristics of the TMCs, the photothermal efficiency was determined using 365 nm excitation source.

3.2 Material Synthesis and Characterization

Group 4 TMC NPs were synthesized as outlined in section 2.1 of this report. Synthesis of birch residue followed the procedure in section 2.1.2, and TMC NPs were made using the procedures in section 2.1.3. For this chapter, TMCs were characterizations using PXRD, Raman, SEM, TEM, UV-Vis, XPS, DLS, zeta potential, FEM simulation, and photothermal measurements.

3.3 Results and Discussion

The synthetic procedure to prepare TMC NPs was an adapted magnesiothermic reduction,[277,337] where magnesium powder was used to facilitate reduction of a metal oxide precursor to then react with the carbon source. Magnesiothermic reduction reactions have been shown to form TMC NPs under 1000 °C.[331,337,381–383] Metal oxide precursors TiO_2 (anatase, 17 ± 4 nm), ZrO_2 (monoclinic, 19 ± 5 nm), and HfO_2 (monoclinic, 43 ± 10 nm) were commercially purchased and used without further purification. TEM was used to analyze the particle size and PXRD to verify phase purity (Appendix A.1, Figure A.1). Biochar was derived from the anaerobic pyrolysis of birch wood residue, followed by treatment with HNO_3 acid before being rinsed and dried. The acid treatment step was done to remove any remaining contaminants and has also been shown to increase the particle surface area for increased reactivity.[384] Further, acid treatment has been shown to disrupt the graphitic structure of charcoals formed from this pyrolysis method. Previous studies in our lab have concluded that graphite is not a suitable carbon source for these carbide forming reactions. Raman spectra show the difference in the graphitic carbon peak at 1580 cm^{-1} (G-band, introduced in section 2.5.1) before and after acid treatment step (Figure 3.1A). PXRD of the collected acid-treated char was characteristic of amorphous carbon (Figure 3.1B). The absorbance of the birch wood char was found to be broad across the UV and visible regions (Figure 3.1C). SEM images show the char to be polydisperse on the micron-scale in size and to be highly roughened on the surface (Figure 3.1D). N_2 adsorption experiments and BET analysis show that compared to the untreated biochar, the acid-treated sample

displayed a much higher surface area. The surface area increased from 22.8 m^2 g^{-1} to 112.4 m^2 g^{-1} after the acid treatment.

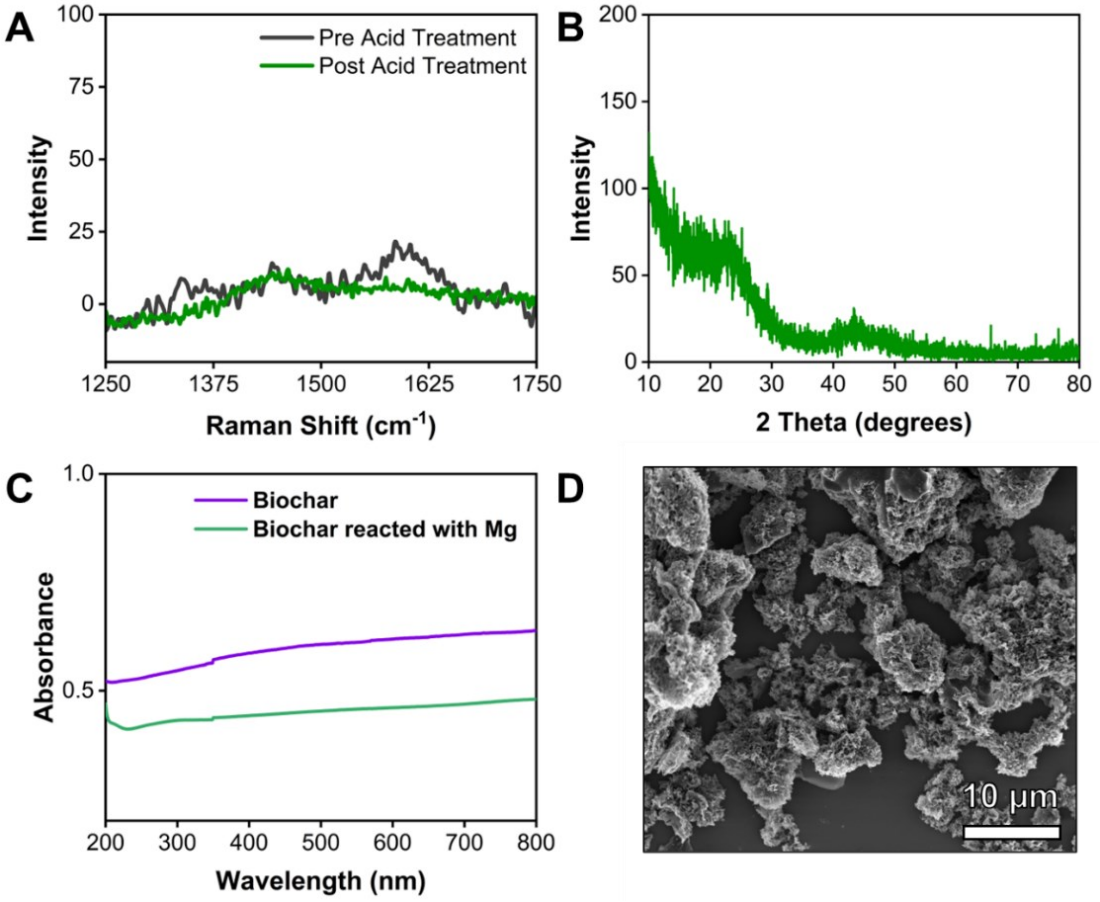

Figure 3.1. (A) Raman spectra of birch biochar before (black) and after (green) acid treatment showing decrease in G-band intensity at 1575 cm^{-1}. (B) PXRD spectrum of the acid treated biochar. (C) Absorbance spectra of biochar (purple) and after reacting with Mg power in the absence of a metal precursor. (D) SEM image of the birch biochar.

For TMC synthesis, the reaction mixture consisting of metal oxide nanopowders, biochar, and Mg was ground together very thoroughly to ensure that the precursors were sufficiently dispersed throughout the entire powder. The temperature and reaction times required to form the TMC NPs varied depending on which metal precursor was used. For TiO_2 and ZrO_2, 950 °C afforded complete conversion to the corresponding carbide with ZrC requiring slightly longer reaction time (4h for TiC,

6 h for ZrC). HfO_2 didn't fully form carbide at 950 °C after reacting for 24 h. Instead, reacting at 1100 °C for 12 h completed the conversion.

Each reaction was heated at a rate of 10 °C min^{-1}, mainly to avoid thermal shock to the reaction tube, though heating rates up to 50 °C min^{-1} didn't have any negative impact on the formed carbides. After cooling, the reaction mixtures were sonicated in 6 M HCl to remove the byproduct MgO, followed by thorough washing with deionized water. The PXRD patterns verified successful formation of each TMC in the cubic crystal phase as expected (Figure 3.2). Particularly for TiC, a broad peak centered around 25° is present which corresponds to small amounts of amorphous carbon remaining in the sample. Additionally, the TiC peaks showed slight tailing to higher angles, which is most likely due to trace amounts of titanium oxycarbide (TiO_xC_y).[385] Interestingly, this remained even over longer reaction times. It is possible that this arises from surface oxidation of the NPs once they are exposed to air and during the acid treatment step.

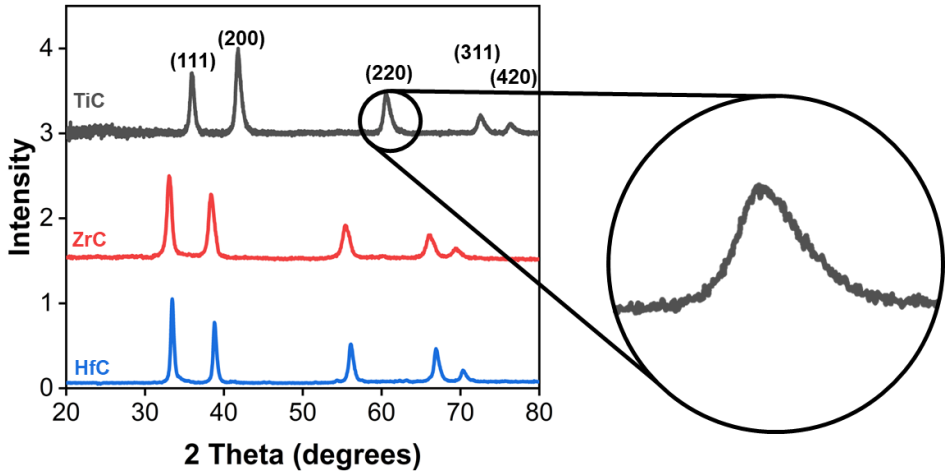

Figure 3.2. PXRD patterns of TiC (black), ZrC (red), and HfC (blue) NPs. On the right: enlarged TiC (220) peak to show peak tailing to right side.

The surface compositions of the TMC NPs were explored using XPS. Although the TMC NPs should be highly conductive, a rigorous charge correction was completed for the obtained high-resolution (HR) XP spectra. An adventitious carbon peak fitting was completed first, with the peak being fit to 284.8 eV. Since it is possible that trace amounts of graphitic carbon could be in the sample, making accurate fitting of the C 1s peak difficult, another charge correction method was

used to verify the accuracy of the peak fitting, known as a Fermi Edge Calibration. It involves finding the location of the Fermi edge at the low binding energy (~0 eV) region of the spectrum (Figure 3.3). A line corresponding to the maximum value of the first derivative (i.e. the steepest point) is located and If this value is not at 0.0 eV binding energy the difference can be applied to the entire data set. In all cases the C 1s charge correction was verified to be sufficient for further analysis.

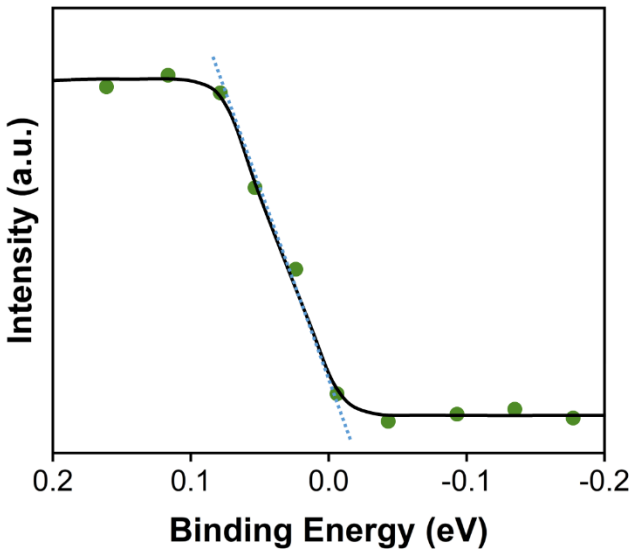

Figure 3.3. Fitting parameters for Fermi Edge Calibration showing inflection point line (blue) and straight line across the step function (red).

Throughout data processing, several steps were taken to ensure accuracy of fitting results. Survey scans provided initial sample composition to verify the surface was pure of other species (Appendix A.1, Figure A.2) For the metal oxide precursors, scans were collected to gain information on the peak locations and widths. These were applied to the data with constraints to allow for minor adjustment of the values. Literature peak position values were also given small constraint ranges to tolerate minor instrument fluctuations.

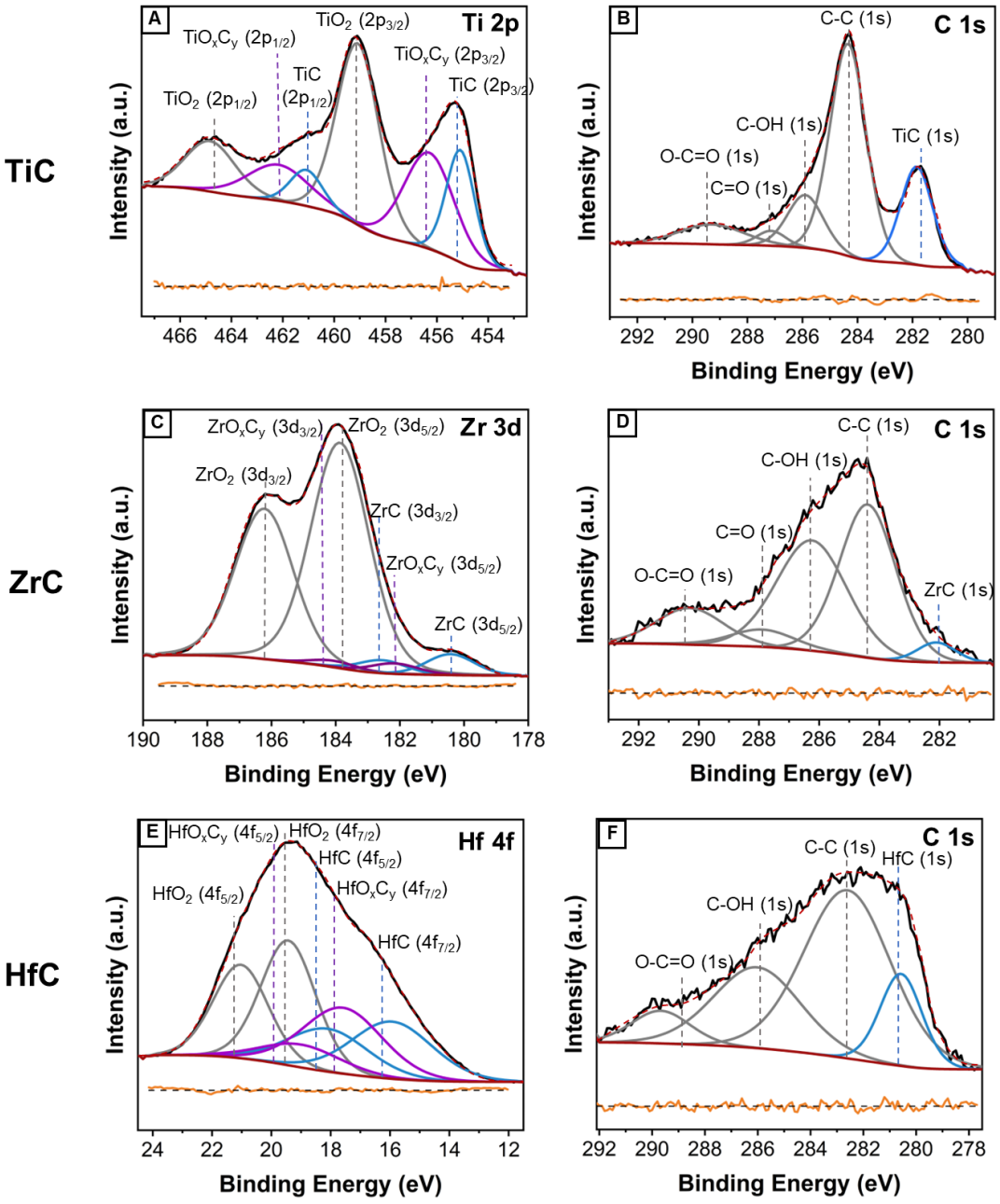

Figure 3.4. High resolution X-ray photoelectron scans for A) TiC (C 1s region), B) TiC (Ti 2p region), C) ZrC (C 1s region), D) ZrC (Zr 3d region), E) HfC (C 1s region), and F) HfC (Hf 4f region). The orange lines below spectra represent the residual after fitting, while the red dashed line represents the fitting envelope.

The HR spectra of the metal regions (Figure 3.4A, C, and E), being Ti 2p, Zr 3d, and Hf 4f, showed the presence of the corresponding carbide along with oxycarbide (MO_xC_y) and metal oxide (MO_2). This indicates that the surface of the carbides in fact undergoes oxidation once exposed to air, which is a well reported phenomenon.[386] Based on previous studies, and the presence of oxycarbide, it is likely that there is a gradient of carbonization between the outer oxide shell and the carbide core (Figure 3.5). HR XP spectra of the C 1s regions (Figure 3.4B, D, and F) confirms the presence of TiC, ZrC, and HfC in the corresponding spectrum. Along with the metal carbide peaks, several associated with free carbon were also observed. Deconvolution of the C–C sp^2 and C–C sp^3 carbon peaks was not possible and was fit as one peak. Other peaks in the carbon HR XP spectra arise from various oxidized carbon species (alcohol, ketone, carboxylic). The position of peaks for all species, fitting parameters, and literature references used for fitting are summarized in Table A.1.

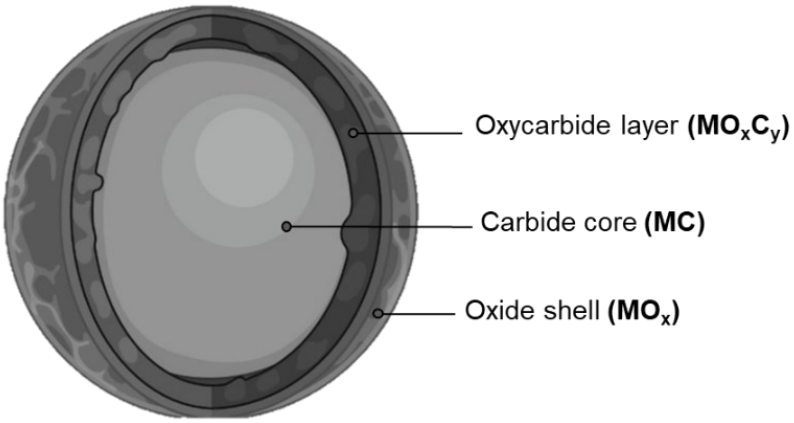

Figure 3.5. Schematic of TMC NPs after undergoing surface oxidation. The formed oxide shell becomes an oxycarbide layer before reaching the carbide core.

TEM analysis, including standard images, HRTEM images and size dispersion plots can be seen in Figures 3.6 and 3.7. TiC was found to form the smallest NPs with an average particle size of 24 ± 8 nm and was found to have larger amounts of amorphous carbon present within the sample (Figure 3.6A). This matches the previous XRD data for TiC NPs which was the only sample to display amorphous carbon peak. HRTEM analysis (Figure 3.6B and C) showed that the crystalline TiC

core was surrounded by an amorphous layer, which is most likely from the oxide and oxycarbide layers that form on the NPs.[387] ZrC samples were composed of carbide NPs having an average size of 31 ± 9 nm along with a small amount of larger (>150 nm) amorphous carbon particles present (Figure 3.6D). The particles themselves had oxide shells 2–3 nm in size (Figure 3.6E) and a crystalline carbide core (Figure 3.6F). Again, based off the XPS analysis, the amorphous surface shell is likely metal oxide (ZrO_2) and oxycarbide (ZrO_xC_y).[388] Lastly, HfC formed from the magnesiothermic reduction reaction was slightly polyhedral, with an average size of 42 ± 15 nm (Figure 3.6G), making them the most polydisperse TMCs. The particles again displayed an amorphous oxide and oxycarbide shell ranging from 2 – 4 nm in thickness.[389] Again, comparison of the TEM images for ZrC and HfC with the XRD spectra show that they have lower amounts of carbon impurities compared to TiC.

EDS elemental mapping confirmed that there is a homogeneous distribution of both the metal and carbon throughout each of the particles (Figure 3.8). Oxygen, however, was also found to be dispersed throughout the sample, coming from the surface oxidation of each particle and perhaps oxidation of the remaining amorphous carbon. Excess carbon could also be identified in certain regions where the metal was not present, consistent with both XRD and TEM analyses. The elemental abundance of each sample obtained from EDS analysis is shown in Table 3.1. Trace metals were noted in each sample, likely from the Cu grid and possible impurities in the biochar.

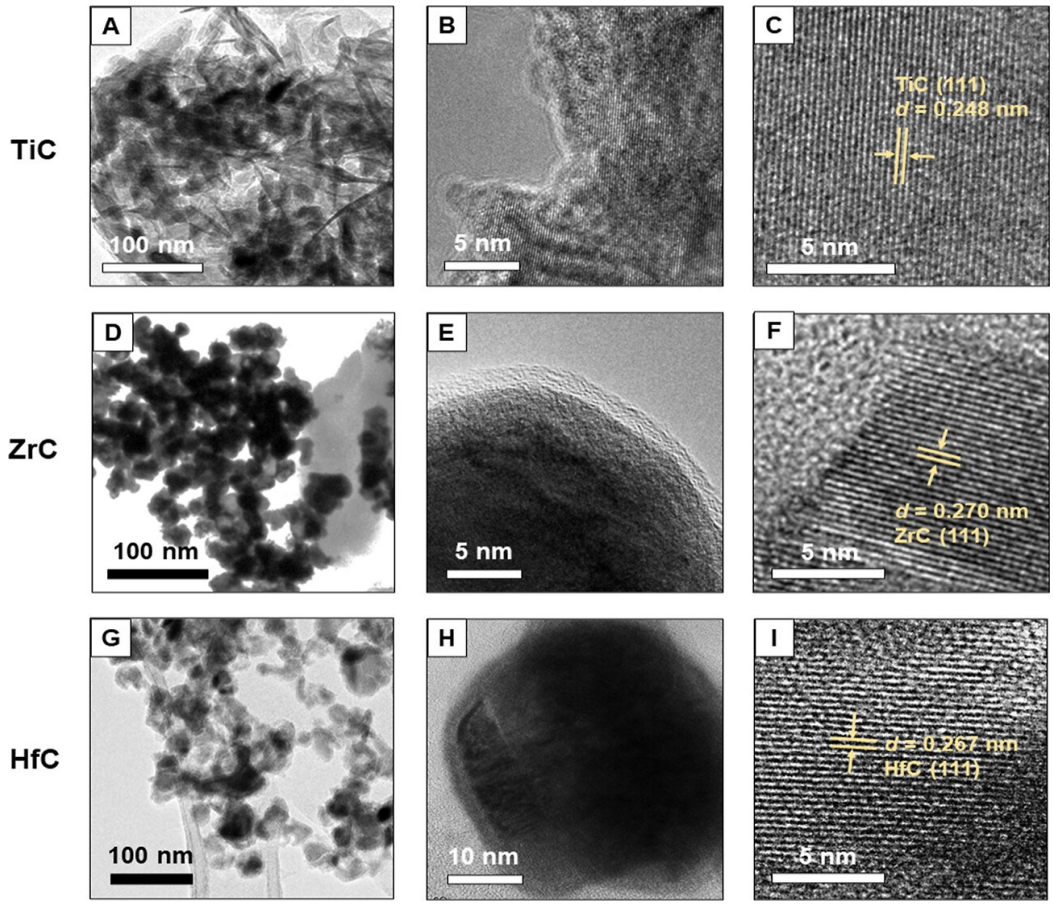

Figure 3.6. TEM and HRTEM images of TiC (A–C), ZrC (D–F), and HfC (G–I) NPs showing particle morphology, amorphous shell surrounding the crystalline carbide core, and lattice spacing.

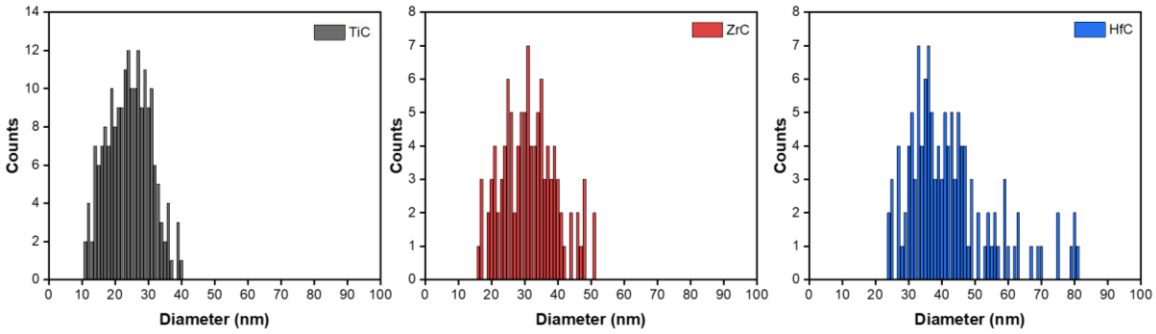

Figure 3.7. TiC, ZrC, and HfC NP size distribution from TEM images using ImageJ software.

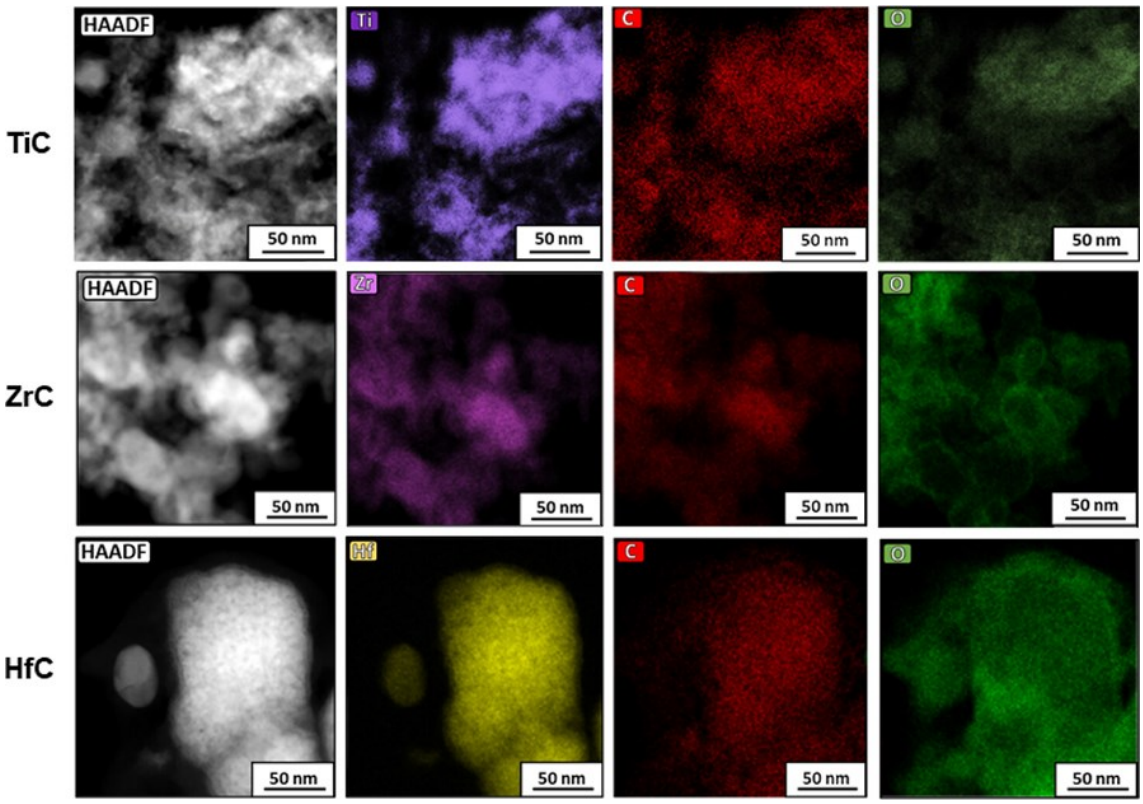

Figure 3.8. HAADF images and EDS elemental maps of TiC, ZrC, and HfC NPs showing the distribution of respective metals (Ti, Zr, and Hf), carbon, and oxygen within the samples.

Table 3.1. Elemental distribution (atomic %) in TMC samples based on EDS analysis.

Sample	Group 4 metal	C	O	Trace metals
TiC	35% (Ti)	38%	24%	Cu, Fe, Si, K (3% total)
ZrC	38% (Zr)	35%	26%	Cu, Fe (1% total)
HfC	43% (Hf)	27%	20%	Cu, Fe (< 1% total)

To determine the surface charge and colloidal stability of each TMC sample, zeta potential was used. These measurements revealed values of 32, 28, and 41 mV for TiC, ZrC, and HfC, respectively. Since the values are much larger than 10 mV (between -10 and +10 mV is considered a neutral particle), it indicates that the surfaces of the carbides are positively charged.[367] This is most likely due to

protonation of surface oxide hydroxyl groups of the metal oxide shell. The values are also large enough to be considered stable colloidal suspensions, making them easy to work with for solution processing as will be discussed in Chapters 4 and 6.

Following the analysis of particle composition and morphology, the optical properties of each TMC NP sample were probed both computationally by FEM analysis and experimentally using UV-vis absorbance measurements. Figure 3.9 shows the experimental and calculated absorbance spectra for TiC, ZrC, and HfC NPs suspended in water. For simulated spectra, particles were modeled as a single spherical NPs with diameters of 24, 31, and 42 nm for TiC, ZrC, and HfC, respectively. These diameters match the average particle size found for each TMC sample by TEM analysis. The calculated spectra show that the LSPR absorbance maxima for TiC, ZrC, and HfC should be in the UV region centered at 160, 150, and 175 nm, respectively. The peaks were expected to be broad, covering much of the UV region and slightly into parts of the visible. The average particle size and inherent material losses led to the HfC simulated absorbance spectrum being the broadest among the group 4 TMCs.[275] Further simulations were completed to study the effect of particle size on the output spectrum (Figure 3.10). This is an important parameter to study as the TMC samples are polydisperse, and the absorbance will be influenced by each different sized particle. For particles between 10 – 100 nm, the trend shows that the LSPR redshifted and the peaks become broader with increasing particle size for all three carbides.

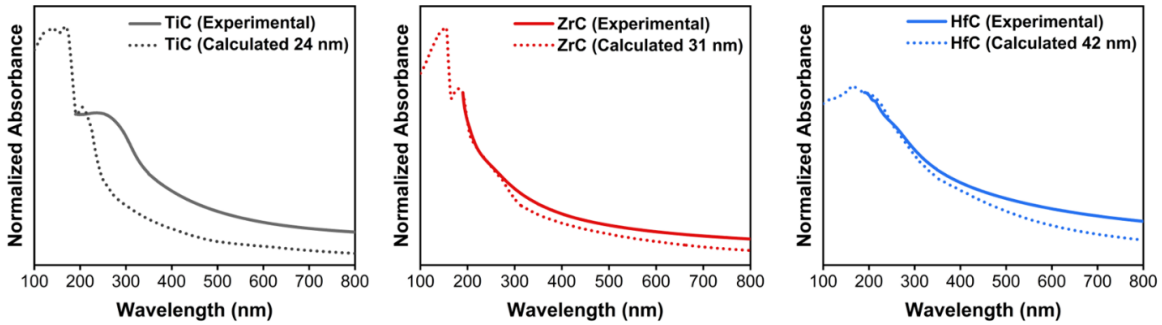

Figure 3.9. Experimental and calculated absorbance spectra of TiC, ZrC, and HfC NPs suspended in water.

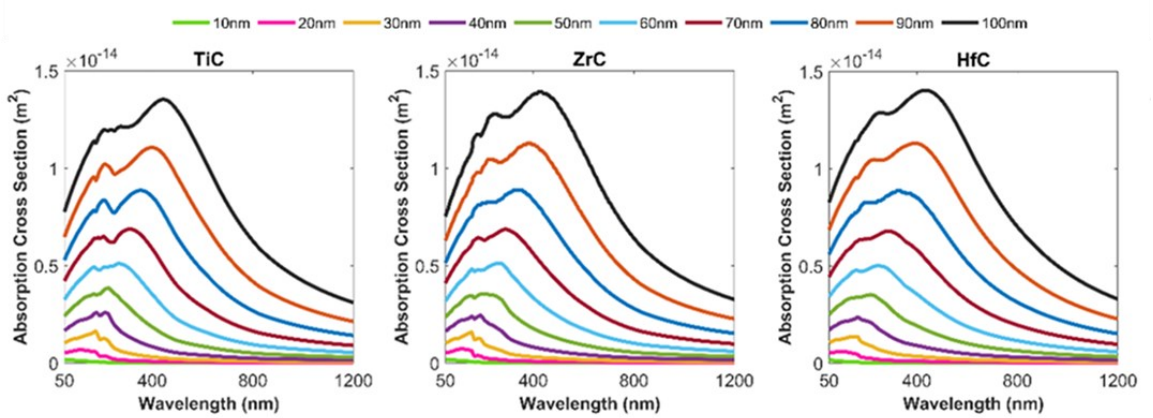

Figure 3.10. Experimental and calculated absorbance spectra of TiC, ZrC, and HfC NPs suspended in water.

The characteristic LSPR peak unfortunately could not be completely visualized in the experimental absorbance spectra due to instrument limitations. The spectrophotometer has a cut-off of 190 nm, with the peak maxima for all three TMCs expected to be below that wavelength. However, there is good agreement between the experimental absorbance spectra and the calculated spectra for ZrC and HfC in the spectrometer range. For the experimental data, the absorption was slightly higher in the visible and NIR region for ZrC and HfC. This can be explained by the polydispersity of the sample, where the small amount of larger sized particles could cause peak broadening and slightly increased absorption at longer wavelengths.[390] Another influencing factor could be the slight deviation of the TMC NPs from being spherical,[391] or the presence of small amounts of amorphous carbon. Presumably, the experimentally observed spectra are likely influenced to a small degree by each of these factors. Looking at the TiC spectra, the experimental absorbance has a peak at ~290 nm, which is redshifted compared to the calculated spectrum. It is hypothesized that because the TiC sample was mixed with much more amorphous carbon according to TEM, the interaction between the TiC NPs and carbon particles could be influencing the absorbance properties.

Another set of calculations was performed to compute the absorbance of the TMCs when embedded in a carbon matrix (Figure 3.11 and 3.12), representing the most extreme scenario. As discussed in Chapter 1, increasing the refractive index surrounding the NPs, like the amorphous carbon would,[392] often leads to redshifting of the LSPR maxima. For all TMCs, the LSPR peaks broadened and

redshifted, with maxima becoming ~350 nm in each case. For TiC, it appears that the shoulder peak occurs between the water and carbon scenarios. This could be caused by TiC NPs being peppered onto the larger amorphous carbon particles, leading to the observed peak. For ZrC and HfC the carbon matrix data was significantly different than the experimental data, indicating that the carbon impurities were not influencing the optical properties.

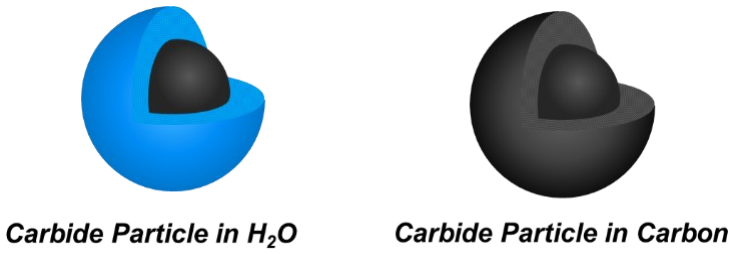

Figure 3.11. Representation of TMC NPs either dispersed in water or embedded in carbon for FEM simulations.

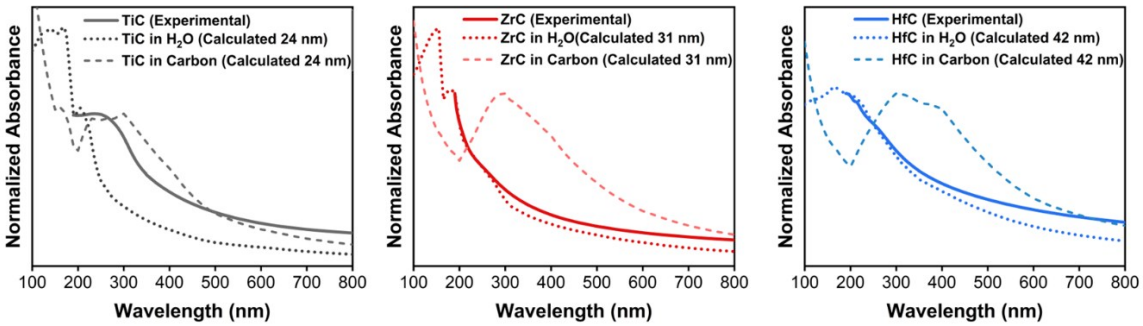

Figure 3.12. Experimental absorbance spectra overlayed with calculated absorbance spectra in H_2O (dotted line) and amorphous carbon (dashed line).

It has been well noted that oxidation of plasmonic NPs can cause damping of the LSPR, as well as broadening and redshifting of the absorbance peak.[339,393–396] Interestingly, when FEM simulations were run on the TMC NPs with varying surface oxide layer thickness (Figure 3.13 and 3.14), it was found that the carbides are relatively resilient to shifting but a decrease in the LSPR intensity was observed with increasing oxide shell thickness. For the simulations, the overall particle size remained the same, with the oxide shell working inwards into the carbide core. TiC experienced the largest fluctuation as the oxidation shell thickness increased, followed by ZrC and then HfC. This is likely due to the relative decrease in volume

for each particle. For example, at a 5 nm oxide shell thickness, the volume of the TiC particle inside the oxide shell will have been reduced by over 50%, compared to 40% and 30% volume reductions for ZrC and HfC, respectively.

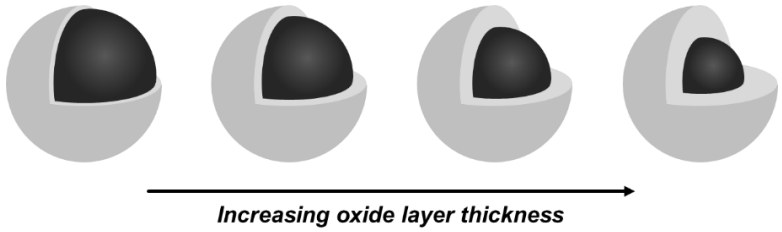

Figure 3.13. Schematic representation of increasing metal oxide shell thickness for simulations.

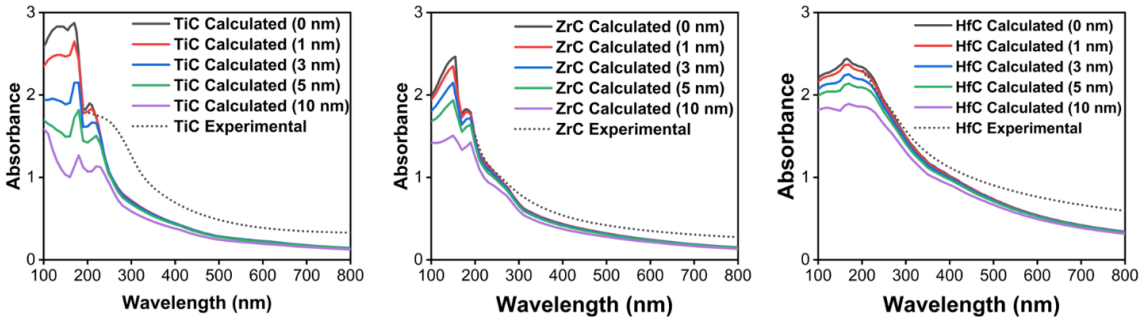

Figure 3.14. Experimental (dotted) and calculated absorbance spectra of 24 nm TiC (left), 31 nm ZrC (middle), and 42 nm HfC (right) with oxide shells ranging from 0 – 10 nm in thickness.

While bulk carbides are chemically quite robust,[315,397] it is important to study the stability of the nanoscale carbides in conditions that could be encountered in real world application. This is particularly important over long periods of time, where even slow oxidation could eventually destroy the optical properties. The stability of the TMCs was monitored first by tracking the absorbance of aqueous dispersions of the carbides over an extended period (Figure 3.15). In each case, there was no observable change to the absorbance after 1250 days of being dispersed in water. The next step focused on studying the chemical stability of the carbides (Figure 3.16) using acidic (3M HCl), basic (3M NaOH), and oxidizing treatments (10% H_2O_2). Each treatment consisted of sonicating the TMC NPs in each solution, followed by careful filtration, washing, and drying of the NPs before redispersing

in water for UV-Vis analysis. No significant in absorbance spectra were observed before and after the various chemical treatments to all three carbides.

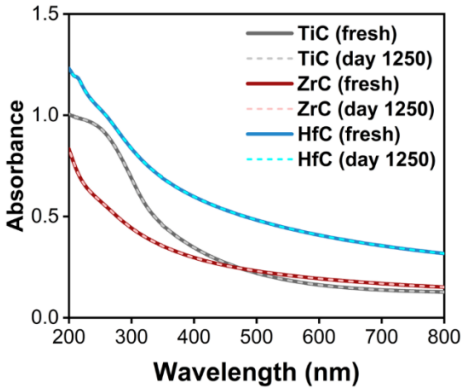

Figure 3.15. Absorbance spectra of TiC, ZrC, and HfC in water immediately (solid lines) and after 1250 days (dashed lines).

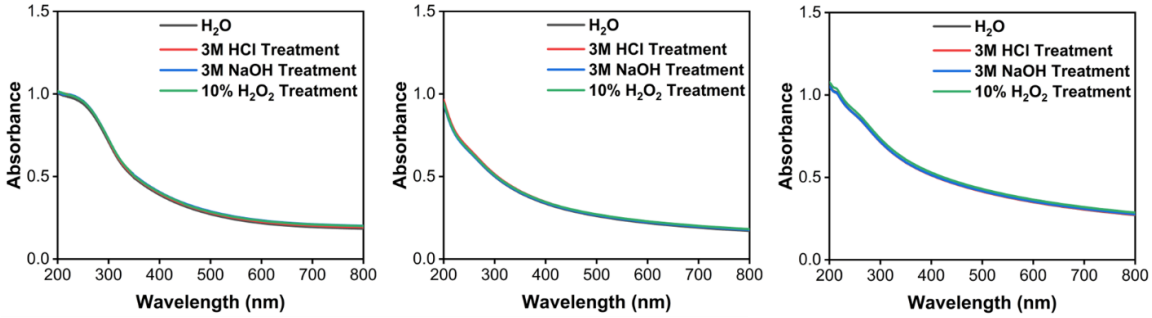

Figure 3.16. Absorbance spectra of TiC (left), ZrC (center), and HfC (right) after treatment with either 3M HCl, 3M NaOH, or 10% H_2O_2.

Given that the LSPR maxima for the TMC NPs were out of the range of the UV-Vis spectrophotometer, measuring the photothermal efficiencies of each is another way to verify the plasmonic characteristics.[398,399] Since plasmonic nanomaterials are some of the most effective photothermal materials reported, a relatively high photothermal efficiency using the method described in Chapter 1 would highlight the plasmonic nature. A simple heating-cooling cycle was used to determine the photothermal efficiency of the TMC NPs as described in section 2.3.8. Aqueous dispersions of each TMC were prepared and illuminated by a UV (365 nm) LED with a 10 nm bandwidth calibrated to 1 W cm^{-2} illumination intensity (Figure 3.17A). For each trial, the NP solutions were continuously illuminated for 30 min,

allowing them to reach a steady state temperature (Figure 3.17B) where the temperature plateaued. After the steady state temperature was reached, the LED was turned off and the solution was given another 30 min to cool back to ambient temperature. The photothermal efficiency was calculated by the energy balance thermal heat transfer equation introduced in section 2.5.7.[370] For these calculations, the optical density value used is defined as the average absorbance of the corresponding TMC sample of the bandwidth range of the LED. While samples were prepared as mass loadings of 0.5 mg mL^{-1}, the absorbance within the range of the UV LED was used for the calculations.

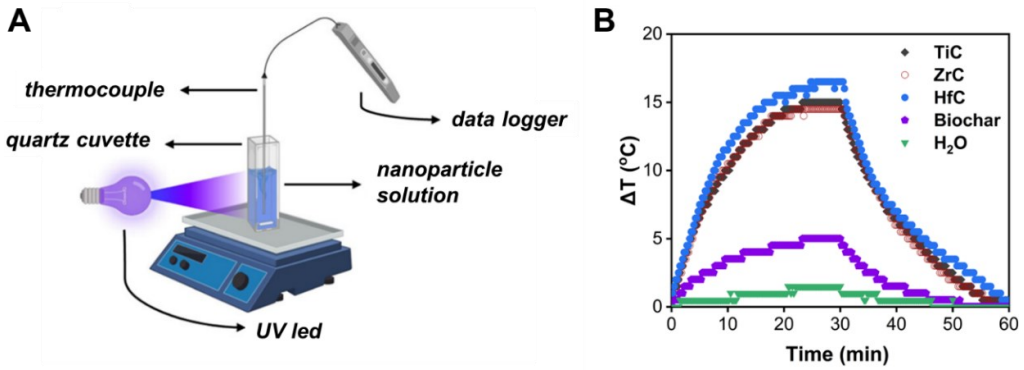

Figure 3.17. (A) Schematic of photothermal heat generation experimental setup. (B) Heating and cooling curves for TMCs, biochar, and blank water during photothermal studies.

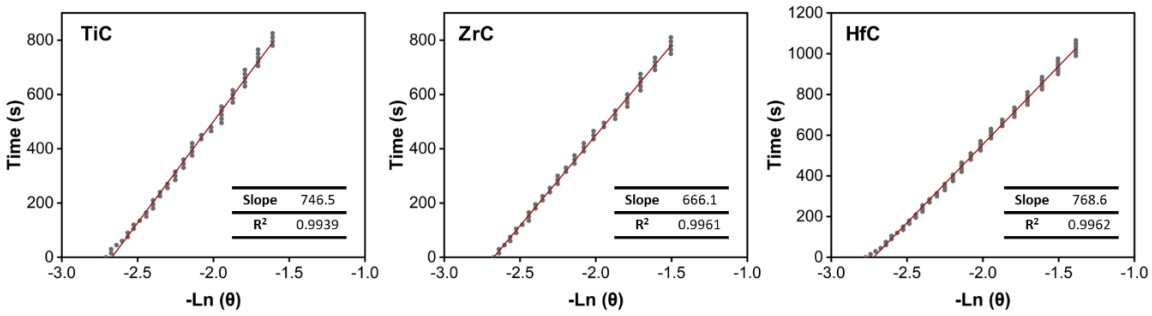

Figure 3.18. Plots of cooling period time vs. negative logarithm of the temperature change during the cooling period used for the calculation of the photothermal transduction efficiency for TiC (left), ZrC (middle), and HfC (right). Inset: Chart showing slope (heat transfer coefficient), and goodness of fit (R^2).

The heat transfer coefficient, *h*, used in the calculations was obtained from the cooling period data as a function of the negative logarithm of the temperature change (Figure 3.18). The full derivation of this equation can be found in Appendix A.2. HfC recorded the highest change in temperature of 16.5 °C and had the highest photothermal efficiency of 73 ± 1% (Figure 3.19A). Both TiC (15.0 °C) and ZrC (14.5 °C) had comparable solution temperature increases; however, the photothermal efficiency for ZrC (69 ± 4%) was higher than for TiC (60 ± 3%). To verify the high efficiency was in fact because of the TMC NPs, birch derived biochar that had been put through the magnesium reduction reaction conditions (without the metal oxide) was tested. A temperature increase of 5.0 °C, equating to an efficiency of 22 ± 2% was found for the birchwood char. To highlight the TMCs performance compared to the starting metal oxides, it was found that TiO_2, ZrO_2, and HfO_2 recorded photothermal efficiencies of 7 ± 1%, 10 ± 3%, and 12 ± 3%, respectively. Finally, carbon black was tested as a well studied photothermal material. Unfortunately, the particles were not stable as a dispersion and crashed out, leading to a similar performance as the blank water (>5%).

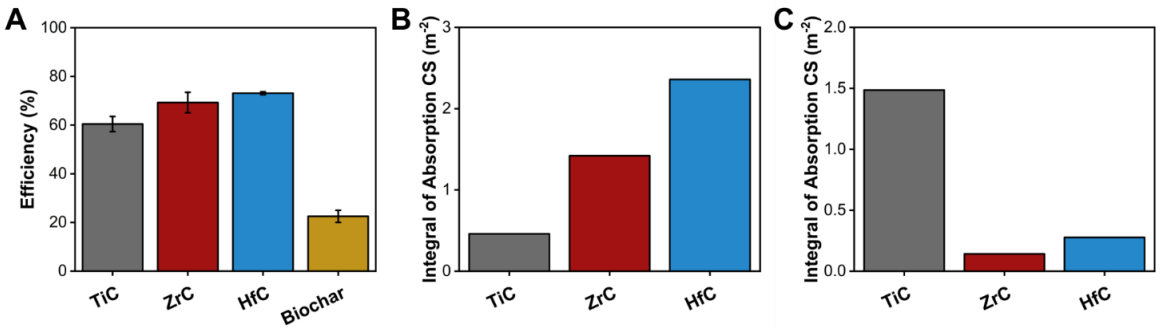

Figure 3.19. (A) Average photothermal transduction efficiencies of TMCs and birch wood char. (B) Calculated absorption cross-section of TMCs between 360 – 370 nm. (C) Calculated scattering cross-section of TMCs between 360 – 370 nm.

To compare the heat generation capabilities and efficiencies of each of the TMCs, the absorption and scattering cross sections at the LED excitation wavelength were calculated using FEM. The absorption cross section can be directly compared to the amount of heat generated by the TMCs, while the scattering cross section is related to the light-to-heat conversion efficiency. Any incoming light that is scattered will be a loss of energy by not contributing to the photothermal heating process. To

account for carbon around TiC in the simulations, the average absorption and scattering of TiC NPs with and without carbon around the NPs were used. To account for the LED bandwidth, the calculations were performed using the integral of absorption and scattering over a 10 nm spectral range (360 – 370 nm). HfC has the largest absorption cross section within the LED bandwidth, followed by ZrC and TiC (Figure 3.19B). This trend agrees with the photothermal heat generation experimental data for the TMCs. The scattering cross section of TiC is significantly larger than that of ZrC and HfC (Figure 3.19C), and this can help explain the lower efficiency of TiC in light-to-heat conversion. Next, focus was turned to the response of the photothermal efficiency of the TMCs over time and under different illumination intensities. Over the course of eight heating and cooling cycles, the TMCs were found to retain their photothermal heating efficiency (Figure 3.20). In addition, as the incident light intensity increased, the corresponding photothermal heating effect was found to increase linearly (Figure 3.21).

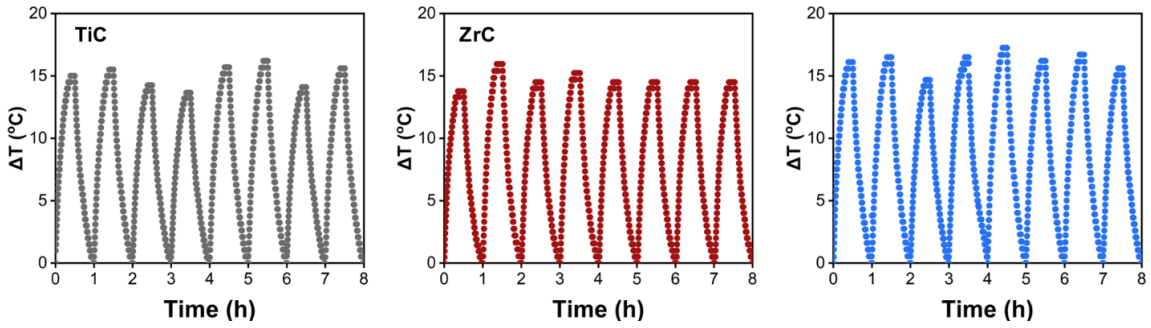

Figure 3.20. Photothermal heating cycles of group 4 TMCs.

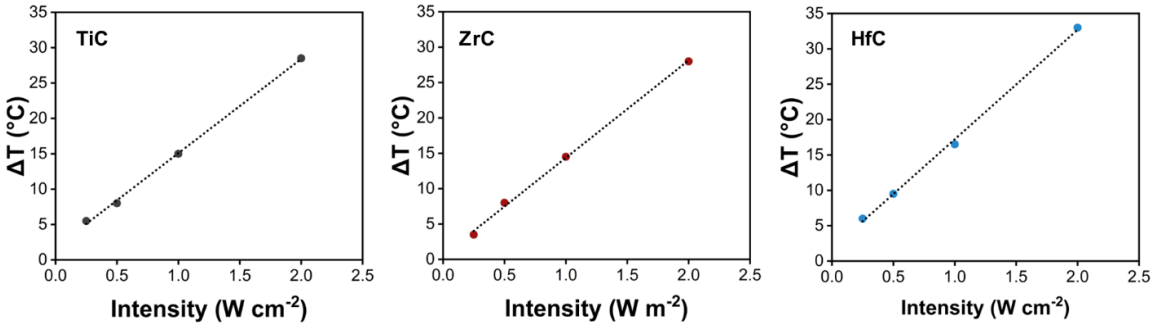

Figure 3.21. Temperature change plots as a function of illumination intensity at 0.25, 0.5, 1.0, and 2.0 W cm^{-2} with 365 nm irradiation.

3.4 Conclusion

A series of group 4 TMC NPs that are UV plasmonic and water dispersible were prepared using a straightforward magnesium reduction reaction of metal oxide NP precursors and Mg powder. The corresponding TMCs were formed between 950 and 1100 °C in relatively short reaction times. TiC, ZrC, and HfC formed with average particle sizes of 24 ± 8, 31 ± 9, and 42 ± 15 nm, respectively, and were comprised of a crystalline carbide core and an oxide/oxycarbide shell. FEM simulations showed the materials to display LSPR in the UV region between 150 and 175 nm. Experimentally, the LSPR maxima were not observed in the absorbance data due to the wavelength cutoff of the spectrophotometer, so complimentary photothermal studies were completed. These showed the TMCs to possess high photothermal efficiencies typical of plasmonic nanomaterials. When illuminated by a 365 nm LED source, TiC, ZrC, and HfC had average photothermal transduction efficiencies of 60, 69, and 73%, respectively. Impressive aqueous and chemical stability was displayed by the carbides with negligible change in the optical response over 1250 days in water or after strong acid, strong base, and oxidizing treatments. The high photothermal efficiencies make TMCs an attractive option for many light-to-heat conversion applications.

CHAPTER 4

EXPLORATION OF GROUP 4 PLASMONIC CARBIDES FOR LAB-SCALE DESALINATION

Part of this chapter is adapted from Margeson, M. J.; Atwood. M.; Monfared, Y. E.; Dasog, M. Plasmonic Group 4 Transition Metal Carbide Interfaces for Solar-Driven Desalination. *Aggregate*. **2024**, e531. Copyright 2024. John Wiley & Sons Australia, Ltd. The synthesis of all Group 4 carbides and interfaces, material characterization, and solar-vapor generation and desalination experiments were performed by me. M. Atwood assisted with performing replicate experiments for the water purification. SEM images were taken by T. Hynes at Dalhousie University and TEM was performed by Dr. Carmen Andrei at the Canadian Center for Electron Microscopy (CCEM). ICP-MS measurements were run by Heather Daurie at the Center for Water Resource Studies at Dalhousie University. Freeze-drying (lyophilization) access was granted by Dr. C. Charron. FEM simulations were conducted by Dr. Yashar Monfared at Dalhousie University. Amorphous carbon generation by birch wood pyrolysis was done by Dr. S. MacQuarrie research group at Cape Breton University.

4.1 Introduction

As discussed in Chapter 1, the growing issue of water scarcity has become one of the largest challenges facing modern society. It is therefore crucial to increase the accessibility to water purification methods and clean water sources across the globe.

While options such as rainwater harvesting, and air condensation are becoming popular, rapid climate change is making traditional water collection methods less reliable. Accessing saltwater and brackish water by desalination to produce freshwater has been viewed as a promising way to address the global water shortage.[137] The vast majority of water desalination processes employ thermal-distillation (TD) techniques[129,133,142] or use reverse osmosis (RO) membranes,[139–141] which permit water transport across a semi-permeable membrane but reject salt ions. The inherent deficiencies of these techniques are the relatively low water flux to energy consumption ratio, durability, fouling, and selectivity issues.[147] Further, the intensive infrastructure needs can make implementation of the systems costly.[400] These drawbacks make the uptake of desalination technology a cumbersome process, particularly in developing nations which bear the brunt of water scarcity issues.

A desirable alternative to TD and RO is solar desalination, where the sole input of energy comes from sunlight.[137] Unfortunately, directly copying the world water cycle is a highly inefficient process due to the low light absorption of water and extensive heat loss by non-evaporative processes.[401] To combat these efficiency issues, an influx of research has gone into developing new materials with the ability to absorb light across the entire solar spectrum and utilize it to generate heat for water evaporation. Known as photothermal materials, the most promising examples include harnessing thermal vibrations in polymers and carbon-based materials,[402–406] non-radiative combination in semiconductors,[174,177,407,408] and localized heating in plasmonic NPs.[180,409] Out of the group, plasmonic materials are perhaps the most promising as they display very efficient light-to-heat conversion (photothermal heating).[410,411] As discussed in section 1.2.2, solar desalination materials are characterized by their solar-to-vapor conversion efficiency.[195] This refers to the ability of a material to effectively convert incident sunlight into localized heat, and ultimately produce water vapor. Top performing materials have surpassed 90% solar-to-vapor conversion efficiency for saltwater under illumination equal to 1 sun.[190,208,412] The strategy of creating high-performance desalination devices requires not only material design, but also engineering to enhance thermal management, water movement, and steam release. This has led to a remarkable number of reports on materials, supports, and even elaborate 3D evaporation scaffolds for solar-vapor generation and desalination.[221,413–418] However, intricate

designs often increase the complexity and cost of evaporation interface fabrication. Therefore, there is still room to enhance the evaporation rate while maintaining simple and scalable designs by targeting highly efficient photothermal materials.

As presented in Chapter 1 and 3, refractory plasmonic NPs including TMNs and TMCs have emerged as promising and relative low-cost photothermal materials.[272,419] While plasmonic NPs such as those mentioned in the previous chapters have LSPR at specific wavelengths, aggregation of particles on a surface or film can broaden the absorption drastically. This is due to the coupling of the individual plasmonic fields with one another, generating secondary plasmonic responses that can allow most of the solar spectrum to be harvested.[420,421] In the past decade, our group and others have highlighted the utility of TMN NPs for solar-driven desalination.[189,422,423] Carbides on the other hand remain a relative newcomer to the field and have yet to be widely explored. Once again, 2D MXene carbides have garnered interest with studies showing their promise for photothermal applications, including desalination.[424,425] Recently, commercial ZrC NPs were used to develop a desalination device by Liu *et al.*, showing an evaporation rate of 1.38 kg m^{-2} h^{-1} under one sun illumination, equating to a 95% solar-to-vapor efficiency.[380] Based on the high photothermal efficiencies calculated for our synthesized group 4 TMC NPs, we report the performance of the carbides for solar vapor generation (SVG) and desalination. Experiments were conducted for a simple paper-based evaporation interface, and a hydrogel-based solar desalinator which can take advantage of the water cluster evaporation discussed in section 1.2.2. The effect of TMC composition, particle loading, and salt concentration on the evaporation performance was evaluated.

4.2 Methods

4.2.1 Material Synthesis and Characterization

Mixed cellulose ester filters (MCE, 0.45 μm pore size, 25 mm), and polyester filters (PE, 0.50 μm pore size, 25 mm) were purchased from Cole Parmer. Deionized water (DI-water, 18.2 MΩ cm) was obtained from a Sartorius Arium water purification system.

Group 4 TMC NPs were synthesized as outlined in section 2.1 of this report. Synthesis of birch residue followed the procedure of section 2.1.2, and TMC NP synthesis followed the procedures of section 2.1.3. For this chapter, characterizations include PXRD, SEM, TEM, reflectance measurements, and ICP-MS as outlined in section 2.3. FEM simulations were performed according to the details outlined in section 2.2.

4.2.2 Fabrication of Solar Desalination Interfaces

The plasmonic metal carbide (TiC, ZrC, or HfC) mixed-cellulose ester (MCE) interfaces were prepared by vacuum-loading a given volume of 1.0 mg mL^{-1} solution of carbide onto a 25 mm diameter MCE filter (Cole Parmer, pore size 0.45 μm) for a loading of either 0.5, 1.0, 1.5, or 2.0 g m^2. The plasmonic carbide filter paper was then placed onto a foam disc (EVA, 2.5 cm diameter x 1 cm thick) with 1D fabric wicks (Zorb®) inserted into the foam.

To prepare the plasmonic TMC hydrogel evaporation interface, a solution of polyvinyl alcohol (PVA, 7.5 wt.%, 3.5 mL) and glutaraldehyde (150 μL) were well mixed through sonication and gentle heating to 60 °C. Separately, a 150 μL dispersion of carbide (TiC, ZrC, or HfC, 0.25 mg mL^{-1}) and HCl (3 wt.%, 150 μL) were mixed. The PVA and TMC solutions were mixed and sonicated for 15 min. The resultant mixture was poured onto a glass slide, with a 1 mm spacer added and a second glass slide laid on top. Gelation was carried out for 90 min. The obtained hydrogel was sonicated in DI water, followed by freeze-drying for 40 h. The obtained aerogel was placed into 80 °C DI water for 60 min to remove any unreacted chemicals and to rehydrate. The rehydrated hydrogel was cut to size (2.5 cm disc) and placed onto a foam disc (EVA, 2.5 cm x 1 cm thick) with 1D fabric wicks (Zorb®) inserted into the foam.

4.2.3 Water Evaporation and Desalination Experiments

Evaporation experiments (freshwater and saltwater) were performed using a solar simulator (Pico™ Small Area LED, G2V). Mass change was recorded to a computer directly connected to a calibrated analytical balance (VWR-164AC) using CoolTerm (Roger Meier). The plasmonic evaporation platform was floated on top of water in a small glass beaker. The interface was illuminated from above and the mass change was measured over 10 min with data points being collected every 5 s. Before starting runs, the interface was illuminated for 5 min to reach a steady temperature. Temperature was recorded using an infrared thermal camera (Perfect Prime IR0005). Ambient temperature was maintained at 22 °C for experiments, and trails were run only when the relative humidity was between 50 – 55%. For variable temperature and humidity studies, a polyethylene and PVC pipe chamber was constructed with temperature and humidity controls connected to a ceramic heater or a humidifier, respectively. Metal ion concentration samples were collected using an enclosed quartz vessel with a slanted cover and a separate collection chamber.

4.3 Results and Discussion

For this study, plasmonic group 4 TMC NPs, TiC, ZrC, and HfC, were prepared using the procedure outlined in Chapter 3.[426] To prepare the paper-based evaporation interfaces, a 1.0 mg mL^{-1} stock solution of each TMC was dropcast under vacuum onto a 2.5 cm diameter mixed cellulose ester (MCE) filter paper with a pore size of 0.45 μm. This pore size proved sufficiently small to not allow the carbide NPs to pass through into the filtrate. This process was completed to achieve interfaces with 0.5, 1.0, 1.5, and 2.0 g m^{-2} of carbide. Looking at images of the 1.0 g m^{-2} MCE interfaces by SEM, there is still clear porosity across the evaporation surface after coating (Figure 4.1A). This is important as it will allow for effective release of the water vapor after the photothermal evaporation. Interestingly, while the absorbance of the TMC NPs in solution peaks in the UV region (Figure 3.10), when dispersed on a solid support it broadens significantly across the entire UV-visible-NIR range of the spectrum (Figure 4.1B). This led to average light

absorption of 86% (TiC), 82% (ZrC), and 95% (HfC) between 300 and 1500 nm. As stated previously, this broadband absorption likely arises from coupling of the individual NP plasmonic resonances when confined to close proximity to one another on the MCE filter.[427,428] Further, the light absorption effect could be enhanced by increased light trapping within the pores of the filter paper. To investigate the expected effect of particle-particle interactions, calculations were performed using finite element method (FEM) simulations to compare two different scenarios. HfC was chosen as it displays the highest broadband absorption, and the two scenarios were for an individual particle and an HfC trimer (Figure 4.2A).

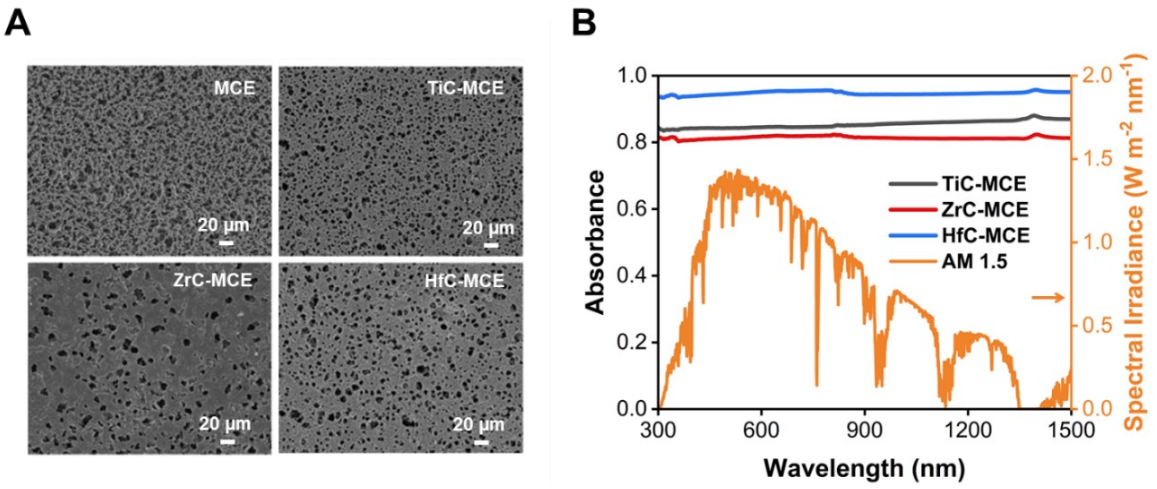

Figure 4.1. (A) Top-down SEM images of blank MCE filter and 1.0 g m^{-2} TMC loaded filters. (B) Absorbance spectra of TiC, ZrC, and HfC NPs loaded onto the MCE filter papers (left axis), with reference solar intensity spectrum for total global AM 1.5 radiation (orange, right axis). Absorbance calculated from reflectance spectra and is read as the fraction of light absorbed at a given wavelength by the interface.

Compared to the scenario of the single HfC particle, the absorbance spectrum of the HfC trimer is much broader and extends across the visible region of the spectrum into the NIR region (Figure 4.2B). On the MCE interface, it is likely that there are many different sizes of particles at slightly varying distances from one another. The addition of contributions from all the different scenarios is hypothesized to lead to the observed broadening on the solid support versus in solution.

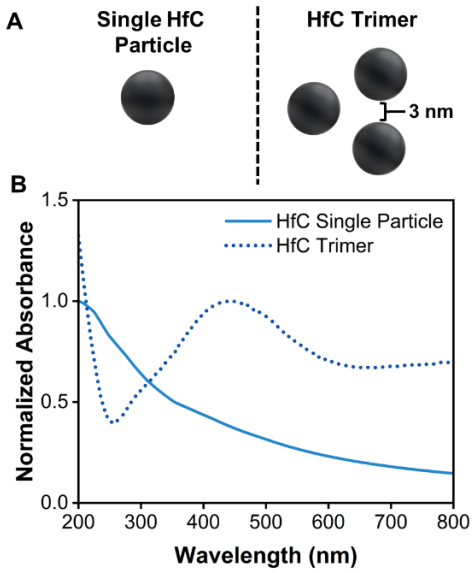

Figure 4.2. (A) Schematic of single 42 nm HfC particle and trimer of 42 nm particles for FEM simulation. (B) Corresponding absorbance spectra from simulations.

A complementary set of simulations were run in addition to the particle-particle coupling effect to see how the effect of TMC particle size would influence the absorbance, scattering, and corresponding photothermal efficiency (Figure 4.3). As displayed by the contour plots, there is a large effect of the particle size on both the absorbance and scattering of TMC NPs. Focusing on the absorbance, the maximum redshifts with increasing size and broadens across a larger range of wavelengths, as has been shown previously for other refractory based plasmonics.[272,426] The absorbance maximum for smaller NPs (10 – 40 nm) lies in the deep UV, while larger particles (70 – 100 nm) absorbs strongest between 280 and 400 nm. The scattering component tends to increase for larger NP sizes, which agrees with trends observed previously for other plasmonic materials.[429] Taking the ratio of the absorption cross section and the total extinction (comprised of both absorption and extinction cross section) gives the overall photothermal efficiency. This decreases in the visible and near IR region as the particle size increases from 10 – 100 nm. The overall indication from these contour plots is that smaller particles (<50 nm) are expected to be more suitable for photothermal applications as they have calculated photothermal efficiencies >80% across the visible and near-IR regions. Important to note is that these simulations do not account for particle-particle coupling, which would occur in tandem with the particle size effect.

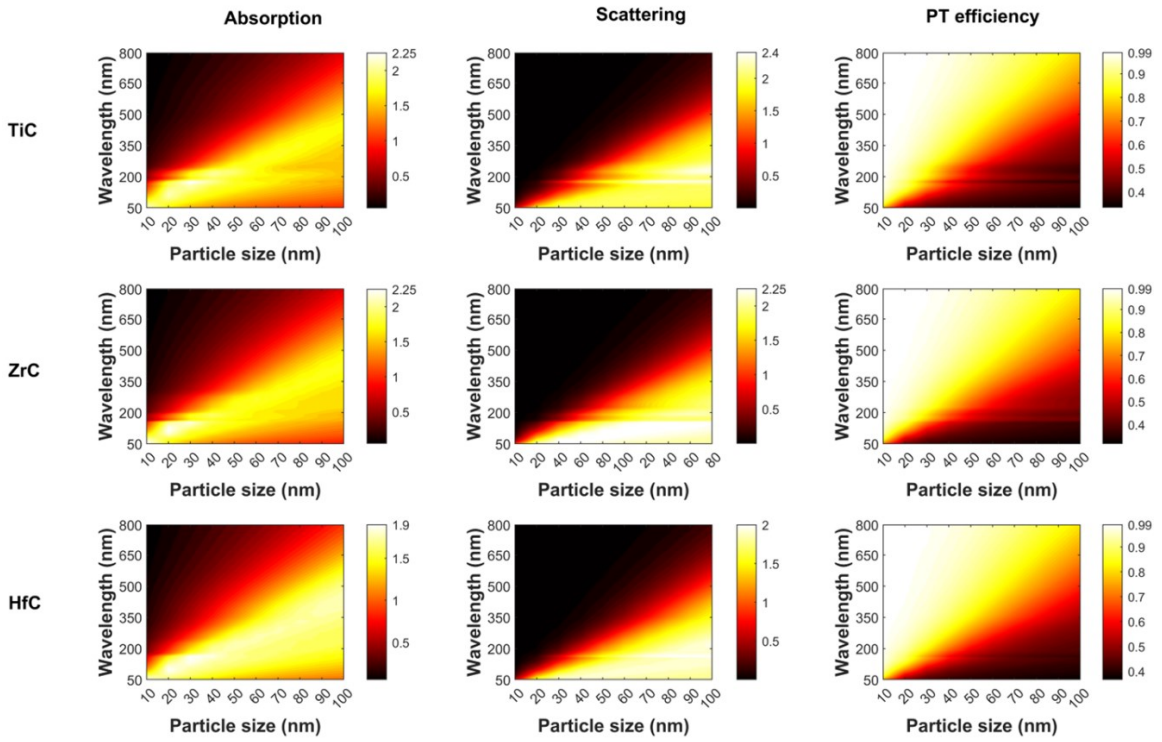

Figure 4.3. Simulated contour plots for absorbance (left), scattering (middle), and photothermal efficiency (right) between 50 and 800 nm for TiC (top), ZrC (middle), and HfC (bottom). Particles were simulated for sizes ranging from 10 – 100 nm in diameter. The color denotes intensity where white to yellow is higher and red to black is lower values for the corresponding plot.

To study the solar-to-vapor generation efficiency of the interfaces, the plasmonic TMC coated MCE interfaces were placed on top of a constructed floating platform. This platform consists of a disc shaped 0.5-in (1.3 cm) thick EVA foam support with one dimensional (1D) cotton fabric wicks protruding through the foam underneath (Figure 4.4). This design concept provides thermal insulation of the evaporation interface from the bulk water below by the EVA foam, while the root-like wicking structure is used to provide sufficient water supply to the interface. This structure has been adapted from a variety of reports to maximize water transport without sacrificing the thermal isolation capacity of the evaporator.[191,237] To assess the potential of the TMCs for solar-vapor generation, initial studies were carried out for one-sun illumination using a Pico LED solar simulator and tap water. Throughout the experiments, the relative humidity was maintained between 50 – 55% with the ambient temperature held at 22 °C. The TMC evaporators were

floated in a water filled container such that the edges of the foam left no gap between the evaporator and the sides of the container. This was to minimize any unaccounted natural evaporation contribution from the surface of the water. After the surface of the evaporator had become saturated, the interfaces were illuminated for 5 minutes to reach a steady state before measuring the surface temperature for the trial (Figure 4.5). The SVG efficiency values that are reported are averaged from five trials.

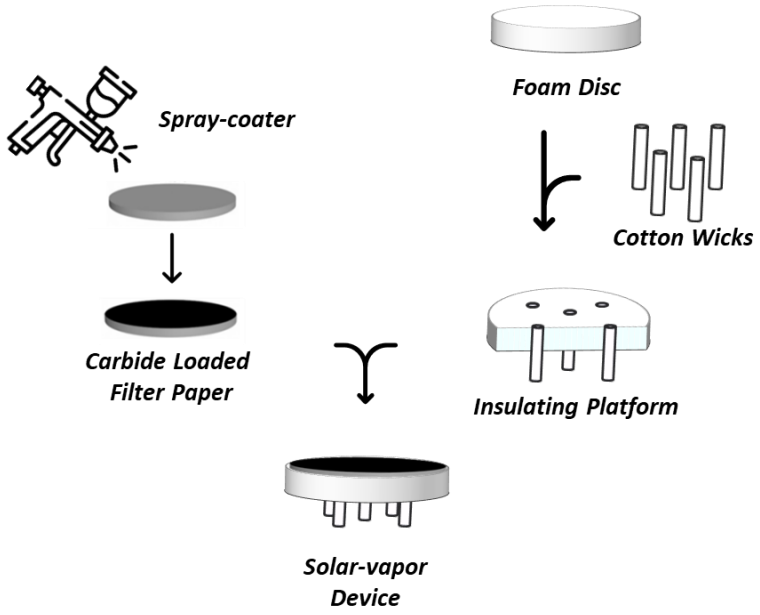

Figure 4.4. Schematic illustration of TMC NP evaporation device fabrication.

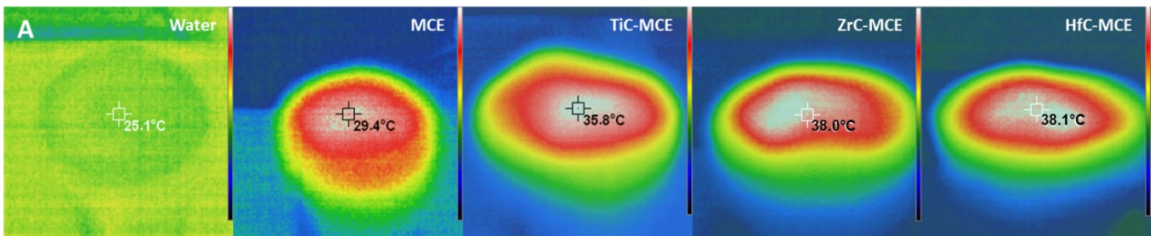

Figure 4.5. Representative IR thermal images acquired from water, blank MCE interface (no carbide), and TiC, ZrC, and HfC interfaces under one-sun illumination. Maximum surface temperature is shown by the target.

The representative plots of mass change over the course of illumination for bare distilled water, the blank solar evaporation device, and for the TMC NP interfaces

are displayed in Figure 4.6A. From this data, the average evaporation rates for pure water and the blank MCE evaporation support were found to be 0.07 ± 0.01 and 0.38 ± 0.08 kg m^{-2} h^{-1}, respectively. For the carbide interfaces, mass loadings of 0.5, 1.0, 1.5, and 2.0 g m^{-2} were investigated (Figure 4.7A). In each case, the 1.0 g m^{-2} loading was determined to be the top performer. This is explained by looking at SEM images of the MCE filters at each mass loading. At lower mass loading, the overall surface coverage was low, leading to white spots across the surface where light can be reflected away. On the other hand, at higher loadings (1.5 and 2.0 g m^{-2}), the pores become heavily and fully blocked, which likely hinders the release of the water vapor from the surface, trapping it in the MCE membrane instead. As every TMC had the same optimized mass loading of 1.0 g m^{-2}, it appears to be more associated with the MCE filters themselves as the balanced point of sufficient material and efficient water release.

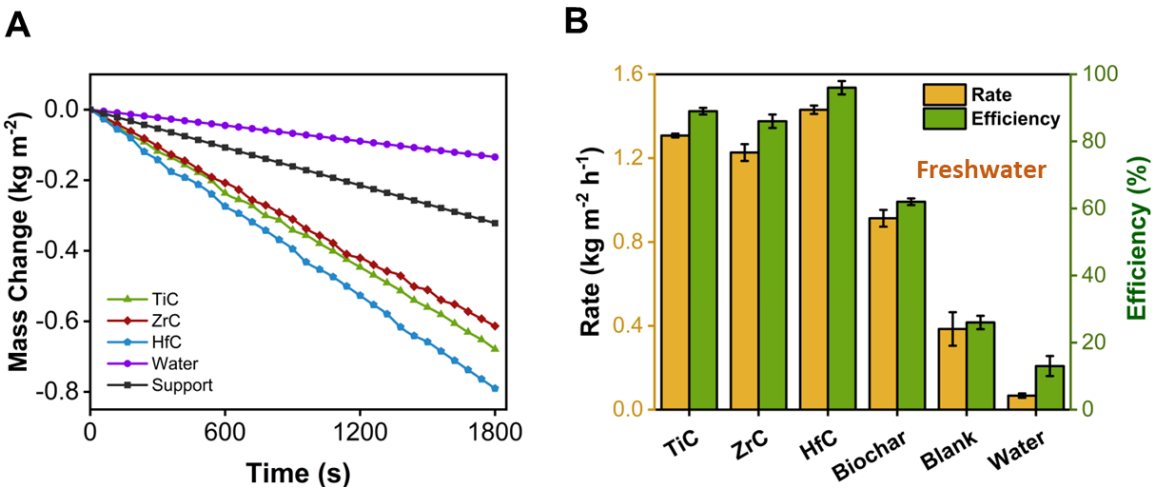

Figure 4.6. (A) Mass change plots and (B) rates (orange, left) with corresponding SVG efficiencies (green, right) from freshwater evaporation studies for the carbide, birch char, blank support and water under one-sun illumination.

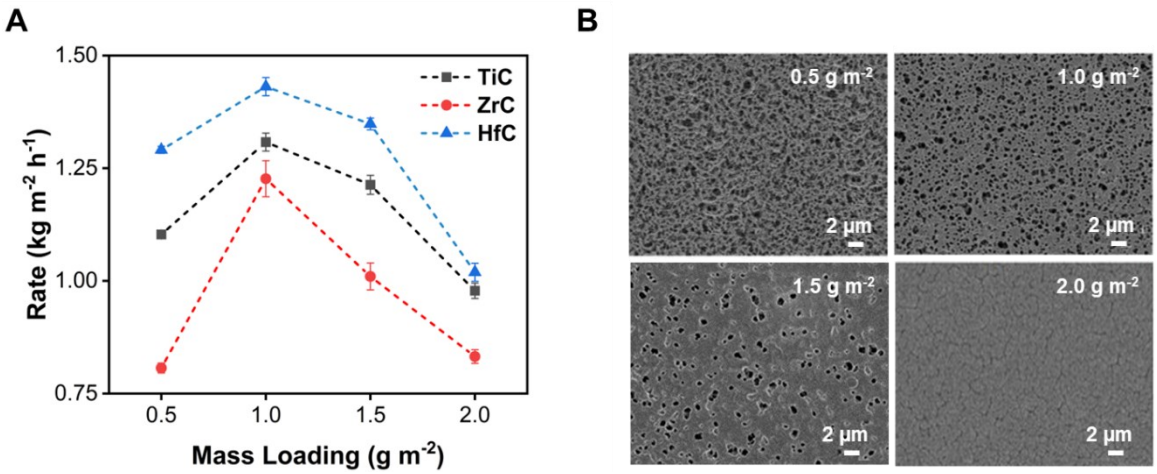

Figure 4.7. (A) Freshwater evaporation rates for TMC NPs and (B) representative top-down SEM images of TiC at mass loadings of 0.5, 1.0, 1.5, and 2.0 g m^{-2} on MCE membranes.

For the optimized TMC loadings, ZrC was found to have the lowest evaporation rate of 1.22 ± 0.04 kg m^{-2} h^{-1}, followed by TiC (1.31 ± 0.01 kg m^{-2} h^{-1}). HfC achieved the highest evaporation rate of the carbide series with an average value of 1.41 ± 0.02 kg m^{-2} h^{-1} (Figure 4.6B). To calculate the corresponding solar-to-vapor efficiency for the materials tested, equation 2.7 introduced in section 2.3.8 for lab-scale SVG efficiency was used. Using this method, the HfC evaporation interface was found to have the highest SVG efficiency value of 97%, followed by TiC and ZrC with efficiencies of 89% and 86%, respectively (Figure 4.6B). Looking at the data, it is noteworthy that the solar evaporation efficiency increases alongside increasing broadband absorbance. That is, HfC absorbing the largest percentage of light between 300 – 1500 nm, followed by TiC then ZrC.

After optimization of the evaporation process using the TMC interfaces with tap water, their potential for desalination was analyzed using water obtained directly from the Atlantic Ocean (Halifax, Canada). Once again, HfC recorded the highest evaporation rate of 1.40 ± 0.01 kg m^{-2} h^{-1}, with TiC and ZrC achieving rates of 1.26 ± 0.01 and 1.18 ± 0.02 kg m^{-2} h^{-1}, respectively. These are all very slightly lower than the freshwater generation rates, though prove the TMCs are able to tolerate saltwater quite well. These represent SVG efficiencies of 86%, 80%, and 96% for TiC, ZrC, and HfC, respectively (Figure 4.8A). The birch wood char was also tested for the desalination process and had a much lower evaporation rate of 0.82 kg m^{-2}

h^{-1} and a SVG efficiency of 56%. While carbonaceous materials are a popular choice for photothermal evaporation, these results highlight the effective enhancement of water evaporation by the plasmonic TMC NPs.

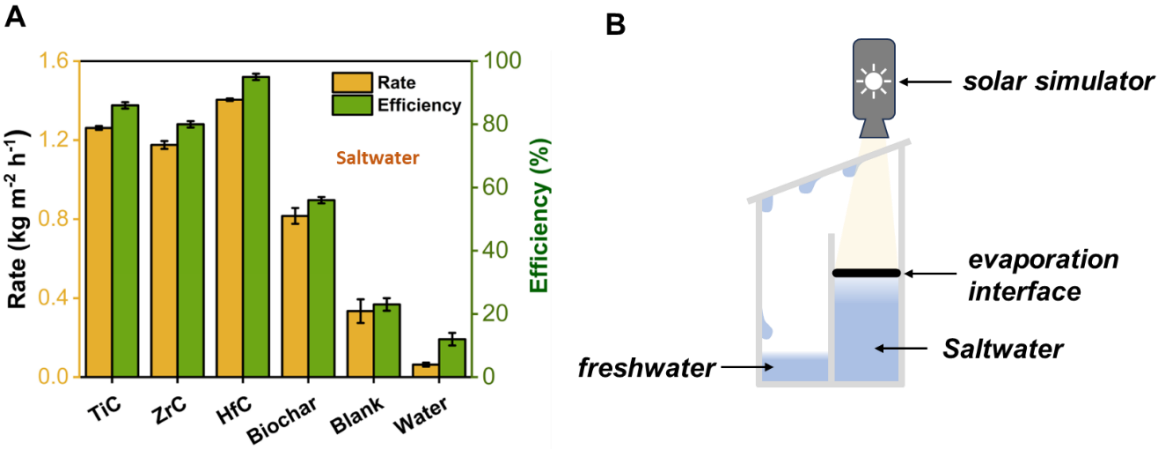

Figure 4.8. (A) Saltwater evaporation rates for TMC NPs on MCE membranes under one-sun illumination. (B) Schematic for the collection of evaporated water during desalination of Atlantic Ocean water by TMC NP interfaces.

Purity of the resulting desalinated water was verified by collecting and performing metal analysis on samples using an enclosed quartz vessel (Figure 4.8B) by inductively coupled plasma mass spectrometry (ICP-MS). Water collected from all three TMC NP interfaces showed 3 – 5 orders of magnitude decrease in the concentration all the salt ions compared to the starting harbour water (Figure 4.9). This dropped them all to concentrations well below those set forward by the World Health Organization (WHO). Additionally, samples were tested for several toxic heavy metals known to contaminate the Halifax Harbour waters (Pb, As, and Cd). Finally, samples were tested for the TMC metals themselves to verify that there is no leaching of the metals into the purified water. None of these metals were presented in the evaporated water at concentrations above the instrument detection limit (~10 ppb). Unfortunately, Hf was not able to be determined though being the heaviest of the three group 4 transition metals it is even less likely to be carried over.

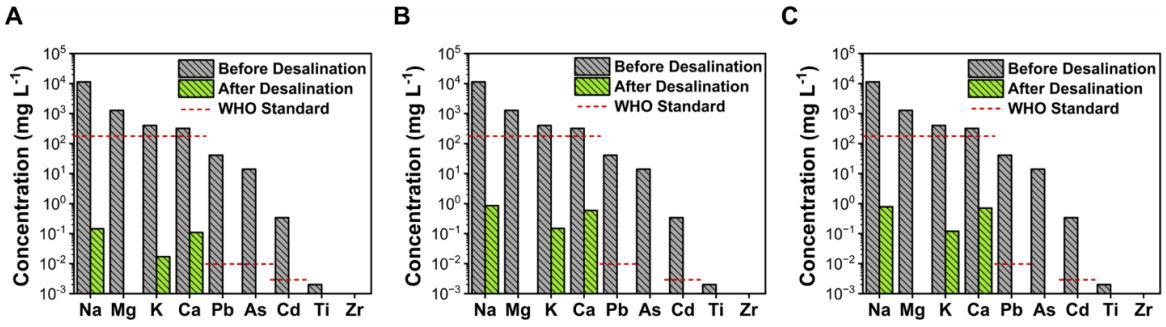

Figure 4.9. ICP-MS metal analysis for water samples before (grey, striped), and after (green striped), desalination using (A) TiC, (B) ZrC, and (C) HfC evaporation interfaces.

The performance of the TMCs were then compared to similar evaporation architectures reported in the literature which demonstrated solar desalination (Table 4.1). ZrC NPs functionalized by aminosilanes were coated onto MCE filters and displayed a desalination rate of 1.38 kg m^{-2} h^{-1} under one-sun illumination.[380] However, a very high mass loading of 85 g m^{-2} was needed to reach this rate, which is over 80 times the amount used in the present study. In another example, MXene phase Ti_2C_3 decorated on multi-walled carbon nanotubes (MWCNT) were vacuum loaded onto MCE paper at a mass loading of 2.0 g m^{-2}.[430] This platform achieved a desalination rate of 1.32 kg m^{-2} h^{-1}. The HfC NP on MCE solar evaporator reported here outperformed all the top performing materials reported at the time. The TMCs also retained the lowest mass loading of all, making them in most cases a more economic option.

Table 4.1. Solar desalination rates, mass loadings, and ambient environmental conditions of selected materials under one-sun illumination.

Desalination Device	Desalination Rate (kg m^{-2} h^{-1})	Loading (g m^{-2})	Temperature (°C)	Humidity (%)
This Work (HfC-MCE)	*1.40*	*1.0*	*22*	*50 – 55*
HfN-AAO[189]	1.20	2.5	19	35 – 45
TiN Aerogel[431]	1.34	8.0	22	NR
ZrC-APTES MCE[380]	1.38	85	20	45 – 50
TiNO Airlaid Paper[432]	1.33	NR	NR	NR
Carbonized Bamboo[187]	1.19	N/A*	28	40
Au Melamine Sponge[433]	1.24	NR	NR	NR
Fe_3O_4 Decorated Cellulose[434]	1.22	NR	25	32
MWCNT PPS/FC[403]	1.34	2.4	NR	NR
Ti_2O_3 MCE[435]	1.32	30	20	55
Al AAO[436]	1.00**	NR	24	48

NR = not reported. * Bamboo is the evaporator with no additional material loaded. ** Estimated from figure in Ref (*).

Moving forward, the effect of light intensity was investigated by running the desalination process at 0.5, 1.0, 1.5, and 2.0 sun-equivalent intensity (0.5 – 2.0 kW m^{-2}). Similar to the response of the photothermal heating discussed in Chapter 3, the rate of desalination scaled linearly with illumination intensity (Figure 4.10A). A couple other experiments were then conducted to highlight one of the major shortcomings in the field of solar desalination, which is the lack of consistent environmental conditions reporting. For example, in Table 4.1, many reports to not

disclose the ambient temperature or relative humidity during the desalination experiments. This can have a profound effect on the SVG efficiency, particularly for the top contending materials which are already quite close in efficiency. We therefore ran experiments where one set altered the ambient temperature while maintaining constant relative humidity (Figure 4.10B), and the other altered relative humidity while maintaining constant temperature (Figure 4.10C). To study the thermal effect, the surrounding temperature was varied between 15 – 30 °C with constant humidity (50%). For relative humidity studies, the temperature was held constant (22 °C), and the humidity was varied between 20 – 80%. The evaporation rates increased with increasing ambient temperature, as the bulk water now requires less additional energy input to make the liquid to vapor transition. Rate changes of 0.04, 0.03, and 0.025 for TiC, ZrC, and HfC, respectively, were marked for every 5 °C increase in temperature. This corresponds to a SVG efficiency increase of ~7%. Variations in relative humidity was also found to influence the recorded rates of desalination, decreasing by 0.024 kg m^{-2} h^{-1} for TiC and ZrC, and 0.005 kg m^{-2} h^{-1} for HfC for every 10% decrease in relative humidity. Previous numerical studies have predicted a linear drop in evaporation performance with increasing relative humidity due to the higher moisture content of the air suppressing evaporation.[232] This study emphasized the importance of monitoring such evaporation conditions for reporting and holding them constant between all trials for a fair comparison among systems.

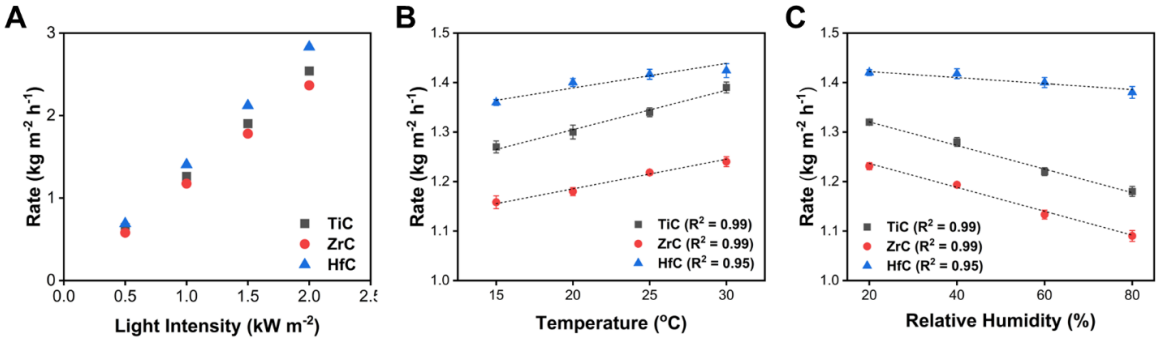

Figure 4.10. (A) Effect of light intensity from 0.5 – 2.0 kW m^{-2}, (B) temperature from 15 – 30 °C, and (C) humidity from 20 – 80% on the desalination rate for TiC, ZrC, and HfC.

The longevity of the TMC interfaces was tested over the course of 10 h each, with the resulting desalination rates remaining unchanged over that period (Figure 4.11A). This highlights the effectiveness of the 1D wicking structure at avoiding salt buildup on the evaporation surface. Salt buildup has been known to destroy the efficiency of certain scaffolds over time by clogging the pores, resulting in no movement of water vapor from the surface.[189,238] To explore the salt tolerance of the TMC NP evaporators further, a series of NaCl solutions ranging from 3.5 – 35% were tested (Figure 4.11B). The HfC interface retained its high desalination rate of 1.40 kg m^{-2} h^{-1} up to the 10% NaCl solution, and only dropped marginally to 1.27 kg m^{-2} h^{-1} at 35% brine. TiC and ZrC saw similar decreases in the evaporation rates of 0.24 and 0.26 kg m^{-2} h^{-1}, respectively.

The ability of the interfaces to tolerate salt buildup is demonstrated by salt dissolution experiments (Figure 4.11C). For example, when NaCl (2 g) was placed onto the TMC interface surfaces under illumination, the crystals quickly became hydrated and within one hour were completely dissolved back into the 3.5% saltwater solution below. Finally, the long-term stability of the carbides was displayed by leaving them in saltwater for 100 days in a sunny windowsill, followed by completely submerging the TMC interfaces in the Atlantic Ocean water for 7 days (Figure 4.12). The stability of the TMC particles on the MCE filter even when submerged likely arises from hydrogen bonding between the TMC surface hydroxyl groups and hydroxyl groups on the MCE membrane. This could help prevent the particles from being washed away when fully submerged.[437]

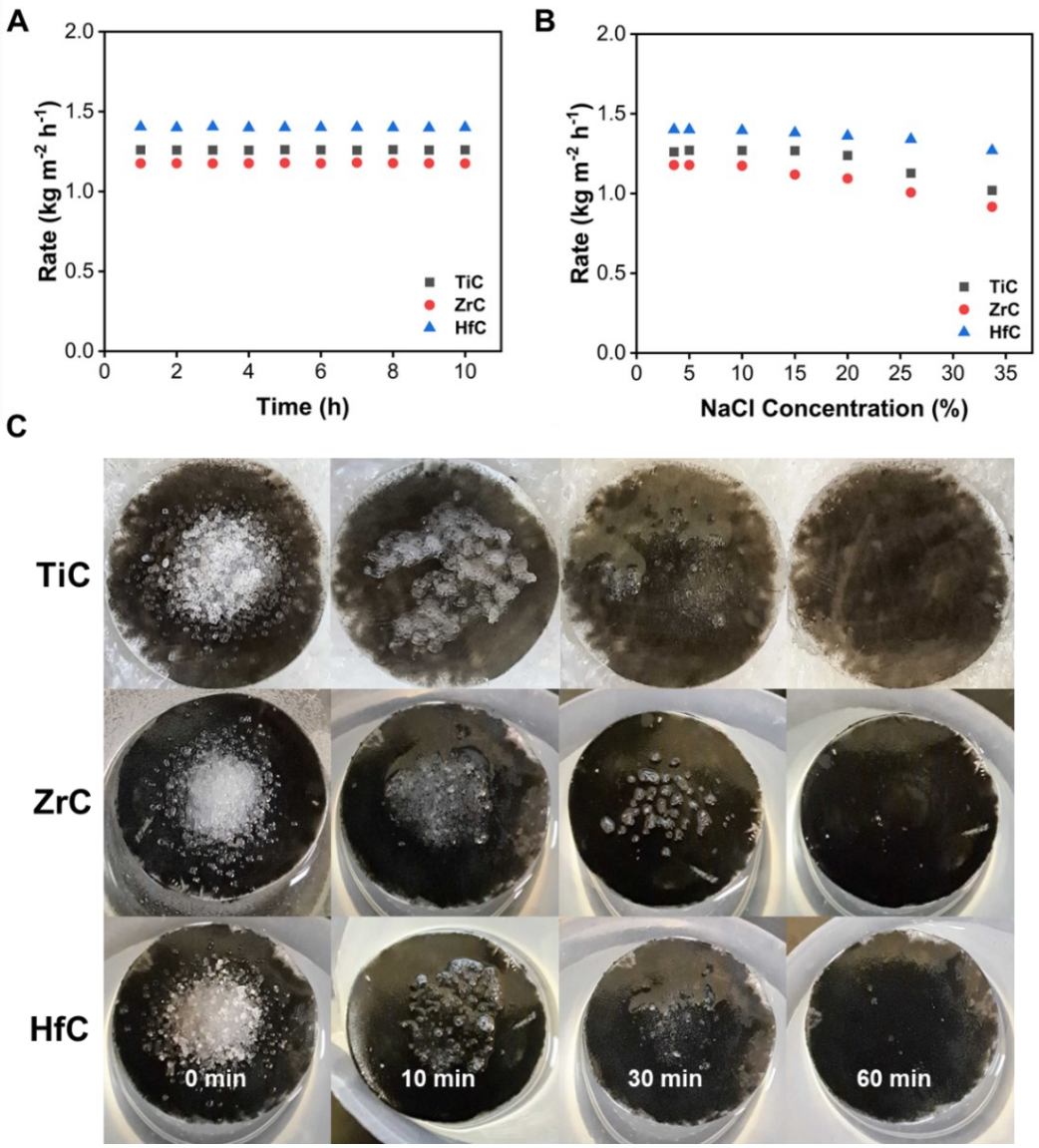

Figure 4.11. (A) Evaporation rates after each hour of illumination over the course of 10 straight hours using TMC evaporation interfaces. (B) Evaporation rates for various NaCl solution concentrations using carbide evaporators under one-sun illumination. (C) Dissolution of salt from the surface of TiC (top), ZrC (middle), and HfC (bottom) over time (0 – 60 min).

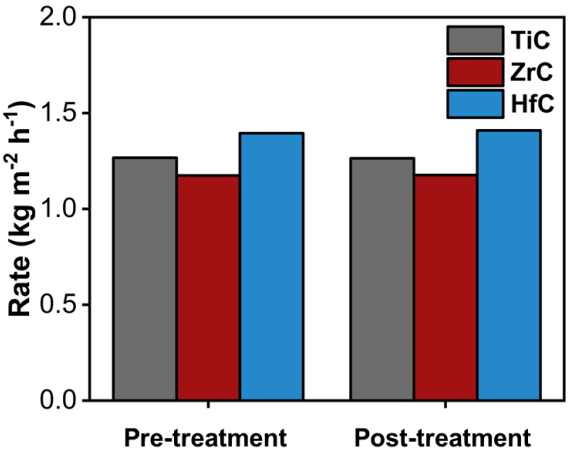

Figure 4.12. Desalination rate of MCE carbide interfaces after being left to float in Atlantic Ocean water for 100 days, followed by being completely submerged for 7 days.

The major limiting factor of the MCE paper based TMC NP solar evaporators is the high energy requirement for the vaporization of water, as discussed in section 1.2.2. The thermodynamic limit of a 2D solar evaporator is ~1.45 kg m^{-2} h^{-1}.[438] Slight variation in the number reported is due to different evaporation devices operating at different surface temperatures. As mentioned, solar concentrators can be used but are quite expensive to install and operate.[439] 3D evaporators take advantage of an increased evaporation surface area within the same footprint, effectively increasing the water output.[440–442] Design of high aspect ratio evaporators becomes increasingly difficult, often requiring elaborate fabrication,[443] making development more costly and difficult. The reduction of the enthalpy of vaporization of water within polymeric structures has become the more promising method of accessing higher desalination rates. This is based off the cluster theory introduced in Chapter 1.[216] Evaporation rates far exceeding the thermodynamic limit have been reported when using certain polymeric supports, such as hydrogels. We therefore investigated the TMCs for desalination when embedded within a simple poly(vinyl) alcohol (PVA) hydrogel matrix.

The synthesis of the hydrogels followed a modified version of a previously reported method in which a PVA and glutaraldehyde mixture was added to an acidic suspension of each TMC.[444] As the hydrogels began to set, they were cast into a 2.5 cm disc to achieve a carbide loading of 1.5 g m^{-2}. Once fully set, the hydrogel interfaces were washed with deionized water and freeze-dried for 48 h. Previous

studies have shown this lyophilization process to increase the surface porosity of the hydrogels, which should increase the release of water vapor from the gel.[444] This porosity is observed by SEM as shown in Figure 4.13. The roughened surface also exposed TMC NP aggregates (Figure 4.14), which can help maintain or even enhance the overall interface light absorption capability.

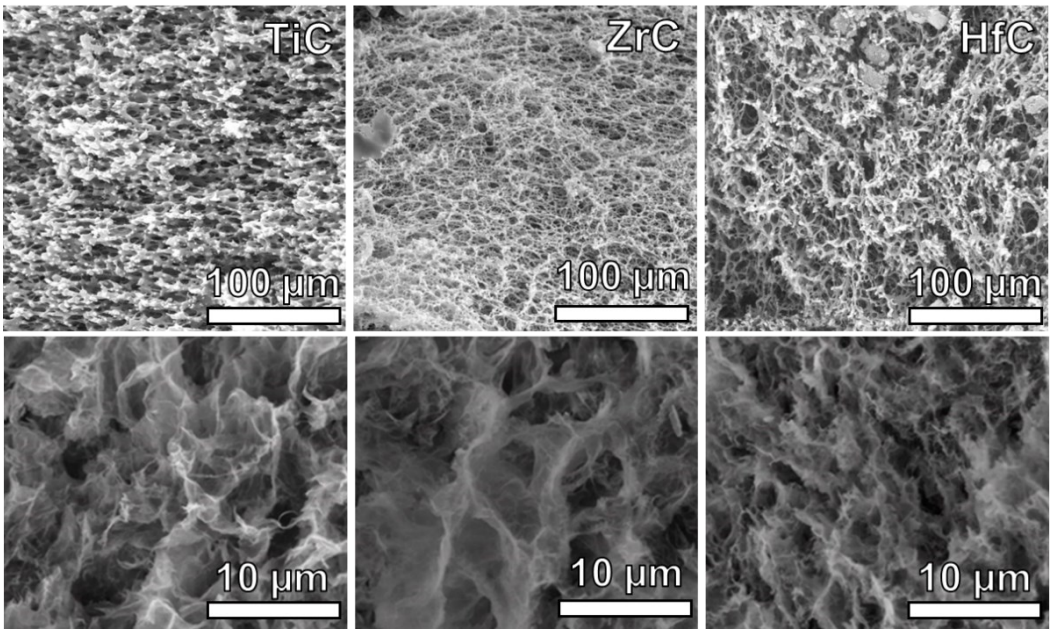

Figure 4.13. SEM image of TMC-PVA hybrids of TiC (left), ZrC (middle), and HfC (right) after freeze-drying for 48 h. Note bright spots in top images is due to slight charging of the membrane surface.

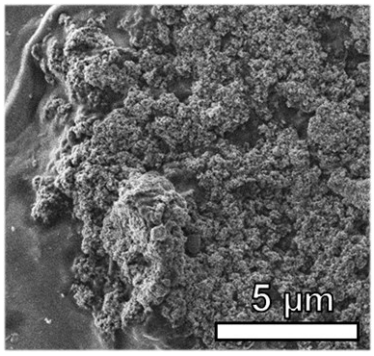

Figure 4.14. Representative image of exposed HfC particle aggregate within the PVA hydrogel network.

To test the TMC hydrogel interfaces in solar desalination, they were placed on the same EVA foam wicking device previously described (Figure 4.4). First, to determine the approximate enthalpy of vaporization of water within the hydrogels, dark evaporation studies were conducted. The ambient evaporation for hydrogel composites in the absence of photothermal heating (i.e. in the dark) provides an accurate value for the decrease in vaporization enthalpy compared to water by itself (Figure 4.15). Using equation 4.1, where $\Delta H_{vap\text{-}PVA}$ is the enthalpy of vaporization for the TMC-PVA hydrogels, ΔH_{vap} is the enthalpy of vaporization for bare water, η_{H2O} is the dark evaporation rate of bare water, and η_{PVA} is the dark evaporation rate of the TMC-PVA hydrogel the enthalpy of vaporization values for the TiC, ZrC, and HfC hydrogels was calculated to be 963 ± 8, 944 ± 10, and 949 ± 9 kJ kg^{-1}, compared to the normal value of 2448 ± 7 kJ kg^{-1}.

With the enthalpy values for each of the TMC hydrogel interfaces, the standard desalination experiment of one-sun illumination with Atlantic Ocean water were ran. HfC reached an impressive desalination rate of 3.69 ± 0.04 kg m^{-2} h^{-1}, while TiC and ZrC exhibited marginally lower rates of 3.31 ± 0.03 and 3.22 ± 0.03 kg m^{-2} h^{-1}, respectively (Figure 4.16A). This desalination rate makes the HfC-PVA hydrogel composite one of the top performing materials out there, maintaining a SVG efficiency of 97%, compared to TiC (89%), and ZrC (87%). The hydrogel evaporators were shown to be equally salt tolerant as the MCE counterparts, with consistent desalination rates recorded over 10 h of evaporation (Figure 4.16B). The osmotic pressure was sufficient in the hydrogel to keep a strong flow of water to the surface for salt removal.[220] Even after ultrasonication for 30 min, followed by submerging in salt water for 24 h, the TMC NP-PVA interfaces retain their desalination efficiency (Figure 4.16C). Once again, NaCl solutions up to 35% were well tolerated by the evaporators. At 35% NaCl, the HfC interface had an evaporation rate of 3.07 ± 0.08 kg m^{-2} h^{-1}, with TiC and ZrC at 2.84 ± 0.10 and 2.79 ± 0.06 kg m^{-2} h^{-1}, respectively. The above results demonstrate the benefit of material optimization prior to incorporation into more intricate designs to maximize desalination performance.

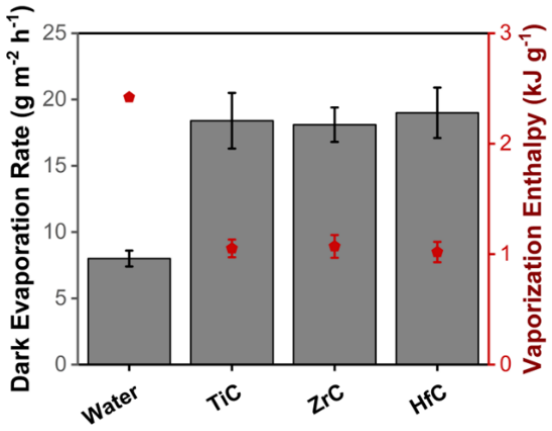

Figure 4.15. Dark evaporation rates and corresponding enthalpy of vaporization rates calculated for bare water and TMCs. Vaporization enthalpy values (red stars, right axis) were calculated using equation 4.1.

$$\Delta H_{vap-PVA} = \Delta H_{vap}\left(\frac{\eta_{H_2O}}{\eta_{PVA}}\right) \tag{4.1}$$

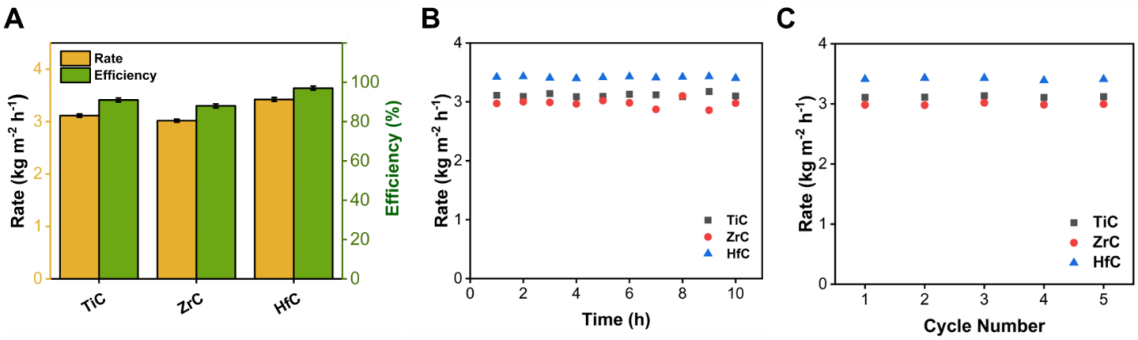

Figure 4.16. SEM image of TMC-PVA hybrids of TiC (left), ZrC (middle), and HfC (right) after freeze-drying for 48 h.

Finally, the high performing HfC-PVA hydrogel evaporation interface was compared to other top performing hydrogel-based desalination devices reported in literature (Table 4.2). Ran *et al.* developed and tested a cylindrical evaporator consisting of a MXene (Ti_3C_2)/polydopamine composite PVA hydrogel shell alongside a polyacrylamide hydrogel core.[444] This structure reached a solar desalination rate of 3.02 kg m^{-2} h^{-1}, and a SVG efficiency of 94%. In a more simplified PVA hydrogel, Yu *et al.* coated reduced graphene oxide across the interface which reached a steam generation rate of 2.53 kg m^{-2} h^{-1}, corresponding to an efficiency of 95%.[445] The same group showed Ti_2O_3 to be an efficient

photothermal desalinator, being able to directly collect freshwater at a rate of 3.00 kg m^{-2} h^{-1}.[446] More recently, Li *et al.* contributed a sponge-like hydrogel evaporator composed of biomass agar and fumed nano-silica aerogel into a PVA backbone.[447] At the time, this displayed the highest evaporation rate of 3.54 kg m^{-2} h^{-1} for saltwater and had a strong tolerance when tested up to 25% NaCl solutions. Finally, a more hierarchical platform by Li *et al.* displayed a mushroom inspired PVA hydrogel structure with an evaporating surface consisting of carbon quantum dots and TiO_2 NPs dispersed evenly throughout.[448] When used for solar desalination, a rate of 3.53 kg m^{-2} h^{-1} and 92% efficiency was recorded. The HfC-PVA support described in this chapter not only presents the thinnest, simplest design of those noted, but is also among the highest desalination rate and SVG efficiency.

Table 4.2. Solar desalination rates, corresponding ambient evaporation rates, and solar vapor efficiencies of selected hydrogel-based materials under one-sun illumination intensity.

Desalination Device	Desalination Rate (kg m^{-2} h^{-1})	Ambient Evaporation (kg m^{-2} h^{-1})	Efficiency (%)
This Work (HfC-PVA)	*3.70*	*0.020*	*97*
Reduced graphene oxide NPs in PVA[445]	2.53	0.025	95
Ti_2O_3 particles in PVA[435]	3.00*	0.015	75
MoS_2 particles in acrylamide/ *N*,*N*-dimethylenebisacrylamide[449]	3.28	NR	93
Nano-silica aerogel/biomass agar PVA[447]	3.54	0.061	93
Carbon quantum dots and TiO_2 particles in mushroom PVA[448]	3.53	0.064	92

NR = not reported. *Air stream used during desalination and water vapor collected to calculate rate.

4.4 Conclusion

Group 4 TMC NPs synthesized by a magnesium reduction reaction in the presence of birch wood char were examined for SVG and desalination. After being loaded onto MCE membranes, they were exposed to one-sun illumination with a mass loading of 1.0 g m^{-2} while floating on Atlantic Ocean water collected from the Halifax Harbour, Canada. The HfC interface was determined to be the top performer, achieving an evaporation rate of 1.40 ± 0.01 kg m^{-2} h^{-1} and a 97% SVG efficiency. Carbides that absorbed a larger percentage of the solar spectrum were found to evaporate water more efficiently, with HfC absorbing 95% of light between 300 – 1500 nm. Post desalination, many salt and common heavy metal ion contaminants were found to be effectively removed. Collected samples were 2 – 3 orders of magnitude below the standards set by the World Health Organization. The TMC MCE interfaces were able to successfully reject salt buildup on the surface over time, and still operate efficiently under hypersaline conditions up to 35% NaCl. Building on the paper-based evaporators, the TMC NPs were then dispersed into a PVA hydrogel matrix. Here, the desalination rate increased to 3.69 ± 0.04 kg m^{-2} h^{-1} for HfC. The hydrogel evaporators maintained the salt tolerance due to their highly porous nature, facilitating continuous removal of salt from the surface. In general, group 4 TMC NPs present an attractive class of solar desalination materials, with potential for facile scaling up of the interfaces.

CHAPTER 5

INFLUENCE OF AMORPHOUS CARBON ON PLASMONIC CARBIDE NANOPARTICLES

The synthesis of amorphous carbon from waste tire rubber, used coffee grounds, ground knotweed stems, and ground lobster shells, TiC NP synthesis, material characterization (XRD, UV Vis), and initial solar-vapor generation and desalination experiments were led and performed by me with assistance from M. Atwood. Birch wood pyrolysis was done by Dr. S. MacQuarrie at Cape Breton University. SEM images were taken by T. Hynes and TEM images were collected by Dr. S. A. Martell at Dalhousie University. ICP-MS measurements were performed by Heather Daurie at the Center for Water Resource Studies.

5.1 Introduction

As the world transitions from fossil fuel-based energy systems and industrial practices to renewable sources, the chemical processes behind them must transition as well.[450–452] Not only is this necessary to decrease the carbon footprint of chemical processes, but as fossil fuel based chemical building blocks become unavailable alternatives will be needed.[453,454] Over the past decade, material circularity has been considered in research groups working towards renewable polymers,[455–457] biomass fuels,[458–460] pharmaceutical discovery and synthesis,[461,462] and fine chemicals production.[463–465] Biomass comes with many potential benefits, namely the widespread availability of different feedstocks, potential for carbon neutrality, and less waste production.[466–468] Most of the time, biomass is produced specifically for

the chemical process of interest, for example corn is grown on massive scales to produce bioethanol.[469,470] More recently though, attention has been turned to implementing waste products into chemical procedures as a means of recycling them.[471,472] Examples of biomass waste include forestry residues,[473,474] agricultural wastes,[475,476] industrial and municipal solid waste,[477] among others.[478–480] The upcycling process of such biomass waste can include extractions, reuse, and carbonization for application as biodegradable packaging materials, catalytic materials, adsorbents, and even battery electrode materials.[481]

The thermal carbonization of biomass waste, known as pyrolysis, is a thermal decomposition process of carbon-containing materials at elevated temperature in the absence of oxygen.[482] This produces a mixture of gas, tar and char fractions, each with various uses ranging from renewable synthetic gases,[483,484] for soil amendment,[485,486] and even in home heating.[487,488] A major benefit of the pyrolysis process is that it can employ waste beyond biomass and can incorporate old rubber and plastic as well.[489] The solid amorphous carbon from these pyrolysis processes has become a major focus recently when derived from waste products.[490,491] Typically, the pyrolytic char is not of sufficient quality to be reused directly and therefore finding appropriate ways to utilize it is of interest.[492,493] Often the char is converted to activated carbon to be use as an adsorbent for treating air and water pollution.[494] In a recent study, plastic-waste derived char was used as an additive in epoxy composites to improve their overall performance.[495] Over the past decade, many research groups have explored synthesizing a variety of carbide materials from pyrolytic chars.[496–498] Transition metal carbide (TMCs) such as tungsten carbide and molybdenum carbide prepared from pyrolytic chars have been used for catalytic reforming of methane to produce syngas (mixture of H_2 and CO).[499,500] In an interesting report, Nourbakhsh *et al.* reported the synthesis of boron carbide (B_4C) using a range of porous carbon precursors. The group found that altering the carbon source use led to differences in the formation of B_4C as well as the resulting properties.[501] This phenomenon has also been shown for the synthesis of molybdenum and tungsten NPs.[502,503]

With these reports in mind, the current study sought to investigate the use of local waste products towards the synthesis of TiC. The goal of this study was to initiate TMC NP synthesis using locally sourced materials, which could be expanded to include waste materials local to wherever the synthesis will take place.

Understanding how the base carbon materials impact the formation of TMCs will allow for informed synthesis planning for developing technologies at the end use site. Titanium was chosen as the candidate as it is desirable to attempt to bring the plasmonic SVG efficiency up as high as possible, potentially to rival the HfC values reported in Chapter 4. Titanium is on average cheaper than both Zr and Hf by more than a factor of 10. There are also more rigorous toxicity studies on both TiO_2 and TiC compared to the other group 4 metals.[504,505] It is believed that the differences in the starting waste product structure could influence the formed TiC NPs. Waste tire rubber, *Reynoutria japonica* (Japanese knotweed) stems, spent coffee grounds, and lobster shells were pyrolyzed to create a carbon-rich char that was used in the magnesium reduction reaction described in Chapters 3 and 4. By varying the carbon source, the effect on the formation of TiC NP was examined. Further, analysis of the chars was completed to explain the observed trends in reactivity of the carbons. Afterwards, the properties of the resulting TiC samples were studied to determine the effect the carbon source had on the final product. This included characterization of the optical properties as well as the SVG and desalination efficiency.

5.2 Methods

5.2.1 Material Synthesis and Characterization

Tires were received from the NAPA Southend auto repair shop in Halifax and the rubber was filed off using a hand rasp file, forming a fine rubber powder for further use. Knotweed was picked as deadfall from Halifax Peninsula and blended into a fine powder. Spent coffee grounds were purchased from North Mountain Fine Coffees, Berwick. Lobster shells were received from Fisherman's Market International Inc., Bedford and ground into a fine powder before use. Polyester filters (PE, 0.50 μm pore size, 25 mm) were purchased from Cole Parmer. All powders were dried at 100 °C for 3 days prior to pyrolyzing.

The pyrolytic chars from local waste materials were prepared according to the process described in section 2.1.2 of this report, and TiC NPs were prepared using the method outlined in section 2.1.3. For this chapter, the characterizations include PXRD, Raman, SEM, TEM, EDS, and BET surface area analysis.

5.2.2 Fabrication of TiC Evaporation Interfaces

TiC-MCE interfaces were prepared by vacuum-loading 0.5 mL of 1.0 mg mL^{-1} solution of carbide onto a 25 mm diameter filter (MCE or polyester, Cole Parmer, pore size 0.45 μm) for a loading of 1.0 g m^2. The plasmonic carbide filter paper was then placed onto a foam disc (EVA, 2.5 cm diameter x 1 cm thick) with 1D fabric wicks (Zorb®) inserted into the foam.

5.3 Results and Discussion

There are many different waste sources and invasive plants in Nova Scotia which quite often find there way into landfills where they will breakdown anaerobically, releasing greenhouse gases such as CH_4 and CO_2.[506] Most waste products come from the agricultural and fishing sectors, two of the largest industries in the province.[507,508] A growing list of invasive plant species have been introduced by gardeners over the years.[509,510] Similarly, Tires are non-biodegradable and can take hundreds of years to decompose. They can leach toxic chemicals into the soil and water if left to decompose in landfills.[511] Incorporating such waste and invasive species, which generally have ongoing supply is an attractive way to upcycle, valorize and utilize such materials. For the current project, a variety of local waste materials were chosen to be converted into plasmonic TiC (Figure 5.1). The effect of the natural product source on the morphology and composition of resulting TiC is explored both through characterization tools and the photothermal properties were examined by applying them in solar-vapor generation (SVG) of saltwater. The waste products chosen were birch wood residue (BW, benchmark explored in Chapters 3 and 4), dried *Reynoutria japonica* (Japanese knotweed) stems (KW), spent coffee grounds (CG), waste tire rubber (TR), and lobster shells (LS). Each product was chosen as they represent a wide range of waste products and structures and are produced or grow in very large supply. They all have different chemical compositions (Figure 5.2), which could influence the reactivity, product morphology and in turn plasmonic properties. The plant waste products are mostly comprised of cellulose, hemicellulose, and lignin, all of which can be effectively pyrolyzed to produce the solid amorphous carbon.[512] Tire rubber mostly consists of

natural and synthetic rubber, carbon black, with other fillers (silica, chalk, sulfur, and antioxidants) making up about 5% of the overall mass.[513] Finally, lobster shells contain chitin, which is a cellulose-like polysaccharide that can be pyrolyzed.[514] The shell, however, also consists of over 30% calcium carbonate which does not pyrolyze and must be removed afterwards.

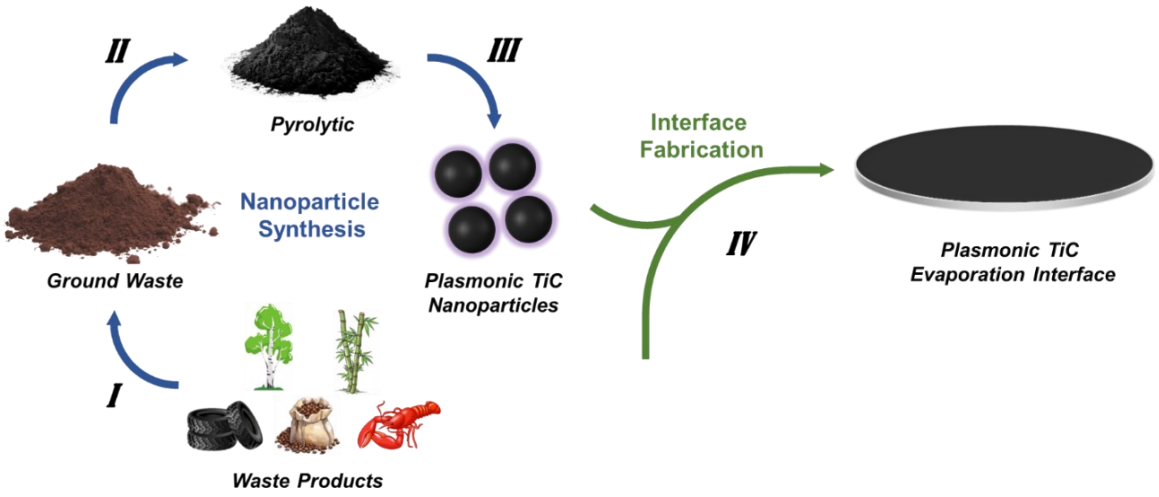

Figure 5.1. Schematic of TiC NP synthesis and evaporation interface fabrication. (I) Waste product cleaning and grinding. (II) Pyrolysis of waste under inert atmosphere. (III) TiC production by magnesiothermic reduction of TiO_2 in the presence of Mg powder and pyrolytic char at 950 °C in Ar. (IV) Vacuum loading TiC NPs onto porous filter paper.

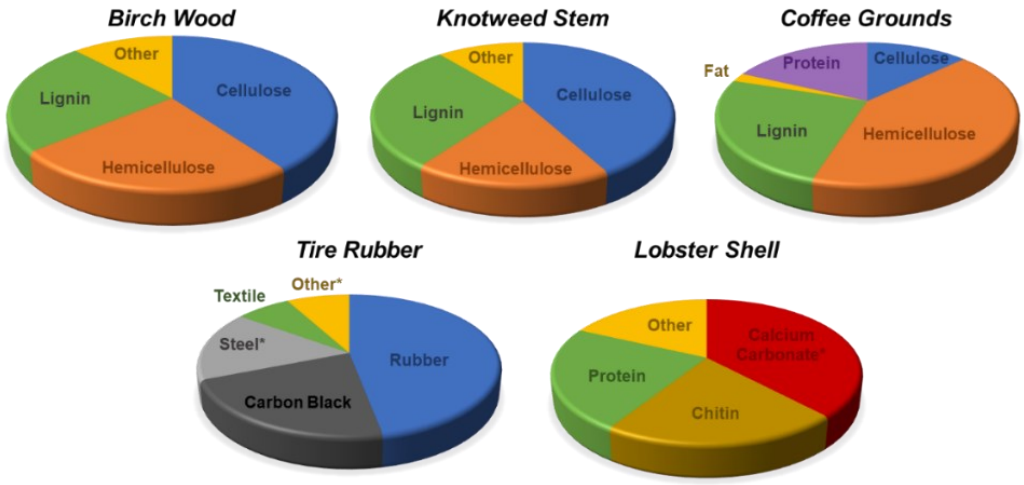

Figure 5.2. Composition of each waste product. *Non-pyrolyzing component.

The raw materials were first thoroughly cleaned and were blended in a spice grinder, or for the case of tire rubber, filed to produce a fine crumb (Appendix A.1, Figure A.3). The powders were then exposed to temperatures between 400 – 600 °C (Table 5.1) for 0.5 – 1 h in a quartz tube furnace. For the lobster shell powder, a variety of pyrolysis reactions were tried to optimize the formation of TiC product, as will be discussed shortly. The pyrolysis produced each of the three products previously mentioned, namely gas, oil, and char, though the gas and oil products were not collected. Once the solid fraction remaining in the tube was cooled below 100 °C, it was poured into deionized water to remove any soluble inorganic solids. After washing with additional water and ethanol to remove any remaining oil fraction, the collected chars were treated with concentrated HNO_3 to further improve the surface area.[384]

The isolated black powders were composed of amorphous carbon (Figure 5.3A) and display broad absorption across the UV-Vis-NIR regions of the electromagnetic spectrum (Figure 5.3B). As introduced in Chapter 3, the acid treatment step is done to roughen the surface and increase the surface area of the char particles (Table 5.2).[515] The Brunauer, Emmett and Teller (BET) specific surface area of each of the chars was determined from N_2 adsorption/desorption isotherms. BW, KW, and CG derived chars had moderate to high surface area of 598, 701, and 327 $m^2\ g^{-1}$ respectively. The TR sample, due to the carbon black NPs present, had the highest surface area of 994 $m^2\ g^{-1}$ and the LS char had the lowest value of 186 $m^2\ g^{-1}$. The average pore size varied between the char samples with LS having the largest pores (22 nm), and the TR sample had the lowest average pore diameter of ~2 nm (Table 5.2).

Table 5.1. Optimized pyrolysis times and temperatures for each of the waste materials.

Waste Material	Pyrolysis Temperature (°C)	Time (h)	Yield (%)
BW	400	0.5	26
KW	400	0.5	31
CG	450	1	26
TR	500	1	24
LS	400 – 900	0.5 – 2	25 - 11

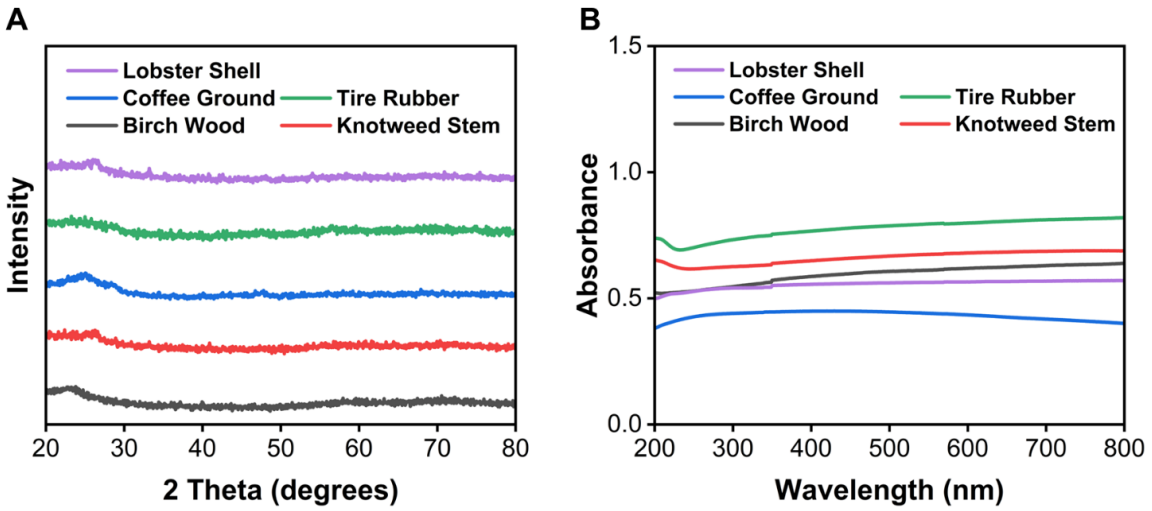

Figure 5.3. (A) PXRD patterns and (B) absorbance spectra of the acid treated pyrolytic char samples.

Table 5.2. BET surface area analysis and pore volume of waste pyrolytic chars after treatment with HNO_3.

Sample	BET Surface Area ($m^2\ g^{-1}$)	Total Pore Volume ($cm^{-3}\ g^{-1}$)	Average Pore Diameter (nm)
BW	598	0.03	12.8
KW	701	0.11	8.2
CG	327	0.04	15.4
TR	994	0.01	2.1
LS	186	0.13	22.0

The surface roughness and porosity of each of the chars was further explored by SEM (Figure 5.4). Based on the images, it was found that BW, KW, CG, and LS pyrolytic carbons form average particle sizes of 18 ± 6 μm, 9 ± 3 μm, 29 ± 11 μm, and 50 ± 15 μm in size, respectively. While BW, KW, and CG form particles with a similar surface morphology, the LS char maintains a much more ordered structure for pyrolysis temperatures ranging from 400 – 900 °C. Interestingly, even though the LS structure looks very porous, the large particle size equates to it being the lowest surface area sample as found by BET. While the surface area increases as the pyrolysis temperature increases, from 72 – 186 $m^2\ g^{-1}$ for 400 – 900 °C, respectively, it remains relatively low. On the other hand, TR (Figure 5.7) forms both large

amorphous carbon particles with an average size of 14 ± 4 μm and very small carbon nanoparticles, from the carbon black in the tire rubber, with sizes <100 nm. EDS analysis was performed of each char to gain compositional information (Table 5.3). BW, KW, CG, and TR had carbon contents of 92, 87, 83, and 93%, respectively, while the lobster char has a carbon content of only 77%. It's possible that inorganic salts and other metals become trapped in the larger particles and are not completely removed during the pyrolysis step or acid treatment for the LS.[516] There are also elevated amounts of oxygen in the samples, most likely from oxidation of the surface carbon during the HNO_3 treatment.

Previous reports have shown that with increasing pyrolysis temperature, the carbon content and surface area of the resulting chars will both increase.[517–520] Unfortunately, higher pyrolysis temperatures and longer reaction times will also result in more of the carbon being lost to the gas and oil fractions. By increasing the temperature of the TR char pyrolysis from 500 to 800 °C, the carbon content reached 95%. Though the overall yield suffered and dropped from 24% down to 6%. This trend remained for each char reaction, and therefore, reactions were done at lower temperatures for shorter periods as the HNO_3 treatment would lead to an increase in the surface area. With the initial characterizations done for each of the five waste product chars, the next step was to investigate their applicability toward to Mg reduction reaction to form TiC. An important reiteration is that TiC was chosen to test the influence of carbon source because the precursor TiO_2 is much more economical than both ZrO_2 and HfO_2. Additionally, there have been preliminary toxicity studies completed on TiC which are promising.[505] If the carbon influence leads to more efficient photothermal properties, TiC could become competitive with the results displayed by the HfC evaporation interfaces in Chapter 4.

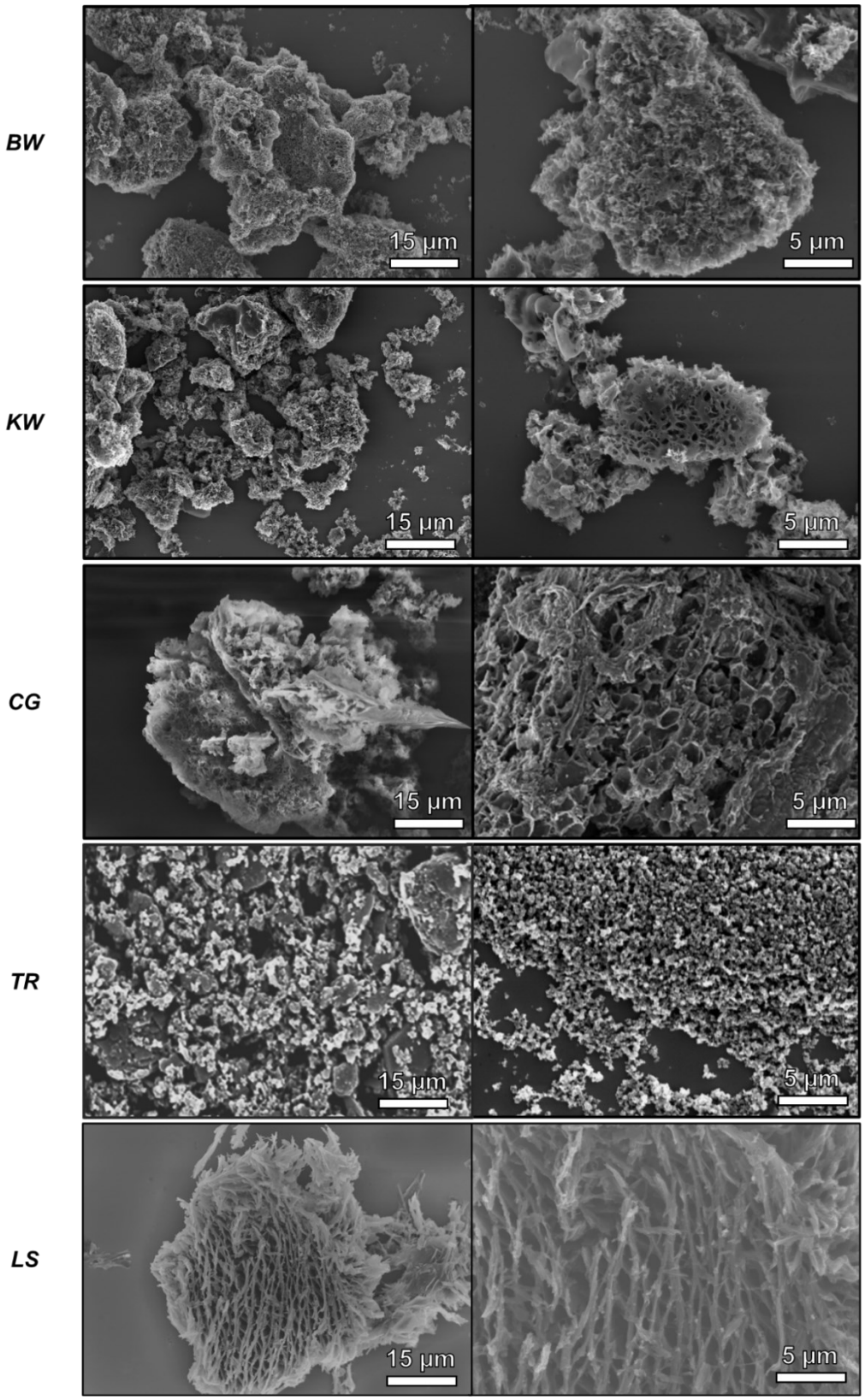

Figure 5.4. SEM images of BW, KW, CG, TR, and LS pyrolysis chars.

Table 5.3. Elemental distribution (atomic %) in char samples obtained from EDS analysis.

Sample	C	O	Na	Mg	Other
BW	91.5	6.2	0.9	0.3	Ca, N, Si (<1% total)
KW	87.4	9.1	1.3	0.4	Ca, N, P, Si, Fe, Mn (<2% total)
CG	82.9	14.9	0.8	0.6	Cl, Fe, N, S, Si (<1% total)
TR	93.2	5.3	0.3	0.4	Al, Ca, Fe, N, S, Si (<1% total)
LS	77.4	16.3	2.5	1.1	Ca, Cl, N, P, S, Si (<3% total)

The Mg reduction reactions were performed similar to the procedures outlined in Chapter 3, which was adapted from a previous report.[280] TiO_2 nanopowder (anatase, 99.9%) with an average particle size of 17 ± 4 nm was reacted with Mg powder and the desired pyrolytic char under flowing Ar gas. In each case that the carbide was formed, holding the temperature at 950 °C for the time specified in Table 5.4 (2 – 4 h) was sufficient for the full conversion to TiC NPs. All the optimized reaction parameters are summarized in Table 5.4. For BW, KW, CG, and TR chars, the resulting TiC PXRD spectra matched to the cubic crystalline TiC pattern (Figure 5.5). Unfortunately, under the same conditions, the LS char did not successfully form TiC NPs. A variety of different reaction conditions were tested, ranging in temperature from 650 – 1100 °C, reaction times between 2 – 12 h, and varying ratios of amorphous carbon and Mg powder. As previously mentioned, alternate pyrolysis reactions were performed as well with varying conditions. In every case, the PXRD spectra was very similar to TiC but corresponded to titanium oxycarbide *(*TiO_xC_y*)*. The deviation can be visualized in the PXRD patterns by looking at the labelled (220) crystal peak in Figure 5.5. It's possible that the higher amount of oxygen in the LS char hinders the formation of pure TiC, or that TiO_xC_y is a reaction intermediate. Alternatively, based on the BET studies, the decreased surface area of the LS char could cause the reaction to become much more kinetically hindered.

Table 5.4. Reaction parameters for the magnesium reduction reaction of TiO_2 with Mg powder and waste-derived amorphous carbon. Reaction consists of 1.0 mmol TiO_2 NPs (80 mg). Green reaction conditions successfully formed TiC NPs, while red conditions were unsuccessful.

Sample	Temperature (°C)	Time (h)	Moles Carbon (mmol)	Moles Mg (mmol)
BW	950	4	2.5	3
KW	950	2	2.5	3
CG	950	4	2.5	3
TR	950	2	2.5	3
LS	650 – 1100	2 – 12	2 – 6	2.5 – 8

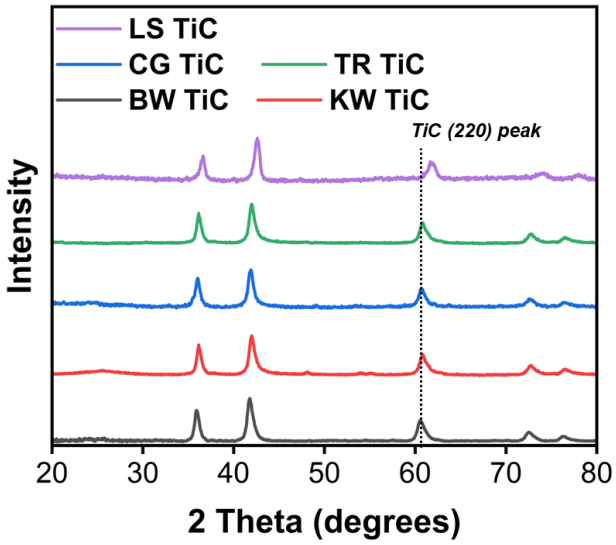

Figure 5.5. PXRD pattens of TiC NPs made from BW, KW, CG, TR, and LS char. Note dotted vertical line shows the location of the TiC (220) peak.

To further understand what could be causing the discrepancy between the LS char and the others, Raman spectroscopy was performed on the char samples (Figure 5.6). The peak in the range of 1420 – 1460 cm^{-1} is the D-band and corresponds to disordered graphite vibrations and appears due to dislocations in

the lattice.[521] When this peak is larger, there is a more disordered, amorphous graphite structure. The other peak, known as the G-band (1580 – 1620 cm^{-1}) arises due to vibrations in the direction of the graphitic sheet, and larger G-band peaks mean there is a more crystalline graphitic structure. Unpublished results from our lab have shown that graphite is not a suitable carbon source for the magnesium reduction reaction. This echoes a study that determined increasing the ratio of graphite to amorphous carbon in the carbothermal reduction and formation of ZrC NPs hinders the overall process.[522] The authors claim that graphite forms around the particles, making it much more difficult for the amorphous carbon to diffuse into the NP. It is also possible that the additional long range graphitic structure of the LS char leads to an intermediate on the reaction path towards TiC NPs unable to react with it. In other words, the graphitic carbon isn't reactive enough under the conditions tested to carry out a step in the TiC NP formation pathway. This could explain why increasing the amount of Mg powder and amorphous carbon does not help the reaction to proceed any further than TiO_xC_y. The reason for the incomplete reactivity currently remans unclear and is under investigation.

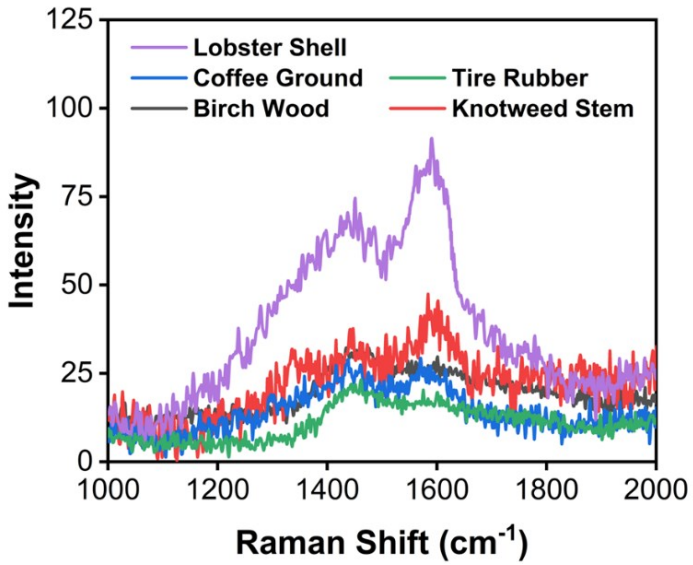

Figure 5.6. Raman spectrum of pyrolytic chars showing the relative amount of amorphous (D-band, 1440 cm^{-1}) and graphitic (G-band, 1600 cm^{-1}) carbon present in each sample.

The four successfully formed carbides were studied further to understand the effect the carbon source on the properties of TiC NPs themselves. TEM images of BW, KW, CG, and TR TiC NPs can be seen in Figure 5.7 and particle size measurements were completed using ImageJ software (Appendix A.1, Figure A.4).[523] BW TiC, as discussed in Chapter 3, forms particles with an average size of 24 ± 8 nm (Figure 5.7, top left). It is likely that all of the TiC samples form an amorphous oxide layer on the surface once they are exposed to air as observed in Chapter 3. The second sample, KW TiC formed slightly larger particles on average diameter of 33 ± 12 nm (Figure 5.7, top right). On the TEM grid, the particles tended to aggregate but it appears as though there is also amorphous carbon present throughout the sample in small amounts. The third TiC sample, made from CG char had the narrowest size distribution with an average particle size of 26 ± 4 nm (Figure 5.7, bottom left). The sample did however have particles that appeared to be sintered together in several locations. Finally, TiC formed from the reaction with TR char yielded much smaller particles on average (Figure 5.7, bottom right). The average size of these particles was 12 ± 5 nm. Ongoing studies seek to probe the mechanism of TiC formation in these reactions, though these results show the potential to have tuneable NP size by simply altering the carbon source used to form the carbide.

The absorbance spectra were measured using 100 μg mL^{-1} solutions of the TiC NPs dispersed in water (Figure 5.8). The BW TiC is similar to that presented in Chapter 3 and 4, with a broad shoulder peak with a maximum at approximately 285 nm. The KW TiC displayed a very broad peak across a large portion of the visible spectrum. This could be in part from the bigger average particle size and the relatively large size dispersion of the sample. As mentioned, each particle size will display a unique LSPR peak, and the overlap of each of these contributions can lead to broadening of the absorbance spectrum. The third sample, the CG TiC, had the lowest absorbance at 800 nm, but as it approached the absorbance maximum at ~290 nm the absorbance increased quickly. The sharpness of this peak could be due to the narrow size dispersion of the CG TiC sample compared to BW, KW, or TR TiCs. Finally, the TiC NPs prepared using TR char had low absorbance across the visible spectrum before rapidly increasing below 200 nm. This sample, having the smallest particle size suggests that the absorbance maximum would be the most blue-shifted and lie out of the spectrometer range.

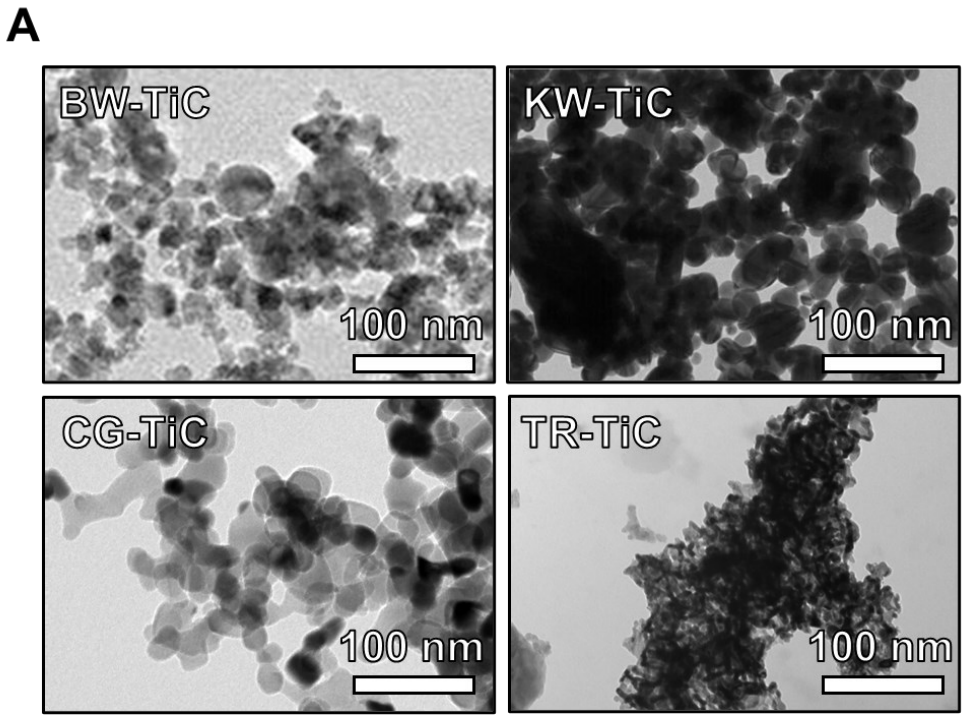

Figure 5.7. TEM images of BW, KW, CG, and TR based TiC NPs. Blue circles show potential regions of amorphous carbon.

The unique particle size and optical characteristics of each of the TiC samples made it of interest to study their ability to photothermally desalinate water. This could make for a very attractive environmentally friendly full circle where locally obtained waste products are upcycled to a specialty material and applied for the renewable generation of freshwater from ocean water. TiC evaporation interfaces were prepared in the same method as Chapter 4, with the exception of the filter paper material. The cost of MCE filter papers increased over the course of the pandemic, and therefore polyester filter papers (Cole Parmer, 25 mm, 0.45 μm pore size) with the same pore size were used in their place. Surprisingly, at just a fraction of the cost of the MCE filters, the BW TiC-polyester interface achieved a higher rate of evaporation (1.34 ± 0.01 kg m^{-2} h^{-1}) compared to the synonymous BW TiC-MCE interface (1.31 ± 0.01 kg m^{-2} h^{-1}).

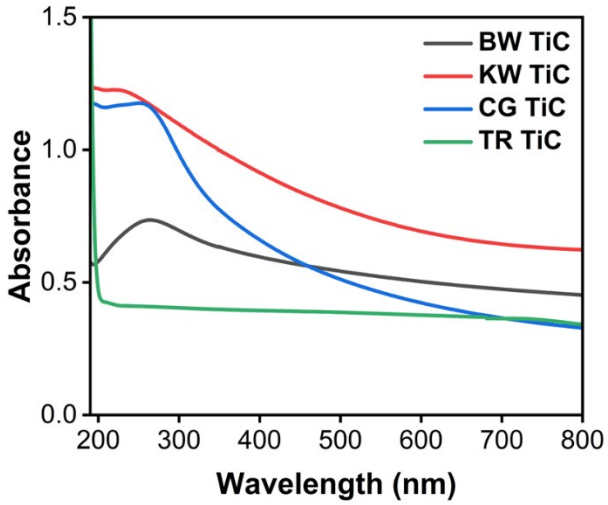

Figure 5.8. Absorbance spectra of 100 μg mL^{-1} dispersions of waste-derived char TiC NPs in water.

As before, by drop-casting the TiC NPs on a solid paper support, the absorbance significantly broadens (Figure 5.9). The confinement of the particles on the surface and within the pores of the polyester filter paper causes coupling of closely neighboring NPs, generating new LSPR absorption.[58] The evaporation interfaces with a carbide loading of 1.0 g m^{-2} all display good broadband absorbance between 300 – 1500 nm (Figure 5.9). The CG and BW derived TiC interfaces had the lowest average absorbance of 86 and 88%, respectively, across the wavelength range studied. KW-based TiC was able to just surpass 90% absorbance, while the TR TiC sample displayed an impressive average absorbance of 96%, the highest of any sample tested. As discussed in Chapter 4, TMC NPs tend to have increased absorption at smaller particle sizes, and as the particle size increases, so does the scattering of light from the particle. It is likely that because the TR TiC sample had the smallest particle sizes on average, there was a stronger contribution towards absorption compared to scattering (Figure 4.3).

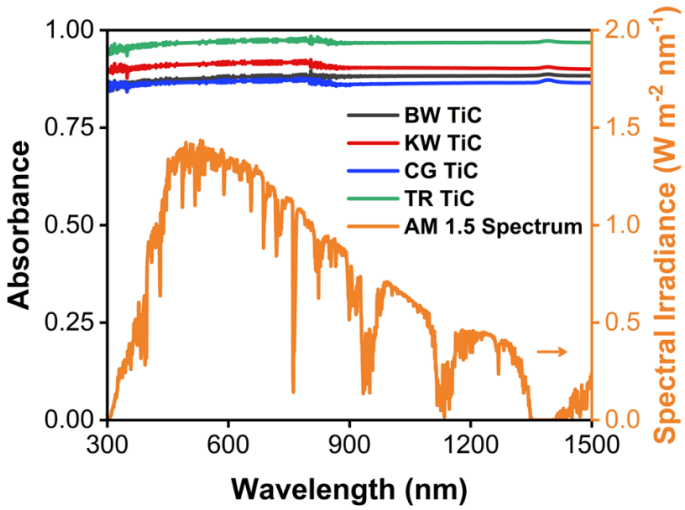

Figure 5.9. Absorbance spectra of BW TiC, KW TiC, CG TiC, and TR TiC NPs loaded onto a polyester filter (left axis), with reference solar intensity spectrum for total global AM 1.5 radiation (orange, right axis). Absorbance was calculated from the diffuse reflectance spectra.

The last step was to verify the translation of broadband absorbance to efficient SVG for the TiC NPs. The carbide interfaces were each tested towards solar driven desalination under one-sun illumination (1 kW m^{-2}) using a solar simulator (Figure 5.10). The process was the same as in Chapter 4, with the interface being mounted onto the insulating, wicking platform shown in Figure 4.7. The birch wood TiC interface reached a water evaporation rate of 1.34 ± 0.01 kg m^{-2} h^{-1}, equating to a solar steam generation efficiency of 89%. The KW TiC interface was slightly higher, with a rate of 1.36 ± 0.02 kg m^{-2} h^{-1}, and an efficiency of 91%. The coffee ground-based evaporator was the lowest of the series, affording freshwater at a rate of 1.29 ± 0.01 kg m^{-2} h^{-1} and efficiency of 81%. Excitingly, the TiC evaporator derived from waste tire rubber evaporated at a rate of 1.40 ± 0.01 kg m^{-2} h^{-1}, corresponding to a SVG efficiency of 95%. This puts the TR TiC polyester evaporation interface on par with the HfC MCE interface reported in Chapter 4. By plotting the obtained SVG efficiency values alongside the corresponding average light absorbance between 300 – 1500 nm, there is a clear trend. As the material absorbs more light, the desalination efficiency increases. Each of the tested pyrolytic chars formed TiC NPs with varying physical and optical properties, leading to the observed water generation efficiencies.

In addition to the desalination rate experiments, the standard set of tests were run on the TR TiC interfaces to explore their purification potential and longevity of use (Figure 11). All tests were performed as outlined in Section 4.3. Purity was evaluated using ICP-MS (Figure 5.11A) on water which was collected using an enclosed quartz vessel. The water before desalination is very similar to those seen in Chapter 4. All salt ions (Na, Mg, K, and Ca) were decreased by a minimum of 3 orders of magnitude and are well below the range of taste and the standards set out by the WHO. Again, heavy metals that are present in the source water, Pb, As, and Cd are decreased to be undetectable by the instrument. The stability of the interface for a standard-length day of desalination was tested (Figure 5.11B). This occurred over the course of 10 h with continuous desalination, and the rate of water evaporation was unchanged over that period. This means that the TR TiC at 1.0 g m^{-2} loading effectively avoided salt buildup over time. This was further highlighted by running the desalination experiment in supersaturated NaCl solutions from 3.5 – 35% (Figure 5.11C). The salt tolerance was once again highly stable, and the rate of desalination only slightly decreased to 1.24 kg m^{-2} h^{-1} at the highest NaCl concentration tested (35%).

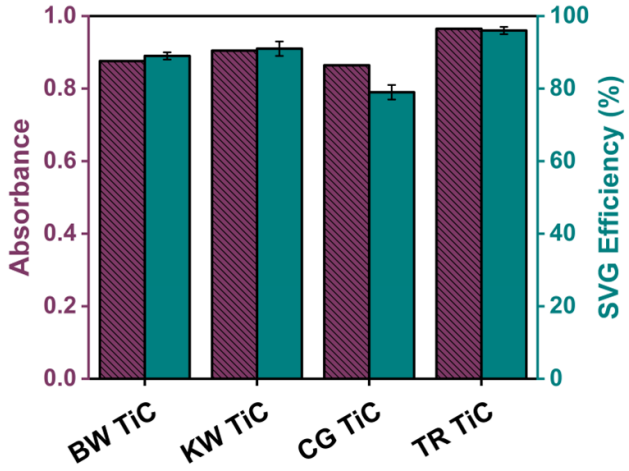

Figure 5.10. Average absorbance of BW, KW, CG, and TR TiC NP interfaces between 300 and 1500 nm (maroon, left), and corresponding desalination efficiencies (teal, right).

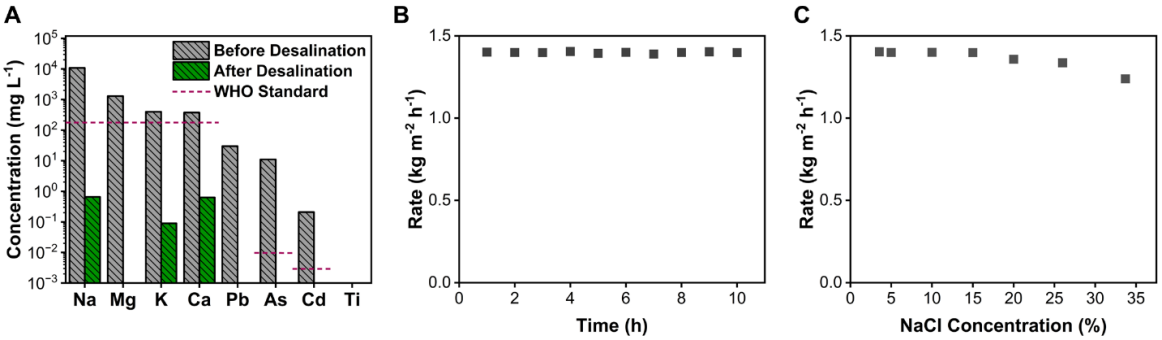

Figure 5.11. (A) ICP-MS metal analysis for water samples before (grey, striped), and after (green striped), desalination. (B) Evaporation rates after each hour of illumination over the course of 10 straight hours using TMC evaporation interfaces. (C) Evaporation rates for various NaCl solution concentrations using carbide evaporators under one-sun illumination.

Through this study, a variety of waste products local to Nova Scotia, Canada were scrutinized for the pyrolysis and subsequent use in the synthesis of TiC NPs. Initial processing and subsequent pyrolysis of the waste products yielded five unique batches of char. While PXRD showed them to be mainly amorphous in nature, Raman studies show that there are varying amounts of graphitic carbon in each sample. Additionally, SEM images shed light on the morphological difference between the chars. The particle size was highly variable, ranging from carbon black particles within the TR sample that were <100 nm in size, to the LS pyrolytic chars with an average size of 50 ± 15 μm in size. Based on the surface porosity and particle size, BET analysis revealed a wide range of surface areas for BW (598 m^2 g^{-1}), KW (701 m^2 g^{-1}), CG (327 m^2 g^{-1}), TR (994 m^2 g^{-1}), and LS (186 m^2 g^{-1}) chars.

5.4 Conclusion

While four of the pyrolytic chars were successfully incorporated into the magnesium reduction reaction of TiO_2 to form TiC NPs, the LS char wasn't able to get past the TiO_xC_y stage. It is hypothesized that this is due to the increased amount of graphitic carbon present in the LS char, and the lower surface area available to react with. Nevertheless, the four TiC samples were studied by TEM, which showed a range of average particle sizes. This is very exciting as it demonstrates the

potential to tune TMC NP size by simply altering the structure of the amorphous carbon starting material. The TiC NPs were formed with an average size of 24 ± 8 nm, 33 ± 12 nm, 26 ± 4 nm, and 12 ± 5 nm for BW, KW, CG, and TR chars, respectively. The optical properties were also influenced by the char source, and variations were explained by the average particle sizes, size distributions, and extent of amorphous carbon present. By vacuum loading the TiC NPs onto polyester filter papers, the correlation between these factors and the broadband sunlight absorbance was studied. TiC NPs made from TR char were capable of absorbing 95% of light between 300 – 1500 nm. Finally, the TiC NP interfaces were tested for their efficacy in solar-driven desalination of Atlantic Ocean water. There was a clear trend of increasing SVG efficiency alongside increasing solar absorbance. BW TiC, KW TiC, CG TiC, and TR TiC reached desalination efficiencies of 89, 91, 81, and 95%, respectively. For the case of the TR TiC, the recorded desalination rate is competitive with the HfC-MCE interface reported in Chapter 4. Additionally, this new evaporator benefits from the lower cost and known toxicity of Ti, while still generating some of the most freshwater from saltwater reported to date. Utilizing TiO_2 as a starting material will allow for much more facile scaling up of the desalination process for real world application.

CHAPTER 6

TANDEM DESALINATION AND ELECTRICITY GENERATION BY A REFRACTORY PLASMONIC FLOATING SOLAR STILL

Part of this chapter has been used to prepare a manuscript available on ChemRxiv (DOI: 10.26434/chemrxiv-2024-dhl01) and submitted for publication. The synthesis of TiC NPs and evaporation interfaces, material characterization (PXRD and absorbance), testing and manufacturing of the floating solar still, and desalination and electricity generation experiments were performed by me. Development of tire rubber char and TiC synthesis was completed by M. Atwood. Initial desalination experiments were carried out with assistance from K. Near. The development of the thermoelectric circuit design and integration into the still was done with assistance from J. Weatherby. SEM images were taken by T. Hynes. ATP assays were completed by J. L. de Larrea and ICP-MS measurements were run by H. Daurie at the Center for Water Resource Studies.

6.1 Introduction

As mentioned throughout Chapters 1 and 4, the freshwater crisis is one of the largest ongoing humanitarian emergencies worldwide.[103,105] This is an ever-growing issue as the demand for clean water generation continues to increase with

population growth and displacement.[524] The floating solar desalination units benefit from the fact that they can be deployed directly on the saltwater source, requiring no additional land use to function.[180,525] Floating solar evaporation platforms generally employ photothermal materials for increased conversion of sunlight to heat used for evaporation. As discussed in Chapter 1, a plethora of different materials and structures have been developed and tested,[526] with the most efficient systems being based off interfacial evaporation as opposed to bottom heating or bulk solution heating (Figure 1.5).[234]

Achieving top efficiencies with floating solar vapor generation (SVG) units requires a strong interplay of material design and support engineering.[190] The photothermal material must absorb as much incoming solar energy as possible, an effective thermal management system must keep that heat where it's needed, and the flow of water throughout the system must avoid salt buildup and contamination of the evaporation surface.[411] The localization of the heat can be achieved by thermally insulating the unit, effectively isolating the evaporation interface from the cold water below.[238] This is known as conductive heat loss and can be almost completely negated by having a strongly insulating material separate the interface from the ocean water.[527] To avoid evaporation interface fouling by salt and contaminant buildup, efficient wicking can be incorporated into the SVG unit, where capillary flow across the surface pulls the solids back to the bulk water.[191,236,237] Studies have shown this to be perhaps the most important aspect for longevity of desalination devices.

Increasing the amount of sunlight absorbed is purely a material consideration, with many photothermally active materials such as carbonaceous materials,[172,186,406] to thermally conductive polymers,[528–530] semiconductors,[174,407,408] and plasmonic nanomaterials[272,431] being studied. The top performers in these categories absorb ≥90% of the solar spectrum and can achieve SVG efficiencies topping 85%.[169,531] The most attractive candidates are plasmonic NPs as the plasmonic conversion of light-to-heat is highly efficient and localized.[421] All of the benefits mentioned throughout this thesis make refractory plasmonic NPs particularly interesting, including their superior photothermal properties, relatively low cost, and stability under stressing conditions.[426,532,533]

Floating solar-driven desalination studies have almost exclusively taken place in controlled lab environments, with larger scale, real world studies remaining

scarce.[401,418,432,441,534] While fundamental studies are crucial, it is important to study how these finding hold up during the scaling up process. This will help to avoid stagnation in the field, proving the potential for floating solar desalination. Of course, this brings new challenges throughout the process, including large scale material preparation, potential for new efficiency losses, and deployment on a much less forgiving saltwater body.[184,535] For these reasons, some of the more elaborate and expensive materials and evaporation scaffolds from lab studies do not scale up economically.[412,442,536–538] There are other concerns as well, such as the vapor collection system, heat loss from conductive currents beneath the SVG unit, and increased humidity within the collection system. Each of these factors can chip away at the overall SVG efficiency of the evaporators. In practice, this has caused drastic decreases for previously reported floating solar stills from ~90% to below 20% in most cases. [539–541]

Regardless, a handful of groups have undertaken the challenge of developing a human scale desalination unit for freshwater generation. Gan *et al.* reported a floating solar still that used carbon coated paper as the photothermal material on top of a polystyrene support.[542] The unit achieved a water generation rate of 0.8 L m^{-2} day^{-1}, corresponding to a solar-to-water efficiency of 7% considering the amount of sunlight energy for the testing period. The likely reason for the low output was a buildup of salt on the evaporation surface, decreasing the efficiency over the course of the testing day. After this report, Chen *et al.* created a desalination unit capable of continuous use by increasing the wicking area to 20% of the overall surface.[372] This, however, led to an increase in thermal loss, and the freshwater production maxed at 2.5 L m^{-2} day^{-1}, or 22% SVG efficiency. Another report from Xie *et al.* used inspiration from the roots of mangrove plants to create a 1D wicking system, decreasing the wicking area to only 2% while maintaining salt rejection.[543] The still was unfortunately plagued by other issues such as tipping over and only produced 1.5 L m^{-2} day^{-1} on the testing day. By incorporating a small vacuum pump onto a floating solar still, Aye *et al.* reached a freshwater yield of 4.3 L m^{-2} day^{-1}.[544] The still was no longer passive in this case and relied on an electrical connection to operate.

This does, however, bring up a final benefit of floating desalination, which is the possibility of generating freshwater and thermoelectric power in tandem. This is accomplished by taking advantage of the temperature gradient between the

illuminated evaporation interface and the colder ocean water below using the Seebeck effect. By placing a Peltier between the hot surface and cold water, a current can flow between the different semiconductor materials within the Peltier, in this case termed thermoelectric generator (TEG). Incorporating these onto the solar still can help generate small electric currents to power on-board devices. While this concept has been explored in lab and in land-based solar stills, there have yet to be experimental results to date for a scaled up floating thermoelectric generating solar still.[545–547]

In this chapter, we develop a plasmonic solar still using the TR TiC NPs evaluated in Chapter 5, which are on par with the best performing photothermal evaporators to date. The still itself was thoroughly engineered to address each of the key concerns mentioned above. The pyrolytic char, made from waste TR becomes a good example of waste material valorization by being incorporated into the TiC NPs for the still. Freshwater generation from the still is stable over a long period of testing, avoiding buildup of salt and other contaminants, and displaying strong thermal isolation. The still structure maintains operational stability with wind, currents, and waves. It also resists bacterial growth over time, and the collected water is free from other contaminants as well. Thermoelectric generation incorporation allows for practical use of small devices within the solar still structure. This project highlights the growing potential for floating solar desalination as an alternative to land stills and tradition methods such as TD and RO desalination.

6.2 Methods

6.2.1 Material Synthesis and Characterization

Polyester filter fabric (10 μm) was purchased from McMaster-Carr. Saltwater was obtained from the Atlantic Ocean (coordinates: 44°38'23.7" N 63°36'48.0" W). Zorb® Fabric was purchased from Wazoodle Fabrics. EVA foam (2.5 cm thick), stainless steel strapping (5 cm x 3mm), PVC transparent umbrella (0.8 m diameter), magnets, and Woods™ camp shower (5 L) were purchased from Canadian Tire. Solar intensity was measured using a TenMars TM-206 digital pyranometer. Wind

speed, humidity, and outdoor ambient temperature were measured using a Kestrel 3000 pocket weather meter. All condition data was compared with data from Environment and Climate Change Canada for Halifax Shearwater (coordinates: 44°38'06.7" N 63°31'32.1" W). During evaporation experiments, temperatures within the still were monitored using either a Perfect Prime IR0005 or a K-type thermocouple. Akozon 40x40 mm semiconductor thermoelectric power generator modules (SP1848-27415) and the buck-boost power converter (Kananana 1.2-24 V step-up, step-down) were purchased from Amazon. The TEG generated voltage and current were measured using a digital multimeter (VSense U1233A).

Waste tire rubber derived pyrolytic char was prepared according to the method described in section 2.1.2 and tire rubber (TR) TiC NPs synthesis followed the procedure in section 2.1.3. For this chapter, characterization include PXRD, SEM, TEM, reflectance, and ICP-MS.

6.2.2 Fabrication of Evaporation Interfaces

The polyester filter TiC evaporation interface was prepared by spray-coating under vacuum a given volume of 0.1 g mL^{-1} solution of TiC NPs onto a 65 cm diameter polyester filter (McMaster-Carr, 10 μm) for a loading of 1.0 g m^{-2}. The interface was then allowed to air dry to increase adsorption of the NPs to the filter. The total evaporation area for use with the solar still is 0.33 m^2. To prepare the large hydrogel interface, a solution of polyvinyl alcohol (PVA, 7.5 wt.%, 52.5 mL) and glutaraldehyde (2.25 mL) were well mixed through sonication and gentle heating to 60 °C in a glass beaker. Separately, a 2.25 mL dispersion of carbide (TiC, ZrC, or HfC, 0.25 mg mL^{-1}) and HCl (3 wt.%, 2.25 mL) were mixed. The PVA and TMC solutions were mixed and sonicated for 15 min. The resultant mixture was poured onto a large glass panel, with a 1 mm spacer added and a second glass panel laid on top. The panels were clamped together and tapped lightly to remove any air bubbles present. Gelation was carried out for 3 h. The hydrogel was washed twice in 80 °C DI water for 60 min to remove any unreacted chemicals. The hydrogel was cut to size (65 cm diameter disc). The total evaporation area for use with the solar still is 0.33 m^2.

6.2.3 Fabrication of Solar Still

EVA foam (2.5 cm thick) was cut into an 80 cm diameter disc, and 3 mm holes were drilled through the foam to cover 2.5% of the total surface area. Absorbent cotton (Zorb®) was rolled into 3 mm wicks and inserted into each hole. An additional ring of EVA foam (2.5 x 2.5 cm, 78.5 cm inner diameter) was cut and adhered to the foam base to elevate a freshwater wick that circled the outer part of the foam support (Figure 6.1). To further avoid splashing of water onto the collection wick, stainless steel strapping (5 cm x 3mm) was inserted upright into the foam around the circumference of the solar still. A 6 mm hole was drilled through the center of the foam support to insert the condensation dome, which was further secured by adding magnetic snaps around the outside of the frame. The net weight of the solar still is 1.5 kg. For thermoelectric generation, the still was modified with Akozon 40x40 mm semiconductor thermoelectric generator modules (SP1848-27415) and a buck-boost converter (Kananana 1.2-24 V step-up/down).

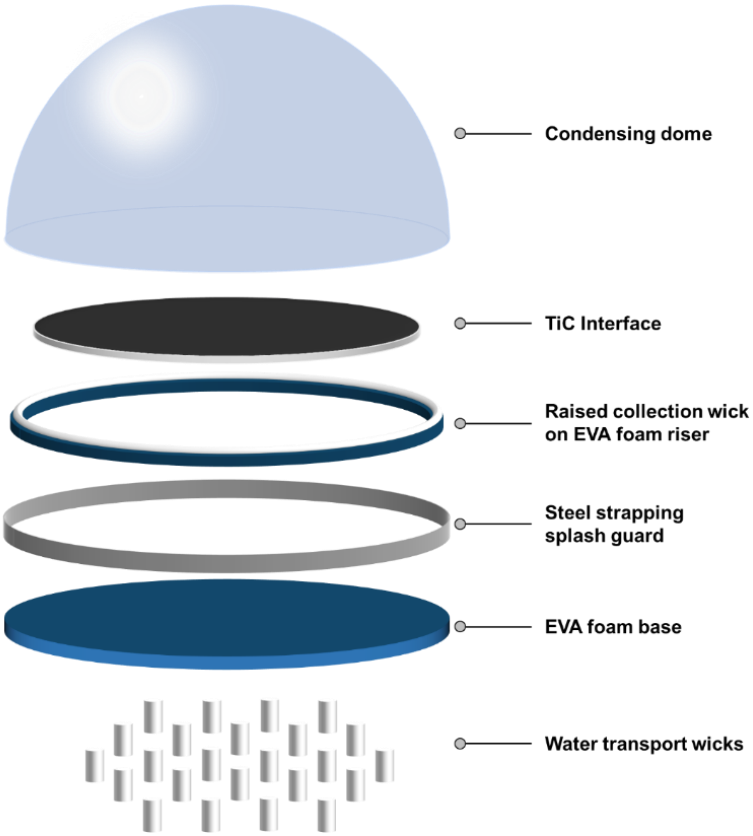

Figure 6.1. Schematic of different components used to build the floating solar still.

6.2.4 Rooftop Desalination Experiments

The solar still equipped with either the polyester or hydrogel TiC NP interface was floated in a 1.5 m diameter pool that was filled with water taken from the Halifax Harbour (latitude: 44° 36' 59.99" N, longitude: -63° 32' 59.99" W). Tested started at 7:00 each testing day and ran until 21:00, with water being continuously collected. Water was collected through the outlet tube into a glass container and the amount collected was measured hourly. Solar intensity, ambient and solar still surface temperature, and wind speed were also recorded hourly. Solar intensity was measured using a TenMars TM-206 digital pyranometer. Wind speed, humidity, and outdoor ambient temperature were measured using a Kestrel 3000 pocket weather meter. All condition data was compared with data from Environment and Climate Change Canada for Halifax Shearwater (coordinates: 44°38'06.7" N 63°31'32.1" W). During evaporation experiments, temperatures within the still were monitored using either a Perfect Prime IR0005 or a K-type thermocouple.

6.2.5 Harbour Desalination Experiments

The solar still equipped with either the polyester or hydrogel TiC NP interface was floated directly in the Halifax Harbour (latitude: 44° 36' 59.99" N, longitude: -63° 32' 59.99" W), starting at 7:00 and ending at 21:00. Water was continuously collected through the outlet tube into a modified Woods™ brand camping shower, designed to be watertight. The amount of water collected was measured at the end of the day. The solar still was tied off to a post to prevent it from drifting. Solar intensity, ambient and solar still surface temperature, and wind speed were also recorded hourly. Solar intensity was measured using a TenMars TM-206 digital pyranometer. Wind speed, humidity, and outdoor ambient temperature were measured using a Kestrel 3000 pocket weather meter. All condition data was compared with data from Environment and Climate Change Canada for Halifax Shearwater (coordinates: 44°38'06.7" N 63°31'32.1" W). During evaporation experiments, temperatures within the still were monitored using either a Perfect Prime IR0005 or a K-type thermocouple. ATP measurements were taken using the LUMINULTRA ATP test kit QuenchGone™ Aqueous (QGA). For analysis, the

samples were collected in sterile 50 mL Falcon tubes and inverted prior to analysis to ensure complete cellular dispersion. Samples were passed over a 0.45 μm syringe filter to retain all biomass in the filter. An elution reagent was poured into the filter to breakdown cells and liberate ATP. The filtrate was collected into a dilution tube and was then mixed with the luminase enzyme. The prepared sample was placed into a luminometer to obtain the relative light units (RLU) of cellular ATP. The RLU is proportional to the amount of biomass present in the sample. For the lab scale desalination only 2 replicates were performed, while for the harbour water and solar still analysis was done 3 times. The thermoelectric generated voltage and current were measured using a digital multimeter (VSense U1233A).

6.2.6 ATP Assay Measurements

ATP measurements were taken using the LUMINULTRA ATP test kit QuenchGone™ Aqueous (QGA). For analysis, the samples were collected in sterile 50 mL Falcon tubes and inverted prior to analysis to ensure complete cellular dispersion. Samples were passed over a 0.45 μm syringe filter to retain all biomass in the filter. An elution reagent was poured into the filter to breakdown cells and liberate ATP. The filtrate was collected into a dilution tube and was then mixed with the luminase enzyme. The prepared sample was placed into a luminometer to obtain the relative light units (RLU) of cellular ATP. The RLU is proportional to the amount of biomass present in the sample. For the lab scale desalination only 2 replicates were performed, while for the harbour water and solar still analysis was done 3 times.

6.2.7 Dye Studies

For dye studies, 3.0 mM stock solutions were made by adding 0.3 mmol of either methylene blue (MB) or rhodamine B (RhB) to 100 mL of deionized H_2O. TiC evaporation interfaces were floated on the stock solutions inside a closed quartz vessel with a sloped cover to recondense water vapor. Water samples were taken from the collection side of the vessel and the absorbance was tested by UV Vis. To monitor the concentration of the stock solution during evaporation, aliquots were

taken at the designated times (5, 10, 15, 30, 60, and 120 minutes). After UV Vis analysis, the sample was added back to the vessel and deionized water was added to maintain the overall water level. Blank experiments were run to determine how much of the dyes were being taken up by the evaporation interface.

6.3 Results and Discussion

As the world transitions from fossil fuel-based energy systems and industrial practices to renewable sources, The TiC NPs using waste tire rubber char was prepared using the method described in Chapter 2 and 5.[497,532] The schematic synthesis of TiC NPs and utilization to create plasmonic evaporation interfaces is shown in Figure 6.2. The tires were first filed to produce a fine rubber crumb before undergoing a fast pyrolysis at 500 °C for 1 h. This was done under an inert atmosphere, forming amorphous carbon which then underwent a concentrated HNO_3 acid treatment to increase the surface roughness. This step was followed by thorough washing with deionized water. The char was composed of a mixture of larger particles with an average size of 14 ± 4 μm, and smaller particles >100 nm corresponding to the carbon black additive in the waste TR. The carbon black NPs, along with other additives of modern tires, make them highly undesirable to end up in landfills. As they breakdown, they can leach these chemicals into the ground, ultimately contaminating nearby water sources. Recycling them in a pyrolysis process can help properly dispose of the fillers (silica, sulfur, etc.)[548] and lock the carbon in an amorphous form instead of as CO_2 or methane. Valorization of the char into TiC NPs is a great way to recycle waste tires moving forward. The TR char was then ground with TiO_2 and Mg powder until a homogenous reaction mixture was obtained. Reaction of the mixture at 950 °C for 2 h under Ar, followed by cooling to ambient temperature and removal of the MgO side product by sonication in 6 M HCl afforded the TiC NPs. As discussed in Chapter 5, this yielded NPs with an average particle diameter of 12 ± 5 nm. The absorbance spectrum of the NPs in water is similar to that recorded in Chapter 5, with low absorption across the visible region of the spectrum before increasing rapidly as the wavelength goes below 200 nm (Figure 6.3A).

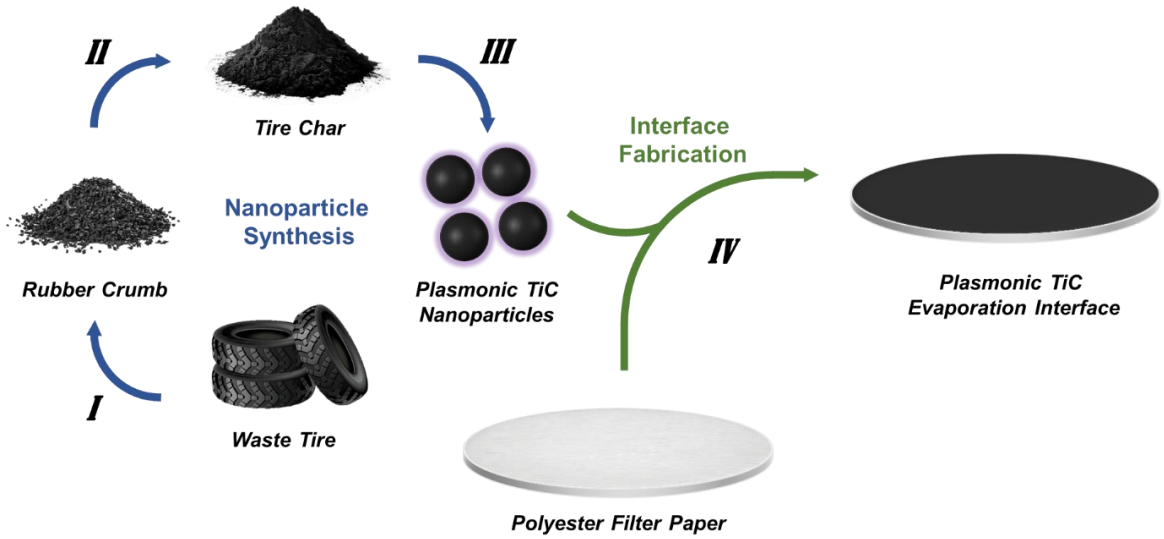

Figure 6.2. Schematic of TiC NP synthesis and evaporation interface fabrication. Steps shown: (I) Tire shredding. (II) Pyrolysis of rubber crumb at 500 °C under inert atmosphere. (III) TiC synthesis by magnesiothermic reduction of TiO_2 in the presence of TR char and Mg Powder at 900 °C in Ar atmosphere. (IV) Vacuum loading of TR-TiC NPs onto porous filter fabric.

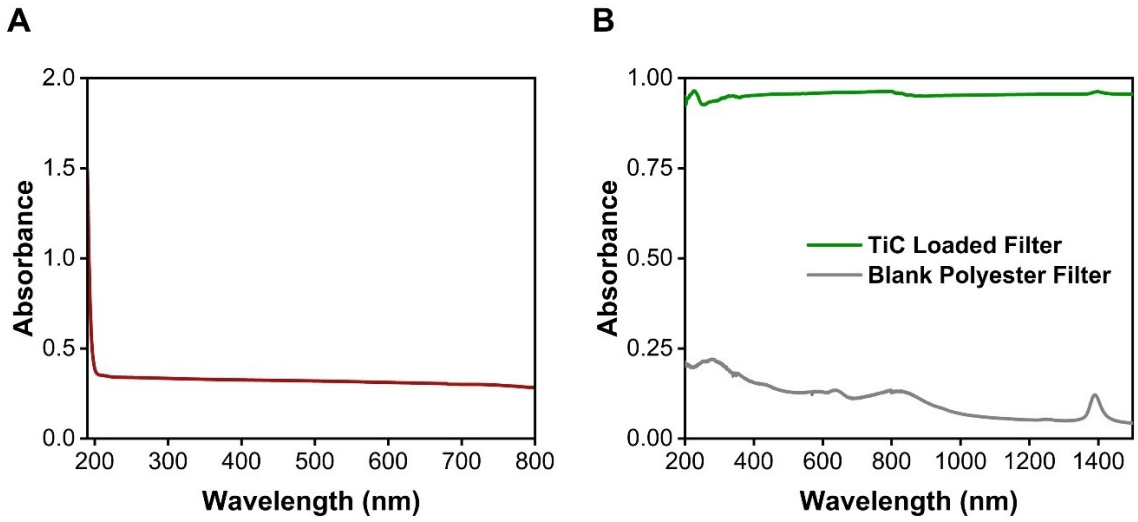

Figure 6.3. (A) UV Vis spectrum of TR-TiC NPs. (B) Absorbance spectra of plain polyester filter fabric (grey) and TR-TiC NPs vacuum loaded onto polyester filter (green).

After preparation, TR-TiC NPs were vacuum loaded onto a large polyester filter using a custom vacuum box constructed in house (Figure 6.4A). Comparison of the

polyester filter before and after loading by SEM (Figure 6.4B). Clearly, many of the spaces between the polyester fibres have been occupied by the TiC particles once loaded on but there remains space for water vapor to efficiently escape the interface. Polyester was chosen based on the enhanced evaporation as shown in Chapter 5, and because it is a low-cost, readily available material with a variety of sizes and porosities. After loading the TiC NPs onto the filter, the absorbance of the plasmonic interface greatly increased across the entire probed spectrum, from 300 – 1500 nm (Figure 6.3B). As previously noted, this increased absorption is due to the coupling of particles within the polyester interface which generate secondary LSPR absorbances at longer wavelengths.[532]

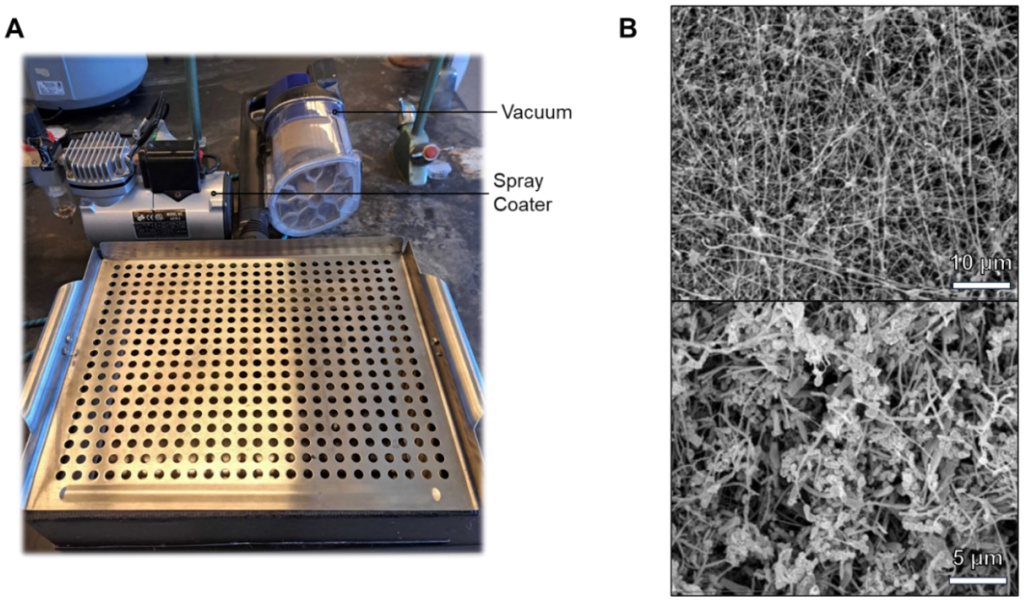

Figure 6.4. (A) Vacuum box built in house to facilitate the large-scale loading of TR-TiC NPs onto the polyester filter. (B) Corresponding SEM images of polyester filter paper before (top) and after (bottom) vacuum loading TiC NPs onto surface.

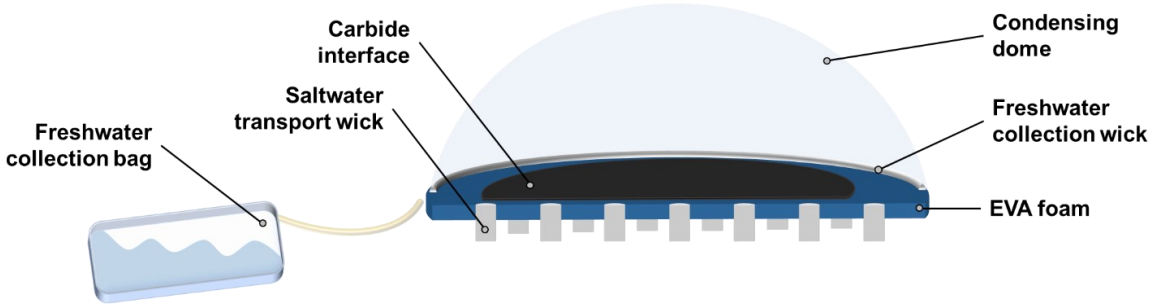

Figure 6.5. Schematic of TiC floating solar still.

The prepared evaporation interfaces were then placed inside the solar still (Figure 6.5). The architecture of the solar still consists of cotton wicks (Zorb®) inserted through a large disc of ethylene-vinyl acetate (EVA) foam. The job of the wicks is to transport water from the bulk water below to the surface of the still to evaporate, with the secondary task of bringing any salt that may buildup back down to the water below. EVA foam provides a good insulation value while being highly durable and shock resistant. The flexibility of EVA also means that it will tolerate movement of water beneath it, and effectively glide over waves. To recondense water, the entire evaporation surface of the still was covered with a polyvinyl chloride (PVC) plastic dome. PVC was chosen for the still as it transmitted more light than other polymers that were tested both when wet and dry (Figure 6.6 and 6.7). This led to faster rates of water evaporation when tested compared to the other polymers as well. To maintain the structural integrity of the condensation dome, a stainless-steel umbrella frame was used. To verify that there wasn't any significant shading from the steel frame, the light intensity was tested at various locations inside of the dome (Figure 6.8), with no substantial difference noted. After recondensing the vapor, the water droplets will fall down the side of the condensing dome and be picked up by another wick that circles the outer perimeter of the still. This will eventually reach an outlet tube where the water droplets will exit the enclosed space and follow an exit tube to collect in a collection bag. As shown in Figure 6.1, the wick is raised and shielded by steel strapping to avoid contamination from saltwater splashing.

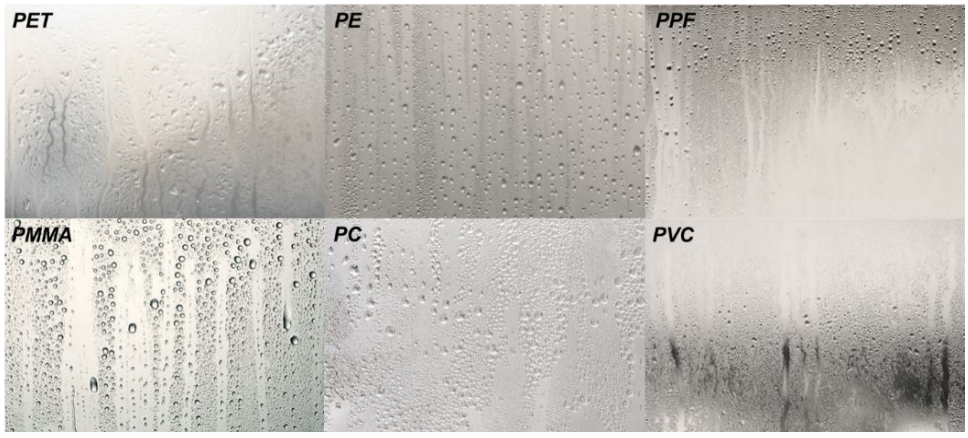

Figure 6.6. Comparison of water droplet formation and sliding off. Plastic swatches were placed in front of a cool mist humidifier at a 45° angle and water was collected for 30 minutes and weighed to determine water removal effectiveness.

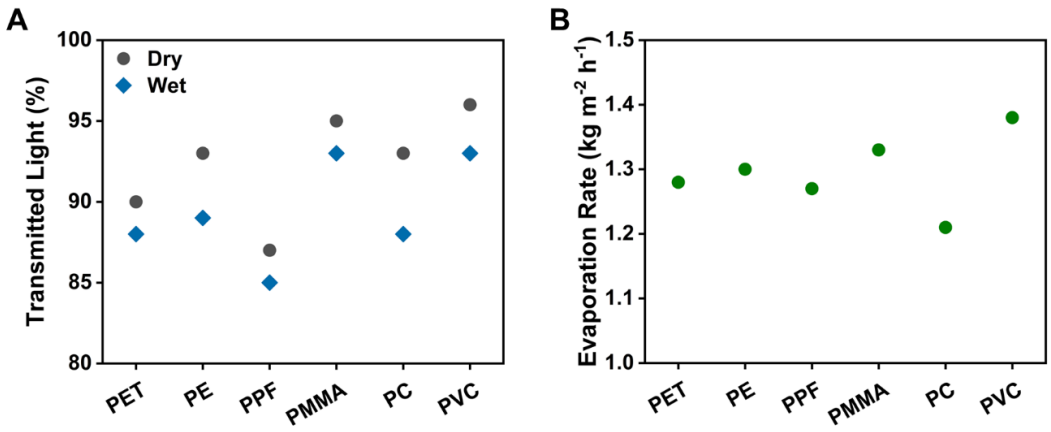

Figure 6.7. (A) Light transmitted through dry and wet samples of various plastics. Light intensity from a solar simulator was measured with and without the plastic samples in the light path. (B) Evaporation rates through various plastic swatches. Evaporation rates were measured using a lab scale TiC interface with plastic swatches in the way of the simulated sunlight. The small evaporator was placed in a beaker of water on a mass balance, and the weight reduction was measured over 30 minutes.

Location	Transmitted Light (%)
1	94
2	94
3	93
4	96

Figure 6.8. Measured light transmittance through the evaporation dome at various locations. The amount of transmitted light was calculated in the same way as discussed for Figure S6.7A.

The effectiveness of the constructed plasmonic solar still was initially tested on a rooftop inside of a pool containing water collected from the Halifax Harbour (latitude: 44° 36' 59.99" N, longitude: -63° 32' 59.99" W), as shown in Figure 6.9A. The evaporated water was collected into a glass container to the side of the pool and the amount collected was measured throughout the testing period. A total of five days of rooftop testing were completed, with the weather ranging from mostly sunny to mostly cloudy. The solar radiation was tracked hourly over the course of each day and is summarized in Figure 6.10. For comparison, the solar still was tested without TR-TiC NPs loaded onto the evaporation interface, which afforded a water production rate of 0.35 L m^{-2} day^{-1}. Using Equation 2.8, the corresponding SVG for the blank solar still was 4%. Using TR char as the photothermal material on the interface led to a water production rate of 1.98 L m^{-2} day (23% SVG efficiency). When the TiC NP polyester evaporation interface was set onto the solar still, the water generation rate was higher, affording 2.03, up to 3.67 L m^{-2} day^{-1} when used on a cloudy (3.67 kW m^{-2}), and mostly sunny day (6.56 kW m^{-2}), respectively. An example water production day, with corresponding water generation rates and efficiencies are found in Figure 6.11. The maximum solar freshwater production efficiency was 40%, and efficiency was found to be similar on cloudy and sunny days. Noteworthy is that the testing location (Halifax, Canada) is higher , with max sunlight intensity in mid summer reaching only an equivalent of ~0.85 suns, or 85% compared to AM1.5. Testing conditions, including ambient temperature, wind speed, and evaporation interface temperatures are summarized in Table 6.1.

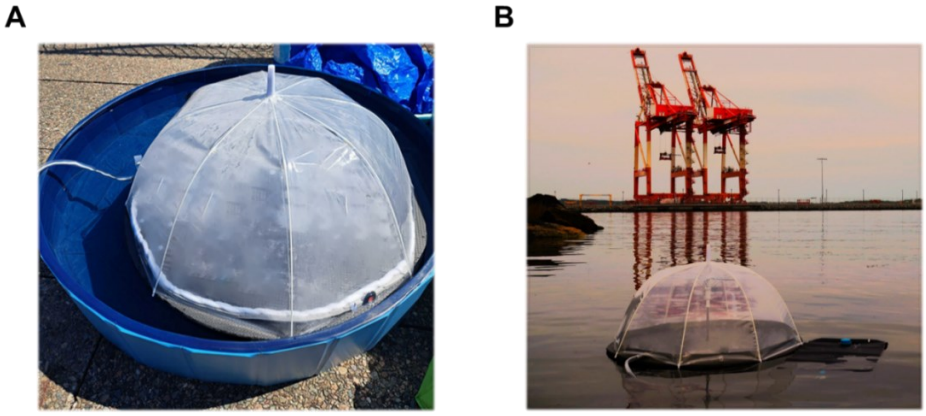

Figure 6.9. (A) Solar still inside rooftop testing pool containing water from the Atlantic Ocean. (B) Location of harbour desalination experiments

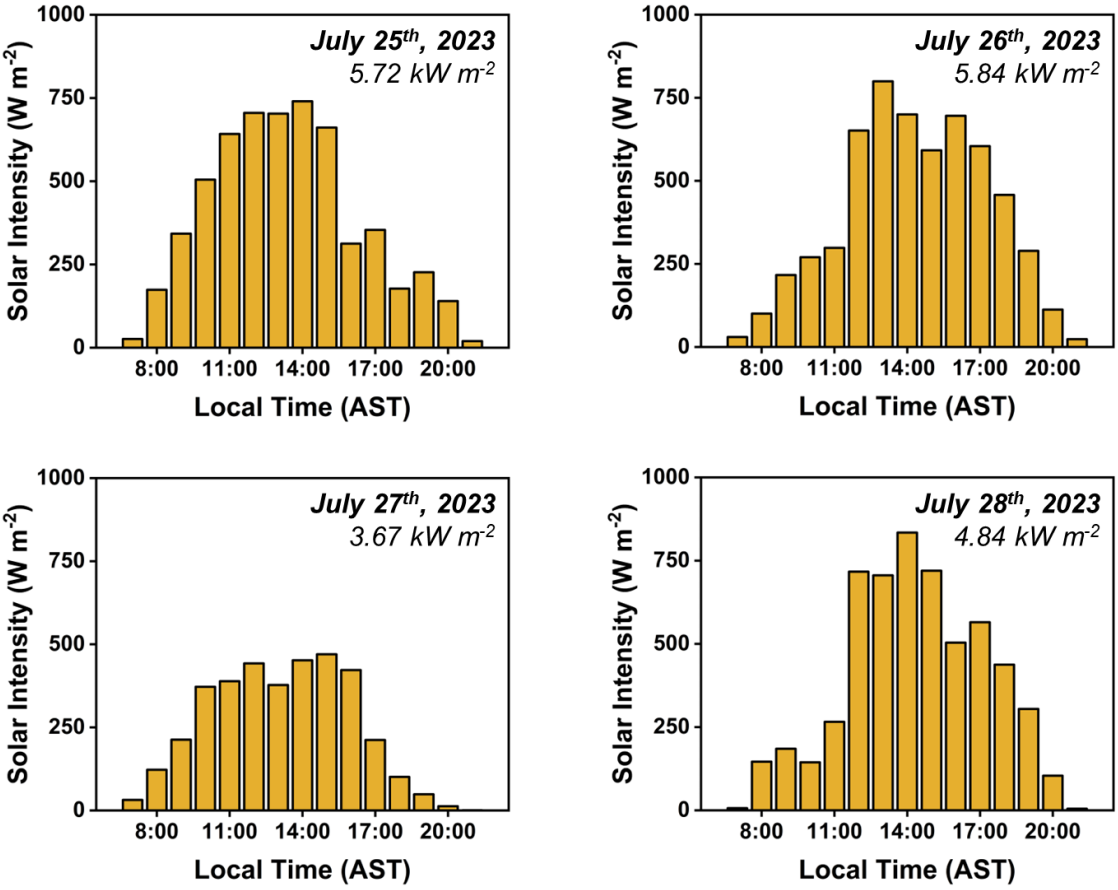

Figure 6.10. Hourly solar insolation values with daily total solar insolation and date inset for rooftop desalination experiments in a pool containing ocean water.

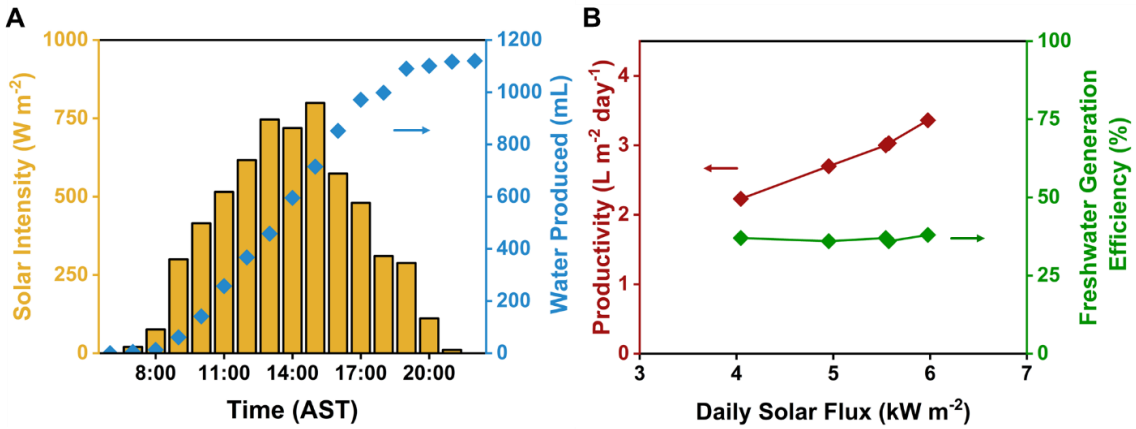

Figure 6.11. (A) Sample solar radiation and freshwater production chart for rooftop pool testing on a sunny day with afternoon intermittent cloud. (B) Freshwater generation rates (red, left) and efficiencies (green, right) for rooftop experiments.

Table 6.1. Daily average temperatures, wind speeds, and solar still surface temperature during rooftop desalination testing. Cloudy days produce less water than sunny days, but the overall process efficiency remains very similar.

Date*	Rate** (L m^{-2} day^{-1})	Ambient Temperature (°C)	Wind Speed (km h^{-1})	Still Surface Temperature (°C)
July 21st (Blank)	0.35 (4%)	23	17	31
July 24th (Char)	1.98 (23%)	22	11	34
July 25th (TiC)	3.29 (38%)	24	18	38
July 26th (TiC)	3.45 (39%)	25	15	39
July 27th (TiC)	2.03 (37%)	21	8	36
July 28th (TiC)	2.98 (40%)	25	29	36
July 29th (TiC)	3.67 (37%)	27	25	39

*Type of interface used is shown in brackets. ″Blank″ is polyester filter with nothing loaded, ″Char″ is using the tire derived char. **Water generation rate shown first followed by solar desalination efficiency in brackets.

Building on the promising results from the rooftop desalination testing, the solar still was then deployed directly onto the Atlantic Ocean (Halifax, Canada) for another five days of testing (Figure 6.9B). To provide a challenging environment for effective desalination, the location was chosen to be directly beside a large seaport. This route is heavily traversed by freight and cruise ships to chop up the water, as well as large tidal currents and moderate wave activity. Additionally, there has historically been concerns over elevated levels of toxic heavy metals such as Pb, Cd, and As. Over the testing period, there was again a range of weather conditions, with sunny to cloudy days encountered (Figure 6.12A and Table 6.2). On the harbour, the max water generation rate was found to be 3.36 L m^{-2} day^{-1}, and the

still was able to produce 2.23 L m^{-2} day^{-1} on a fully cloudy day. The corresponding SVG efficiencies ranged from 36 – 38% (Figure 6.12B). This put them just slightly below the efficiencies obtained for the rooftop desalination experiments. The discrepancy is likely due to the increased movement of water underneath the solar still, leading to an increase in heat conduction from the surface to the cold ocean water.

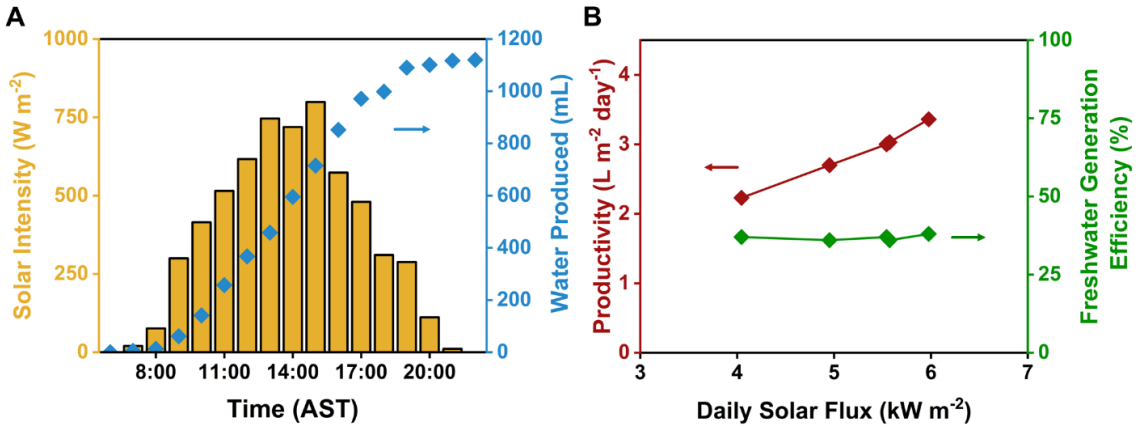

Figure 6.12. (A) Sample solar radiation and freshwater production chart for harbour testing on a sunny with afternoon intermittent cloud. (B) Freshwater generation rates (red, left) and efficiencies (green, right) for the harbour experiments.

Table 6.2. Daily solar insolation, average temperatures, wind speeds, and solar still surface temperatures.

Date	Rate* ($L\ m^{-2}\ day^{-1}$)	Solar Insolation ($W\ m^{-2}\ day^{-1}$)	Ambient Temperature (°C)	Wind Speed ($km\ h^{-1}$)	Still Surface Temperature (°C)
Aug 28th	3.36 (38%)	5.98	27	9	39
Aug 29h	2.23 (37%)	4.05	22	12	36
Aug 30th	3.00 (37%)	5.54	23	19	37
Aug 31st	2.70 (36%)	4.95	21	11	35
Sept 1st	3.03 (36%)	5.57	23	21	36

*Water generation rate shown first followed by solar desalination efficiency in brackets.

Once the five full days of testing on the rooftop, followed by another five days on the harbour, the solar still was deployed again to collect a purified water sample. The microbial content of this sample was then tested using cellular adenosine triphosphate (cATP) assay. ATP is a molecule that carries energy within cells and is essential for various cellular processes, making it a key indicator of cellular metabolic activity and viability.[549] ATP assays are commonly used to assess cell viability and proliferation because the amount of ATP present correlates with the number of living cells. The total content of ATP is assessed in this method by adding the firefly lighting enzyme, luciferase, to the sample.[549] This will react with any ATP present in solution, which can then be detected and quantified by the amount of light produced using a luminometer. The amount of light produced is directly proportional to the amount of ATP in the sample. Since ATP degrades quite quickly in the environment, the cATP assay gives a snapshot into the concentration of living organisms in each sample. It is believed that the localized photothermal heat generation by the TiC NPs has the potential to destroy microorganisms and avoid fouling of the evaporation interface and water transport system within the still. The cATP levels of water collected from the still were compared to water taken directly from the Halifax Harbour (Figure 6.13). A third sample was tested which was obtained using the lab-scale desalination setup and enclosed quartz chamber discussed in Chapter 4. All glassware was disinfected with bleach prior to use. The water collected in lab and from the solar still were both

significantly decreased to 0.25 ± 0.02 and 0.48 ± 0.17 pg cATP mL^{-1}, respectively, compared to the harbour water which had a level of 123 ± 40 pg cATP mL^{-1}. Both desalinated samples were below the guidelines set by Health Canada, set at 1.0 pg cATP mL^{-1}. The levels from each of the desalinated samples was approaching the standard value for high purity water of 0.1 pg cATP mL^{-1}.[549] There was a small difference in the ATP concentrations of the two collected freshwater samples, which is likely due to the rigorous disinfection done to all glassware for the lab-scale sample. This, compared to the solar still being used for of testing outdoors, shows the effectiveness of the photothermally generated heat by the TiC NPs to resist bacteria and mold growth.

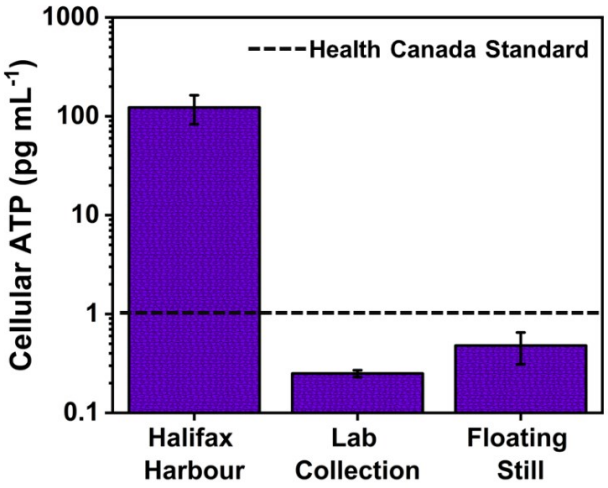

Figure 6.13. ATP test results on logarithmic scale.

To follow up on the cATP results, several lab-scale dye separation and degradation experiments were conducted using methylene blue (MB) and rhodamine B (RhB) under one-sun illumination (1 kW m^{-2}). The priority of these tests was to verify that organic pollutants, which are more volatile than inorganic compounds and heavy metals, do not get escorted through the solar evaporation process and into the freshwater. Solutions of MB and RhB were prepared, and the absorbance spectra of the stock solutions was compared to the collected water after SVG (Figure 6.14A). Visually, the collected samples were completely clear, and the dye absorbance in the collected water was negligible, indicating no contamination from either dye. To investigate whether the photothermal heat generation, or

potentially even hot electron injection (section 1.1) could help to destroy certain organic pollutants, the absorbance of the stock solution was followed. As the dye solutions were transported to the surface for evaporation, the TiC NPs could facilitate the destruction of the dye molecules, which could then be transported back to the bulk solution below. Over time this could decrease the concentration of the stock solution. As shown in Figure 6.14B, the concentration of MB dropped by over 60%, and the RhB concentration dropped 32% over 2 hours of evaporation. This drop in concentration is visualized easily in Figure 6.14C, where the blank evaporation interface (shown with black stripes) only very slightly decreased the dye concentration. This is presumably just from adsorption of the dye into the filter paper. Looking once again at the collected water from the solar still, ICP MS measurements show that all tested metal ions are decreased by 3 – 5 orders of magnitude, putting them well below the WHO guidelines, in line with results from Chapter 4 (Figure 6.15A).

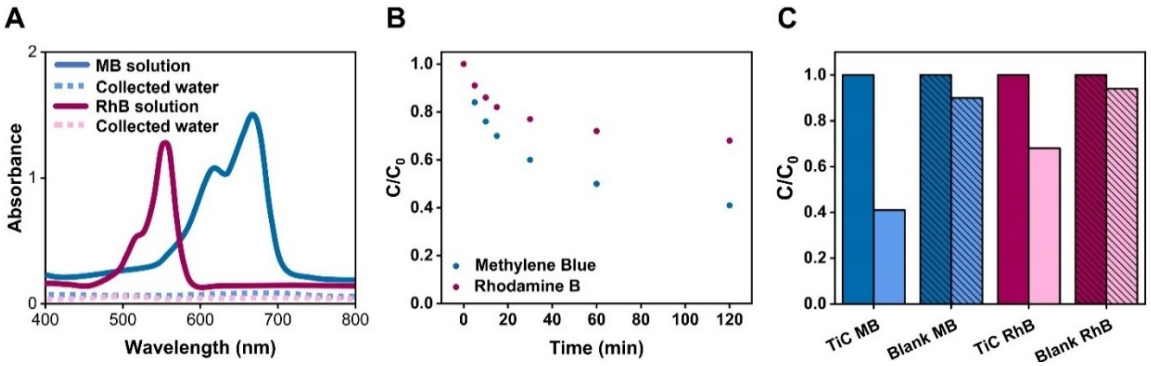

Figure 6.14. (A) MB and RhB solutions before (solid lines) and after (dotted lines) solar evaporation. (B) Monitoring of MB and RhB concentrations over the course of evaporation experiments in lab. (C) Comparison of TiC interfaces (solid colors) and blank polyester filter paper evaporation interface (striped colors) before (darker colors) and after (lighter colors) 120 minutes of evaporation.

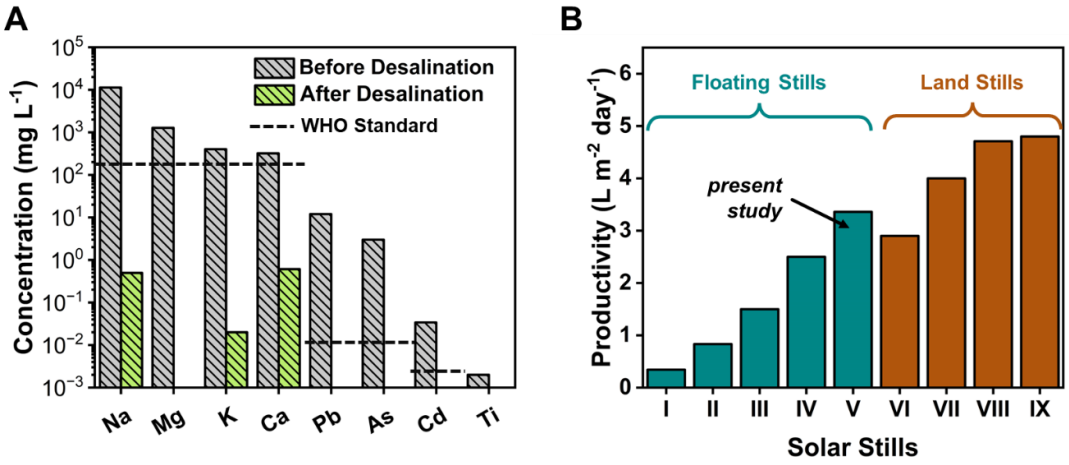

Figure 6.15. (A) ICPMS ion concentration results before (grey striped) and after (green striped) desalination. (B) Productivity of select solar stills in literature.

The TR-TiC solar still was compared to other passive floating solar stills, as well as some of the top performing passive land stills (Figure 6.15B and Table 6.3). The current project still obtained higher productivity values and efficiencies than any other floating solar still reported to date. It is even higher than many land-based solar still in the literature. This is mostly attributed to the highly efficient photothermal heating of the TiC NPs across a broad spectrum of light. Additionally, the solar still engineering to create a strong water transport balance, effectively insulate the evaporation interface, and environmental stability helps to maintain the desalination efficiency over time. Other floating solar stills have used asymmetric condensation domes, which can cause shading of the evaporation surface unless they maintain a perfect alignment with incoming sunlight.[543] Other reported floating stills can be overturned when used in water with moderate waves. Not only does this decrease the effectiveness of solar desalination, but it also shortens the lifespan and increases the need for more regular maintenance. The symmetric nature of the still reported herein means that no mater how it is oriented towards the sunlight, it will allow a maximum amount of solar radiation to transmit onto the TiC evaporation interface. As mentioned, the flexibility of the EVA foam, and the large footprint of the still allowed it to easily ride over waves, avoiding splashing of saltwater onto the surface.

Table 6.3. Comparison of productivity and economics of proposed floating solar still with selected literature floating and land solar stills.

Ref.	Type of Still	Solar Insolation (kW m^{-2} day^{-1})	Water Productivity* (L m^{-1} day^{-1})	Cost Per Litre ($ L^{-1})
3	Floating	6.69	0.34 (3%)	1.0665
3	Floating	6.69	0.83 (7%)	0.0663
4	Floating	6.49	2.50 (22%)	0.0061
5	Floating	6.10	1.50 (16%)	0.0209
This work	***Floating***	***5.98***	***3.36 (38%)***	***0.0045***
6	Land	6.82**	2.90 (28%)	0.0064
7	Land	6.08**	3.65 (40%)	0.0096
8	Land	6.91**	4.00 (39%)	0.0095
9	Land	7.15**	4.80 (45%)	0.0100

* Water generation rate shown first followed by solar desalination efficiency in brackets. ** Calculated from reference tables.

While land solar stills can reach higher water generation productivities than floating solar stills on average, they also often cost more to build and maintain.[550] This is mostly caused by the need to continuously replenish water into the trough of the still, and to contain it within the basins, adding electric pumps into the scaffolds. The requirement of land also makes them potentially less desirable than floating solar stills. Therefore, this project sought to compare the economics of the TR-TiC solar still with those compared to previously. This was done using a basic cost analysis of the entire production process of the solar still. The method was adapted from Fath *et al.* and Bait *et al.* to ultimately calculate the cost per litre (CPL) using the still.[112,551] This provides a dollar value for every litre produced by the solar stills over their entire lifetime and includes any potential costs over that same time period. This included initial investment cost, estimated annual interest rates (10%), service life (2 years), and operational days each year (320 days). All other values used through the CPL calculation process can be seen in Table 6.4. The wholesale costs for each component of TiC NP synthesis and solar still production were sourced from the Alibaba website. Electricity ($ 0.11 kwh^{-1}) and water prices ($0.004 L^{-1}) were taken from Nova Scotia Power, and Halifax Municipal Water, respectively. The annual costs include cleaning of the solar still, replacement of

transport wicks and collection bags, and regular collection of desalinated water. To account for the seasonal and daily fluctuations in solar intensity, the average daily solar insolation value over the entire year was used (2.84 kW m^{-2} during daylight hours). This data was sourced from Environment and Climate Change Canada. This contrasts with many other reports which assess the daily productivity of solar stills based on the test days, often taking place in the middle of summer. This can falsely inflate the amount of water produced over the lifetime of the still, leading to an inaccurate CPL. To estimate the amount of water produced daily with 2.84 kW m^{-2} sunlight intensity, a linear relationship between sunlight and intensity and water production was assumed (see Figure 4.13A for information). This equates to a daily productivity of 1.83 L m^{-2} in Halifax, Canada. Interestingly, when considering a more likely desalination location such as San Diego, California, the average daily production jumps to 3.03 L m^{-2}. The CPL values associated with the TR-TiC solar still being used in Halifax and San Diego are \$0.0086 and \$0.0052 L^{-1}. Comparing this to the previous stills (Table 6.3), the solar still reported here has the lowest CPL and while being comparable in productivity to some of the best performing land stills. This value could be much lower still if the buying price of distilled water was considered for the calculations, dropping the CPL to \$0.0012 L^{-1} when used in Halifax.[543]

Table 6.4. Component cost for still production, annual cost structure, and profit margin values used for cost per litre (CPL) calculation for proposed still operating in Halifax, NS.

Production Cost Type	Components	Cost* ($ m^{-2})
TiC NPs	*TiO_2 NPs*	**0.16**
	Tire crumb	**0.01**
	Mg	**0.35**
Reaction	*Electricity cost*	**0.11**
	Purification	**0.05**
Solar still	*EVA foam*	**0.15**
	PVC plastic	**0.01**
	Polyester filter	**0.10**
	Steel frame	**0.12**
	Cotton wick	**0.04**
	Tubing	**0.08**
	Collection bag	**0.31**
Production costs	*Total fixed cost*	**1.51**
	Total annual cost	**0.43**
Water Yearly Profit	*Cost of water (Halifax Water)*	**2.41**
	Annual production	

* Costs shown in red show investments, while in green show returns. Prices for TiC NP synthesis materials and solar still components were sourced from Alibaba and normalized to produce 1 m^2 of evaporation surface. Electricity and water prices were taken from Nova Scotia Power (0.11 $ kwh^{-1}) and Halifax Water (0.004 $ L^{-1}), respectively. All prices in USD.

The final step in the analysis of the constructed solar still was to modify the evaporation surface to incorporate thermoelectric generation capabilities. This works due to the large temperature gradient between the evaporation interface and the cold ocean water below. Thermoelectric generation works of the Seebeck effect, where the flow of charge carriers at *p-n* junctions between semiconductors can induce an electric current and voltage.[552] There have been several publications that have suggested coupling solar desalination with thermoelectric generation based on

lab-scale experiments.[546,547,553,554] Several groups studying land solar stills have successfully incorporated thermoelectric generators (Peltiers) into the still design, but because land stills contain water in a basin, it will warm up, and the temperature difference will decrease along with the electricity generation. This means of electricity production has yet to be tested for a scaled up floating solar still. To accomplish this, 12 thermoelectric generators (TGs) were incorporated into the foam support of the TR-TiC solar still. They were adhered to aluminium heat sinks which were long enough to protrude through the bottom of the foam and into the cold ocean water below (Figure 6.16). The TGs were set in series and connected to a buck boost power converter to stabilize power to whatever load was to be connected. As a proof of concept of the technology, a small fan and then a USB-C port for phone charging were tested (Figure 6.17).

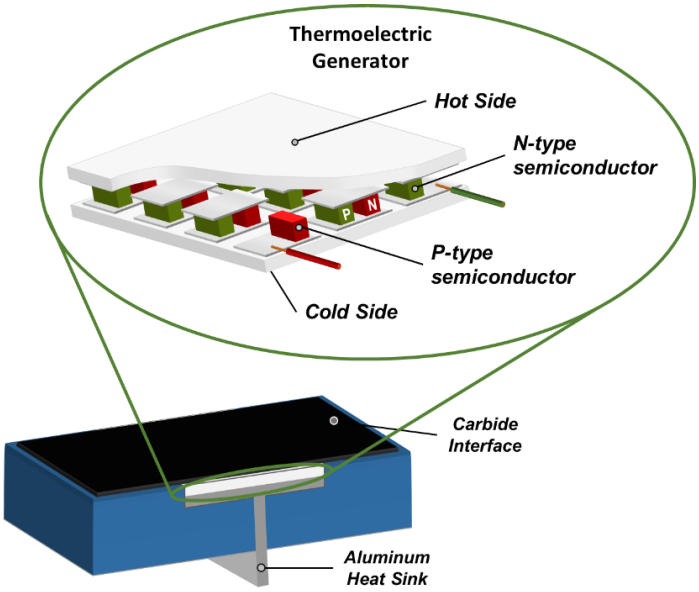

Figure 6.16. Schematic of thermoelectric integration into the TiC solar still.

Thermoelectric tests were completed in a pool which was filled with Atlantic Ocean water directly at beach nearby. The testing took place in February, when the average air temperature and water temperature over the testing period were both 0 °C. During operation, the surface of the still reached a stable operation temperature of 32 °C. Although the ambient temperature was more than 20 °C lower than when the still was tested in the summer, the temperature different between the evaporation surface and ocean water was similar. While testing, it was

found that at peak solar radiation (13:00), almost 100 mL of water was distilled for the hour, highlighting the utility of the plasmonic solar still even at freezing temperatures (Figure 6.17B). The SVG efficiency peaked at 33% on testing day, compared to 38% during the summer testing period. The cold wind and cold ocean water likely caused heat to be more rapidly displaced from the evaporation surface, leading to the decreased efficiency. On testing day, the maximum induced open-circuit voltage ($V_{open\text{-}circuit}$) was measured at 3.34 V, with the short-circuit ($I_{short\text{-}circuit}$) reaching 486 mA (Figure 6.18A). The impressive ability of the thermoelectrically driven solar still to operate year-round in Canada highlights once again the strong photothermal action of the TR-TiC NPs. Estimation of the solar still's maximum output involved connecting an external resistor (10 Ω) close to the resistance of the TG series (10.64 Ω). The circuit resistance was calculated using the Thevenin equivalent resistance method proposed by Tsang *et al.*,[553] which afforded the maximum power output of 1.32 W (Figure 6.18B).

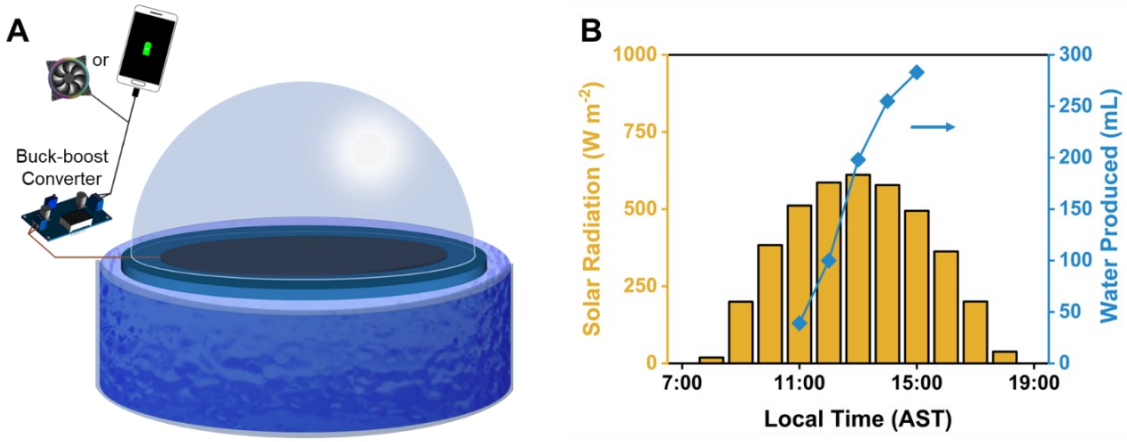

Figure 6.17. (A) Schematic of thermoelectric generation setup to power either a small fan or charge a smartphone. (B) Solar intensity, and water production on testing day (February 19th, 2024, from 11:00 until 15:00).

After the measurement of $V_{open\text{-}circuit}$, $I_{short\text{-}circuit}$, and max power output, the resistor was removed, and in its place a small fan was connected to the thermoelectric circuit. In this case, the buck boost converter was not needed as the fan will operate at any voltage between 1 – 3 V. Therefore, the fan terminals could be connected directly to the protruding wires from the solar still, causing the fan to operate at maximum speed without faltering at all (Figure 6.19 A and B). With the

buck boost converter and USB-C cord connected, the TG solar still is capable of charging a smartphone, though at a slower rate than when plugged into a standard wall electrical socket (Figure 6.19C). While it was slower, it provided a steady current, and the phone was receiving charge the entire time, gaining ~3% battery life in 15 min. Results here demonstrate the expanded utility of the TR TiC solar still for powering small devices even in the middle of winter. This concept could be extended to have on-board sensors for monitoring the quality of the distillate. While the concept of SVG with simultaneous thermoelectric generation has garnered attention in the field, this is the first example of a largescale floating solar still capable of running devices while desalinating ocean water.

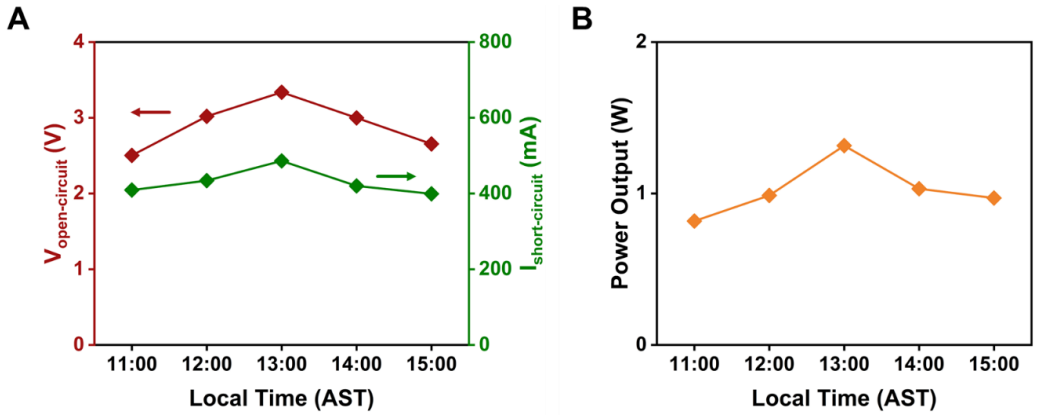

Figure 6.18. (A) Open-circuit voltage (red) and short-circuit current (green) measured each hour of testing. (B) Maximum power output of the TG TiC solar still when connected to a 10 Ω resistor (equal to internal TG resistance).

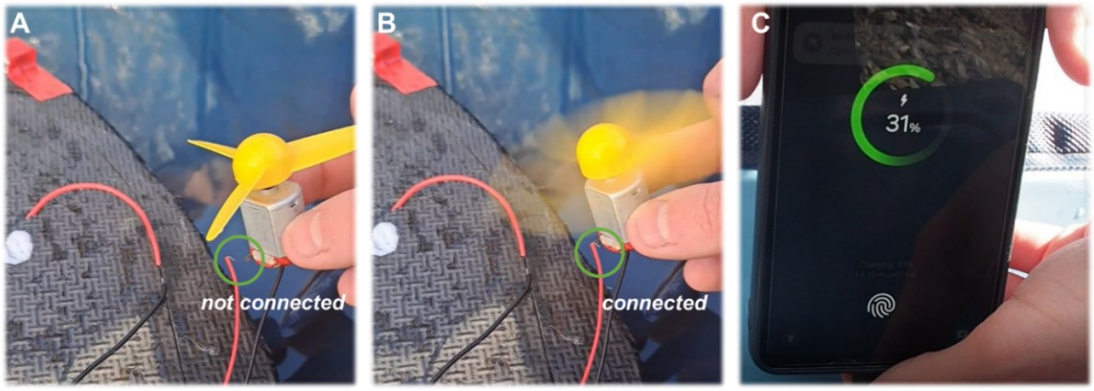

Figure 6.19. Still images taken from video of (A) fan not connected and still, and (B) fan connected and spinning. (C) Phone charging while plugged into solar still.

6.4 Conclusion

This chapter introduced a TR TiC NP based solar still which has been shown to generate freshwater from Atlantic Ocean water with the highest productivity reached for a floating solar still to date. Starting from waste tire rubber, this marks a promising avenue for the upcycling of waste tires and incorporating them into an environmentally friendly water generation process. The design of the solar still, working in tandem with the high photothermal efficiency of the TiC NPs creates a strong environment for effective water evaporation and collection. The still was able to desalinate water in the rooftop pool experiments at a rate of 3.67 L m^{-2} day^{-1}, equating to an SVG efficiency of up to 40%. Even when deployed directly on the ocean, where currents, waves, and sediment can interrupt the production of water, the still generated freshwater with a slightly decreased efficiency of 38%. Monitoring of the microbe concentration of water being distilled through the solar still after 10 days of operation, it was found to effectively avoid growth of microbes and mold. Inorganic salts and heavy metals were found to be decreased in concentration by 3 – 5 orders of magnitude. In both tests, levels of cATP and metal ions were over 1000x lower than the current guidelines published by Health Canada and the WHO, which are some of the strictest policies worldwide. An economic evaluation of the solar still water production over its lifetime afforded a CPL of \$0.005 L^{-1}, with full repayment of costs in just 290 days of operation in Halifax, Canada. Not only does the still produce water on par with top performing land solar stills, but it also costs less than almost any other still reported to date. Thermoelectric generation was effectively incorporated into the solar still design, providing a peak power generation of 1.32 W in the middle of the winter, while maintaining a SVG efficiency of 33%. The efficient heat generation of the TiC NPs benefits from the very cold ocean water to reach such high electricity generation levels. The power generated was found to be sufficient to run fans, and even charge a smartphone which highlights the potential utility for the still itself powering onboard electrics that might be needed.

CHAPTER 7

TOWARD THE SYNTHESIS OF GROUP 5 METAL CARBIDE NANOPARTICLES

The synthesis of all Group 5 carbides, material characterization (XRD, UV Vis) were performed by me. TEM images were taken by Dr. R. Karaballi and Dr. S. A. Martell. FEM simulations were performed by Dr. Y. E. Monfared at Dalhousie University. Amorphous carbon generation by birch wood residue pyrolysis was done by Dr. S. MacQuarrie at Cape Breton University.

7.1 Introduction

Carbides of the group 5 transition metals, V, Nb, and Ta have long been materials of interest for a variety of chemical application and processes.[397,555] They form several carbide phases, including MC, M_8C_7, M_4C_3, and M_2C (where M is the group 5 transition metal) which are stable under standard conditions.[556–559] Each of the group 5 TMCs have historically been used as ultrahard and ultrahigh melting point materials for cutting tools, and aerospace protective coatings.[560–562] Additional studies have been on group 5 TMC NPs for applications ranging from catalytic H_2 production[563,564] to reported use as a component in sodium ion batteries and capacitors.[565–567] More recently, they have been exploited for their unique electronic properties.[568–571] The dielectric functions of the group 5 TMCs vary depending on the metal used (Figure 7.1), striking the balance between negative real dielectric (electron plasma interaction with light), and small imaginary dielectric (optical

losses). NbC dielectric data was not available in the format needed for FEM simulations and therefore the dielectric data presented is for bulk NbC as determined by electron energy-loss spectroscopy (EELS).[572] Based on the data, pure metal VC NPs are expected to display LSPR in the UV region, while TaC NPs can display LSPR absorbance across the UV, visible and NIR regions. NbC NPs weren't directly modeled, but the bulk dielectric data suggests that LSPR could exist in the UV region as well. It is important to note here that different TMC phases (M_xC) can display different LSPR properties than those predicted in Figure 7.1, and dielectric data is not available for all examples. The MC phase dielectric functions can potentially however provide insight into the behaviour of the other carbide phases. Experimental data has been presented in literature for several examples, which will be presented to shed light on the plasmonic properties of these carbides.

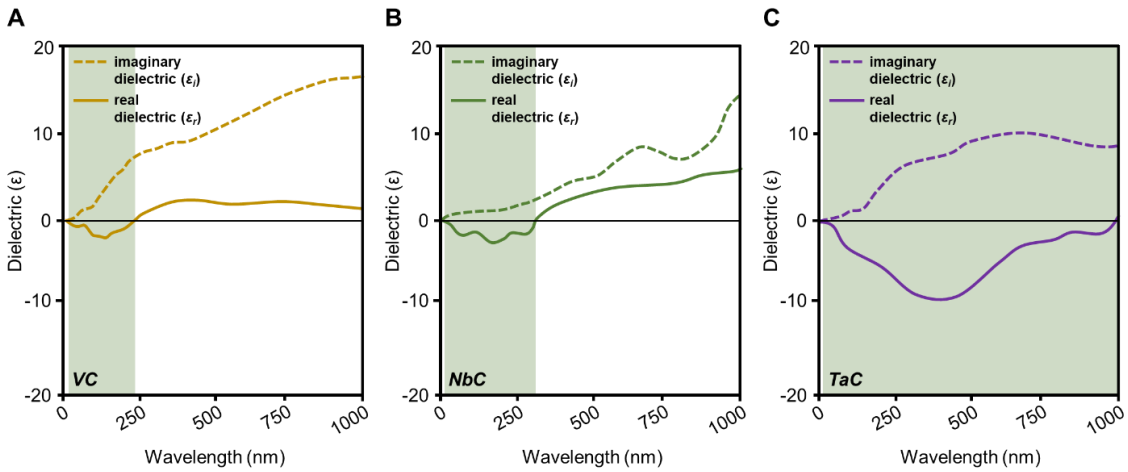

Figure 7.1. Real (solid lines), and imaginary (dashed lines) dielectric functions for (A) VC, (B) NbC, and (C) TaC. Green and white regions show where LSPR formation could and could not occur, respectively. Data for VC and TaC from unpublished results in our lab. Data for NbC used from reference (31).

MXene phase NPs exist for all three group 5 TMCs, with several including analysis of the absorbance spectra of the synthesized materials. MXenes of V_xC_y have displayed LSPR ranging from the UV to visible region, and it has been shown that the surface functionality influences the location and characteristics of the absorbance. For example, when triethylamine was used to intercalate 5 nm thick

V_2C MXene nanoflakes, an absorption maximum was observed at 400 nm,[573] while similar sized V_2C NPs without an intercalation agent displayed LSPR maximum at 550 nm.[574] For MXene Nb_xC NPs, LSPR generally produce slightly broadened absorbance peaks which cross the visible spectrum and into the NIR region in some cases.[575,576] Interestingly, nanopatterned Nb_2C wafers were shown to display a sharper absorbance peak at ~550 nm, which led to an impressive Raman signal enhancement of 10^5.[577] MXene Ta_xC_y tend to display the broadest absorbance spectra, as anticipated from the dielectric data (Figure 7.1). Ta_4C_3 NPs presented by Dhingra *et al* displayed broad absorbance across the entire region from 300 – 1000 nm scanned.[578] The particles were small nanosheets with an average size of 5 nm.

2D group 5 TMC NPs have garnered interest as substrates for surface enhanced Raman spectroscopy (SERS).[575,577,579] Both Nb_xC_y and Ta_xC_y have been used for SERS detection as well, but more recently, Nb_2C NPs have been successful as a photothermal catalytic support for the reduction of CO_2.[580] Here, the plasmonic heat generation from the Nb_2C NPs maintains a high reaction temperature which helps to drive the reduction process on the active catalyst. MXene phase Ta_4C_3 NPs have been shown to be effective in photothermal tumor therapy.[581] In one report, Ta_4C_3 NPs were functionalized with Fe_3O_2, making the composite superparamagnetic.[582] The particles could then be selectively aggregated near tumor cells for plasmonically-driven photothermal destruction of the cancerous cells. Very recently, both NbC and TaC NP films have demonstrated their effectiveness photothermally aiding nitrogen reduction catalysis.[583] In this scenario, the TMC NPs were formed and selectively surface oxidized to create a semiconductor suboxide (NbO_x or Ta_xO) layer which was the electrocatalytically active species. The carbide cores, which both absorbed at ~700 nm was then able to photothermally generate heat when illuminated to maintain the reactivity of the endothermic reaction. More and more of the reactivity of the group 5 TMCs is thought to be due to their strong photothermal heating, leading to heat induced, or photothermal, catalysis.[584,585] This makes them an incredibly interesting class of materials to explore for their plasmonic properties.

Throughout this thesis, the synthesis of group 4 TMC NPs was successful using the magnesium reduction of metal oxide precursors in the presence of various pyrolytic chars as the carbon source. Expanding the utility of this reaction to

include other metals across the periodic table is of interest in the ever-growing demand for new and unique plasmonic materials. The electronic structure of group 5 metal carbides shows that they have potential to be effective plasmonic materials on the nanoscale (Figure 7.1).[290,299,569,570,572] In fact, a theoretical study by Kumar *et al.*, which first identified group 4 TMC and TMN NPs as favorable plasmonic materials noted that 3D tantalum carbide (TaC) NPs could be the most promising plasmonic carbide material known.[277] This is due to a strong interaction with light not only in the UV region, but broad absorbance across the majority of the visible region of the light spectrum as well. This was based on calculations looking at particles of 100 nm size where, as previously discussed, scattering of light becomes a more dominant mechanism and absorbance decreases drastically.[339] This chapter highlights the preliminary attempts made to synthesize and characterize group 5 TMC NPs using the familiar magnesiothermic reduction reaction, with efforts ongoing. Synthetic patterns corresponding to reaction temperature, time, and ratios of reactants are investigated by tracking crystalline intermediates by PXRD. Due to the variety of carbide phases that can exist at atmospheric pressure and temperature for the group 5 TMCs, isolating pure phase carbides is more synthetically challenging.

7.2 Material Synthesis and Characterization

Group 5 TMC NPs were synthesized as outlined in section 2.1 of this report. Synthesis of birch residue pyrolytic char followed the procedure of section 2.1.2. Synthesis of V_2O_5 NPs followed the procedure outlined in section 2.1.4, and TMC NP synthesis followed the procedures of section 2.1.5. For this chapter, characterizations include PXRD, TEM, UV-Vis, and FEM.

7.3 Results and Discussion

The synthesis of group 5 TMC NPs followed the procedure outlined in section 2.1.4. Throughout the studies, a wide variety of reaction temperatures, ramp rates, times, and reactant amounts were studied to form each of the corresponding TMCs. For each metal, V, Nb, and Ta, reactions were monitored using PXRD, and some of the reaction conditions attempted are laid out. One of the major things to point out is that group 5 metal oxides (M_2O_5) are difficult to produce on the nanoscale compared to their group 4 counterparts. For that reason, they were generally unavailable commercially. V_2O_5 was previously synthesized following a previously reported method.[586] While this synthesis was reported to produce small crystallite sizes (10 nm) as determined from analysis of XRD data, TEM images showed that the particles were generally 100 nm or larger in size (Figure A.5). Both Nb and Ta oxides were unavailable on the nanoscale, and so commercially available 325-mesh Nb_2O_5 and Ta_2O_5 oxide powders were used. The reason for this is choice is that several reports have proved successful preparation of TMC NPs even when starting from microscale precursors.[587,588] The theory behind this is that as oxygen atoms (60 pm radii) in the crystal lattice are removed and replaced with larger atoms of carbon (70 pm radii), causing strain on the particle which can result in fracturing of larger structures thus creating much smaller particles in the process. Identifying this as a potential route to TMC NP synthesis would be of interest for metals across the entire periodic table as larger mesh particles are often much more affordable than prepared oxide nanopowders.

Interestingly, the reaction outcomes were found to be influenced by the ramp rate of the reaction. This contrasts with the synthesis of group 4 TMC NPs, where heating rates of 5 – 50 °C min^{-1} were tested without altering the product NPs. For group 5 TMC synthesis, increasing the heating rate above 15 °C min^{-1} led to inconsistent results, with the same reaction sometimes forming carbide, while other times forming undesired products such as the magnesium metalate (MgV_2O_6, $MgNb_2O_6$, or $MgTa_2O_6$), as shown by the XRD spectrum of a VC reaction (Figure 7.2). Previous reports on the magnesiothermic reduction have shown it to be a highly exothermic reaction, which once initiated can be self-sustaining.[335,589] It is possible that by heating the reaction mixture too rapidly, a thermal runaway effect occurs, and the temperature of the powder reached may reach significantly

higher temperatures then the set temperature of the furnace. Therefore, moving forward, the synthesis reaction for group 5 TMC NPs were performed at a heating rate of 10 °C min^{-1}.

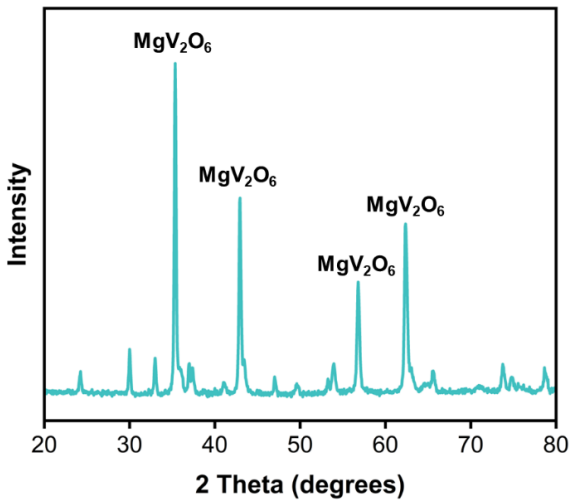

Figure 7.2. XRD spectrum of VC reaction at 50 °C min^{-1} heating rate, showing formation of MgV_2O_6.

Initial attempts were made towards the synthesis of VC by mixing the precursor oxide powders with birch-derived char and Mg powder in a glovebox. The various reaction conditions are presented in the general form as follows: 800 °C, 6 h, 1:4:6 (M_2O_5:C:Mg), showing the reaction temperature, reaction time, and ratio of metal oxide to C and Mg powders, respectively. PXRD patterns of several synthesis attempts are shown in Figure 7.3. The formation of VC is observed at temperatures as low as 650 °C. However, the majority of the material remaining is from the starting oxide. Increasing the temperature to 750 °C leads to complete conversion of the V_2O_5, but the powder contains another vanadium carbide phase, V_2C, as shown by the black dots. Increasing the temperature by another 100 °C doesn't remove all the V_2C, and other reactions going above this temperature lead to formation of MgV_2O_6 as an unwanted byproduct. Interestingly, by increasing the amount of carbon, the complete conversion to cubic phase VC is realized (Figure 7.3, top). This formation temperature is lower than for any of the group 4 TMC NPs discussed in Chapter 4. In a recent paper by Feng *et al.* a series of thermodynamic calculations were conducted to investigate the formation of various metal carbides (TiC, ZrC, HfC, NbC, and TaC).[590] These calculations were based on

the direct reduction and subsequent reaction of amorphous carbon with the corresponding metal oxides (TiO_2, ZrO_2, HfO_2, Nb_2O_5, and Ta_2O_5). The authors found that the Gibb's Free Energy became negative (spontaneous) at a lower temperature for both NbC and TaC formation. Replacing amorphous carbon with Mg for the reduction step could follow a similar trend, and this could be the reason the group 5 TMCs form at lower temperatures than the group 4 TMCs.

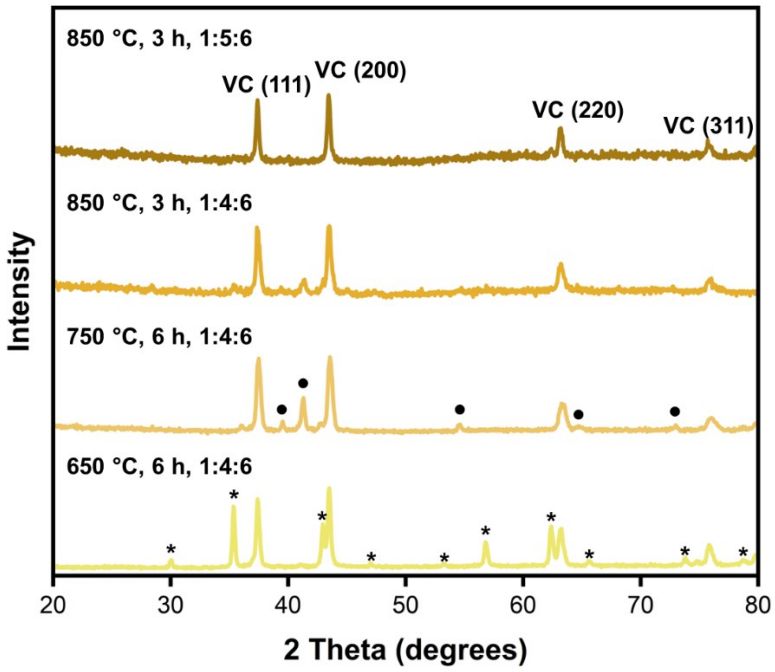

Figure 7.3. Select PXRD spectra for several attempts at the formation of VC. *V_2O_5. ●V_2C.

The UV Vis spectrum of the obtained VC NPs showed a relatively sharp LSPR peak starting around 300 nm and increasing into the deep UV region (Figure 7.4A). The peak displayed some shoulders, likely arising from the interaction between particles, or the presence of amorphous carbon such as in Chapter 3. This could additionally be caused by the particles being not completely spherical, leading to slight variation in the observed LSPRs as discussed in Chapter 1. Based on previous reports, it was expected that VC would display LSPR in the UV region, particularly as the particle size decreases. This is an interesting result as it means that the large starting V_2O_5 particles could in fact be getting sheared to create smaller VC NPs.

TEM analysis on the obtained product confirmed that the new particles are much smaller than the synthesized oxide, with a measured average particle size of 18 ± 7 nm (Figure 7.4B and A.6A). Size measurements were difficult as the NPs were quite aggregated on the TEM grid, and the overlap of particles made determining the particle edges impossible in certain regions. Since the VC NPs were prepared at a lower temperature than the previously described group 4 TMCs, it is possible that the amorphous carbon wasn't burned away to the same extent. This could cause a slightly larger amount to remain at the end of the reaction and potentially aggregate the VC NPs onto the surface as the solution evaporates.

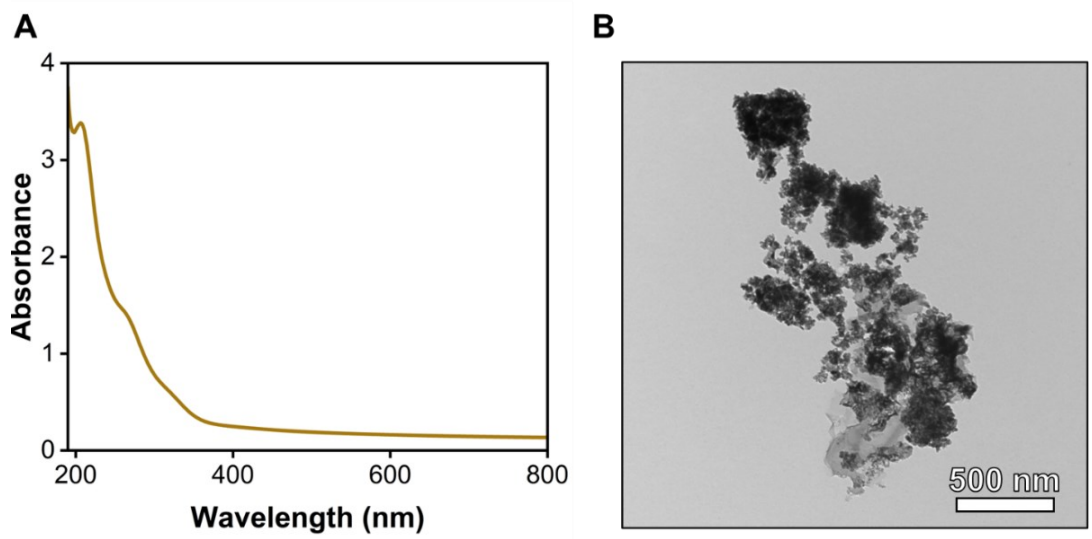

Figure 7.4. (A) Absorbance spectrum of VC NPs dispersed in water. (B) TEM image of VC NPs.

Efforts were then turned to synthesize NbC, and the pathway exhibited a similar trend to that observed with VC. In this case though, even at lower temperatures of 650 °C for 3 h all the starting Nb_2O_5 had disappeared (Figure 7.5). Just like before, there was a mixture of carbide phases though, with approximate peak intensities being 1:1 between NbC and Nb_2C. By increasing the reaction time to 6 hours, the amount of Nb_2C was drastically reduced though some remained in the isolated reaction product. Full removal of the peaks associates with the undesired carbide phase (Nb_2C) was realized by increasing the temperature to 750 °C. In this scenario though, it became clear that there were trace amounts of unreacted starting oxide in the mixture. To help try and remove this, an additional equivalent of Mg powder

was added and then reacted under the same conditions as before. This provided a single phase, NbC product as indicated by the PXRD spectrum (Figure 7.5, top). It is worth noting that while these reactions proceed at lower temperatures, the reactions themselves are quite sensitive to slight changes in temperature and time. This provides a strong foundation with which the material synthesis could be tuned to try and form different phases, depending on the desired end use.

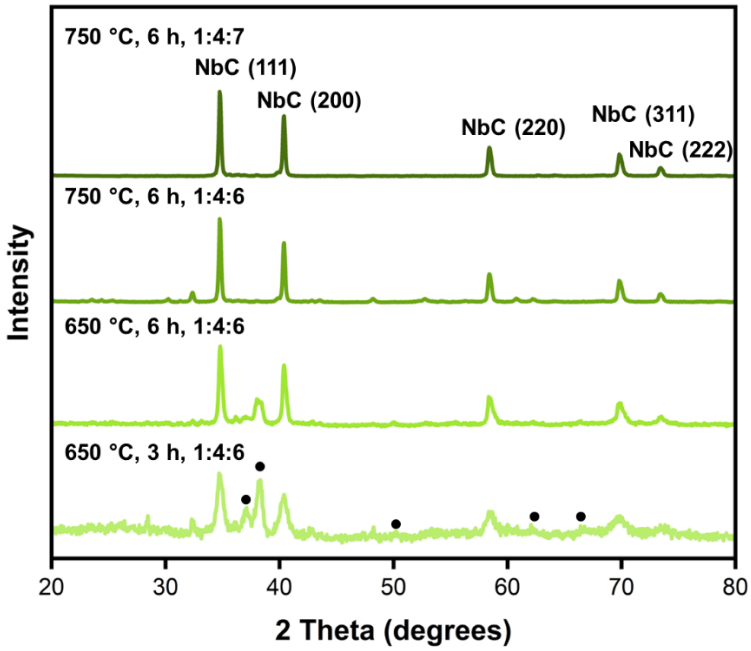

Figure 7.5. Select PXRD spectra for several attempts at the formation of NbC. ●Nb_2C.

Absorbance measurements were performed to analyze the optical properties of the obtained NbC NPs (Figure 7.6A). The spectrum once again has some shoulders present as the absorbance increases into the deep part of the UV region, caused by shape variations from spherical or from the presence of amorphous carbon impurities. The major difference in the spectrum compared to that obtained from VC NPs was that it slowly increased from 500 – 800 nm, indicating some form of absorbance process occurring across these wavelengths. While it isn't a strong absorbance it contrasts any of the other TMC NPs reported in this thesis. Evidence for what may be causing this could be taken from the obtained TEM image (Figure 7.6B). Some of the NPs appear to be quite elongated and oblong, similar in

appearance to nanorods. Based on other plasmonic nanorod reports, it is possible that the low intensity broad absorbance peak arises from longitudinal excitation (Figure 1.2)[591] of a small number of these rod shaped NbC NPs. An average particle size was determined from the TEM images and was found to be 20 ± 9 nm (Figure A.6B), once again indicating the useability of micron scale powders to synthesize TMC NPs.

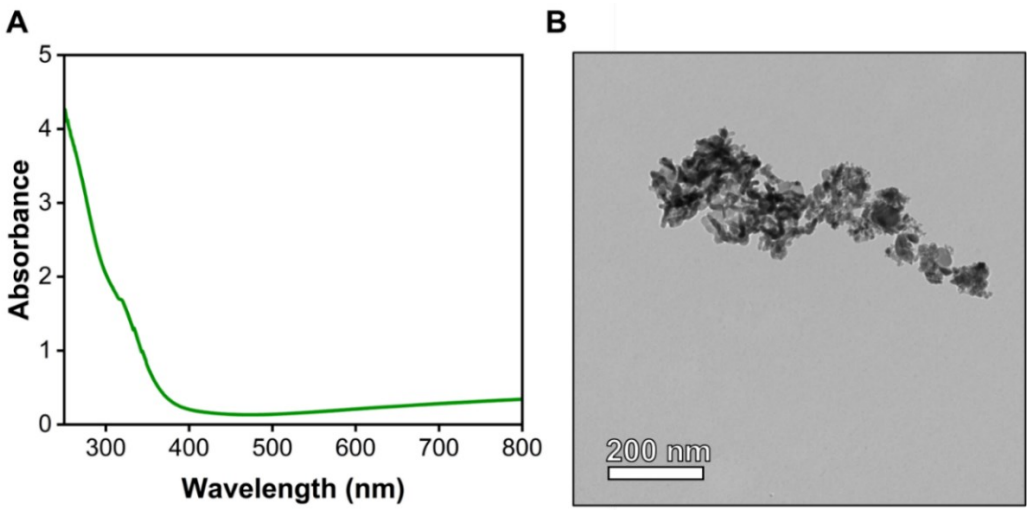

Figure 7.6. (A) Absorbance spectrum of NbC NPs dispersed in water. (B) TEM image of NbC NPs.

Finally, attempts were made at synthesizing plasmonic TaC NPs using the magnesium reduction reaction. Several of the reactions with their corresponding conditions are summarized in Figure 7.7. Similar to the other group 5 metals, the formation of TaC began at 650 °C, though even when increasing the reaction time to 12 h at this temperature, there was no complete conversion to the carbide. The majority appeared to be the starting Ta_2O_5, which could be confirmed visually as the reaction powder was light grey compared to the deep black color of most TMCs. To fully remove the oxide precursor, it was necessary to increase the temperature to 950 °C, with an additional two equivalents (six total) of carbon added with respect to the metal oxide. If the temperature was increased beyond 1000 °C, formation of magnesium tantalate ($MgTa_2O_6$) was observed which cannot be easily separated from the reaction mixture. Unfortunately, under the tested conditions isolation of the pure TaC was not successful. Even with a 12-fold excess of carbon or Mg powder over various reaction times, the collected product contained both the TaC phase

and the Ta_2C phase. The large particle size of the starting oxide could in this case be the cause of the observed reactivity. If the large particles do not cleave to sufficiently small sizes, then the amorphous carbon may not be able to diffuse deep enough over the reaction time periods tested. This could lead to a deficiency of carbon in the center of the particle, stopping the formation at the Ta_2C phase. More studies are underway to verify this and produce phase pure TaC. Furthermore, commercial sources of each of the group 5 metal oxides have recently become available, and so investigating them for the carbide forming reactions will be the next step towards the total synthesis of group 5 TMC NPs.

The need for smaller starting materials is further demonstrated by the inability of the obtained TaC/Ta_2C composite material to readily disperse in water or any other solvent. It was therefore difficult to obtain an accurate and reproducible absorbance spectrum as a large portion of the material crashed immediately to the bottom. The observed absorbance (Figure 7.8) could be mainly coming from the small particles that were able to remain in solution. For the same reason, TEM images were not recorded for the TaC product obtained in this study, with further studies looking to produce a more consistent and phase pure material.

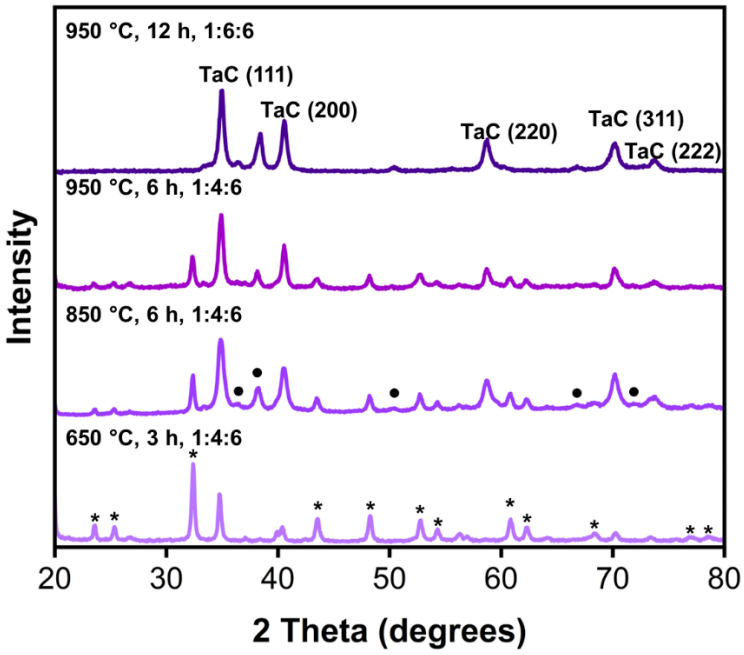

Figure 7.7. Select PXRD spectra for several attempts at the formation of TaC. * Ta_2O_5. ●Ta_2C.

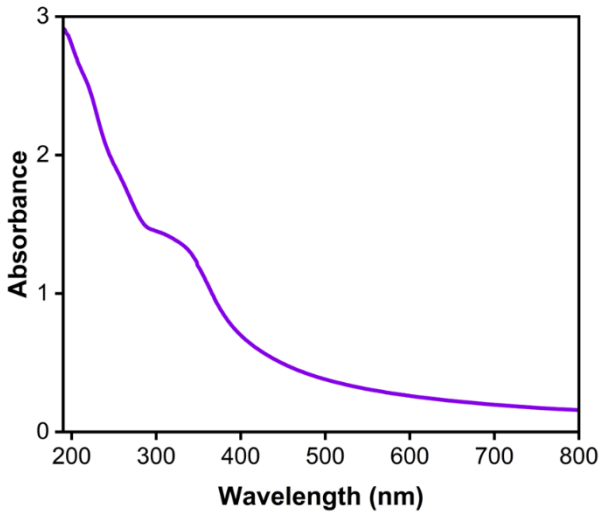

Figure 7.8. UV Vis spectrum of TaC and Ta_2C composite mixture.

7.4 Conclusion

In this study, the magnesiothermic reduction reaction explored in this thesis was applied to the group 5 transition metals, V, Nb, and Ta. Based on PXRD analysis throughout the many synthesis attempts, it appears that the group 5 TMC formation exhibits a more complicated mechanism. This is highlighted by the presence of a second carbide phase (M_2C) in each case, compared to the presence of metal oxycarbides such as TiO_xC_y in Chapter 3. Nevertheless, both VC and NbC were successfully synthesized and further characterized. The absorbance spectra for both compare with the results expected based on literature reports, particularly for the small particle sizes of 18 ± 7 nm and 20 ± 9 nm for VC and NbC, respectively. While the results here highlight the broad utility of the proposed synthetic method, phase pure TaC was not successfully produced, and instead a composite with the Ta_2C phase was produced under the tested reaction conditions. Future studies should focus on improving the NP dispersity, more detailed analysis of the surface chemistry of these carbides, and their photothermal properties.

CHAPTER 8

CONCLUSIONS AND FUTURE DIRECTIONS

8.1 Conclusions

The overarching goal of the presented study was to implement and study the magnesium reduction reaction for the synthesis of TMC NPs. The reaction produced new carbide materials with interesting physical and optical properties, namely their plasmonic characteristics. By looking into how different source materials could influence the reaction and products, the ability to fine tune the plasmonic TMCs was possible. An additional benefit to the rigorous testing of the magnesiothermic reduction reaction of metal oxide precursors was the ease of upscaling for broadened application. For this study, the plasmonic photothermally generated heating was exploited for solar driven freshwater generation.

The major focus of the reduction reaction was looking at conversion of group 4 transition metal oxides to the corresponding carbide using Mg powder and amorphous carbon derived from the pyrolysis of waste birch wood residue. Choosing this synthesis pathway benefits from decreased reaction temperature requirements relative to standard carbothermal reductions (950 – 1100 °C compared to ≥1750 °C). It also involves a simple one-step acidic workup to isolate the final product. This was presented in Chapter 3, and included intensive characterization of each carbide sample obtained, TiC, ZrC, and HfC. This was necessary as at the time there had yet to be any experimental reports examining the plasmonic

properties of 3D group 4 TMCs even though 2D MXene phase carbides had already been well reported. The formed particles were small at 24 ± 8, 31 ± 9, and 42 ± 15 nm for TiC, ZrC, and HfC, respectively, and they were comprised of a crystalline carbide core with an oxide (MO_2)/oxycarbide (MO_xC_y) shell. The experimentally observed LSPR absorption by UV Vis spectroscopy matched with the conducted FEM simulations, showing the TMC NPs to absorb strongly in the deep UV region between 150 and 175 nm. Since the LSPR maxima were below the spectrophotometer range, complementary photothermal studies were completed to verify the strong plasmonic behaviour. By shining UV (365 nm LED source) light on a TMC NP solution, they were able to quickly heat the solution. While theoretical studies on TMC NPs show they undergo more optical losses than Au or Ag, it wasn't detrimental to their photothermal heating capabilities. In fact, TiC, ZrC, and HfC NPs reached photothermal heating efficiencies of 60, 69, and 73%, topping the list of reported photothermal materials. The TMC NPs displayed impressive aqueous stability, being shelf stable in water for >3 years with no deleterious effects to the optical properties. Stability was further highlighted by treatment under strongly acidic, basic, and oxidative conditions. In this first report, potential of 3D group 4 carbides was well displayed for photothermal applications (Figure 8.1).

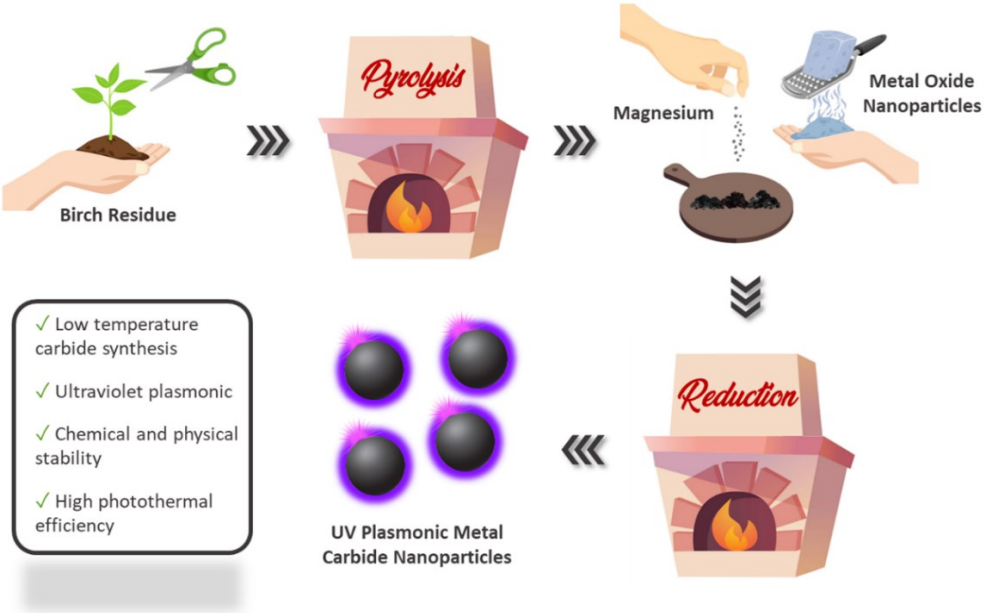

Figure 8.1. TOC graphic for synthesis and photothermal heating efficiency of group 4 TMC NPs (Chapter 3).

The photothermal heating efficiency of the TMC NPs was then tested in a real-world application for the distillation of water using sunlight as the only energy input to the system. This is important from a fundamental standpoint, but also an attractive process to help alleviate the increasing demand for clean water across the globe. At the current production rate, millions of people do not have sufficient access to clean water which will become further exacerbated by more frequent climate disasters and increased geopolitical tension.[592] For these reasons, the solar evaporation process was extended to include the desalination of ocean water using a plasmonic TMC evaporation interface constructed in lab. By vacuum loading the particles directly onto a porous paper filter at a loading of 1 g m^{-2} and under one-sun illumination, desalination rates reached as high as 1.40 ± 0.01 kg m^{-2} h^{-1}. This is equivalent to a solar-to-vapor generation (SVG) efficiency of 97%, meaning that almost all incoming solar energy was successfully used for the evaporation process. This is in part due to the strong broadband absorbance of the TMC interfaces, up to 95% between 300 and 1500 nm, but also relies on the meticulously engineered floatation platform. This provided effective heat isolation of the evaporation surface, and a steady supply of Atlantic Ocean water to the surface, which further helped to avoid salt buildup. The collected water was proven to be of highly pure quality, with salt and heavy metal ions 2 – 3 orders of magnitude below the stringent standards put out by the World Health Organization. In hypersaline conditions up to 35% NaCl, the evaporation interfaces maintained their effectiveness and were stable in operation over long periods of time. To increase the water generation rate beyond the thermodynamic limit for a standard 2D interface, the TMC NPs were incorporated into a polyvinyl alcohol (PVA) hydrogel to form another set of evaporation interfaces. The corresponding desalination increased to rates of 3.69 ± 0.04 kg m^{-2} h^{-1} for HfC which was the top performing interface and the most efficient reported to date at 96% SCG efficiency. The salt tolerance and purification standards of the hydrogel interfaces was retained. The effectiveness of TMC NP solar desalination is a step in the direction of realizing cost-effective and readily scalable solar-driven freshwater generation (Figure 8.2).

Figure 8.2. TOC graphic for plasmonic TMC NP Lab-Scale Interfacial Solar Evaporation and Desalination (Chapter 4).

While all three tested TMC NP samples exhibited high solar desalination rates and efficiencies, HfC was the top performer, with TiC and ZrC 10 – 15% less efficient. From an economic standpoint however, titanium and zirconium cost on average ~100 times less than hafnium.[593–595] Tuning the properties to increase the optical efficiency of TiC was therefore completed, advancing the potential for widespread use. Further, this project highlighted the ease of introducing different carbon source materials into the reaction pathway using locally available waste materials. This shows the potential of forming TMC NPs from local waste materials no matter where that may be, or what is available. Here, along with the birch wood (BW) used in previous chapters, four other unique chars derived from invasive *Reynoutria japonica* stems (KW), spent coffee grounds (CG), discarded tire rubber (TR), and waste lobster shells (LS). Studying the pyrolytic carbons themselves showed there to be both morphological and chemical differences. Raman spectra

proved each varies in the amount of graphitic carbon, with the LS char graphitic content the highest. Additionally, while LS char had the largest average particle size of 50 ± 15 μm, carbon black NPs (>100 nm) were observed in the TR sample. BET analysis showed BW, KW, CG, TR, and LS chars to have surface areas of 598, 701, 327, 994, and 186 g m^{-2}, respectively. The only char not successfully incorporated into the TiC formation reaction was LS, which formed oxycarbide (TiO_xC_y), possibly due to the increased graphitic carbon content or lower surface area. Formation of TiC NPs from the other pyrolytic chars confirms the ability to use carbon sources local to the synthesis location. Average particle sizes of 24 ± 8 nm, 33 ± 12 nm, 26 ± 4 nm, and 12 ± 5 nm were found for BW, KW, CG, and TR TiC samples, respectively.

The optical properties were influenced by the corresponding TiC NP properties such as particle size, size distribution, and amount of amorphous carbon present. Studying the effectiveness for desalination under one-sun illumination allowing probing of the photothermal properties for each sample. After loading the NPs onto a polyester filter, each showed slight variance in the amount of broadband light absorbed, with the TR TiC absorbing up to 95% of light between 300 – 1500 nm. This translated to a high SVG efficiency of 95%, with BW, KW, and CG TiC samples reaching efficiencies of 89, 91, and 81%, respectively. The desalination rate for TR TiC was competitive with the HfC evaporation interface (96%), while benefitting from the lower cost and more in-depth toxicity knowledge associated with titanium. Combining TiO_2 and locally sourced carbon containing waste products to realize efficiency solar desalination makes this a highly attractive scaffold for low-lifetime emissions and high availability (Figure 8.3).

Figure 8.3. TOC graphic for the influence of waste material carbon source on TiC NP properties (Chapter 5).

With a more efficient evaporation interface using the TR TiC NPs, the real-world utility was tested by scaling up the process and constructing a floating solar still 32" in diameter (Figure 8.4). All components of the solar still were rigorously tested to maximize the total yield of freshwater. The still generated the highest amount of daily freshwater for a floating solar still to date at 3.67 L m^{-2} in rooftop pool experiments, and 3.36 L m^{-2} while floating on the Atlantic Ocean. These productions equated to solar desalination efficiencies of 40% and 38%, respectively based on the total solar radiation for the testing day. The TR TiC still effectively avoided microbe growth over more than 10 days of operation, emphasized by the ATP content of collected distilled samples. Further, all tested metal ions, including salts and heavy metals were decreased over 1000x below the guidelines set by Health Canada (ATP), and the World Health Organization (metal ions).[549] Over the lifetime of the still, the cost per litre (CPL) was found to be \$0.005 L^{-1}, and only 290 days needed for repayment. This makes it more productive and more economical than most land solar stills and all floating solar stills. Thermoelectric generation was realized, maxing out at 1.32 W generation in winter, owing to the strong

photothermal heat generation and cold ocean waters. This allowed for small fans to operate at full speed, and moderate charging speed of smartphones, showcasing further the potential for TMC NPs integrated into solar distillation devices.

Figure 8.4. TOC graphic for plasmonic TiC based solar still production and testing (Chapter 6).

Finally, the scope of the magnesium reduction reaction used to form TMC NPs was explored for the group 5 metals, V, Nb, and Ta (Figure 8.5). These carbides are anticipated to display broad LSPR absorbances in the UV to visible regions, and their precedence as efficient catalytic materials makes them attractive to explore further.[567,577,580,583] The formation mechanisms appear to be different than observed for TiC, ZrC, and HfC, with different carbide phases observed in XRD spectra for group 5 TMCs. Both VC and NbC were synthesized to be phase pure and displayed

absorption the increases rapidly below 400 nm into the deep UV region. While TaC formation occurred, it has yet to be isolated phase pure, instead forming a composite with Ta_2C. Nevertheless, the results from this project show the potential for TMC NP synthesis incorporating metals across the periodic table using the magnesiothermic reduction reaction.

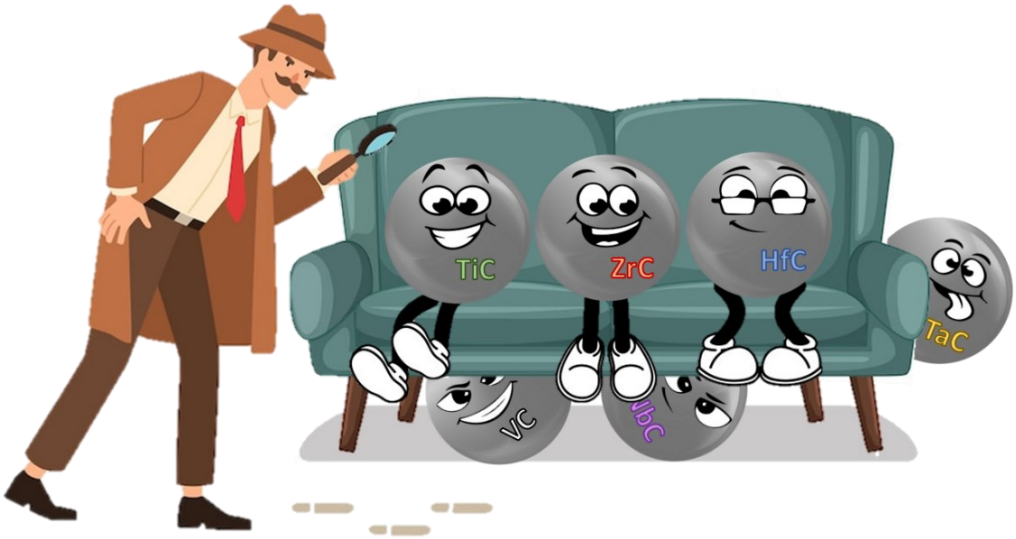

Figure 8.5. TOC graphic for the synthesis of group 5 TMC NPs (Chapter 7).

In summary, the studies presented provide a full account of synthesis, characterization, and application of various plasmonic TMC NPs using a simple and low temperature method. The work introduces a strong foundational understanding of this new and exciting class of plasmonic materials. The project further sets a precedent of incorporating locally available waste materials to upcycle into the synthesis process, and enhancement of the optical properties was observed by doing so. Analysis of the plasmonic efficiency was completed by following the photothermal heating effectiveness of each TMC sample through a solar-to-vapor conversion process and was extended to ocean water desalination. This work is an important step in not only providing a strong understanding of the practicality of carbide nanomaterials, but towards developing a roadmap for production of TMC NPs wherever the location may be.

8.2 Future Directions

There are many potential avenues to continue the work presented in this project. While many of these involve altering the synthesis to obtain new interesting plasmonic TMC scaffolds, others can further develop the application of the obtained TMC NPs discussed throughout the report. Among the most pressing aspects is to gain a full understanding of how each reaction progresses mechanistically by identifying reaction intermediates and understanding at what temperature they form. With this understanding, reaction precursors and conditions could be selected based on the desired NP outcome. It will further simplify the discovery process of new TMC materials formed by the magnesium reduction reaction as reaction conditions can be altered knowing the effect it will have. For solid state reactions, where reaction progression is quite difficult to monitor, solutions are limited. However, *in situ* XRD studies using a synchrotron source are one of the potentially strongest candidates for reaction mapping.[596,597] The additional benefit of *in situ* studies would be to verify the minimum temperatures and times required for total formation of the TMC NPs. Since many decisions throughout this project were made to decrease the overall environmental footprint associated with the material synthesis and application, any decrease in energy input is important. Finally, for applications where a small size dispersion is required, for example UV plasmonic carbides to enhance UV-light water sanitizing,[598] keeping the temperature as low as possible is a large benefit. This will reduce sintering of particles, and result in a sharper, more intense absorption at a specific wavelength.[45,599]

Depending on the various temperatures for each step of the carbide formation, it could also be more efficient to create a one-pot reaction process. In this case, incorporating the raw carbon-containing waste material powder into the magnesium reduction reaction would save time and cost. The pyrolysis process (400 – 500 °C) tends to occur at temperatures several hundred degrees lower than the carbide formation processes (≥650 °C). This means that in a one-pot reaction, the pyrolysis could form the solid carbon finely dispersed throughout the mixture to increase the reaction kinetics. In the same realm of thinking, incorporating pyrolytic carbon without blending them into fine powders, for example directly carbonizing Japanese knotweed stems could provide a template to form the TMC

NPs. By isolating the precursors into a channel or pore, interesting shape control could be tuned during the formation reaction.[600] While these modifications all depend on altering the carbon source, a lot of research focus could be put on the metal precursors as well. Of course, improvements to the synthesis of group 5 TMC NPs is important to develop their full potential. Further, expanding reaction to incorporate other potentially interesting plasmonic and/or catalytic TMC NPs (group 5 and beyond) would further prove the utility of the magnesiothermic reduction. Several of these materials (MoC, WC, and Fe_3C) have already been flagged for plasmonic or catalytic application, with more discoveries likely to be made in years to come. [277,601,602]

The TMCs don't need to be confined to just a single metal, and mixed metal carbides, known as high-entropy carbides (HECs) are an interesting research avenue. Such materials have been known for almost a century, with Ta_4HfC_5 exhibiting one of the highest experimentally reported melting points (~4000 °C).[603] Others have reached hardness values of 50 – 60 GPa (compared to diamond at ~70 GPa). The influence of different metal atoms within the crystal lattice could have profound effects on the optical properties as well. So far, only theoretical studies have been completed on the plasmonic properties of HECs, albeit with very promising results.[604] A mixture of carbides could also be introduced as a core-shell type NP (Figure 8.6) to create bifunctional NPs. One attractive option would be creating magnetic plasmonic materials, aptly named magnetoplasmonics. Synthesizing Fe_2O_3-TiO_2 core-shell NPs as described in literature,[605] followed by magnesiothermic reduction in the presence of pyrolytic char, magnetic-plasmonic NPs would be achieved. Interestingly, even if the Fe_2O_3 core reacts with carbon, the formed Fe_3C is still magnetic. These materials have far-reaching potential in magnetically guided biomedical imaging or photothermal therapy, to fabrication of optoelectronic devices.[606] The ability to guide particles to desired locations using magnets to optimize the collection and use of the LSPR energy has led to major interest in magnetoplasmonics. An additional benefit would be the isolation of the magnetic TMC NPs for recycling. Another core-shell model of interest would be creating a single particle plasmonic-semiconductor photocatalyst. In a similar manner, a SiO_2 shell could be grown onto a TiO_2 NP[607] and subsequently converted into the carbides (TiC, and SiC). SiC has been shown to be effective photocatalysts and would be of interest in tandem with the plasmonic contribution.[608] The direct

connection between the plasmonic core and the semiconductor shell would allow for generated hot electrons to pass very efficiently to the semiconductor surface to enhance the catalytic activity.[609]

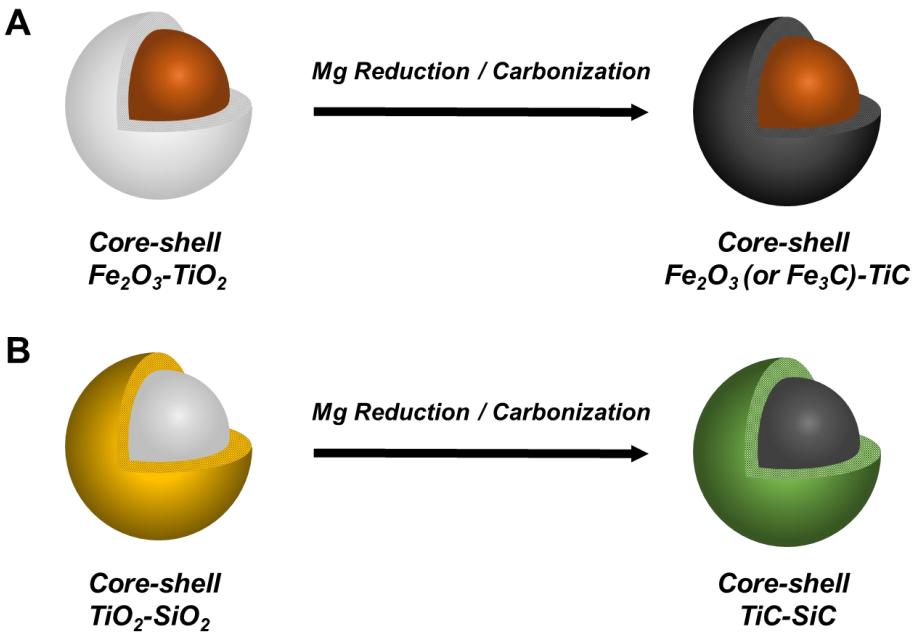

Figure 8.6. Schematic of core-shell (A) magnetic-plasmonic, and (B) plasmonic-semiconductor photocatalyst NP synthesis by magnesiothermic reduction.

While the landscape available for synthetic alteration to produce new and exciting TMC structures is broad, there are many application areas to explore as well. Focusing first on the method of desalination investigated in this project, several advancements could be made. As previously mentioned, one of the largest issues with desalination is the production of high concentration brine which must be dealt with.[138] Pumping back into the ocean can cause rapid local salinity increase, negatively impacting wildlife. Zero-liquid discharge (ZLD) seeks to completely remove any brine byproducts from the desalination process.[610] For a solar desalination process, this would likely involve the selective crystallization of salt (Figure 8.7). This can be done by reducing the flow of replenishing water across the evaporation interface (Figure 8.7A) so that the salt is unable to return to the bulk water below and must instead crystallize.[611] It can also be done by isolating it to a sharp point (Figure 8.7B) again forcing it to crystallize there opposed to across

the entire surface.[204] The salt can be collected when the water is to restart the process.

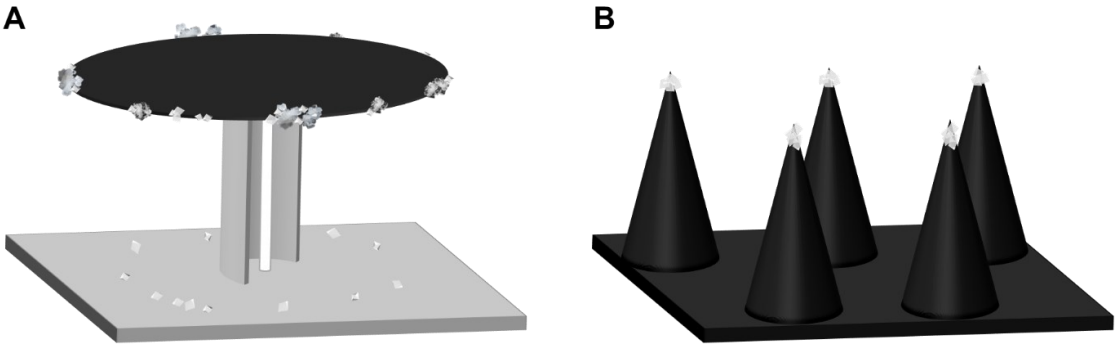

Figure 8.7. Selective crystallization of salt by (A) edge-preferential and (B) point-preferential crystallization

A second modification that could be made to the evaporation interfaces and plasmonic solar still presented in this project is regarding the hydrogel interfaces that were prepared. A major component of this study was to avoid using fossil-fuel based chemicals where possible. The polyvinyl alcohol used to prepare the hydrogel interface is derived from petroleum or natural gas cracking products, therefore alternative materials should be considered. Hydrogels based on cellulose or chitin, two biopolymers from plant material and crustacean exoskeletons, have attracted attention lately and would be a renewable source to produce the hydrogels.[612,613] Another option that has recently become more popular to prepare hydrogels is using casein, which is derived from mammalian milk.[614] Exploring these options and their interactions when incorporating TMC NPs is an important consideration to maximize the overall environmentally friendliness of the synthesis and desalination processes.

Apart from material engineering as discussed above, future designs for the solar still itself could model after some of the more effective strategies used for land-based solar stills. More specifically, factors like heat recycling can drastically increase the overall productivity of solar stills.[615] In these systems, multiple chambers can be stacked on top of one another, so that as the water from the lower chambers condenses, the heat released is transferred to the water chamber above.[616] For a passive device such as a floating solar still, this is more difficult to introduce as containing water above the surface would increase the weight too much.

Potentially, another water wicking system could be implemented to transport water to a second, raised evaporation interface to harvest the latent heat of condensation. Alternatively, using 3D photothermal layers as mentioned previously can enhance the overall water generation per given unit area by increasing the evaporation surface area. It is important to do this in a way that doesn't increase the overall complexity of the build too much. For example, instead of using 3D printing to form various surface structures, a simple mould could be prepared, and a hydrogel could be set inside to generate 3D shapes. Simple designs often scale much more readily and therefore avoiding intensive infrastructures and instruments makes the technology much more readily available. Also, by combining the benefits of both 3D and hydrogel evaporation scaffolds, the rates achieved could have single solar still units provide freshwater for families, not just individuals.

While the TMC NPs have been shown to be highly photothermally efficient for solar driven desalination, there are many other photothermal applications beyond desalination that could be explored.[617] One photothermal application that is in some ways complementary to solar desalination is the harvesting of moisture. Such materials are hygroscopic to harvest water from the air during the night, with photothermally active materials incorporated to release it once the sun comes up.[618] This could be used in tandem with a solar desalination process to multiply the water output and achieve 24/7 water production, even in arid climates. Another interesting application is for the cleanup of spilled oil, which is often difficult for traditional sorbents. This is particularly so for heavy oils, as they are not able to diffuse into the pores of the sorbents, leading to ineffective oil capture.[619] By increasing the temperature of the oil, it can be more efficiently captured and removed. By incorporating photothermal materials into the sorbent structure, they can heat up the oil at the surface to pull it more readily into the deeper pores. A further alternative example is the de-icing or anti-icing of certain surfaces in cold climates, particularly for the windward surfaces of aircrafts and wind turbine blades, or for coating electrical lines.[620] This concept has even been demonstrated for anti-fogging films for glasses, though in cases like this the material must still transmit light effectively. Finally, the photothermal steam generation can be applied to sanitizing medical equipment.[621] As discussed in Chapter 3, steam production increases with light intensity, and other reports have shown that the temperature of the steam also increases. By concentrating light or using lasers,

steam generation could reach high enough temperature (~130 °C) to kill bacteria and viruses. This could be useful for medical equipment, or also for first aid equipment used in off-grid locations.

Facilitating chemical reactions using photothermally generated heat has become a topic of interest over the past few years. Known as photothermal catalysis, a wide variety of reactions have been successful using just photothermal materials.[622] Focusing on plasmonic nanostructures, a variety of possible mechanisms are at work in a photothermal catalytic process. Ozin *et al.* determined recently that the thermal generation effects work synergistically with hot carrier generation (hot electrons) to enhance the overall reaction rate.[623] The degree of contribution from each depends on the reaction conditions and material properties. This phenomenon is not isolated to plasmonic structures and is also possible for semiconductor catalysts though the thermal mechanism component has been less studied in these cases.[624] As described in Chapter 1, the formation of hot electrons in plasmonic NPs is a very fast process, with the thermal decay process occurring slower as the energy is converted to heat.[625] Therefore, it has been theorized that for fast processes (below 100 fs) direct hot electron transfer from the plasmonic NP to the analyte is the dominant mechanism. For processes above 100 fs, the hot electron decay to heat allows for contribution from the photothermal heating mechanism. This process follows Arrhenius behaviour, where the reaction rate increases with temperature and is like applying external heating. Several groups have designed catalytic systems using the plasmon-mediated heating. Boyd *et al.* achieved catalytic steam reforming of ethanol in a catalytic flow reactor embedded with Au NPs, producing CO, CO_2, and H_2.[626]

The photothermal heating aspect is thought to maintain the reactivity of this endothermic reaction by preventing the temperature from dropping. Important to note is that there remains a lack of consensus across the literature of the extent of thermal contributions to the catalytic activity. This makes distinguishing photochemical reaction and photothermal effects difficult, with new methodologies being investigated to help identify each contribution.[627] Most commonly, photothermal materials are paired with semiconductors as previously described, where the photothermal aspect is used to combat the endothermic nature of reactions. In select examples though, one material can facilitate both the photothermal heating and electron generation. For example, CO_2 reduction with

H_2O was displayed by Zhou *et al.* using a MoO_{3-x} catalyst.[628] By introducing oxygen vacancies, LSPR in the NIR region was triggered and carrier (electron-hole pairs) separation was promoted in the UV and visible regions. This led to increases in the generation of CO (20x) and CH_4 (52x) compared to MoO_3, attributed to better adsorption of CO_2 and increase of the reaction temperature from the photothermal heating. These results show the potential for other plasmonic photothermal materials to facilitate reactions or increase the efficiency when used in tandem with photocatalysts, which will be explored in the future.

Overall, fully understanding the mechanism of formation of TMC NPs using the magnesiothermic reduction reaction will allow for tailoring of materials to be application specific. Many different material aspects can be altered, from the carbon source to the metal precursors used to achieve the desired products. This project sought to kickstart the production of a TMC synthesis roadmap which can be added to and modified as further studies are completed. The most interesting case would be to produce bifunctional materials which can easily harness the energy captured by the plasmonic material. On the application side, within solar desalination there is room for improvements to the solar still design, and materials chosen to further increase the efficiency of freshwater generation. Further, there are a wide variety of photothermal applications which could line up well with the high photothermal heating efficiencies demonstrated by the TMC NPs. Carbides represent a highly useful class of materials both for their physical and optical characteristics which should bloom into a very productive research area in the near future.

BIBLIOGRAPHY

(1) Weiner, J.; Ho, P.-T. *Light-Matter Interaction: Fundamentals and Applications*; John Wiley & Sons, 2008; Vol. 1.

(2) Britnell, L.; Ribeiro, R. M.; Eckmann, A.; Jalil, R.; Belle, B. D.; Mishchenko, A.; Kim, Y.-J.; Gorbachev, R. V; Georgiou, T.; Morozov, S. V; Grigorenko, A. N.; Geim, A. K.; Casiraghi, C.; Neto, A. H. C.; Novoselov, K. S. Strong Light-Matter Interactions in Heterostructures of Atomically Thin Films. *Science (1979)* **2013**, *340* (6138), 1311–1314. https://doi.org/10.1126/science.1235547.

(3) Hertzog, M.; Wang, M.; Mony, J.; Börjesson, K. Strong Light–Matter Interactions: A New Direction within Chemistry. *Chem Soc Rev* **2019**, *48* (3), 937–961. https://doi.org/10.1039/C8CS00193F.

(4) Rivera, N.; Kaminer, I. Light–Matter Interactions with Photonic Quasiparticles. *Nature Reviews Physics* **2020**, *2* (10), 538–561. https://doi.org/10.1038/s42254-020-0224-2.

(5) Lininger, A.; Palermo, G.; Guglielmelli, A.; Nicoletta, G.; Goel, M.; Hinczewski, M.; Strangi, G. Chirality in Light–Matter Interaction. *Advanced Materials* **2023**, *35* (34), 2107325. https://doi.org/https://doi.org/10.1002/adma.202107325.

(6) Fonash, S. *Solar Cell Device Physics*; Elsevier, 2012.

(7) Schubert, E. F. *Light-Emitting Diodes (2018)*; E. Fred Schubert, 2018.

(8) Montanarella, F.; Kovalenko, M. V. Three Millennia of Nanocrystals. *ACS Nano* **2022**, *16* (4), 5085–5102.

(9) Colomban, P.; Tournie, A.; Ricciardi, P. Raman Spectroscopy of Copper Nanoparticle-containing Glass Matrices: Ancient Red Stained-glass Windows. *Journal of Raman Spectroscopy: An International Journal for Original Work in all Aspects of Raman Spectroscopy, Including Higher Order Processes, and also Brillouin and Rayleigh Scattering* **2009**, *40* (12), 1949–1955.

(10) Song, M.; Wang, D.; Peana, S.; Choudhury, S.; Nyga, P.; Kudyshev, Z. A.; Yu, H.; Boltasseva, A.; Shalaev, V. M.; Kildishev, A. V. Colors with Plasmonic Nanostructures: A Full-Spectrum Review. *Appl Phys Rev* **2019**, *6* (4).

(11) Wood, R. W. On a Remarkable Case of Uneven Distribution of Light in a Diffraction Grating Spectrum. *The London, Edinburgh, and Dublin Philosophical Magazine and Journal of Science* **1902**, *4* (21), 396–402. https://doi.org/10.1080/14786440209462857.

(12) Bohm, D.; Pines, D. Coulomb Interactions in a Degenerate Electron Gas. *Physical Review* **1953**, *92* (3), 609–625. https://doi.org/10.1103/PhysRev.92.609.

(13) Chuang, S. L. *Physics of Photonic Devices*; John Wiley & Sons, 2012.

(14) Saleh, B. E. A.; Teich, M. C. *Fundamentals of Photonics*; john Wiley & sons, 2019.

(15) Wang, Y.; Plummer, E. W.; Kempa, K. Foundations of Plasmonics. *Adv Phys* **2011**, *60* (5), 799–898.

(16) Boholm, M.; Arvidsson, R. A Definition Framework for the Terms Nanomaterial and Nanoparticle. *Nanoethics* **2016**, *10*, 25–40.

(17) Habibullah, G.; Viktorova, J.; Ruml, T. Current Strategies for Noble Metal Nanoparticle Synthesis. *Nanoscale Res Lett* **2021**, *16* (1), 47.

(18) Akgönüllü, S.; Denizli, A. Plasmonic Nanosensors for Pharmaceutical and Biomedical Analysis. *J Pharm Biomed Anal* **2023**, 115671.

(19) Araujo, T. P.; Quiroz, J.; Barbosa, E. C. M.; Camargo, P. H. C. Understanding Plasmonic Catalysis with Controlled Nanomaterials Based on Catalytic and Plasmonic Metals. *Curr Opin Colloid Interface Sci* **2019**, *39*, 110–122.
(20) Karker, N.; Dharmalingam, G.; Carpenter, M. A. Thermal Energy Harvesting Plasmonic Based Chemical Sensors. *ACS Nano* **2014**, *8* (10), 10953–10962.
(21) Smith, J. G.; Faucheaux, J. A.; Jain, P. K. Plasmon Resonances for Solar Energy Harvesting: A Mechanistic Outlook. *Nano Today* **2015**, *10* (1), 67–80.
(22) Mott, N. F.; Zener, C. The Optical Properties of Metals. In *Mathematical Proceedings of the Cambridge Philosophical Society*; Cambridge University Press, 1934; Vol. 30, pp 249–270.
(23) Hass, G.; Schroeder, H. H.; Turner, A. F. Mirror Coatings for Low Visible and High Infrared Reflectance. *J Opt Soc Am* **1956**, *46* (1), 31–35.
(24) Herzfeld, K. F. On Atomic Properties Which Make an Element a Metal. *Physical Review* **1927**, *29* (5), 701.
(25) Schulz, L. G. The Experimental Study of the Optical Properties of Metals and the Relation of the Results to the Drude Free Electron Theory. *Adv Phys* **1957**, *6* (21), 102–144.
(27) Raimes, S. The Theory of Plasma Oscillations in Metals. *Reports on progress in physics* **1957**, *20* (1), 1.
(28) Zhang, J. Z.; Noguez, C. Plasmonic Optical Properties and Applications of Metal Nanostructures. *Plasmonics* **2008**, *3*, 127–150.
(29) Wang, L.; Hasanzadeh Kafshgari, M.; Meunier, M. Optical Properties and Applications of Plasmonic-metal Nanoparticles. *Adv Funct Mater* **2020**, *30* (51), 2005400.
(30) Maier, S. A.; Maier, S. A. Electromagnetics of Metals. *Plasmonics: fundamentals and applications* **2007**, 5–19.
(31) Choudhary, R. N. P.; Patri, S. K. *Dielectric Materials: Introduction, Research and Applications*; Nova Science Publishers xx, 2009.
(32) Derkachova, A.; Kolwas, K.; Demchenko, I. Dielectric Function for Gold in Plasmonics Applications: Size Dependence of Plasmon Resonance Frequencies and Damping Rates for Nanospheres. *Plasmonics* **2016**, *11*, 941–951.
(33) Aspnes, D. E. Electric Field Effects on the Dielectric Constant of Solids. *Physical Review* **1967**, *153* (3), 972.
(34) Abdeddaïm, R.; Guida, G.; Priou, A.; Gallas, B.; Rivory, J. Negative Permittivity and Permeability of Gold Square Nanospirals. *Appl Phys Lett* **2009**, *94* (8).
(35) Sambles, J. R.; Bradbery, G. W.; Yang, F. Optical Excitation of Surface Plasmons: An Introduction. *Contemp Phys* **1991**, *32* (3), 173–183.
(36) Aslam, U.; Rao, V. G.; Chavez, S.; Linic, S. Catalytic Conversion of Solar to Chemical Energy on Plasmonic Metal Nanostructures. *Nat Catal* **2018**, *1* (9), 656–665. https://doi.org/10.1038/s41929-018-0138-x.
(37) Sannomiya, T.; Scholder, O.; Jefimovs, K.; Hafner, C.; Dahlin, A. B. Investigation of Plasmon Resonances in Metal Films with Nanohole Arrays for Biosensing Applications. *Small* **2011**, *7* (12), 1653–1663.
(38) Schasfoort, R. B. M. *Handbook of Surface Plasmon Resonance*; Royal Society of Chemistry, 2017.
(39) Tang, Y.; Zeng, X.; Liang, J. Surface Plasmon Resonance: An Introduction to a Surface Spectroscopy Technique. *J Chem Educ* **2010**, *87* (7), 742–746.
(40) Odom, T. W.; Schatz, G. C. Introduction to Plasmonics. *Chem Rev* **2011**, *111* (6), 3667–3668. https://doi.org/10.1021/cr2001349.

(41) Yu, R.; Liz-Marzán, L. M.; de Abajo, F. J. G. Universal Analytical Modeling of Plasmonic Nanoparticles. *Chem Soc Rev* **2017**, *46* (22), 6710–6724.
(42) Murray, W. A.; Barnes, W. L. Plasmonic Materials. *Advanced Materials* **2007**, *19* (22), 3771–3782. https://doi.org/https://doi.org/10.1002/adma.200700678.
(43) Khurgin, J. B. Replacing Noble Metals with Alternative Materials in Plasmonics and Metamaterials: How Good an Idea? *Philosophical Transactions of the Royal Society A: Mathematical, Physical and Engineering Sciences* **2017**, *375* (2090), 20160068. https://doi.org/10.1098/rsta.2016.0068.
(44) Shafiqa, A. R.; Abdul Aziz, A.; Mehrdel, B. Nanoparticle Optical Properties: Size Dependence of a Single Gold Spherical Nanoparticle. *J Phys Conf Ser* **2018**, *1083* (1), 012040. https://doi.org/10.1088/1742-6596/1083/1/012040.
(45) Xiang, H.; Zhang, X.; Neuhauser, D.; Lu, G. Size-Dependent Plasmonic Resonances from Large-Scale Quantum Simulations. *J Phys Chem Lett* **2014**, *5* (7), 1163–1169. https://doi.org/10.1021/jz500216t.
(46) Yang, C.-T.; Xu, Y.; Pourhassan-Moghaddam, M.; Tran, D. P.; Wu, L.; Zhou, X.; Thierry, B. Surface Plasmon Enhanced Light Scattering Biosensing: Size Dependence on the Gold Nanoparticle Tag. *Sensors* **2019**, *19* (2). https://doi.org/10.3390/s19020323.
(47) Ershov, A. E.; Gavrilyuk, A. P.; Karpov, S. V; Semina, P. N. Optodynamic Phenomena in Aggregates of Polydisperse Plasmonic Nanoparticles. *Applied Physics B* **2014**, *115* (4), 547–560. https://doi.org/10.1007/s00340-013-5636-6.
(48) Nehl, C. L.; Hafner, J. H. Shape-Dependent Plasmon Resonances of Gold Nanoparticles. *J Mater Chem* **2008**, *18* (21), 2415–2419. https://doi.org/10.1039/B714950F.
(49) González, A. L.; Noguez, C.; Beránek, J.; Barnard, A. S. Size, Shape, Stability, and Color of Plasmonic Silver Nanoparticles. *The Journal of Physical Chemistry C* **2014**, *118* (17), 9128–9136.
(50) Amirjani, A.; Koochak, N. N.; Haghshenas, D. F. Investigating the Shape and Size-Dependent Optical Properties of Silver Nanostructures Using UV–Vis Spectroscopy. *J Chem Educ* **2019**, *96* (11), 2584–2589.
(51) Link, S.; Wang, Z. L.; El-Sayed, M. A. Alloy Formation of Gold− Silver Nanoparticles and the Dependence of the Plasmon Absorption on Their Composition. *J Phys Chem B* **1999**, *103* (18), 3529–3533.
(52) Major, K. J.; De, C.; Obare, S. O. Recent Advances in the Synthesis of Plasmonic Bimetallic Nanoparticles. *Plasmonics* **2009**, *4*, 61–78.
(53) Grady, N. K.; Halas, N. J.; Nordlander, P. Influence of Dielectric Function Properties on the Optical Response of Plasmon Resonant Metallic Nanoparticles. *Chem Phys Lett* **2004**, *399* (1–3), 167–171.
(54) Miller, M. M.; Lazarides, A. A. Sensitivity of Metal Nanoparticle Surface Plasmon Resonance to the Dielectric Environment. *J Phys Chem B* **2005**, *109* (46), 21556–21565.
(55) Mock, J. J.; Smith, D. R.; Schultz, S. Local Refractive Index Dependence of Plasmon Resonance Spectra from Individual Nanoparticles. *Nano Lett* **2003**, *3* (4), 485–491.
(56) Su, K.-H.; Wei, Q.-H.; Zhang, X.; Mock, J. J.; Smith, D. R.; Schultz, S. Interparticle Coupling Effects on Plasmon Resonances of Nanogold Particles. *Nano Lett* **2003**, *3* (8), 1087–1090.
(57) Davis, T. J.; Vernon, K. C.; Gómez, D. E. Designing Plasmonic Systems Using Optical Coupling between Nanoparticles. *Phys Rev B* **2009**, *79* (15), 155423.
(58) Jain, P. K.; El-Sayed, M. A. Plasmonic Coupling in Noble Metal Nanostructures. *Chem Phys Lett* **2010**, *487* (4–6), 153–164.

(59) Wang, L.; Hasanzadeh Kafshgari, M.; Meunier, M. Optical Properties and Applications of Plasmonic-metal Nanoparticles. *Adv Funct Mater* **2020**, *30* (51), 2005400.
(60) Stockman, M. I.; Kneipp, K.; Bozhevolnyi, S. I.; Saha, S.; Dutta, A.; Ndukaife, J.; Kinsey, N.; Reddy, H.; Guler, U.; Shalaev, V. M.; Boltasseva, A.; Gholipour, B.; Krishnamoorthy, H. N. S.; MacDonald, K. F.; Soci, C.; Zheludev, N. I.; Savinov, V.; Singh, R. et al. Roadmap on Plasmonics. *Journal of Optics* **2018**, *20* (4), 043001. https://doi.org/10.1088/2040-8986/aaa114.
(61) Chang, W.-S.; Willingham, B.; Slaughter, L. S.; Dominguez-Medina, S.; Swanglap, P.; Link, S. Radiative and Nonradiative Properties of Single Plasmonic Nanoparticles and Their Assemblies. *Acc Chem Res* **2012**, *45* (11), 1936–1945.
(62) Ghobadi, T. G. U.; Ghobadi, A.; Ozbay, E.; Karadas, F. Strategies for Plasmonic Hot-Electron-Driven Photoelectrochemical Water Splitting. *ChemPhotoChem* **2018**, *2* (3), 161–182. https://doi.org/https://doi.org/10.1002/cptc.201700165.
(63) Borghei, Y.-S.; Hosseinkhani, S.; Ganjali, M. R. "Plasmonic Nanomaterials": An Emerging Avenue in Biomedical and Biomedical Engineering Opportunities. *J Adv Res* **2022**, *39*, 61–71. https://doi.org/https://doi.org/10.1016/j.jare.2021.11.006.
(64) Chen, X.; Zhou, P.; Yan, H.; Chen, M. Systematically Investigating Solar Absorption Performance of Plasmonic Nanoparticles. *Energy* **2021**, *216*, 119254.
(65) Daneshfar, N. The Study of Scattering-to-Absorption Ratio in Plasmonic Nanoparticles for Photovoltaic Cells and Sensor Applications. *Plasmonics* **2021**, *16* (6), 2017–2023.
(66) Piltan, S.; Sievenpiper, D. Field Enhancement in Plasmonic Nanostructures. *Journal of Optics* **2018**, *20* (5), 055401.
(67) Campion, A.; Kambhampati, P. Surface-Enhanced Raman Scattering. *Chem Soc Rev* **1998**, *27* (4), 241–250.
(68) Langer, J.; Jimenez de Aberasturi, D.; Aizpurua, J.; Alvarez-Puebla, R. A.; Auguié, B.; Baumberg, J. J.; Bazan, G. C.; Bell, S. E. J.; Boisen, A.; Brolo, A. G. Present and Future of Surface-Enhanced Raman Scattering. *ACS Nano* **2019**, *14* (1), 28–117.
(69) Lakowicz, J. R.; Geddes, C. D.; Gryczynski, I.; Malicka, J.; Gryczynski, Z.; Aslan, K.; Lukomska, J.; Matveeva, E.; Zhang, J.; Badugu, R. Advances in Surface-Enhanced Fluorescence. *J Fluoresc* **2004**, *14*, 425–441.
(70) Fort, E.; Grésillon, S. Surface Enhanced Fluorescence. *J Phys D Appl Phys* **2007**, *41* (1), 013001.
(71) Le Ru, E. C.; Blackie, E.; Meyer, M.; Etchegoin, P. G. Surface Enhanced Raman Scattering Enhancement Factors: A Comprehensive Study. *The Journal of Physical Chemistry C* **2007**, *111* (37), 13794–13803. https://doi.org/10.1021/jp0687908.
(72) Taylor, A. B.; Zijlstra, P. Single-Molecule Plasmon Sensing: Current Status and Future Prospects. *ACS Sens* **2017**, *2* (8), 1103–1122.
(73) Spitzberg, J. D.; Zrehen, A.; van Kooten, X. F.; Meller, A. Plasmonic-nanopore Biosensors for Superior Single-molecule Detection. *Advanced materials* **2019**, *31* (23), 1900422.
(74) Ma, J.; Wang, X.; Feng, J.; Huang, C.; Fan, Z. Individual Plasmonic Nanoprobes for Biosensing and Bioimaging: Recent Advances and Perspectives. *Small* **2021**, *17* (8), 2004287.
(75) Ou, X.; Liu, Y.; Zhang, M.; Hua, L.; Zhan, S. Plasmonic Gold Nanostructures for Biosensing and Bioimaging. *Microchimica Acta* **2021**, *188* (9), 304.
(76) Reguera, J.; de Aberasturi, D. J.; Henriksen-Lacey, M.; Langer, J.; Espinosa, A.; Szczupak, B.; Wilhelm, C.; Liz-Marzán, L. M. Janus Plasmonic–Magnetic Gold–Iron Oxide Nanoparticles as Contrast Agents for Multimodal Imaging. *Nanoscale* **2017**, *9* (27), 9467–9480.

(77) Bindra, A. K.; Sreejith, S.; Prasad, R.; Gorain, M.; Thomas, R.; Jana, D.; Nai, M. H.; Wang, D.; Tharayil, A.; Kundu, G. C. A Plasmonic Supramolecular Nanohybrid as a Contrast Agent for Site-selective Computed Tomography Imaging of Tumor. *Adv Funct Mater* **2022**, *32* (12), 2110575.
(78) Jacak, W.; Krasnyj, J.; Jacak, J.; Donderowicz, W.; Jacak, L. Mechanism of Plasmon-Mediated Enhancement of Photovoltaic Efficiency. *J Phys D Appl Phys* **2011**, *44* (5), 055301.
(79) Gan, Q.; Bartoli, F. J.; Kafafi, Z. H. Plasmonic-enhanced Organic Photovoltaics: Breaking the 10% Efficiency Barrier. *Advanced materials* **2013**, *25* (17), 2385–2396.
(80) Zhou, N.; López-Puente, V.; Wang, Q.; Polavarapu, L.; Pastoriza-Santos, I.; Xu, Q.-H. Plasmon-Enhanced Light Harvesting: Applications in Enhanced Photocatalysis, Photodynamic Therapy and Photovoltaics. *RSC Adv* **2015**, *5* (37), 29076–29097.
(81) Zhang, Z.; Zhang, C.; Zheng, H.; Xu, H. Plasmon-Driven Catalysis on Molecules and Nanomaterials. *Acc Chem Res* **2019**, *52* (9), 2506–2515.
(82) Indhu, A. R.; Keerthana, L.; Dharmalingam, G. Plasmonic Nanotechnology for Photothermal Applications–an Evaluation. *Beilstein Journal of Nanotechnology* **2023**, *14* (1), 380–419.
(83) Kowalska, E. Plasmonic Photocatalysts. *Catalysts*. MDPI 2021, p 410.
(84) Gellé, A.; Moores, A. Plasmonic Nanoparticles: Photocatalysts with a Bright Future. *Curr Opin Green Sustain Chem* **2019**, *15*, 60–66. https://doi.org/https://doi.org/10.1016/j.cogsc.2018.10.002.
(85) Nazir, A.; Huo, P.; Wang, H.; Weiqiang, Z.; Wan, Y. A Review on Plasmonic-Based Heterojunction Photocatalysts for Degradation of Organic Pollutants in Wastewater. *J Mater Sci* **2023**, *58* (15), 6474–6515. https://doi.org/10.1007/s10853-023-08391-w.
(86) Wang, F.; Lu, Z.; Guo, H.; Zhang, G.; Li, Y.; Hu, Y.; Jiang, W.; Liu, G. Plasmonic Photocatalysis for CO2 Reduction: Advances, Understanding and Possibilities. *Chemistry – A European Journal* **2023**, *29* (25), e202202716. https://doi.org/https://doi.org/10.1002/chem.202202716.
(87) Valenti, M.; Jonsson, M. P.; Biskos, G.; Schmidt-Ott, A.; Smith, W. A. Plasmonic Nanoparticle-Semiconductor Composites for Efficient Solar Water Splitting. *J Mater Chem A Mater* **2016**, *4* (46), 17891–17912. https://doi.org/10.1039/C6TA06405A.
(88) Wu, K.; Chen, J.; McBride, J. R.; Lian, T. Efficient Hot-Electron Transfer by a Plasmon-Induced Interfacial Charge-Transfer Transition. *Science (1979)* **2015**, *349* (6248), 632–635. https://doi.org/10.1126/science.aac5443.
(89) Kale, M. J.; Avanesian, T.; Christopher, P. Direct Photocatalysis by Plasmonic Nanostructures. *ACS Catal* **2014**, *4* (1), 116–128. https://doi.org/10.1021/cs400993w.
(90) An, X.; Erramilli, S.; Reinhard, B. M. Plasmonic Nano-Antimicrobials: Properties, Mechanisms and Applications in Microbe Inactivation and Sensing. *Nanoscale* **2021**, *13* (6), 3374–3411. https://doi.org/10.1039/D0NR08353D.
(91) Hassan Afandy, H.; Sabir, D. K.; Aziz, S. B. Antibacterial Activity of the Green Synthesized Plasmonic Silver Nanoparticles with Crystalline Structure against Gram-Positive and Gram-Negative Bacteria. *Nanomaterials* **2023**, *13* (8). https://doi.org/10.3390/nano13081327.
(92) Kim, M.; Lee, J.-H.; Nam, J.-M. Plasmonic Photothermal Nanoparticles for Biomedical Applications. *Advanced Science* **2019**, *6* (17), 1900471. https://doi.org/https://doi.org/10.1002/advs.201900471.
(93) Brown, A. M.; Sundararaman, R.; Narang, P.; Goddard, W. A.; Atwater, H. A. Ab Initio Phonon Coupling and Optical Response of Hot Electrons in Plasmonic Metals. *Phys Rev B* **2016**, *94* (7), 75120. https://doi.org/10.1103/PhysRevB.94.075120.

(94) Hwang, E. H.; Sensarma, R.; Das Sarma, S. Plasmon-Phonon Coupling in Graphene. *Phys Rev B* **2010**, *82* (19), 195406. https://doi.org/10.1103/PhysRevB.82.195406.
(95) Huang, X.; Jain, P. K.; El-Sayed, I. H.; El-Sayed, M. A. Plasmonic Photothermal Therapy (PPTT) Using Gold Nanoparticles. *Lasers Med Sci* **2008**, *23* (3), 217–228. https://doi.org/10.1007/s10103-007-0470-x.
(96) Kannadorai, R. K.; Chiew, G. G. Y.; Luo, K. Q.; Liu, Q. Dual Functions of Gold Nanorods as Photothermal Agent and Autofluorescence Enhancer to Track Cell Death during Plasmonic Photothermal Therapy. *Cancer Lett* **2015**, *357* (1), 152–159. https://doi.org/https://doi.org/10.1016/j.canlet.2014.11.022.
(97) Zhang, Y.; Zhan, X.; Xiong, J.; Peng, S.; Huang, W.; Joshi, R.; Cai, Y.; Liu, Y.; Li, R.; Yuan, K.; Zhou, N.; Min, W. Temperature-Dependent Cell Death Patterns Induced by Functionalized Gold Nanoparticle Photothermal Therapy in Melanoma Cells. *Sci Rep* **2018**, *8* (1), 8720. https://doi.org/10.1038/s41598-018-26978-1.
(98) Luo, S.; Ren, X.; Lin, H.; Song, H.; Ye, J. Plasmonic Photothermal Catalysis for Solar-to-Fuel Conversion: Current Status and Prospects. *Chem Sci* **2021**, *12* (16), 5701–5719. https://doi.org/10.1039/D1SC00064K.
(99) Mateo, D.; Cerrillo, J. L.; Durini, S.; Gascon, J. Fundamentals and Applications of Photo-Thermal Catalysis. *Chem Soc Rev* **2021**, *50* (3), 2173–2210. https://doi.org/10.1039/D0CS00357C.
(100) Park, E.; Selvaraj, R.; Kim, Y. High-Efficiency Photothermal Sterilization on PDMS Film with Au@CuS Yolk-Shell Nanoparticles. *Journal of Industrial and Engineering Chemistry* **2022**, *113*, 522–529. https://doi.org/https://doi.org/10.1016/j.jiec.2022.06.029.
(101) Tao, F.; Zheng, J.; Wang, L.; Yuan, Y.; Wan, F.; Xu, W.; Huang, Z.; Wang, S.; Huang, Y. Plasmonic Photothermal Film for Defogging and Anti-Icing/Deicing on PTFE. *J Alloys Compd* **2021**, *866*, 158827. https://doi.org/https://doi.org/10.1016/j.jallcom.2021.158827.
(102) Selvam, A.; Jain, G.; Chaudhuri, R. G.; Mandal, M. K.; Chakrabarti, S. Avant-Garde Solar–Thermal Nanostructures: Nascent Strategy into Effective Photothermal Desalination. *Solar RRL* **2022**, *6* (8), 2200321. https://doi.org/https://doi.org/10.1002/solr.202200321.
(103) Kummu, M.; Guillaume, J. H. A.; de Moel, H.; Eisner, S.; Flörke, M.; Porkka, M.; Siebert, S.; Veldkamp, T. I. E.; Ward, P. J. The World's Road to Water Scarcity: Shortage and Stress in the 20th Century and Pathways towards Sustainability. *Sci Rep* **2016**, *6* (1), 38495. https://doi.org/10.1038/srep38495.
(104) Boretti, A.; Rosa, L. Reassessing the Projections of the World Water Development Report. *NPJ Clean Water* **2019**, *2* (1), 15. https://doi.org/10.1038/s41545-019-0039-9.
(105) Veldkamp, T. I. E.; Wada, Y.; Aerts, J. C. J. H.; Döll, P.; Gosling, S. N.; Liu, J.; Masaki, Y.; Oki, T.; Ostberg, S.; Pokhrel, Y.; Satoh, Y.; Kim, H.; Ward, P. J. Water Scarcity Hotspots Travel Downstream Due to Human Interventions in the 20th and 21st Century. *Nat Commun* **2017**, *8* (1), 15697. https://doi.org/10.1038/ncomms15697.
(106) Fielding, K. S.; Gardner, J.; Leviston, Z.; Price, J. Comparing Public Perceptions of Alternative Water Sources for Potable Use: The Case of Rainwater, Stormwater, Desalinated Water, and Recycled Water. *Water Resources Management* **2015**, *29* (12), 4501–4518. https://doi.org/10.1007/s11269-015-1072-1.
(107) Hurlimann, A.; Dolnicar, S. Public Acceptance and Perceptions of Alternative Water Sources: A Comparative Study in Nine Locations. *Int J Water Resour Dev* **2016**, *32* (4), 650–673. https://doi.org/10.1080/07900627.2016.1143350.

(108) Hinkebein, T. Desalination: Limitations and Challenges. In *Water and sustainable development: Opportunities for the chemical sciences: A workshop report to the chemical sciences roundtable*; National Academies Press, 2004; pp 29–39.
(109) Abimbola, T. O.; Yusof, K. W.; Takaijudin, H.; Abdurrasheed, A. S.; Al-Qadami, E. H. H.; Ishola, S. A.; Owoseni, T. A.; Akilu, S. A Concise Review of Major Desalination Techniques: Features and Limitations. In *ICCOEE2020: Proceedings of the 6th International Conference on Civil, Offshore and Environmental Engineering (ICCOEE2020)*; Springer, 2021; pp 154–162.
(110) Sharon, H.; Reddy, K. S. A Review of Solar Energy Driven Desalination Technologies. *Renewable and Sustainable Energy Reviews* **2015**, *41*, 1080–1118.
(111) Thakkar, H.; Sankhala, A.; Ramana, P. V; Panchal, H. A Detailed Review on Solar Desalination Techniques. *International journal of ambient energy* **2020**, *41* (9), 1066–1087.
(112) Ali, M. T.; Fath, H. E. S.; Armstrong, P. R. A Comprehensive Techno-Economical Review of Indirect Solar Desalination. *Renewable and Sustainable Energy Reviews* **2011**, *15* (8), 4187–4199.
(113) Chauhan, V. K.; Shukla, S. K.; Tirkey, J. V.; Rathore, P. K. S. A Comprehensive Review of Direct Solar Desalination Techniques and Its Advancements. *J Clean Prod* **2021**, *284*, 124719.
(114) Angelakis, A. N.; Valipour, M.; Choo, K.-H.; Ahmed, A. T.; Baba, A.; Kumar, R.; Toor, G. S.; Wang, Z. Desalination: From Ancient to Present and Future. *Water (Basel)* **2021**, *13* (16), 2222.
(115) Likhachev, D. S.; Li, F.-C. Large-Scale Water Desalination Methods: A Review and New Perspectives. *Desalination Water Treat* **2013**, *51* (13–15), 2836–2849.
(116) Essa, F. A. Thermal Desalination Systems: From Traditionality to Modernity and Development. *Distillation Processes-From Conventional to Reactive Distillation Modeling, Simulation and Optimization. London: IntechOpen* **2022**, 23.
(117) Semiat, R. Energy Issues in Desalination Processes. *Environ Sci Technol* **2008**, *42* (22), 8193–8201.
(118) Saidur, R.; Elcevvadi, E. T.; Mekhilef, S.; Safari, A.; Mohammed, H. A. An Overview of Different Distillation Methods for Small Scale Applications. *Renewable and sustainable energy reviews* **2011**, *15* (9), 4756–4764.
(119) Gugulothu, R.; Somanchi, N. S.; Reddy, K. V. K.; Gantha, D. A Review on Solar Water Distillation Using Sensible and Latent Heat. *Procedia Earth and Planetary Science* **2015**, *11*, 354–360.
(120) Prabu, D.; Giriprasath, A.; Viknesh, S. Design and Development of a Prototype Thermal Power Plant for Recycling of Sea Water by Distillation Process. In *IOP Conference Series: Earth and Environmental Science*; IOP Publishing, 2020; Vol. 573, p 012014.
(121) Kronenberg, G.; Lokiec, F. Low-Temperature Distillation Processes in Single-and Dual-Purpose Plants. *Desalination* **2001**, *136* (1–3), 189–197.
(122) El-Dessouky, H. T.; Ettouney, H. M.; Al-Roumi, Y. Multi-Stage Flash Desalination: Present and Future Outlook. *Chemical Engineering Journal* **1999**, *73* (2), 173–190.
(123) Tareemi, A. A.; Sharshir, S. W. A State-of-Art Overview of Multi-Stage Flash Desalination and Water Treatment: Principles, Challenges, and Heat Recovery in Hybrid Systems. *Solar Energy* **2023**, *266*, 112157.
(124) El-Dessouky, H.; Shaban, H. I.; Al-Ramadan, H. Steady-State Analysis of Multi-Stage Flash Desalination Process. *Desalination* **1995**, *103* (3), 271–287.

(125) Nannarone, A.; Toro, C.; Sciubba, E. Multi-Stage Flash Desalination Process: Modeling and Simulation. In *Proceedings of the 30th International Conference on Efficiency, Cost, Optimization, Simulation and Environmental Impact Of Energy Systems, San Diego, CA, USA*; 2017; pp 2–6.
(126) Shakib, S. E.; Amidpour, M.; Aghanajafi, C. Simulation and Optimization of Multi Effect Desalination Coupled to a Gas Turbine Plant with HRSG Consideration. *Desalination* **2012**, *285*, 366–376.
(127) El-Dessouky, H. T.; Ettouney, H. M.; Al-Juwayhel, F. Multiple Effect Evaporation—Vapour Compression Desalination Processes. *Chemical Engineering Research and Design* **2000**, *78* (4), 662–676.
(128) El-Dessouky, H. T.; Ettouney, H. M. Multiple-Effect Evaporation Desalination Systems. Thermal Analysis. *Desalination* **1999**, *125* (1–3), 259–276.
(129) Zhao, D.; Xue, J.; Li, S.; Sun, H.; Zhang, Q. Theoretical Analyses of Thermal and Economical Aspects of Multi-Effect Distillation Desalination Dealing with High-Salinity Wastewater. *Desalination* **2011**, *273* (2), 292–298. https://doi.org/https://doi.org/10.1016/j.desal.2011.01.048.
(130) Aly, N. H.; El-Figi, A. K. Mechanical Vapor Compression Desalination Systems—a Case Study. *Desalination* **2003**, *158* (1–3), 143–150.
(131) Bahar, R.; Hawlader, M. N. A.; Woei, L. S. Performance Evaluation of a Mechanical Vapor Compression Desalination System. *Desalination* **2004**, *166*, 123–127.
(132) Jamil, M. A.; Zubair, S. M. On Thermoeconomic Analysis of a Single-Effect Mechanical Vapor Compression Desalination System. *Desalination* **2017**, *420*, 292–307.
(133) Sharaf, M. A.; Nafey, A. S.; García-Rodríguez, L. Thermo-Economic Analysis of Solar Thermal Power Cycles Assisted MED-VC (Multi Effect Distillation-Vapor Compression) Desalination Processes. *Energy* **2011**, *36* (5), 2753–2764. https://doi.org/https://doi.org/10.1016/j.energy.2011.02.015.
(134) Olabi, A. G.; Elsaid, K.; Rabaia, M. K. H.; Askalany, A. A.; Abdelkareem, M. A. Waste Heat-Driven Desalination Systems: Perspective. *Energy* **2020**, *209*, 118373.
(135) Elsaid, K.; Sayed, E. T.; Yousef, B. A. A.; Rabaia, M. K. H.; Abdelkareem, M. A.; Olabi, and A. G. Recent Progress on the Utilization of Waste Heat for Desalination: A Review. *Energy Convers Manag* **2020**, *221*, 113105.
(137) Ghaffour, N.; Bundschuh, J.; Mahmoudi, H.; Goosen, M. F. A. Renewable Energy-Driven Desalination Technologies: A Comprehensive Review on Challenges and Potential Applications of Integrated Systems. *Desalination* **2015**, *356*, 94–114.
(138) Jones, E.; Qadir, M.; van Vliet, M. T. H.; Smakhtin, V.; Kang, S. The State of Desalination and Brine Production: A Global Outlook. *Science of the Total Environment* **2019**, *657*, 1343–1356.
(139) Panagopoulos, A.; Haralambous, K.-J. Environmental Impacts of Desalination and Brine Treatment-Challenges and Mitigation Measures. *Mar Pollut Bull* **2020**, *161*, 111773.
(140) Abushawish, A.; Bouaziz, I.; Almanassra, I. W.; AL-Rajabi, M. M.; Jaber, L.; Khalil, A. K. A.; Takriff, M. S.; Laoui, T.; Shanableh, A.; Atieh, M. A. Desalination Pretreatment Technologies: Current Status and Future Developments. *Water (Basel)* **2023**, *15* (8), 1572.
(141) Elimelech, M.; Phillip, W. A. The Future of Seawater Desalination: Energy, Technology, and the Environment. *Science (1979)* **2011**, *333* (6043), 712–717. https://doi.org/10.1126/science.1200488.

(142) Khawaji, A. D.; Kutubkhanah, I. K.; Wie, J.-M. Advances in Seawater Desalination Technologies. *Desalination* **2008**, *221* (1), 47–69. https://doi.org/https://doi.org/10.1016/j.desal.2007.01.067.
(143) Greenlee, L. F.; Lawler, D. F.; Freeman, B. D.; Marrot, B.; Moulin, P. Reverse Osmosis Desalination: Water Sources, Technology, and Today's Challenges. *Water Res* **2009**, *43* (9), 2317–2348. https://doi.org/https://doi.org/10.1016/j.watres.2009.03.010.
(144) Peñate, B.; García-Rodríguez, L. Current Trends and Future Prospects in the Design of Seawater Reverse Osmosis Desalination Technology. *Desalination* **2012**, *284*, 1–8. https://doi.org/https://doi.org/10.1016/j.desal.2011.09.010.
(145) Qasim, M.; Badrelzaman, M.; Darwish, N. N.; Darwish, N. A.; Hilal, N. Reverse Osmosis Desalination: A State-of-the-Art Review. *Desalination* **2019**, *459*, 59–104. https://doi.org/https://doi.org/10.1016/j.desal.2019.02.008.
(146) Caldera, U.; Breyer, C. Learning Curve for Seawater Reverse Osmosis Desalination Plants: Capital Cost Trend of the Past, Present, and Future. *Water Resour Res* **2017**, *53* (12), 10523–10538.
(147) AlSawaftah, N.; Abuwatfa, W.; Darwish, N.; Husseini, G. A Comprehensive Review on Membrane Fouling: Mathematical Modelling, Prediction, Diagnosis, and Mitigation. *Water (Basel)* **2021**, *13* (9). https://doi.org/10.3390/w13091327.
(148) Bartholomew, T. V; Mey, L.; Arena, J. T.; Siefert, N. S.; Mauter, M. S. Osmotically Assisted Reverse Osmosis for High Salinity Brine Treatment. *Desalination* **2017**, *421*, 3–11.
(149) Lee, S.; Choi, J.; Park, Y.-G.; Shon, H.; Ahn, C. H.; Kim, S.-H. Hybrid Desalination Processes for Beneficial Use of Reverse Osmosis Brine: Current Status and Future Prospects. *Desalination* **2019**, *454*, 104–111.
(150) Hailemariam, R. H.; Woo, Y. C.; Damtie, M. M.; Kim, B. C.; Park, K.-D.; Choi, J.-S. Reverse Osmosis Membrane Fabrication and Modification Technologies and Future Trends: A Review. *Adv Colloid Interface Sci* **2020**, *276*, 102100.
(151) Liu, C.; Wang, W.; Yang, B.; Xiao, K.; Zhao, H. Separation, Anti-Fouling, and Chlorine Resistance of the Polyamide Reverse Osmosis Membrane: From Mechanisms to Mitigation Strategies. *Water Res* **2021**, *195*, 116976.
(152) Guo, Y.; Liu, C.; Liu, H.; Zhang, J.; Li, H.; Zhang, C. Contemporary Antibiofouling Modifications of Reverse Osmosis Membranes: State-of-the-Art Insights on Mechanisms and Strategies. *Chemical Engineering Journal* **2022**, *429*, 132400.
(153) Wang, J.; Liu, X. Forward Osmosis Technology for Water Treatment: Recent Advances and Future Perspectives. *J Clean Prod* **2021**, *280*, 124354.
(154) Suwaileh, W.; Pathak, N.; Shon, H.; Hilal, N. Forward Osmosis Membranes and Processes: A Comprehensive Review of Research Trends and Future Outlook. *Desalination* **2020**, *485*, 114455.
(155) Blandin, G.; Ferrari, F.; Lesage, G.; Le-Clech, P.; Héran, M.; Martinez-Lladó, X. Forward Osmosis as Concentration Process: Review of Opportunities and Challenges. *Membranes (Basel)* **2020**, *10* (10), 284.
(156) Mohammadifakhr, M.; de Grooth, J.; Roesink, H. D. W.; Kemperman, A. J. B. Forward Osmosis: A Critical Review. *Processes* **2020**, *8* (4), 404.
(157) Ndiaye, I.; Vaudreuil, S.; Bounahmidi, T. Forward Osmosis Process: State-of-the-Art of Membranes. *Separation & Purification Reviews* **2021**, *50* (1), 53–73.
(158) Hafiz, M.; Hassanein, A.; Talhami, M.; Maryam, A.-E.; Hassan, M. K.; Hawari, A. H. Magnetic Nanoparticles Draw Solution for Forward Osmosis: Current Status and Future Challenges in Wastewater Treatment. *J Environ Chem Eng* **2022**, *10* (6), 108955.

(159) Wu, X.; Lau, C. H.; Pramanik, B. K.; Zhang, J.; Xie, Z. State-of-the-Art and Opportunities for Forward Osmosis in Sewage Concentration and Wastewater Treatment. *Membranes (Basel)* **2021**, *11* (5), 305.
(160) Al-Amshawee, S.; Yunus, M. Y. B. M.; Azoddein, A. A. M.; Hassell, D. G.; Dakhil, I. H.; Hasan, H. A. Electrodialysis Desalination for Water and Wastewater: A Review. *Chemical Engineering Journal* **2020**, *380*, 122231.
(161) Sedighi, M.; Usefi, M. M. B.; Ismail, A. F.; Ghasemi, M. Environmental Sustainability and Ions Removal through Electrodialysis Desalination: Operating Conditions and Process Parameters. *Desalination* **2023**, *549*, 116319.
(162) Tristán, C.; Fallanza, M.; Ibáñez, R.; Ortiz, I. Reverse Electrodialysis: Potential Reduction in Energy and Emissions of Desalination. *Applied Sciences* **2020**, *10* (20), 7317.
(164) He, L.; Rosa, L. Solutions to Agricultural Green Water Scarcity under Climate Change. *PNAS Nexus* **2023**, *2* (4), pgad117. https://doi.org/10.1093/pnasnexus/pgad117.
(165) Pourkiaei, S. M.; Ahmadi, M. H.; Ghazvini, M.; Moosavi, S.; Pourfayaz, F.; Kumar, R.; Chen, L. Status of Direct and Indirect Solar Desalination Methods: Comprehensive Review. *The European Physical Journal Plus* **2021**, *136* (5), 602.
(166) Tarazona-Romero, B. E.; Campos-Celador, A.; Maldonado-Muñoz, Y. A. Can Solar Desalination Be Small and Beautiful? A Critical Review of Existing Technology under the Appropriate Technology Paradigm. *Energy Res Soc Sci* **2022**, *88*, 102510.
(167) Chauhan, V. K.; Shukla, S. K.; Tirkey, J. V.; Rathore, P. K. S. A Comprehensive Review of Direct Solar Desalination Techniques and Its Advancements. *J Clean Prod* **2021**, *284*, 124719.
(168) Yang, D.; Yang, Y.; Xia, J. Hydrological Cycle and Water Resources in a Changing World: A Review. *Geography and Sustainability* **2021**, *2* (2), 115–122.
(169) Fuzil, N. S.; Othman, N. H.; Alias, N. H.; Marpani, F.; Othman, M. H. D.; Ismail, A. F.; Lau, W. J.; Li, K.; Kusworo, T. D.; Ichinose, I. A Review on Photothermal Material and Its Usage in the Development of Photothermal Membrane for Sustainable Clean Water Production. *Desalination* **2021**, *517*, 115259.
(170) Delgado, W. R.; Beach, T.; Luzzadder-Beach, S. Solar Desalination: Cases, Synthesis, and Challenges. *Wiley Interdisciplinary Reviews: Water* **2020**, *7* (3), e1434.
(171) Zheng, Y.; Gonzalez, R. A. C.; Hatzell, K. B.; Hatzell, M. C. Large-Scale Solar-Thermal Desalination. *Joule* **2021**, *5* (8), 1971–1986.
(172) Li, Y.; Shi, Y.; Wang, H.; Liu, T.; Zheng, X.; Gao, S.; Lu, J. Recent Advances in Carbon-based Materials for Solar-driven Interfacial Photothermal Conversion Water Evaporation: Assemblies, Structures, Applications, and Prospective. *Carbon Energy* **2023**, *5* (11), e331.
(173) Xiao, L.; Chen, X.; Yang, X.; Sun, J.; Geng, J. Recent Advances in Polymer-Based Photothermal Materials for Biological Applications. *ACS Appl Polym Mater* **2020**, *2* (10), 4273–4288.
(174) Tan, K. W.; Yap, C. M.; Zheng, Z.; Haw, C. Y.; Khiew, P. S.; Chiu, W. S. State-of-the-Art Advances, Development, and Challenges of Metal Oxide Semiconductor Nanomaterials for Photothermal Solar Steam Generation. *Adv Sustain Syst* **2022**, *6* (4), 2100416.
(175) Chen, J.; Ye, Z.; Yang, F.; Yin, Y. Plasmonic Nanostructures for Photothermal Conversion. *Small Science* **2021**, *1* (2), 2000055.
(176) Luo, S.; Ren, X.; Lin, H.; Song, H.; Ye, J. Plasmonic Photothermal Catalysis for Solar-to-Fuel Conversion: Current Status and Prospects. *Chem Sci* **2021**, *12* (16), 5701–5719.

(177) Cui, X.; Ruan, Q.; Zhuo, X.; Xia, X.; Hu, J.; Fu, R.; Li, Y.; Wang, J.; Xu, H. Photothermal Nanomaterials: A Powerful Light-to-Heat Converter. *Chem Rev* **2023**, *123* (11), 6891–6952.
(178) Baffou, G.; Cichos, F.; Quidant, R. Applications and Challenges of Thermoplasmonics. *Nat Mater* **2020**, *19* (9), 946–958.
(179) Kim, J.; Hwang, J.; Kim, S.; Cho, S. H.; Choi, H.; Kim, H.-Y.; Lee, Y. S. Interfacial Solar Evaporator - Physical Principles and Fabrication Methods. *International Journal of Precision Engineering and Manufacturing-Green Technology* **2021**, *8* (4), 1347–1367. https://doi.org/10.1007/s40684-021-00337-4.
(180) Min, X.; Zhu, B.; Li, B.; Li, J.; Zhu, J. Interfacial Solar Vapor Generation: Materials and Structural Design. *Acc Mater Res* **2021**, *2* (4), 198–209.
(181) Shi, L.; Wang, X.; Hu, Y.; He, Y.; Yan, Y. Solar-Thermal Conversion and Steam Generation: A Review. *Appl Therm Eng* **2020**, *179*, 115691.
(182) Younis, O.; Hussein, A. K.; Attia, M. E. H.; Aljibori, H. S. S.; Kolsi, L.; Togun, H.; Ali, B.; Abderrahmane, A.; Subkrajang, K.; Jirawattanapanit, A. Comprehensive Review on Solar Stills—Latest Developments and Overview. *Sustainability* **2022**, *14* (16). https://doi.org/10.3390/su141610136.
(183) Iqbal, A.; Mahmoud, M. S.; Sayed, E. T.; Elsaid, K.; Abdelkareem, M. A.; Alawadhi, H.; Olabi, A. G. Evaluation of the Nanofluid-Assisted Desalination through Solar Stills in the Last Decade. *J Environ Manage* **2021**, *277*, 111415.
(184) Sun, Z.; Zhang, L.; Liu, L.; Chen, W.; Xie, G.; Zha, J.; Wei, X. Optimal Design for Floating Solar Still by Structural Modification: A Review. *Desalination* **2023**, *566*, 116937.
(185) Guan, W.; Guo, Y.; Yu, G. Carbon Materials for Solar Water Evaporation and Desalination. *Small* **2021**, *17* (48), 2007176.
(186) Arunkumar, T.; Lim, H. W.; Denkenberger, D.; Lee, S. J. A Review on Carbonized Natural Green Flora for Solar Desalination. *Renewable and Sustainable Energy Reviews* **2022**, *158*, 112121.
(187) Bian, Y.; Du, Q.; Tang, K.; Shen, Y.; Hao, L.; Zhou, D.; Wang, X.; Xu, Z.; Zhang, H.; Zhao, L.; Zhu, S.; Ye, J.; Lu, H.; Yang, Y.; Zhang, R.; Zheng, Y.; Gu, S. Carbonized Bamboos as Excellent 3D Solar Vapor-Generation Devices. *Adv Mater Technol* **2019**, *4* (4), 1800593. https://doi.org/https://doi.org/10.1002/admt.201800593.
(188) Li, G.; Law, W.-C.; Chan, K. C. Floating, Highly Efficient, and Scalable Graphene Membranes for Seawater Desalination Using Solar Energy. *Green Chemistry* **2018**, *20* (16), 3689–3695. https://doi.org/10.1039/C8GC01347K.
(189) Traver, E.; Karaballi, R. A.; Monfared, Y. E.; Daurie, H.; Gagnon, G. A.; Dasog, M. TiN, ZrN, and HfN Nanoparticles on Nanoporous Aluminum Oxide Membranes for Solar-Driven Water Evaporation and Desalination. *ACS Appl Nano Mater* **2020**, *3* (3), 2787–2794. https://doi.org/10.1021/acsanm.0c00107.
(190) Yu, S.; Gu, Y.; Chao, X.; Huang, G.; Shou, D. Recent Advances in Interfacial Solar Vapor Generation: Clean Water Production and Beyond. *J Mater Chem A Mater* **2023**, *11* (12), 5978–6015.
(191) He, F.; You, H.; Liu, X.; Shen, X.; Zhang, J.; Wang, Z. Interfacial-Heating Solar Desalination of High-Salinity Brine: Recent Progress on Salt Management and Water Production. *Chemical Engineering Journal* **2023**, 144332.
(192) Kim, S.; Tahir, Z.; Rashid, M. U.; Jang, J. I.; Kim, Y. S. Highly Efficient Solar Vapor Generation via a Simple Morphological Alteration of TiO2 Films Grown on a Glassy Carbon Foam. *ACS Appl Mater Interfaces* **2021**, *13* (43), 50911–50919.

(193) Khajevand, M.; Azizian, S.; Jaleh, B. A Bio-Based 3D Evaporator Nanocomposite for Highly Efficient Solar Desalination. *Sep Purif Technol* **2022**, *284*, 120278.
(194) Chang, C.; Liu, M.; Li, L.; Chen, G.; Pei, L.; Wang, Z.; Ji, Y. Salt-Rejecting RGO-Coated Melamine Foams for High-Efficiency Solar Desalination. *J Mater Res* **2022**, *37* (1), 294–303. https://doi.org/10.1557/s43578-021-00328-w.
(195) Li, X.; Ni, G.; Cooper, T.; Xu, N.; Li, J.; Zhou, L.; Hu, X.; Zhu, B.; Yao, P.; Zhu, J. Measuring Conversion Efficiency of Solar Vapor Generation. *Joule* **2019**, *3* (8), 1798–1803. https://doi.org/https://doi.org/10.1016/j.joule.2019.06.009.
(196) Nawaz, F.; Yang, Y.; Zhao, Q.; Mo, Y.; Jiang, Z.; Wu, J.; Liu, Y.; Liu, B.; Gao, B.; Que, W. Can the Interfacial Solar Vapor Generation Performance Be Really "Beyond" Theoretical Limit? *Adv Energy Mater* **2024**, 2400135.
(197) Wang, Z.; Horseman, T.; Straub, A. P.; Yip, N. Y.; Li, D.; Elimelech, M.; Lin, S. Pathways and Challenges for Efficient Solar-Thermal Desalination. *Sci Adv* **2019**, *5* (7), eaax0763.
(198) Sales, M. Solar Powered Desalination System Using Fresnel Lens. In *IOP Conference Series: Materials Science and Engineering*; IOP Publishing, 2016; Vol. 162, p 012002.
(199) Wu, G.; Zheng, H.; Ma, X.; Kutlu, C.; Su, Y. Experimental Investigation of a Multi-Stage Humidification-Dehumidification Desalination System Heated Directly by a Cylindrical Fresnel Lens Solar Concentrator. *Energy Convers Manag* **2017**, *143*, 241–251.
(200) Chittalakkotte, V.; Vincent, V. L.; Valiyaparambil, P. Development of a Solar Energy Based Desalination System Using a Hyperboloid Concentrator. *Mater Today Proc* **2021**, *46*, 9771–9775.
(201) Jelley, N.; Smith, T. Concentrated Solar Power: Recent Developments and Future Challenges. *Proceedings of the Institution of Mechanical Engineers, Part A: Journal of Power and Energy* **2015**, *229* (7), 693–713.
(202) Wiesenfarth, M.; Anton, I.; Bett, A. W. Challenges in the Design of Concentrator Photovoltaic (CPV) Modules to Achieve Highest Efficiencies. *Appl Phys Rev* **2018**, *5* (4).
(203) Masood, F.; Nor, N. B. M.; Elamvazuthi, I.; Saidur, R.; Alam, M. A.; Akhter, J.; Yusuf, M.; Ali, S. M.; Sattar, M.; Baba, M. The Compound Parabolic Concentrators for Solar Photovoltaic Applications: Opportunities and Challenges. *Energy Reports* **2022**, *8*, 13558–13584.
(204) Wu, L.; Dong, Z.; Cai, Z.; Ganapathy, T.; Fang, N. X.; Li, C.; Yu, C.; Zhang, Y.; Song, Y. Highly Efficient Three-Dimensional Solar Evaporator for High Salinity Desalination by Localized Crystallization. *Nat Commun* **2020**, *11* (1), 521.
(205) Koh, J. J.; Lim, G. J. H.; Chakraborty, S.; Zhang, Y.; Liu, S.; Zhang, X.; Tan, S. C.; Lyu, Z.; Ding, J.; He, C. Robust, 3D-Printed Hydratable Plastics for Effective Solar Desalination. *Nano Energy* **2021**, *79*, 105436.
(206) Song, C.; Chen, X.; Hao, R.; Cai, D.; Zhu, X.; Liu, H.; Chen, J.; Liu, W. A Cocoon-Based 3D Solar Steam Generator for High-Performance Saline Water Desalination. *Sustain Energy Fuels* **2021**, *5* (16), 4126–4132.
(207) Guan, Q.-F.; Han, Z.-M.; Ling, Z.-C.; Yang, H.-B.; Yu, S.-H. Sustainable Wood-Based Hierarchical Solar Steam Generator: A Biomimetic Design with Reduced Vaporization Enthalpy of Water. *Nano Lett* **2020**, *20* (8), 5699–5704.
(208) Wei, D.; Wang, C.; Zhang, J.; Zhao, H.; Asakura, Y.; Eguchi, M.; Xu, X.; Yamauchi, Y. Water Activation in Solar-Powered Vapor Generation. *Advanced Materials* **2023**, *35* (47), 2212100.
(209) Guo, Y.; Yu, G. Engineering Hydrogels for Efficient Solar Desalination and Water Purification. *Acc Mater Res* **2021**, *2* (5), 374–384.

(210) Salehi, A. A.; Ghannadi-Maragheh, M.; Torab-Mostaedi, M.; Torkaman, R.; Asadollahzadeh, M. Hydrogel Materials as an Emerging Platform for Desalination and the Production of Purified Water. *Separation & Purification Reviews* **2021**, *50* (4), 380–399.
(211) Ahmed, E. M. Hydrogel: Preparation, Characterization, and Applications: A Review. *J Adv Res* **2015**, *6* (2), 105–121.
(212) Deligkaris, K.; Tadele, T. S.; Olthuis, W.; van den Berg, A. Hydrogel-Based Devices for Biomedical Applications. *Sens Actuators B Chem* **2010**, *147* (2), 765–774.
(213) Cascone, S.; Lamberti, G. Hydrogel-Based Commercial Products for Biomedical Applications: A Review. *Int J Pharm* **2020**, *573*, 118803.
(214) Sánchez-Cid, P.; Jiménez-Rosado, M.; Romero, A.; Pérez-Puyana, V. Novel Trends in Hydrogel Development for Biomedical Applications: A Review. *Polymers (Basel)* **2022**, *14* (15), 3023.
(215) Nagata, Y.; Usui, K.; Bonn, M. Molecular Mechanism of Water Evaporation. *Phys Rev Lett* **2015**, *115* (23), 236102.
(216) Tu, Y.; Zhou, J.; Lin, S.; Alshrah, M.; Zhao, X.; Chen, G. Plausible Photomolecular Effect Leading to Water Evaporation Exceeding the Thermal Limit. *Proceedings of the National Academy of Sciences* **2023**, *120* (45), e2312751120.
(217) Lv, G.; Tu, Y.; Zhang, J. H.; Chen, G. Photomolecular Effect: Visible Light Interaction with Air–Water Interface. *Proceedings of the National Academy of Sciences* **2024**, *121* (18), e2320844121. https://doi.org/10.1073/pnas.2320844121.
(218) Chen, Z.; Lin, Y.; Qian, Q.; Su, P.; Ding, Y.; Tuan, P. D.; Chen, L.; Feng, D. Picosecond Laser Treated Aluminium Surface for Photothermal Seawater Desalination. *Desalination* **2022**, *528*, 115561.
(219) Lin, L.; Wang, W.; Li, D.; Xu, S.; Sun, Y.; Li, L.; Fan, K.; Xing, C.; Zhang, L.; Li, J. Multifunctional Graphene/Ag Hydrogel with Antimicrobial and Catalytic Properties for Efficient Solar-Driven Desalination and Wastewater Purification. *Chemical Engineering Journal* **2023**, *478*, 147249.
(220) Richter, T.; Landsgesell, J.; Košovan, P.; Holm, C. On the Efficiency of a Hydrogel-Based Desalination Cycle. *Desalination* **2017**, *414*, 28–34.
(221) Kaviti, A. K.; Balaji, J. S. G.; Ram, A. S.; Kumari, A. A. An Overview on Hydrogel Materials for Solar Desalination. *Mater Today Proc* **2021**, *44*, 2526–2532.
(222) Wenten, I. G.; Khoiruddin, K.; Aryanti, P. T. P.; Hakim, A. N. Scale-up Strategies for Membrane-Based Desalination Processes: A Review. *Journal of Membrane Science and Research* **2016**, *2* (2), 42–58.
(223) Amusat, O. O.; Atia, A. A.; Dudchenko, A. V; Bartholomew, T. V. Modeling Framework for Cost Optimization of Process-Scale Desalination Systems with Mineral Scaling and Precipitation. *ACS ES&T Engineering* **2024**.
(224) Delyannis, E. Historic Background of Desalination and Renewable Energies. *Solar Energy* **2003**, *75* (5), 357–366. https://doi.org/https://doi.org/10.1016/j.solener.2003.08.002.
(225) Katekar, V. P.; Deshmukh, S. S. A Review on Research Trends in Solar Still Designs for Domestic and Industrial Applications. *J Clean Prod* **2020**, *257*, 120544.
(226) Nougriaya, S. K.; Chopra, M. K.; Gupta, B.; Baredar, P. Stepped Solar Still: A Review on Designs Analysis. *Mater Today Proc* **2021**, *46*, 5647–5660.
(227) Kumar, H. A.; Venkateswaran, H.; Kabeel, A. E.; Chamkha, A.; Athikesavan, M. M.; Sathyamurthy, R.; Kasi, K. Recent Advancements, Technologies, and Developments in Inclined Solar Still—a Comprehensive Review. *Environmental Science and Pollution Research* **2021**, *28* (27), 35346–35375.

(228) Peng, G.; Sharshir, S. W. Progress and Performance of Multi-Stage Solar Still–A Review. *Desalination* **2023**, *565*, 116829.
(229) Dao, V.-D.; Vu, N. H.; Yun, S. Recent Advances and Challenges for Solar-Driven Water Evaporation System toward Applications. *Nano Energy* **2020**, *68*, 104324.
(230) Shoeibi, S.; Rahbar, N.; Esfahlani, A. A.; Kargarsharifabad, H. A Comprehensive Review of Enviro-Exergo-Economic Analysis of Solar Stills. *Renewable and Sustainable Energy Reviews* **2021**, *149*, 111404.
(231) Jathar, L. D.; Ganesan, S.; Shahapurkar, K.; Soudagar, M. E. M.; Mujtaba, M. A.; Anqi, A. E.; Farooq, M.; Khidmatgar, A.; Goodarzi, M.; Safaei, M. R. Effect of Various Factors and Diverse Approaches to Enhance the Performance of Solar Stills: A Comprehensive Review. *J Therm Anal Calorim* **2022**, *147* (7), 4491–4522.
(232) Zhong, J.; Huang, C.; Wu, D.; Lin, Z. Influence Factors of the Evaporation Rate of a Solar Steam Generation System: A Numerical Study. *Int J Heat Mass Transf* **2019**, *128*, 860–864. https://doi.org/https://doi.org/10.1016/j.ijheatmasstransfer.2018.09.079.
(233) Kabeel, A. E.; Hamed, A. M.; El-Agouz, S. A. Cost Analysis of Different Solar Still Configurations. *Energy* **2010**, *35* (7), 2901–2908. https://doi.org/https://doi.org/10.1016/j.energy.2010.03.021.
(234) Luo, X.; Shi, J.; Zhao, C.; Luo, Z.; Gu, X.; Bao, H. The Energy Efficiency of Interfacial Solar Desalination. *Appl Energy* **2021**, *302*, 117581. https://doi.org/https://doi.org/10.1016/j.apenergy.2021.117581.
(235) Wang, C. M.; Wang, B. T. Floating Solutions for Challenges Facing Humanity. In *ICSCEA 2019: Proceedings of the International Conference on Sustainable Civil Engineering and Architecture*; Springer, 2020; pp 3–29.
(236) Xu, K.; Wang, C.; Li, Z.; Wu, S.; Wang, J. Salt Mitigation Strategies of Solar-driven Interfacial Desalination. *Adv Funct Mater* **2021**, *31* (8), 2007855.
(237) Liu, G.; Chen, T.; Xu, J.; Yao, G.; Xie, J.; Cheng, Y.; Miao, Z.; Wang, K. Salt-Rejecting Solar Interfacial Evaporation. *Cell Rep Phys Sci* **2021**, *2* (1).
(238) Nawaz, F.; Yang, Y.; Zhao, S.; Sheng, M.; Pan, C.; Que, W. Innovative Salt-Blocking Technologies of Photothermal Materials in Solar-Driven Interfacial Desalination. *J Mater Chem A Mater* **2021**, *9* (30), 16233–16254.
(239) Zheng, J.; Cheng, X.; Zhang, H.; Bai, X.; Ai, R.; Shao, L.; Wang, J. Gold Nanorods: The Most Versatile Plasmonic Nanoparticles. *Chem Rev* **2021**, *121* (21), 13342–13453.
(240) Gahlaut, S. K.; Pathak, A.; Gupta, B. D. Recent Advances in Silver Nanostructured Substrates for Plasmonic Sensors. *Biosensors (Basel)* **2022**, *12* (9), 713.
(241) Zhou, J.; Ralston, J.; Sedev, R.; Beattie, D. A. Functionalized Gold Nanoparticles: Synthesis, Structure and Colloid Stability. *J Colloid Interface Sci* **2009**, *331* (2), 251–262.
(242) Balasubramanian, S. K.; Yang, L.; Yung, L.-Y. L.; Ong, C.-N.; Ong, W.-Y.; Liya, E. Y. Characterization, Purification, and Stability of Gold Nanoparticles. *Biomaterials* **2010**, *31* (34), 9023–9030.
(243) Enoch, S.; Bonod, N. *Plasmonics: From Basics to Advanced Topics*; Springer, 2012; Vol. 167.
(244) Verma, H. N.; Singh, P.; Chavan, R. M. Gold Nanoparticle: Synthesis and Characterization. *Vet World* **2014**, *7* (2), 72.
(245) Herizchi, R.; Abbasi, E.; Milani, M.; Akbarzadeh, A. Current Methods for Synthesis of Gold Nanoparticles. *Artif Cells Nanomed Biotechnol* **2016**, *44* (2), 596–602.
(246) Iravani, S.; Korbekandi, H.; Mirmohammadi, S. V.; Zolfaghari, B. Synthesis of Silver Nanoparticles: Chemical, Physical and Biological Methods. *Res Pharm Sci* **2014**, *9* (6), 385–406.

(247) Verny, J.; Oulmakki, O.; Meza, A. H. Perspective Chapter: Gold Nanoparticles Market – A Global Overview and New Challenges in the Post-Pandemic Economy. In *Gold Nanoparticles and Their Applications in Engineering*; Al-Humairi, S. N. S., Ed.; IntechOpen: Rijeka, 2022; p Ch. 3. https://doi.org/10.5772/intechopen.107071.
(248) West, P. R.; Ishii, S.; Naik, G. V; Emani, N. K.; Shalaev, V. M.; Boltasseva, A. Searching for Better Plasmonic Materials. *Laser Photon Rev* **2010**, *4* (6), 795–808.
(249) Wang, Y.; Capretti, A.; Dal Negro, L. Wide Tuning of the Optical and Structural Properties of Alternative Plasmonic Materials. *Opt Mater Express* **2015**, *5* (11), 2415–2430.
(250) Naik, G. V; Shalaev, V. M.; Boltasseva, A. Alternative Plasmonic Materials: Beyond Gold and Silver. *Advanced Materials* **2013**, *25* (24), 3264–3294.
(251) Gutiérrez, Y.; Brown, A. S.; Moreno, F.; Losurdo, M. Plasmonics beyond Noble Metals: Exploiting Phase and Compositional Changes for Manipulating Plasmonic Performance. *J Appl Phys* **2020**, *128* (8), 080901. https://doi.org/10.1063/5.0020752.
(252) Karpiński, K.; Zielińska-Raczyńska, S.; Ziemkiewicz, D. Aluminium-Based Plasmonic Sensors in Ultraviolet. *Sensors* **2021**, *21* (12), 4096.
(253) Mandal, P. Application of Plasmonics in Solar Cell Efficiency Improvement: A Brief Review on Recent Progress. *Plasmonics* **2022**, *17* (3), 1247–1267.
(254) Mkhitaryan, V.; March, K.; Tseng, E. N.; Li, X.; Scarabelli, L.; Liz-Marzán, L. M.; Chen, S.-Y.; Tizei, L. H. G.; Stéphan, O.; Song, J.-M. Can Copper Nanostructures Sustain High-Quality Plasmons? *Nano Lett* **2021**, *21* (6), 2444–2452.
(255) Preston, A. S.; Hughes, R. A.; Demille, T. B.; Neretina, S. Plasmonics under Attack: Protecting Copper Nanostructures from Harsh Environments. *Chemistry of Materials* **2020**, *32* (15), 6788–6799.
(256) Wang, Y.; Zhang, Q.; Wang, Y.; Besteiro, L. V; Liu, Y.; Tan, H.; Wang, Z. M.; Govorov, A. O.; Zhang, J. Z.; Cooper, J. K. Ultrastable Plasmonic Cu-Based Core–Shell Nanoparticles. *Chemistry of Materials* **2020**, *33* (2), 695–705.
(257) Bayles, A.; Tian, S.; Zhou, J.; Yuan, L.; Yuan, Y.; Jacobson, C. R.; Farr, C.; Zhang, M.; Swearer, D. F.; Solti, D. Al@ TiO2 Core–Shell Nanoparticles for Plasmonic Photocatalysis. *ACS Nano* **2022**, *16* (4), 5839–5850.
(258) Li, J.; Lou, Z.; Li, B. Engineering Plasmonic Semiconductors for Enhanced Photocatalysis. *J Mater Chem A Mater* **2021**, *9* (35), 18818–18835.
(259) Bai, H.; Lam, S. H.; Yang, J.; Cheng, X.; Li, S.; Jiang, R.; Shao, L.; Wang, J. A Schottky-barrier-free Plasmonic Semiconductor Photocatalyst for Nitrogen Fixation in a "One-Stone-Two-Birds" Manner. *Advanced Materials* **2022**, *34* (2), 2104226.
(260) Guo, Y.; Xu, Z.; Curto, A. G.; Zeng, Y.-J.; Van Thourhout, D. Plasmonic Semiconductors: Materials, Tunability and Applications. *Prog Mater Sci* **2023**, *138*, 101158. https://doi.org/https://doi.org/10.1016/j.pmatsci.2023.101158.
(261) Taliercio, T.; Biagioni, P. Semiconductor Infrared Plasmonics. **2019**, *8* (6), 949–990. https://doi.org/doi:10.1515/nanoph-2019-0077.
(262) Zhong, Y.; Malagari, S. D.; Hamilton, T.; Wasserman, D. Review of Mid-Infrared Plasmonic Materials. *J Nanophotonics* **2015**, *9* (1), 93791.
(263) Naik, G. V; Shalaev, V. M.; Boltasseva, A. Semiconductor Plasmonic Metamaterials for Near-Infrared and Telecommunication Wavelength. In *Metamaterials: Fundamentals and Applications III*; SPIE, 2010; Vol. 7754, pp 59–63.
(264) Guler, U.; Boltasseva, A.; Shalaev, V. M. Refractory Plasmonics. *Science (1979)* **2014**, *344* (6181), 263–264.
(265) Selmy, A. E.; Soliman, M.; Allam, N. K. Refractory Plasmonics Boost the Performance of Thin-Film Solar Cells. *Emergent Mater* **2018**, *1* (3), 185–191.

(266) Soref, R.; Peale, R. E.; Buchwald, W. Longwave Plasmonics on Doped Silicon and Silicides. *Opt Express* **2008**, *16* (9), 6507–6514.
(267) Cho, S.-Y.; Soref, R. A. Low-Loss Silicide/Silicon Plasmonic Ribbon Waveguides for Mid-and Far-Infrared Applications. *Opt Lett* **2009**, *34* (12), 1759–1761.
(268) Hsin, C.-L.; Tsai, Y.-Y.; Wang, S.-M. The Discovery of Plasmon Resonance in Germanide Nanowires Grown on Cu Foil. *IEEE Trans Nanotechnol* **2015**, *14* (4), 608–611.
(269) Smith, E. M.; Streyer, W. H.; Nader, N.; Vangala, S.; Grzybowski, G.; Soref, R.; Wasserman, D.; Cleary, J. W. Metal Germanides for Practical On-Chip Plasmonics in the Mid Infrared. *Opt Mater Express* **2018**, *8* (4), 968–982.
(270) Geng, W.; Gao, H.; Ding, C.; Sun, L.; Ma, X.; Li, Y.; Zhao, M. Highly-Anisotropic Plasmons in Two-Dimensional Hyperbolic Copper Borides. *Opt Express* **2022**, *30* (4), 5596–5607.
(271) Hwang, K. C.; Banerjee, P.; Shanmugam, M. Mid-IR Light-Activatable Full Spectrum LaB6 Plasmonic Photocatalyst. *Advanced Materials* **2024**, *36* (9), 2307054.
(272) Dasog, M. Transition Metal Nitrides Are Heating Up the Field of Plasmonics. *Chemistry of Materials* **2022**, *34* (10), 4249–4258. https://doi.org/10.1021/acs.chemmater.2c00305.
(273) Ishii, S.; Shinde, S. L.; Nagao, T. Nonmetallic Materials for Plasmonic Hot Carrier Excitation. *Adv Opt Mater* **2019**, *7* (1), 1800603.
(274) Rahman, M. K.; Nemouchi, F.; Chevolleau, T.; Gergaud, P.; Yckache, K. Ni and Ti Silicide Oxidation for CMOS Applications Investigated by XRD, XPS and FPP. *Mater Sci Semicond Process* **2017**, *71*, 470–476. https://doi.org/https://doi.org/10.1016/j.mssp.2017.06.025.
(275) Koutsokeras, L. E.; Hastas, N.; Kassavetis, S.; Valassiades, O.; Charitidis, C.; Logothetidis, S.; Patsalas, P. Electronic Properties of Binary and Ternary, Hard and Refractory Transition Metal Nitrides. *Surf Coat Technol* **2010**, *204* (12–13), 2038–2041.
(276) Sangiovanni, D. G. Inherent Toughness and Fracture Mechanisms of Refractory Transition-Metal Nitrides via Density-Functional Molecular Dynamics. *Acta Mater* **2018**, *151*, 11–20.
(277) Kumar, M.; Umezawa, N.; Ishii, S.; Nagao, T. Examining the Performance of Refractory Conductive Ceramics as Plasmonic Materials: A Theoretical Approach. *ACS Photonics* **2016**, *3* (1), 43–50.
(278) Guler, U.; Shalaev, V. M.; Boltasseva, A. Nanoparticle Plasmonics: Going Practical with Transition Metal Nitrides. *Materials Today* **2015**, *18* (4), 227–237.
(279) Patsalas, P.; Kalfagiannis, N.; Kassavetis, S.; Abadias, G.; Bellas, D. V; Lekka, C.; Lidorikis, E. Conductive Nitrides: Growth Principles, Optical and Electronic Properties, and Their Perspectives in Photonics and Plasmonics. *Materials Science and Engineering: R: Reports* **2018**, *123*, 1–55.
(280) Karaballi, R. A.; Humagain, G.; Fleischman, B. R. A.; Dasog, M. Synthesis of Plasmonic Group-4 Nitride Nanocrystals by Solid-State Metathesis. *Angewandte Chemie International Edition* **2019**, *58* (10), 3147–3150. https://doi.org/https://doi.org/10.1002/anie.201813134.
(281) Karaballi, R. A.; Esfahani Monfared, Y.; Dasog, M. Photothermal Transduction Efficiencies of Plasmonic Group 4 Metal Nitride Nanocrystals. *Langmuir* **2020**, *36* (18), 5058–5064. https://doi.org/10.1021/acs.langmuir.9b03975.
(282) Karaballi, R. A.; Monfared, Y. E.; Bicket, I. C.; Coridan, R. H.; Dasog, M. Solid-State Synthesis of UV-Plasmonic Cr2N Nanoparticles. *J Chem Phys* **2022**, *157* (15), 154706. https://doi.org/10.1063/5.0109806.

(283) Margeson, M. J.; Dasog, M. Plasmonic Metal Nitrides for Solar-Driven Water Evaporation. *Environ Sci (Camb)* **2020**, *6* (12), 3169–3177.
(284) Dong, Y.; Du, W.; Gao, X.; Guo, M. A TiO2/CN-Decorated Wood Carbon for Efficient Clean Water Production via Simultaneous Decontamination and Evaporation. *J Clean Prod* **2022**, *365*, 132827. https://doi.org/https://doi.org/10.1016/j.jclepro.2022.132827.
(285) Caha, I.; Alves, A. C.; Affonço, L. J.; Lisboa-Filho, P. N.; da Silva, J. H. D.; Rocha, L. A.; Pinto, A. M. P.; Toptan, F. Corrosion and Tribocorrosion Behaviour of Titanium Nitride Thin Films Grown on Titanium under Different Deposition Times. *Surf Coat Technol* **2019**, *374*, 878–888.
(286) Avasarala, B.; Haldar, P. Durability and Degradation Mechanism of Titanium Nitride Based Electrocatalysts for PEM (Proton Exchange Membrane) Fuel Cell Applications. *Energy* **2013**, *57*, 545–553.
(287) Toth, L. *Transition Metal Carbides and Nitrides*; Elsevier, 2014.
(288) Oyama, S. T. Introduction to the Chemistry of Transition Metal Carbides and Nitrides. In *The chemistry of transition metal carbides and nitrides*; Springer, 1996; pp 1–27.
(289) Santhanam, A. T. Application of Transition Metal Carbides and Nitrides in Industrial Tools. In *The chemistry of transition metal carbides and nitrides*; Springer, 1996; pp 28–52.
(290) Johansson, L. I. Electronic and Structural Properties of Transition-Metal Carbide and Nitride Surfaces. *Surf Sci Rep* **1995**, *21* (5–6), 177–250.
(291) Grossman, J. C.; Mizel, A.; Côté, M.; Cohen, M. L.; Louie, S. G. Transition Metals and Their Carbides and Nitrides: Trends in Electronic and Structural Properties. *Phys Rev B* **1999**, *60* (9), 6343.
(292) Michalsky, R.; Zhang, Y.-J.; Peterson, A. A. Trends in the Hydrogen Evolution Activity of Metal Carbide Catalysts. *ACS Catal* **2014**, *4* (5), 1274–1278.
(293) Sullivan, M. M.; Chen, C.-J.; Bhan, A. Catalytic Deoxygenation on Transition Metal Carbide Catalysts. *Catal Sci Technol* **2016**, *6* (3), 602–616.
(294) Pang, J.; Sun, J.; Zheng, M.; Li, H.; Wang, Y.; Zhang, T. Transition Metal Carbide Catalysts for Biomass Conversion: A Review. *Appl Catal B* **2019**, *254*, 510–522.
(295) Sher Shah, Md. S. A.; Jang, G. Y.; Zhang, K.; Park, J. H. Transition Metal Carbide-Based Nanostructures for Electrochemical Hydrogen and Oxygen Evolution Reactions. *EcoEnergy* **2023**, *1* (2), 344–374. https://doi.org/https://doi.org/10.1002/ece2.18.
(296) Wan, J.; Liu, Q.; Wang, T.; Yuan, H.; Zhang, P.; Gu, X. Theoretical Investigation of Platinum-like Catalysts of Molybdenum Carbides for Hydrogen Evolution Reaction. *Solid State Commun* **2018**, *284*, 25–30.
(297) Hossaın, Md. T.; Repon, Md. R.; Shahid, Md. A.; Ali, A.; Islam, T. Progress, Prospects and Challenges of MXene Integrated Optoelectronics Devices. *ChemElectroChem* **2024**, *n/a* (n/a), e202400008. https://doi.org/https://doi.org/10.1002/celc.202400008.
(298) Pacheco-Peña, V.; Hallam, T.; Healy, N. MXene Supported Surface Plasmons on Telecommunications Optical Fibers. *Light Sci Appl* **2022**, *11* (1), 22. https://doi.org/10.1038/s41377-022-00710-1.
(299) Hantanasirisakul, K.; Gogotsi, Y. Electronic and Optical Properties of 2D Transition Metal Carbides and Nitrides (MXenes). *Advanced Materials* **2018**, *30* (52), 1804779. https://doi.org/https://doi.org/10.1002/adma.201804779.
(300) Nguyen, V.-H.; Nguyen, B.-S.; Hu, C.; Nguyen, C. C.; Nguyen, D. L. T.; Nguyen Dinh, M. T.; Vo, D.-V. N.; Trinh, Q. T.; Shokouhimehr, M.; Hasani, A.; Kim, S. Y.; Le, Q. Van. Novel Architecture Titanium Carbide (Ti3C2Tx) MXene Cocatalysts toward Photocatalytic Hydrogen Production: A Mini-Review. *Nanomaterials* **2020**, *10* (4). https://doi.org/10.3390/nano10040602.

(301) Khazaei, M.; Mishra, A.; Venkataramanan, N. S.; Singh, A. K.; Yunoki, S. Recent Advances in MXenes: From Fundamentals to Applications. *Curr Opin Solid State Mater Sci* **2019**, *23* (3), 164–178. https://doi.org/https://doi.org/10.1016/j.cossms.2019.01.002.
(302) Bilyk, T.; Benchakar, M.; Bugnet, M.; Loupias, L.; Chartier, P.; Pazniak, H.; David, M.-L.; Habrioux, A.; Celerier, S.; Pacaud, J.; Mauchamp, V. Electronic Structure Sensitivity to Surface Disorder and Nanometer-Scale Impurity of 2D Titanium Carbide MXene Sheets as Revealed by Electron Energy-Loss Spectroscopy. *The Journal of Physical Chemistry C* **2020**, *124* (49), 27071–27081. https://doi.org/10.1021/acs.jpcc.0c06798.
(303) Huang, Z.; Cui, X.; Li, S.; Wei, J.; Li, P.; Wang, Y.; Lee, C.-S. Two-Dimensional MXene-Based Materials for Photothermal Therapy. *Nanophotonics* **2020**, *9* (8), 2233–2249.
(304) Al-Hadeethi, Y.; Patil, C.; Haridh, W. S. B.; Ahmed, M.; Alassafi, J. E.; Bedaiwi, N. M.; Heidari, E.; Dalir, H. Towards Developing Mid-Infrared Photonics Using Mxenes. *arXiv preprint arXiv:2310.03876* **2023**.
(305) Patel, A.; Singh, R. K. Application of MXenes in Photodetectors. *Recent Advances and Allied Applications of Mxenes* **2024**, *155*, 81–102.
(306) Pacheco-Peña, V.; Hallam, T.; Healy, N. MXene Supported Surface Plasmons on Telecommunications Optical Fibers. *Light Sci Appl* **2022**, *11* (1), 22.
(307) Zhang, C. J.; Nicolosi, V. Graphene and MXene-Based Transparent Conductive Electrodes and Supercapacitors. *Energy Storage Mater* **2019**, *16*, 102–125.
(308) Nahirniak, S.; Ray, A.; Saruhan, B. Challenges and Future Prospects of the MXene-Based Materials for Energy Storage Applications. *Batteries* **2023**, *9* (2), 126.
(309) Panda, S.; Deshmukh, K.; Pasha, S. K. K.; Theerthagiri, J.; Manickam, S.; Choi, M. Y. MXene Based Emerging Materials for Supercapacitor Applications: Recent Advances, Challenges, and Future Perspectives. *Coord Chem Rev* **2022**, *462*, 214518.
(310) Ikeda, K. Plasmonic Applications of Lossy Transition Metals. In *JSAP-OSA Joint Symposia 2014 Abstracts*; Optica Publishing Group: Sapporo, Hokkaido, 2014; p 20a_C3_1. https://doi.org/10.1364/JSAP.2014.20a_C3_1.
(311) Olson, J.; Dominguez-Medina, S.; Hoggard, A.; Wang, L.-Y.; Chang, W.-S.; Link, S. Optical Characterization of Single Plasmonic Nanoparticles. *Chem Soc Rev* **2015**, *44* (1), 40–57. https://doi.org/10.1039/C4CS00131A.
(312) Tretnak, V.; Hohenester, U.; Krenn, J. R.; Hohenau, A. The Role of Particle Size in the Dispersion Engineering of Plasmonic Arrays. *The Journal of Physical Chemistry C* **2019**, *124* (3), 2104–2112.
(313) Bai, H.; Liu, W.; Yi, W.; Li, X.; Zhai, J.; Li, J.; Liu, J.; Yang, H.; Xi, G. Metallic Carbide Nanoparticles as Stable and Reusable Substrates for Sensitive Surface-Enhanced Raman Spectroscopy. *Chemical communications* **2018**, *54* (77), 10843–10846.
(314) Huang, W.; Meng, H.; Gao, Y.; Wang, J.; Yang, C.; Liu, D.; Liu, J.; Guo, C.; Yang, B.; Cao, W. Metallic Tungsten Carbide Nanoparticles as a Near-Infrared-Driven Photocatalyst. *J Mater Chem A Mater* **2019**, *7* (31), 18538–18546.
(315) Xiao, Y.; Hwang, J.-Y.; Sun, Y.-K. Transition Metal Carbide-Based Materials: Synthesis and Applications in Electrochemical Energy Storage. *J Mater Chem A Mater* **2016**, *4* (27), 10379–10393.
(316) Oyama, S. T.; Schlatter, J. C.; Metcalfe III, J. E.; Lambert Jr, J. M. Preparation and Characterization of Early Transition Metal Carbides and Nitrides. *Ind Eng Chem Res* **1988**, *27* (9), 1639–1648.
(317) Lengauer, W. Carbides: Transition-Metal Solid-State Chemistry. *Encyclopedia of inorganic and bioinorganic chemistry* **2011**.

(318) Medeiros, F. F. P.; De Oliveira, S. A.; De Souza, C. P.; Da Silva, A. G. P.; Gomes, U. U.; De Souza, J. F. Synthesis of Tungsten Carbide through Gas–Solid Reaction at Low Temperatures. *Materials Science and Engineering: A* **2001**, *315* (1–2), 58–62.
(319) Ahmad, S.; Ashraf, I.; Mansoor, M. A.; Rizwan, S.; Iqbal, M. An Overview of Recent Advances in the Synthesis and Applications of the Transition Metal Carbide Nanomaterials. *Nanomaterials* **2021**, *11* (3), 776.
(320) Yao, Z. W. Exploration on Synthesis of Activated Carbon Supported Molybdenum Carbide, Nitride and Phosphide via Carbothermal Reduction Route. *J Alloys Compd* **2009**, *475* (1–2), L38–L41.
(321) Koc, R.; Folmer, J. S. Carbothermal Synthesis of Titanium Carbide Using Ultrafine Titania Powders. *J Mater Sci* **1997**, *32*, 3101–3111.
(322) Mhadhbi, M.; Driss, M. Titanium Carbide: Synthesis, Properties and Applications. *J. Brill. Eng* **2021**, *2*, 1–11.
(323) Giordano, C.; Erpen, C.; Yao, W.; Antonietti, M. Synthesis of Mo and W Carbide and Nitride Nanoparticles via a Simple "Urea Glass" Route. *Nano Lett* **2008**, *8* (12), 4659–4663.
(324) Lei, M.; Zhao, H. Z.; Yang, H.; Song, B.; Tang, W. H. Synthesis of Transition Metal Carbide Nanoparticles through Melamine and Metal Oxides. *J Eur Ceram Soc* **2008**, *28* (8), 1671–1677.
(325) Tao, X.; Li, Y.; Du, J.; Xia, Y.; Yang, Y.; Huang, H.; Gan, Y.; Zhang, W.; Li, X. A Generic Bamboo-Based Carbothermal Method for Preparing Carbide (SiC, B4C, TiC, TaC, NbC, TixNb1−xC, and TaxNb1−xC) Nanowires. *J Mater Chem* **2011**, *21* (25), 9095–9102. https://doi.org/10.1039/C1JM10730E.
(326) Essaki, K.; Rees, E. J.; Burstein, G. T. Synthesis of Nanoparticulate Tungsten Carbide under Microwave Irradiation. *Journal of the American Ceramic Society* **2010**, *93* (3), 692–695.
(327) Zhao, Z.; Chen, F.; Wang, M.; Zheng, H. Synthesis of Chromium Carbide Nanopowders via a Microwave Heating Method. *Int J Refract Metals Hard Mater* **2015**, *51*, 212–215.
(328) Huang, H.; Yu, C.; Huang, H.; Guo, W.; Zhang, M.; Han, X.; Wei, Q.; Cui, S.; Tan, X.; Qiu, J. Microwave-Assisted Ultrafast Synthesis of Molybdenum Carbide Nanoparticles Grown on Carbon Matrix for Efficient Hydrogen Evolution Reaction. *Small Methods* **2019**, *3* (11), 1900259.
(329) Jiang, H.; Li, J.; Xiao, Z.; Wang, B.; Fan, M.; Xu, S.; Wan, J. The Rapid Production of Multiple Transition Metal Carbides via Microwave Combustion under Ambient Conditions. *Nanoscale* **2020**, *12* (30), 16245–16252.
(330) Fernique, R. M. T.; Savoie, S.; Gariépy, M.; Braidy, N.; Schulz, R. A Simple Route to Produce Tungsten Carbide Powders by High-Energy Ball Milling and Annealing. *Ceram Int* **2020**, *46* (2), 1736–1742.
(331) Bokhonov, B. B.; Dudina, D. V. Synthesis of ZrC and HfC Nanoparticles Encapsulated in Graphitic Shells from Mechanically Milled Zr-C and Hf-C Powder Mixtures. *Ceram Int* **2017**, *43* (16), 14529–14532.
(332) Rasaki, S. A.; Zhang, B.; Anbalgam, K.; Thomas, T.; Yang, M. Synthesis and Application of Nano-Structured Metal Nitrides and Carbides: A Review. *Progress in Solid State Chemistry* **2018**, *50*, 1–15.
(333) Ahmad, S.; Ashraf, I.; Mansoor, M. A.; Rizwan, S.; Iqbal, M. An Overview of Recent Advances in the Synthesis and Applications of the Transition Metal Carbide Nanomaterials. *Nanomaterials* **2021**, *11* (3), 776.
(334) Ma, J.; Du, Y.; Wu, M.; Pan, M. One Simple Synthesis Route to Nanocrystalline Tantalum Carbide via the Reaction of Tantalum Pentachloride and Sodium Carbonate

with Metallic Magnesium. *Mater Lett* **2007**, *61* (17), 3658–3661. https://doi.org/https://doi.org/10.1016/j.matlet.2006.12.010.
(335) Haouli, S.; Boudebane, S.; Slipper, I. J.; Lemboub, S.; Gębara, P.; Mezrag, S. Combustion Synthesis of Silicon by Magnesiothermic Reduction. *Phosphorus Sulfur Silicon Relat Elem* **2018**, *193* (5), 280–287.
(336) Deng, B.; Wang, Z.; Chen, W.; Li, J. T.; Luong, D. X.; Carter, R. A.; Gao, G.; Yakobson, B. I.; Zhao, Y.; Tour, J. M. Phase Controlled Synthesis of Transition Metal Carbide Nanocrystals by Ultrafast Flash Joule Heating. *Nat Commun* **2022**, *13* (1), 262. https://doi.org/10.1038/s41467-021-27878-1.
(337) Humagain, G.; MacDougal, K.; MacInnis, J.; Lowe, J. M.; Coridan, R. H.; MacQuarrie, S.; Dasog, M. Highly Efficient, Biochar-Derived Molybdenum Carbide Hydrogen Evolution Electrocatalyst. *Adv Energy Mater* **2018**, *8* (29), 1801461. https://doi.org/10.1002/aenm.201801461.
(338) Farahmandjou, M.; Abaeiyan, N. Chemical Synthesis of Vanadium Oxide (V2O5) Nanoparticles Prepared by Sodium Metavanadate. *J Nanomed Res* **2017**, *5* (1), 00103.
(339) Esfahani Monfared, Y.; Dasog, M. Computational Investigation of the Plasmonic Properties of TiN, ZrN, and HfN Nanoparticles: The Role of Particle Size, Medium, and Surface Oxidation. *Can J Chem* **2021**, *99* (7), 576–584. https://doi.org/10.1139/cjc-2020-0335.
(340) Linge, K. L.; Jarvis, K. E. Quadrupole ICP-MS: Introduction to Instrumentation, Measurement Techniques and Analytical Capabilities. *Geostand Geoanal Res* **2009**, *33* (4), 445–467.
(341) Dinnebier, R. E.; Billinge, S. J. L. *Powder Diffraction: Theory and Practice*; Royal society of chemistry, 2008.
(342) Ermrich, M.; Opper, D. X-Ray Powder Diffraction. *XRD for the Analyst, Getting Acquainted with the Principles,* **2011**, 63–85.
(343) Bunaciu, A. A.; UdriŞTioiu, E. G.; Aboul-Enein, H. Y. X-Ray Diffraction: Instrumentation and Applications. *Crit Rev Anal Chem* **2015**, *45* (4), 289–299.
(344) Holder, C. F.; Schaak, R. E. Tutorial on Powder X-Ray Diffraction for Characterizing Nanoscale Materials. *Acs Nano*. ACS Publications 2019, pp 7359–7365.
(345) Wischnitzer, S. *Introduction to Electron Microscopy*; Elsevier, 2013.
(346) Egerton, R. F. *Physical Principles of Electron Microscopy*; Springer, 2005; Vol. 56.
(347) Goldstein, J.; Joy, D. C.; Romig Jr, A. D. *Principles of Analytical Electron Microscopy*; Springer Science & Business Media, 2013.
(348) Kaech, A. An Introduction to Electron Microscopy Instrumentation, Imaging and Preparation. *Center for Microscopy and Image Analysis, University of Zurich* **2013**.
(349) Goldstein, J. I.; Newbury, D. E.; Michael, J. R.; Ritchie, N. W. M.; Scott, J. H. J.; Joy, D. C.; Goldstein, J. I.; Newbury, D. E.; Michael, J. R.; Ritchie, N. W. M. Scanning Electron Microscope (SEM) Instrumentation. *Scanning Electron Microscopy and X-Ray Microanalysis* **2018**, 65–91.
(350) Ezzahmouly, M.; Elmoutaouakkil, A.; Ed-Dhahraouy, M.; Khallok, H.; Elouahli, A.; Mazurier, A.; ElAlbani, A.; Hatim, Z. Micro-Computed Tomographic and SEM Study of Porous Bioceramics Using an Adaptive Method Based on the Mathematical Morphological Operations. *Heliyon* **2019**, *5* (12), e02557. https://doi.org/https://doi.org/10.1016/j.heliyon.2019.e02557.
(351) Inkson, B. J. Scanning Electron Microscopy (SEM) and Transmission Electron Microscopy (TEM) for Materials Characterization. In *Materials characterization using nondestructive evaluation (NDE) methods*; Elsevier, 2016; pp 17–43.

(352) Maaz, K. *The Transmission Electron Microscope: Theory and Applications*; BoD–Books on Demand, 2015.
(353) O'Keefe, M. A.; Allard, L. F.; Blom, D. A. HRTEM Imaging of Atoms at Sub-Ångström Resolution. *J Electron Microsc (Tokyo)* **2005**, *54* (3), 169–180.
(354) Thust, A. Theory and Applications of Focal-Series Reconstruction in HRTEM. *Microscopy and Microanalysis* **2005**, *11* (S02), 602–603.
(355) Sohlberg, K.; Pennycook, T. J.; Zhou, W.; Pennycook, S. J. Insights into the Physical Chemistry of Materials from Advances in HAADF-STEM. *Physical Chemistry Chemical Physics* **2015**, *17* (6), 3982–4006.
(356) Wang, Z. L. Dynamical Theories of Dark-Field Imaging Using Diffusely Scattered Electrons in STEM and TEM. *Acta Crystallogr A* **1995**, *51* (4), 569–585.
(357) Lugg, N. R.; Kothleitner, G.; Shibata, N.; Ikuhara, Y. On the Quantitativeness of EDS STEM. *Ultramicroscopy* **2015**, *151*, 150–159.
(358) Schneider, C. A.; Rasband, W. S.; Eliceiri, K. W. NIH Image to ImageJ: 25 Years of Image Analysis. *Nat Methods* **2012**, *9* (7), 671–675. https://doi.org/10.1038/nmeth.2089.
(359) Watts, J. F.; Wolstenholme, J. *An Introduction to Surface Analysis by XPS and AES*; John Wiley & Sons, 2019.
(360) Armelao, L.; Barreca, D.; Bottaro, G.; Gross, S.; Gasparotto, A.; Maragno, C.; Tondello, E.; Zattin, A. Introduction to XPS Studies of Metal and Metal-Oxide Nanosystems. *Surface Science Spectra* **2003**, *10* (1), 137–142.
(361) Bagus, P. S.; Ilton, E. S.; Nelin, C. J. The Interpretation of XPS Spectra: Insights into Materials Properties. *Surf Sci Rep* **2013**, *68* (2), 273–304.
(362) Baer, D. R.; Artyushkova, K.; Richard Brundle, C.; Castle, J. E.; Engelhard, M. H.; Gaskell, K. J.; Grant, J. T.; Haasch, R. T.; Linford, M. R.; Powell, C. J. Practical Guides for X-Ray Photoelectron Spectroscopy: First Steps in Planning, Conducting, and Reporting XPS Measurements. *Journal of Vacuum Science & Technology A* **2019**, *37* (3).
(363) Chastain, J.; King Jr, R. C. Handbook of X-Ray Photoelectron Spectroscopy. *Perkin-Elmer Corporation* **1992**, *40*, 221.
(364) Greczynski, G.; Hultman, L. X-Ray Photoelectron Spectroscopy: Towards Reliable Binding Energy Referencing. *Prog Mater Sci* **2020**, *107*, 100591. https://doi.org/https://doi.org/10.1016/j.pmatsci.2019.100591.
(365) Mulvaney, S. P.; Keating, C. D. Raman Spectroscopy. *Anal Chem* **2000**, *72* (12), 145–158. https://doi.org/10.1021/a10000155.
(366) Schmitz, K. S. *Introduction to Dynamic Light Scattering by Macromolecules*; Elsevier, 2012.
(367) Bhattacharjee, S. DLS and Zeta Potential–What They Are and What They Are Not? *Journal of controlled release* **2016**, *235*, 337–351.
(368) Babick, F. Dynamic Light Scattering (DLS). In *Characterization of nanoparticles*; Elsevier, 2020; pp 137–172.
(369) Hunter, R. J. *Zeta Potential in Colloid Science: Principles and Applications*; Academic press, 2013; Vol. 2.
(370) Roper, D. K.; Ahn, W.; Hoepfner, M. Microscale Heat Transfer Transduced by Surface Plasmon Resonant Gold Nanoparticles. *The Journal of Physical Chemistry C* **2007**, *111* (9), 3636–3641. https://doi.org/10.1021/jp064341w.
(371) Cole, J. R.; Mirin, N. A.; Knight, M. W.; Goodrich, G. P.; Halas, N. J. Photothermal Efficiencies of Nanoshells and Nanorods for Clinical Therapeutic Applications. *The Journal of Physical Chemistry C* **2009**, *113* (28), 12090–12094. https://doi.org/10.1021/jp9003592.

(372) Ni, G.; Zandavi, S. H.; Javid, S. M.; Boriskina, S. V; Cooper, T. A.; Chen, G. A Salt-Rejecting Floating Solar Still for Low-Cost Desalination. *Energy Environ Sci* **2018**, *11* (6), 1510–1519.
(373) Ifijen, I. H.; Maliki, M. A Comprehensive Review on the Synthesis and Photothermal Cancer Therapy of Titanium Nitride Nanostructures. *Inorganic and Nano-Metal Chemistry* **2023**, *53* (4), 366–387.
(374) Monfared, Y. E.; Kurylyk, B. L.; Dasog, M. Highly Sensitive Plasmonic Fiber-Optic Sensors Using Group IV Transition Metal Nitrides: A Numerical Investigation. *Plasmonics* **2022**, 1–10.
(375) Akhtary, N.; Zubair, A. Titanium Nitride Based Plasmonic Nanoparticles for Photovoltaic Application. *Optics Continuum* **2023**, *2* (7), 1701–1715.
(376) Oh, M.; Carlson, E. S.; Vandervelde, T. E. Localized Surface Plasmon Resonance in Refractory Metamaterials. In *Advanced Fabrication Technologies for Micro/Nano Optics and Photonics XIV*; SPIE, 2021; Vol. 11696, pp 91–95.
(377) Yao, Y.; Zhou, J.; Liu, Z.; Liu, X.; Fu, G.; Liu, G. Refractory Materials and Plasmonics Based Perfect Absorbers. *Nanotechnology* **2021**, *32* (13), 132002.
(378) Verger, L.; Xu, C.; Natu, V.; Cheng, H.-M.; Ren, W.; Barsoum, M. W. Overview of the Synthesis of MXenes and Other Ultrathin 2D Transition Metal Carbides and Nitrides. *Curr Opin Solid State Mater Sci* **2019**, *23* (3), 149–163.
(379) Lan, L.; Fan, X.; Gao, Y.; Li, G.; Hao, Q.; Qiu, T. Plasmonic Metal Carbide SERS Chips. *J Mater Chem C Mater* **2020**, *8* (41), 14523–14530.
(380) Ai, S.; Ma, M.; Chen, Y.-Z.; Gao, X.-H.; Liu, G. Metal-Ceramic Carbide Integrated Solar-Driven Evaporation Device Based on ZrC Nanoparticles for Water Evaporation and Desalination. *Chemical Engineering Journal* **2022**, *429*, 132014.
(381) Hidayat, N.; Ardiansyah; Fuad, A.; Mufti, N.; Amalia Fibriyanti, A.; Insjaf Yogihati, C.; Prihandoko, B. Magnesiothermic Reduction Synthesis of Silicon Carbide with Varying Temperatures: Structural and Mechanical Features. *IOP Conf Ser Mater Sci Eng* **2019**, *515* (1), 012079. https://doi.org/10.1088/1757-899X/515/1/012079.
(382) Torabi, O.; Golabgir, M. H.; Tajizadegan, H.; Torabi, H. A Study on Mechanochemical Behavior of MoO3–Mg–C to Synthesize Molybdenum Carbide. *Int J Refract Metals Hard Mater* **2014**, *47*, 18–24. https://doi.org/https://doi.org/10.1016/j.ijrmhm.2014.06.001.
(383) Asgarian, P.; Nourbakhsh, A.; Amin, P.; Ebrahimi-Kahrizsangi, R.; MacKenzie, K. J. D. The Effect of Different Sources of Porous Carbon on the Synthesis of Nanostructured Boron Carbide by Magnesiothermic Reduction. *Ceram Int* **2014**, *40* (10, Part B), 16399–16408. https://doi.org/https://doi.org/10.1016/j.ceramint.2014.07.147.
(384) Anstey, A.; Vivekanandhan, S.; Rodriguez-Uribe, A.; Misra, M.; Mohanty, A. K. Oxidative Acid Treatment and Characterization of New Biocarbon from Sustainable Miscanthus Biomass. *Science of The Total Environment* **2016**, *550*, 241–247. https://doi.org/10.1016/j.scitotenv.2016.01.015.
(385) Xie, Z.; Deng, Y.; Yang, Y.; Su, H.; Zhou, D.; Liu, C.; Yang, W. Preparation of Nano-Sized Titanium Carbide Particles via a Vacuum Carbothermal Reduction Approach Coupled with Purification under Hydrogen/Argon Mixed Gas. *RSC Adv.* **2017**, *7* (15), 9037–9044. https://doi.org/10.1039/C6RA28264D.
(386) Fang, D.; Wang, C.; Lv, C.; Lv, Y.; Huang, G.; Yang, J.; Pan, S. XPS Studies of Surface Oxidation of Metal Carbides. *Fullerenes, Nanotubes and Carbon Nanostructures* **2022**, *30* (7), 718–726. https://doi.org/10.1080/1536383X.2021.2014456.
(387) Saba, F.; Zhang, F.; Sajjadi, S. A.; Haddad-Sabzevar, M. Surface-Modified-CNTs/Al Matrix Nanocomposites Produced via Spark Plasma Sintering: Microstructures,

Properties, and Formation Mechanism. *Spark Plasma Sintering of Materials: Advances in Processing and Applications* **2019**, 119–159.
(388) Wei, B.; Wang, D.; Wang, Y.; Zhang, H.; Peng, S.; Xu, C.; Song, G.; Zhou, Y. Corrosion Kinetics and Mechanisms of ZrC1−x Ceramics in High Temperature Water Vapor. *RSC Adv.* **2018**, *8* (32), 18163–18174. https://doi.org/10.1039/C8RA02386G.
(389) Gu, X.; Yang, L.; Ma, X.; Dai, X.; Wang, J.; Wen, M.; Zhang, K. Ta Addition Effects on the Structure, Mechanical and Thermal Properties of Sputtered Hf-Ta-C Film. *Ceram Int* **2019**, *45* (12), 15596–15602. https://doi.org/https://doi.org/10.1016/j.ceramint.2019.05.069.
(390) Tang, H.; Zhu, C.; Meng, G.; Wu, N. Review—Surface-Enhanced Raman Scattering Sensors for Food Safety and Environmental Monitoring. *J Electrochem Soc* **2018**, *165* (8), B3098. https://doi.org/10.1149/2.0161808jes.
(391) Nehl, C. L.; Hafner, J. H. Shape-Dependent Plasmon Resonances of Gold Nanoparticles. *J Mater Chem* **2008**, *18* (21), 2415–2419. https://doi.org/10.1039/B714950F.
(392) Stagg, B. J.; Charalampopoulos, T. T. Refractive Indices of Pyrolytic Graphite, Amorphous Carbon, and Flame Soot in the Temperature Range 25° to 600°C. *Combust Flame* **1993**, *94* (4), 381–396. https://doi.org/https://doi.org/10.1016/0010-2180(93)90121-I.
(393) Ziashahabi, A.; Poursalehi, R. The Effects of Surface Oxidation and Interparticle Coupling on Surface Plasmon Resonance Properties of Aluminum Nanoparticles as a UV Plasmonic Material. *Procedia Materials Science* **2015**, *11*, 434–437. https://doi.org/https://doi.org/10.1016/j.mspro.2015.11.030.
(394) Kuzma, A.; Weis, M.; Flickyngerova, S.; Jakabovic, J.; Satka, A.; Dobrocka, E.; Chlpik, J.; Cirak, J.; Donoval, M.; Telek, P.; Uherek, F.; Donoval, D. Influence of Surface Oxidation on Plasmon Resonance in Monolayer of Gold and Silver Nanoparticles. *J Appl Phys* **2012**, *112* (10), 103531. https://doi.org/10.1063/1.4767688.
(395) Powell, C. J.; Swan, J. B. Effect of Oxidation on the Characteristic Loss Spectra of Aluminum and Magnesium. *Physical Review* **1960**, *118* (3), 640–643. https://doi.org/10.1103/PhysRev.118.640.
(396) Fang, Y.; Cheng, Z.; Wang, S.; Hao, H.; Li, L.; Zhao, S.; Chu, X.; Zhu, R. Effects of Oxidation on the Localized Surface Plasmon Resonance of Cu Nanoparticles Fabricated via Vacuum Coating. *Vacuum* **2021**, *184*, 109965. https://doi.org/https://doi.org/10.1016/j.vacuum.2020.109965.
(397) Kosolapova, T. Y. *Carbides: Properties, Production, and Applications*; Springer Science & Business Media, 2012.
(398) Manrique-Bedoya, S.; Abdul-Moqueet, M.; Lopez, P.; Gray, T.; Disiena, M.; Locker, A.; Kwee, S.; Tang, L.; Hood, R. L.; Feng, Y.; Large, N.; Mayer, K. M. Multiphysics Modeling of Plasmonic Photothermal Heating Effects in Gold Nanoparticles and Nanoparticle Arrays. *The Journal of Physical Chemistry C* **2020**, *124* (31), 17172–17182. https://doi.org/10.1021/acs.jpcc.0c02443.
(399) Norton, S. J.; Vo-Dinh, T. Photothermal Effects of Plasmonic Metal Nanoparticles in a Fluid. *J Appl Phys* **2016**, *119* (8), 083105. https://doi.org/10.1063/1.4942623.
(400) Najid, N.; Fellaou, S.; Kouzbour, S.; Gourich, B.; Ruiz-García, A. Energy and Environmental Issues of Seawater Reverse Osmosis Desalination Considering Boron Rejection: A Comprehensive Review and a Case Study of Exergy Analysis. *Process Safety and Environmental Protection* **2021**, *156*, 373–390. https://doi.org/https://doi.org/10.1016/j.psep.2021.10.014.

(401) Xu, N.; Li, J.; Finnerty, C.; Song, Y.; Zhou, L.; Zhu, B.; Wang, P.; Mi, B.; Zhu, J. Going beyond Efficiency for Solar Evaporation. *Nature Water* **2023**, *1* (6), 494–501. https://doi.org/10.1038/s44221-023-00086-5.
(402) Yang, H.-C.; Chen, Z.; Xie, Y.; Wang, J.; Elam, J. W.; Li, W.; Darling, S. B. Chinese Ink: A Powerful Photothermal Material for Solar Steam Generation. *Adv Mater Interfaces* **2019**, *6* (1), 1801252. https://doi.org/https://doi.org/10.1002/admi.201801252.
(403) Liu, H.; Huang, G.; Wang, R.; Huang, L.; Wang, H.; Hu, Y.; Cong, G.; Bao, F.; Xu, M.; Zhu, C.; Xu, J.; Ji, M. Carbon Nanotubes Grown on the Carbon Fibers to Enhance the Photothermal Conversion toward Solar-Driven Applications. *ACS Appl Mater Interfaces* **2022**, *14* (28), 32404–32411. https://doi.org/10.1021/acsami.2c07970.
(404) Xie, Z.; Wang, H.; Geng, Y.; Li, M.; Deng, Q.; Tian, Y.; Chen, R.; Zhu, X.; Liao, Q. Carbon-Based Photothermal Superhydrophobic Materials with Hierarchical Structure Enhances the Anti-Icing and Photothermal Deicing Properties. *ACS Appl Mater Interfaces* **2021**, *13* (40), 48308–48321. https://doi.org/10.1021/acsami.1c15028.
(405) Yang, T.; Lin, H.; Lin, K.-T.; Jia, B. Carbon-Based Absorbers for Solar Evaporation: Steam Generation and Beyond. *Sustainable Materials and Technologies* **2020**, *25*, e00182. https://doi.org/https://doi.org/10.1016/j.susmat.2020.e00182.
(406) Dao, V.-D.; Choi, H.-S. Carbon-Based Sunlight Absorbers in Solar-Driven Steam Generation Devices. *Global Challenges* **2018**, *2* (2), 1700094. https://doi.org/https://doi.org/10.1002/gch2.201700094.
(407) Ibrahim, I.; Seo, D. H.; McDonagh, A. M.; Shon, H. K.; Tijing, L. Semiconductor Photothermal Materials Enabling Efficient Solar Steam Generation toward Desalination and Wastewater Treatment. *Desalination* **2021**, *500*, 114853. https://doi.org/https://doi.org/10.1016/j.desal.2020.114853.
(408) El-Sapa, S.; El-Bary, A. A.; Chtioui, H.; Becheikh, N.; Lotfy, K. Photothermal Excitation in Non-Local Semiconductor Materials with Variable Moisture Thermal Conductivity According to Moisture Diffusivity. *Front Mater* **2023**, *10*. https://doi.org/10.3389/fmats.2023.1193423.
(409) Deng, Z.; Zhou, J.; Miao, L.; Liu, C.; Peng, Y.; Sun, L.; Tanemura, S. The Emergence of Solar Thermal Utilization: Solar-Driven Steam Generation. *J. Mater. Chem. A* **2017**, *5* (17), 7691–7709. https://doi.org/10.1039/C7TA01361B.
(410) Zhao, F.; Guo, Y.; Zhou, X.; Shi, W.; Yu, G. Materials for Solar-Powered Water Evaporation. *Nat Rev Mater* **2020**, *5* (5), 388–401. https://doi.org/10.1038/s41578-020-0182-4.
(411) Liu, X.; Mishra, D. D.; Wang, X.; Peng, H.; Hu, C. Towards Highly Efficient Solar-Driven Interfacial Evaporation for Desalination. *J Mater Chem A Mater* **2020**, *8* (35), 17907–17937.
(412) Wang, Z.; Liu, H.; Chen, F.; Zhang, Q. A Three-Dimensional Printed Biomimetic Hierarchical Graphene Architecture for High-Efficiency Solar Steam-Generation. *J Mater Chem A Mater* **2020**, *8* (37), 19387–19395. https://doi.org/10.1039/D0TA06797K.
(413) Gao, T.; Wu, X.; Wang, Y.; Owens, G.; Xu, H. A Hollow and Compressible 3D Photothermal Evaporator for Highly Efficient Solar Steam Generation without Energy Loss. *Solar RRL* **2021**, *5* (5), 2100053. https://doi.org/https://doi.org/10.1002/solr.202100053.
(414) Alketbi, A. S.; Raza, A.; Sajjad, M.; Li, H.; AlMarzooqi, F.; Zhang, T. Direct Solar Vapor Generation with Micro-3D Printed Hydrogel Device. *EcoMat* **2022**, *4* (1), e12157. https://doi.org/https://doi.org/10.1002/eom2.12157.
(415) Liu, Y.; Luo, B.; Liu, H.; He, M.; Wang, R.; Wang, L.; Quan, Z.; Yu, J.; Qin, X. 3D Printed Electrospun Nanofiber-Based Pyramid-Shaped Solar Vapor Generator with

Hierarchical Porous Structure for Efficient Desalination. *Chemical Engineering Journal* **2023**, *452*, 139402. https://doi.org/https://doi.org/10.1016/j.cej.2022.139402.
(416) Zhao, X.; Meng, X.; Zou, H.; Zhang, Y.; Ma, Y.; Du, Y.; Shao, Y.; Qi, J.; Qiu, J. Nano-Enabled Solar Driven-Interfacial Evaporation: Advanced Design and Opportunities. *Nano Res* **2023**, *16* (5), 6015–6038. https://doi.org/10.1007/s12274-023-5488-2.
(417) Zang, L.; Finnerty, C.; Zheng, S.; Conway, K.; Sun, L.; Ma, J.; Mi, B. Interfacial Solar Vapor Generation for Desalination and Brine Treatment: Evaluating Current Strategies of Solving Scaling. *Water Res* **2021**, *198*, 117135. https://doi.org/https://doi.org/10.1016/j.watres.2021.117135.
(418) Hu, X.; Zhu, J. Tailoring Aerogels and Related 3D Macroporous Monoliths for Interfacial Solar Vapor Generation. *Adv Funct Mater* **2020**, *30* (3), 1907234. https://doi.org/https://doi.org/10.1002/adfm.201907234.
(419) Ghosh, S. K.; Pal, T. Interparticle Coupling Effect on the Surface Plasmon Resonance of Gold Nanoparticles: From Theory to Applications. *Chem Rev* **2007**, *107* (11), 4797–4862. https://doi.org/10.1021/cr0680282.
(420) Wu, Q.; Liu, C.; Cui, C.; Li, L.; Yang, L.; Liu, Y.; Safari Yazd, H.; Xu, S.; Li, X.; Chen, Z.; Tan, W. Plasmon Coupling in DNA-Assembled Silver Nanoclusters. *J Am Chem Soc* **2021**, *143* (36), 14573–14580. https://doi.org/10.1021/jacs.1c04949.
(421) Lee, Y.-M.; Kim, S.-E.; Park, J.-E. Strong Coupling in Plasmonic Metal Nanoparticles. *Nano Converg* **2023**, *10* (1), 34. https://doi.org/10.1186/s40580-023-00383-5.
(422) Bricchi, B. R.; Mascaretti, L.; Garattoni, S.; Mazza, M.; Ghidelli, M.; Naldoni, A.; Li Bassi, A. Nanoporous Titanium (Oxy)Nitride Films as Broadband Solar Absorbers. *ACS Appl Mater Interfaces* **2022**, *14* (16), 18453–18463. https://doi.org/10.1021/acsami.2c01185.
(423) Mascaretti, L.; Schirato, A.; Zbořil, R.; Kment, Š.; Schmuki, P.; Alabastri, A.; Naldoni, A. Solar Steam Generation on Scalable Ultrathin Thermoplasmonic TiN Nanocavity Arrays. *Nano Energy* **2021**, *83*, 105828. https://doi.org/https://doi.org/10.1016/j.nanoen.2021.105828.
(424) Huang, W.; Hu, L.; Tang, Y.; Xie, Z.; Zhang, H. Recent Advances in Functional 2D MXene-Based Nanostructures for Next-Generation Devices. *Adv Funct Mater* **2020**, *30* (49), 2005223. https://doi.org/https://doi.org/10.1002/adfm.202005223.
(425) Wang, M.; Zhu, J.; Zi, Y.; Huang, W. 3D MXene Sponge: Facile Synthesis, Excellent Hydrophobicity, and High Photothermal Efficiency for Waste Oil Collection and Purification. *ACS Appl Mater Interfaces* **2021**, *13* (39), 47302–47312. https://doi.org/10.1021/acsami.1c15064.
(426) Margeson, M. J.; Monfared, Y. E.; Dasog, M. Synthesis and Photothermal Properties of UV-Plasmonic Group IV Transition Metal Carbide Nanoparticles. *ACS Applied Optical Materials* **2023**, *1* (5), 1004–1011. https://doi.org/10.1021/acsaom.3c00073.
(427) Fei Guo, C.; Sun, T.; Cao, F.; Liu, Q.; Ren, Z. Metallic Nanostructures for Light Trapping in Energy-Harvesting Devices. *Light Sci Appl* **2014**, *3* (4), e161–e161. https://doi.org/10.1038/lsa.2014.42.
(428) Chen, J.; Gong, M.; Fan, Y.; Feng, J.; Han, L.; Xin, H. L.; Cao, M.; Zhang, Q.; Zhang, D.; Lei, D.; Yin, Y. Collective Plasmon Coupling in Gold Nanoparticle Clusters for Highly Efficient Photothermal Therapy. *ACS Nano* **2022**, *16* (1), 910–920. https://doi.org/10.1021/acsnano.1c08485.
(429) Jain, P. K.; Lee, K. S.; El-sayed, I. H.; El-sayed, M. A. Calculated Absorption and Scattering Properties of Gold Nanoparticles of Different Size , Shape , and Composition : Applications in Biological Imaging and Biomedicine. *J. Phys. Chem. B* **2006**, *110*, 7238–7248.

(430) Yang, Y.; Han, Y.; Zhao, J.; Que, W. 2D/1D MXene/MWCNT Hybrid Membrane-Based Evaporator for Solar Desalination. *Materials* **2022**, *15* (3), 929. https://doi.org/10.3390/ma15030929.
(431) Farid, M. U.; Kharraz, J. A.; Wang, P.; An, A. K. High-Efficiency Solar-Driven Water Desalination Using a Thermally Isolated Plasmonic Membrane. *J Clean Prod* **2020**, *271*, 122684. https://doi.org/https://doi.org/10.1016/j.jclepro.2020.122684.
(432) Chang, C.; Liu, M.; Pei, L.; Chen, G.; Wang, Z.; Ji, Y. Porous TiNO Solar-Driven Interfacial Evaporator for High-Efficiency Seawater Desalination. *AIP Adv* **2021**, *11* (4), 045228. https://doi.org/10.1063/5.0047390.
(433) Liu, Y.; Liu, Z.; Huang, Q.; Liang, X.; Zhou, X.; Fu, H.; Wu, Q.; Zhang, J.; Xie, W. A High-Absorption and Self-Driven Salt-Resistant Black Gold Nanoparticle-Deposited Sponge for Highly Efficient, Salt-Free, and Long-Term Durable Solar Desalination. *J. Mater. Chem. A* **2019**, *7* (6), 2581–2588. https://doi.org/10.1039/C8TA10227A.
(434) Qin, Y.; Li, Y.; Wu, R.; Wang, X.; Qin, J.; Fu, Y.; Qin, M.; Wang, Z.; Zhang, Y.; Zhang, F. Bilayer Designed Paper-Based Solar Evaporator for Efficient Seawater Desalination. *Nanomaterials* **2022**, *12* (19), 3487. https://doi.org/10.3390/nano12193487.
(435) Wang, J.; Li, Y.; Deng, L.; Wei, N.; Weng, Y.; Dong, S.; Qi, D.; Qiu, J.; Chen, X.; Wu, T. High-Performance Photothermal Conversion of Narrow-Bandgap Ti2O3 Nanoparticles. *Advanced Materials* **2017**, *29* (3), 1603730. https://doi.org/https://doi.org/10.1002/adma.201603730.
(436) Zhou, L.; Tan, Y.; Wang, J.; Xu, W.; Yuan, Y.; Cai, W.; Zhu, S.; Zhu, J. 3D Self-Assembly of Aluminium Nanoparticles for Plasmon-Enhanced Solar Desalination. *Nat Photonics* **2016**, *10* (6), 393–398. https://doi.org/10.1038/nphoton.2016.75.
(437) Tang, C.; Li, X.; Li, Z.; Hao, J. Interfacial Hydrogen Bonds and Their Influence Mechanism on Increasing the Thermal Stability of Nano-SiO2-Modified Meta-Aramid Fibres. *Polymers (Basel)* **2017**, *9* (10). https://doi.org/10.3390/polym9100504.
(438) Li, X.; Li, J.; Lu, J.; Xu, N.; Chen, C.; Min, X.; Zhu, B.; Li, H.; Zhou, L.; Zhu, S.; Zhang, T.; Zhu, J. Enhancement of Interfacial Solar Vapor Generation by Environmental Energy. *Joule* **2018**, *2* (7), 1331–1338. https://doi.org/https://doi.org/10.1016/j.joule.2018.04.004.
(439) Lyu, G.; Kendall, J.; Meazzini, I.; Preis, E.; Bayseç, S.; Scherf, U.; Clément, S.; Evans, R. C. Luminescent Solar Concentrators Based on Energy Transfer from an Aggregation-Induced Emitter Conjugated Polymer. *ACS Appl Polym Mater* **2019**, *1* (11), 3039–3047. https://doi.org/10.1021/acsapm.9b00718.
(440) Wang, Y.; Wu, X.; Gao, T.; Lu, Y.; Yang, X.; Chen, G. Y.; Owens, G.; Xu, H. Same Materials, Bigger Output: A Reversibly Transformable 2D–3D Photothermal Evaporator for Highly Efficient Solar Steam Generation. *Nano Energy* **2021**, *79*, 105477. https://doi.org/https://doi.org/10.1016/j.nanoen.2020.105477.
(441) Xu, Z.; Ran, X.; Wang, D.; Zhong, M.; Zhang, Z. High Efficient 3D Solar Interfacial Evaporator: Achieved by the Synergy of Simple Material and Structure. *Desalination* **2022**, *525*, 115495. https://doi.org/https://doi.org/10.1016/j.desal.2021.115495.
(442) Lv, F.; Miao, J.; Hu, J.; Orejon, D. 3D Solar Evaporation Enhancement by Superhydrophilic Copper Foam Inverted Cone and Graphene Oxide Functionalization Synergistic Cooperation. *Small* **2023**, *19* (30), 2208137. https://doi.org/https://doi.org/10.1002/smll.202208137.
(443) Zhang, X.; Yan, Y.; Li, N.; Yang, P.; Yang, Y.; Duan, G.; Wang, X.; Xu, Y.; Li, Y. A Robust and 3D-Printed Solar Evaporator Based on Naturally Occurring Molecules. *Sci Bull (Beijing)* **2023**, *68* (2), 203–213. https://doi.org/https://doi.org/10.1016/j.scib.2023.01.017.

(444) Pi, M.; Wang, X.; Wang, Z.; Ran, R. Sustainable MXene/PDA Hydrogel with Core-Shell Structure Tailored for Highly Efficient Solar Evaporation and Long-Term Desalination. *Polymer (Guildf)* **2021**, *230*, 124075. https://doi.org/https://doi.org/10.1016/j.polymer.2021.124075.
(445) Zhou, X.; Zhao, F.; Guo, Y.; Zhang, Y.; Yu, G. A Hydrogel-Based Antifouling Solar Evaporator for Highly Efficient Water Desalination. *Energy Environ. Sci.* **2018**, *11* (8), 1985–1992. https://doi.org/10.1039/C8EE00567B.
(446) Guo, Y.; Zhou, X.; Zhao, F.; Bae, J.; Rosenberger, B.; Yu, G. Synergistic Energy Nanoconfinement and Water Activation in Hydrogels for Efficient Solar Water Desalination. *ACS Nano* **2019**, *13* (7), 7913–7919. https://doi.org/10.1021/acsnano.9b02301.
(447) Chu, A.; Yang, M.; Chen, J.; Zhao, J.; Fang, J.; Yang, Z.; Li, H. Biomass-Enhanced Janus Sponge-like Hydrogel with Salt Resistance and High Strength for Efficient Solar Desalination. *Green Energy & Environment* **2023**. https://doi.org/https://doi.org/10.1016/j.gee.2023.04.003.
(448) Zhang, H.; Li, X.; Liu, X.; Du, Y.; Xie, W.; Zheng, S.; Yang, L.; Shi, J.; Jing, D. Biomimetic Hydrogel with Directional Heat Regulation for Efficient Solar Desalination. *Chemical Engineering Journal* **2023**, *473*, 145484. https://doi.org/https://doi.org/10.1016/j.cej.2023.145484.
(449) Liu, P.; Hu, Y.; Li, X.-Y.; Xu, L.; Chen, C.; Yuan, B.; Fu, M.-L. Enhanced Solar Evaporation Using a Scalable MoS2-Based Hydrogel for Highly Efficient Solar Desalination. *Angewandte Chemie International Edition* **2022**, *61* (37), e202208587. https://doi.org/https://doi.org/10.1002/anie.202208587.
(450) Rodrik, D. Green Industrial Policy. *Oxf Rev Econ Policy* **2014**, *30* (3), 469–491.
(451) Nyangchak, N. Emerging Green Industry toward Net-Zero Economy: A Systematic Review. *J Clean Prod* **2022**, *378*, 134622.
(452) de Mello Santos, V. H.; Campos, T. L. R.; Espuny, M.; de Oliveira, O. J. Towards a Green Industry through Cleaner Production Development. *Environmental Science and Pollution Research* **2022**, 1–22.
(453) Liu, Q.; Wu, L.; Jackstell, R.; Beller, M. Using Carbon Dioxide as a Building Block in Organic Synthesis. *Nat Commun* **2015**, *6* (1), 1–15.
(454) Coumans, F. J. A. G.; Overchenko, Z.; Wiesfeld, J. J.; Kosinov, N.; Nakajima, K.; Hensen, E. J. M. Protection Strategies for the Conversion of Biobased Furanics to Chemical Building Blocks. *ACS Sustain Chem Eng* **2022**, *10* (10), 3116–3130.
(455) Van Beilen, J. B.; Poirier, Y. Production of Renewable Polymers from Crop Plants. *The Plant Journal* **2008**, *54* (4), 684–701.
(456) Zhu, Y.; Romain, C.; Williams, C. K. Sustainable Polymers from Renewable Resources. *Nature* **2016**, *540* (7633), 354–362.
(457) Pellis, A.; Malinconico, M.; Guarneri, A.; Gardossi, L. Renewable Polymers and Plastics: Performance beyond the Green. *N Biotechnol* **2021**, *60*, 146–158.
(458) Chum, H. L.; Overend, R. P. Biomass and Renewable Fuels. *Fuel processing technology* **2001**, *71* (1–3), 187–195.
(459) Klass, D. L. Biomass for Renewable Energy and Fuels. *Encyclopedia of energy* **2004**, *1* (1), 193–212.
(460) Serrano-Ruiz, J. C.; West, R. M.; Dumesic, J. A. Catalytic Conversion of Renewable Biomass Resources to Fuels and Chemicals. *Annu Rev Chem Biomol Eng* **2010**, *1*, 79–100.
(461) Kar, S.; Sanderson, H.; Roy, K.; Benfenati, E.; Leszczynski, J. Green Chemistry in the Synthesis of Pharmaceuticals. *Chem Rev* **2021**, *122* (3), 3637–3710.

(462) Murtaza, A.; Qamar, M. A.; Saleem, K.; Hardwick, T.; Shirinfar, B.; Ahmed, N. Renewable Electricity Enables Green Routes to Fine Chemicals and Pharmaceuticals. *The Chemical Record* **2022**, *22* (5), e202100296.
(463) Oelgemöller, M.; Jung, C.; Mattay, J. Green Photochemistry: Production of Fine Chemicals with Sunlight. *Pure and Applied Chemistry* **2007**, *79* (11), 1939–1947.
(464) Ballini, R. *Eco-Friendly Synthesis of Fine Chemicals*; Royal Society of Chemistry, 2009; Vol. 3.
(465) Schwab, W.; Fuchs, C.; Huang, F. Transformation of Terpenes into Fine Chemicals. *European journal of lipid science and technology* **2013**, *115* (1), 3–8.
(466) Kenney, K. L.; Smith, W. A.; Gresham, G. L.; Westover, T. L. Understanding Biomass Feedstock Variability. *Biofuels* **2013**, *4* (1), 111–127.
(467) Liu, B.; Rajagopal, D. Life-Cycle Energy and Climate Benefits of Energy Recovery from Wastes and Biomass Residues in the United States. *Nat Energy* **2019**, *4* (8), 700–708.
(468) Kożuch, A.; Cywicka, D.; Górna, A. Forest Biomass in Bioenergy Production in the Changing Geopolitical Environment of the EU. *Energies (Basel)* **2024**, *17* (3), 554.
(469) Mojović, L.; Nikolić, S.; Rakin, M.; Vukasinović, M. Production of Bioethanol from Corn Meal Hydrolyzates. *Fuel* **2006**, *85* (12–13), 1750–1755.
(470) Mohanty, S. K.; Swain, M. R. Bioethanol Production from Corn and Wheat: Food, Fuel, and Future. In *Bioethanol production from food crops*; Elsevier, 2019; pp 45–59.
(471) Briens, C.; Piskorz, J.; Berruti, F. Biomass Valorization for Fuel and Chemicals Production--A Review. *International Journal of Chemical Reactor Engineering* **2008**, *6* (1).
(472) Okolie, J. A.; Epelle, E. I.; Tabat, M. E.; Orivri, U.; Amenaghawon, A. N.; Okoye, P. U.; Gunes, B. Waste Biomass Valorization for the Production of Biofuels and Value-Added Products: A Comprehensive Review of Thermochemical, Biological and Integrated Processes. *Process Safety and Environmental Protection* **2022**, *159*, 323–344.
(473) Gregg, J. S.; Jürgens, J.; Happel, M. K.; Strøm-Andersen, N.; Tanner, A. N.; Bolwig, S.; Klitkou, A. Valorization of Bio-Residuals in the Food and Forestry Sectors in Support of a Circular Bioeconomy: A Review. *J Clean Prod* **2020**, *267*, 122093.
(474) Braghiroli, F. L.; Passarini, L. Valorization of Biomass Residues from Forest Operations and Wood Manufacturing Presents a Wide Range of Sustainable and Innovative Possibilities. *Current Forestry Reports* **2020**, *6*, 172–183.
(475) Rao, P.; Rathod, V. Valorization of Food and Agricultural Waste: A Step towards Greener Future. *The Chemical Record* **2019**, *19* (9), 1858–1871.
(476) Capanoglu, E.; Nemli, E.; Tomas-Barberan, F. Novel Approaches in the Valorization of Agricultural Wastes and Their Applications. *J Agric Food Chem* **2022**, *70* (23), 6787–6804.
(477) Koutinas, A. A.; Vlysidis, A.; Pleissner, D.; Kopsahelis, N.; Garcia, I. L.; Kookos, I. K.; Papanikolaou, S.; Kwan, T. H.; Lin, C. S. K. Valorization of Industrial Waste and By-Product Streams via Fermentation for the Production of Chemicals and Biopolymers. *Chem Soc Rev* **2014**, *43* (8), 2587–2627.
(478) Arancon, R. A. D.; Lin, C. S. K.; Chan, K. M.; Kwan, T. H.; Luque, R. Advances on Waste Valorization: New Horizons for a More Sustainable Society. *Energy Sci Eng* **2013**, *1* (2), 53–71.
(479) Liguori, R.; Amore, A.; Faraco, V. Waste Valorization by Biotechnological Conversion into Added Value Products. *Appl Microbiol Biotechnol* **2013**, *97*, 6129–6147.
(480) Rajendran, N.; Gurunathan, B.; Han, J.; Krishna, S.; Ananth, A.; Venugopal, K.; Priyanka, R. B. S. Recent Advances in Valorization of Organic Municipal Waste into

Energy Using Biorefinery Approach, Environment and Economic Analysis. *Bioresour Technol* **2021**, *337*, 125498.
(481) Segneanu, A.-E.; Cziple, F.; Vlazan, P.; Sfirloaga, P.; Grozescu, I.; Gherman, V. D. Biomass Extraction Methods. *Biomass now-sustainable growth and use* **2013**, 390–399.
(482) Demirbas, A.; Arin, G. An Overview of Biomass Pyrolysis. *Energy sources* **2002**, *24* (5), 471–482.
(483) Ahmed, I.; Gupta, A. K. Syngas Yield during Pyrolysis and Steam Gasification of Paper. *Appl Energy* **2009**, *86* (9), 1813–1821.
(484) Zhou, N.; Zhou, J.; Dai, L.; Guo, F.; Wang, Y.; Li, H.; Deng, W.; Lei, H.; Chen, P.; Liu, Y. Syngas Production from Biomass Pyrolysis in a Continuous Microwave Assisted Pyrolysis System. *Bioresour Technol* **2020**, *314*, 123756.
(485) Wang, L.; Ok, Y. S.; Tsang, D. C. W.; Alessi, D. S.; Rinklebe, J.; Wang, H.; Mašek, O.; Hou, R.; O'Connor, D.; Hou, D. New Trends in Biochar Pyrolysis and Modification Strategies: Feedstock, Pyrolysis Conditions, Sustainability Concerns and Implications for Soil Amendment. *Soil Use Manag* **2020**, *36* (3), 358–386.
(486) Vilas-Boas, A. C. M.; Tarelho, L. A. C.; Kamali, M.; Hauschild, T.; Pio, D. T.; Jahanianfard, D.; Gomes, A. P. D.; Matos, M. A. A. Biochar from Slow Pyrolysis of Biological Sludge from Wastewater Treatment: Characteristics and Effect as Soil Amendment. *Biofuels, Bioproducts and Biorefining* **2021**, *15* (4), 1054–1072.
(487) Martin, J. A.; Boateng, A. A. Combustion Performance of Pyrolysis Oil/Ethanol Blends in a Residential-Scale Oil-Fired Boiler. *Fuel* **2014**, *133*, 34–44.
(488) Huang, Z.; Manzo, M.; Xia, C.; Cai, L.; Zhang, Y.; Liu, Z.; Nadda, A. K.; Van Le, Q.; Sonne, C.; Lam, S. S. Effects of Waste-Based Pyrolysis as Heating Source: Meta-Analyze of Char Yield and Machine Learning Analysis. *Fuel* **2022**, *318*, 123578.
(489) Carmo-Calado, L.; Hermoso-Orzáez, M. J.; Mota-Panizio, R.; Guilherme-Garcia, B.; Brito, P. Co-Combustion of Waste Tires and Plastic-Rubber Wastes with Biomass Technical and Environmental Analysis. *Sustainability* **2020**, *12* (3), 1036.
(490) Sohi, S. P.; Krull, E.; Lopez-Capel, E.; Bol, R. A Review of Biochar and Its Use and Function in Soil. *Advances in agronomy* **2010**, *105*, 47–82.
(491) Wang, J.; Wang, S. Preparation, Modification and Environmental Application of Biochar: A Review. *J Clean Prod* **2019**, *227*, 1002–1022.
(492) Qian, K.; Kumar, A.; Zhang, H.; Bellmer, D.; Huhnke, R. Recent Advances in Utilization of Biochar. *Renewable and Sustainable Energy Reviews* **2015**, *42*, 1055–1064.
(493) Cha, J. S.; Park, S. H.; Jung, S.-C.; Ryu, C.; Jeon, J.-K.; Shin, M.-C.; Park, Y.-K. Production and Utilization of Biochar: A Review. *Journal of Industrial and Engineering Chemistry* **2016**, *40*, 1–15.
(494) Tan, X.; Liu, S.; Liu, Y.; Gu, Y.; Zeng, G.; Hu, X.; Wang, X.; Liu, S.; Jiang, L. Biochar as Potential Sustainable Precursors for Activated Carbon Production: Multiple Applications in Environmental Protection and Energy Storage. *Bioresour Technol* **2017**, *227*, 359–372.
(495) Ahmetli, G.; Kocaman, S.; Ozaytekin, I.; Bozkurt, P. Epoxy Composites Based on Inexpensive Char Filler Obtained from Plastic Waste and Natural Resources. *Polym Compos* **2013**, *34* (4), 500–509.
(496) Mojaki, S. C.; Mishra, S. B.; Mishra, A. K. Synthesis, Characterization and Material Properties of Titanium Carbide Nanocomposite Derived from Biochar. *Mater Lett* **2020**, *264*, 127317.
(497) Humagain, G.; MacDougal, K.; MacInnis, J.; Lowe, J. M.; Coridan, R. H.; MacQuarrie, S.; Dasog, M. Highly Efficient, Biochar-derived Molybdenum Carbide Hydrogen Evolution Electrocatalyst. *Adv Energy Mater* **2018**, *8* (29), 1801461.

(498) Itatani, K.; Hasegawa, M.; Aizawa, M.; Howell, F. S.; Kishioka, A.; Kinoshita, M. Some Properties of Aluminum Carbide Powder Prepared by the Pyrolysis of Alkylaluminu. *Journal of the American Ceramic Society* **1995**, *78* (3), 801–804.
(499) Yan, Q.; Lu, Y.; To, F.; Li, Y.; Yu, F. Synthesis of Tungsten Carbide Nanoparticles in Biochar Matrix as a Catalyst for Dry Reforming of Methane to Syngas. *Catal Sci Technol* **2015**, *5* (6), 3270–3280.
(500) Li, R.; Shahbazi, A.; Wang, L.; Zhang, B.; Chung, C.-C.; Dayton, D.; Yan, Q. Nanostructured Molybdenum Carbide on Biochar for CO2 Reforming of CH4. *Fuel* **2018**, *225*, 403–410.
(501) Hayun, S.; Dilman, H.; Dariel, M. P.; Frage, N.; Dub, S. The Effect of Carbon Source on the Microstructure and the Mechanical Properties of Reaction Bonded Boron Carbide. *Advances in Sintering Science and Technology: Ceramic Transactions* **2010**, 29–39.
(502) Mo, T.; Xu, J.; Yang, Y.; Li, Y. Effect of Carburization Protocols on Molybdenum Carbide Synthesis and Study on Its Performance in CO Hydrogenation. *Catal Today* **2016**, *261*, 101–115.
(503) Wang, Q.; Wu, H.; Qin, M.; Li, Z.; Jia, B.; Chu, A.; Qu, X. Study on Influencing Factors and Mechanism of High-Quality Tungsten Carbide Nanopowders Synthesized via Carbothermal Reduction. *J Alloys Compd* **2021**, *867*, 158959.
(504) Kim, K. T.; Eo, M. Y.; Nguyen, T. T. H.; Kim, S. M. General Review of Titanium Toxicity. *Int J Implant Dent* **2019**, *5*, 1–12.
(505) Laloy, J.; Lozano, O.; Alpan, L.; Mejia, J.; Toussaint, O.; Masereel, B.; Dogné, J.-M.; Lucas, S. Can TiC Nanoparticles Produce Toxicity in Oral Administration to Rats? *Toxicol Rep* **2014**, *1*, 172–187.
(506) Sani, M. M.; Afshari, H.; Saif, A. A Robust Framework for Waste-to-Energy Technology Selection: A Case Study in Nova Scotia, Canada. *Energy Convers Manag* **2023**, *284*, 116965.
(507) Freedman, B.; Duinker, P. N.; Barclay, H.; Morash, R.; Prager, U. Forest Biomass and Nutrient Studies in Central Nova Scotia. *Forest biomass and nutrient studies in central Nova Scotia.* **1982**, No. MX–134.
(508) Hotel, D. E. S. Regional Challenges and Opportunities for Agricultural Biomass in Nova Scotia. **2015**.
(509) Turner, K.; Lefler, L.; Freedman, B. Plant Communities of Selected Urbanized Areas of Halifax, Nova Scotia, Canada. *Landsc Urban Plan* **2005**, *71* (2–4), 191–206.
(510) Hill, N. M.; Blaney, C. S. Exotic and Invasive Vascular Plants of the Atlantic Maritime Ecozone. *Assessment of Species Diversity in the Atlantic Maritime Ecozone. Edited by DF McAlpine and IM Smith. NRC Research Press, Ottawa, Ontario* **2010**, 215–232.
(511) Horner, J. M. Environmental Health Implications of Heavy Metal Pollution from Car Tires. *Rev Environ Health* **1996**, *11* (4), 175–178.
(512) Liu, Q.; Wang, S.; Wang, K.; Luo, Z.; Cen, K. Pyrolysis of Wood Species Based on the Compositional Analysis. *Korean Journal of Chemical Engineering* **2009**, *26*, 548–553.
(513) Xaydarali, F. Analysis of the Chemical Composition of Car Tire Rubber. *International Journal of Advance Scientific Research* **2022**, *2* (12), 183–191.
(514) Boßelmann, F.; Romano, P.; Fabritius, H.; Raabe, D.; Epple, M. The Composition of the Exoskeleton of Two Crustacea: The American Lobster Homarus Americanus and the Edible Crab Cancer Pagurus. *Thermochim Acta* **2007**, *463* (1–2), 65–68.
(515) Griffin, G. J.; Ward, L. P.; Madapusi, S.; Shah, K. V; Parthasarathy, R. A Study of Chemical Pre-Treatment and Pyrolysis Operating Conditions to Enhance Biochar Production from Rice Straw. *J Anal Appl Pyrolysis* **2022**, *163*, 105455.

(516) Nasir, M.; Rahmawati, T.; Dara, F. Synthesis and Characterization of Biochar from Crab Shell by Pyrolysis. In *IOP Conference Series: Materials Science and Engineering*; IOP Publishing, 2019; Vol. 553, p 012031.
(517) Demiral, İ.; Ayan, E. A. Pyrolysis of Grape Bagasse: Effect of Pyrolysis Conditions on the Product Yields and Characterization of the Liquid Product. *Bioresour Technol* **2011**, *102* (4), 3946–3951.
(518) Açıkalın, K.; Karaca, F.; Bolat, E. Pyrolysis of Pistachio Shell: Effects of Pyrolysis Conditions and Analysis of Products. *Fuel* **2012**, *95*, 169–177.
(519) Crombie, K.; Mašek, O.; Sohi, S. P.; Brownsort, P.; Cross, A. The Effect of Pyrolysis Conditions on Biochar Stability as Determined by Three Methods. *Gcb Bioenergy* **2013**, *5* (2), 122–131.
(520) Kan, T.; Strezov, V.; Evans, T. J. Lignocellulosic Biomass Pyrolysis: A Review of Product Properties and Effects of Pyrolysis Parameters. *Renewable and sustainable energy reviews* **2016**, *57*, 1126–1140.
(521) Jorio, A.; Ferreira, E. H. M.; Moutinho, M. V. O.; Stavale, F.; Achete, C. A.; Capaz, R. B. Measuring Disorder in Graphene with the G and D Bands. *physica status solidi (b)* **2010**, *247* (11-12), 2980–2982.
(522) Davoodi, D.; Tayebi, M.; Emami, A. H.; Miri, R.; Salahshour, S. An Investigation of the Reduction Mechanisms and Magnesiothermic Reactions in ZrC-Ni Nanocomposite Synthesis. *Mater Chem Phys* **2019**, *222*, 351–360. https://doi.org/https://doi.org/10.1016/j.matchemphys.2018.10.014.
(523) Igathinathane, C.; Pordesimo, L. O.; Columbus, E. P.; Batchelor, W. D.; Methuku, S. R. Shape Identification and Particles Size Distribution from Basic Shape Parameters Using ImageJ. *Comput Electron Agric* **2008**, *63* (2), 168–182.
(524) Energy, D.; Elimelech, M.; Phillip, W. A. The Future of Seawater and the Environment. *Science (1979)* **2011**, *333*, 712–718.
(525) Zhou, L.; Li, X.; Ni, G. W.; Zhu, S.; Zhu, J. The Revival of Thermal Utilization from the Sun: Interfacial Solar Vapor Generation. *Natl Sci Rev* **2019**, *6* (3), 562–578. https://doi.org/10.1093/nsr/nwz030.
(526) Pang, Y.; Zhang, J.; Ma, R.; Qu, Z.; Lee, E.; Luo, T. Solar–Thermal Water Evaporation: A Review. *ACS Energy Lett* **2020**, *5* (2), 437–456. https://doi.org/10.1021/acsenergylett.9b02611.
(527) Liu, H.; Huang, Z.; Liu, K.; Hu, X.; Zhou, J. Interfacial Solar-to-heat Conversion for Desalination. *Adv Energy Mater* **2019**, *9* (21), 1900310.
(528) Chen, Q.; Pei, Z.; Xu, Y.; Li, Z.; Yang, Y.; Wei, Y.; Ji, Y. A Durable Monolithic Polymer Foam for Efficient Solar Steam Generation. *Chem Sci* **2018**, *9* (3), 623–628.
(529) Meng, S.; Gong, T.; Zhao, X.; Tang, C.-Y.; Yu, P.; Bao, R.-Y.; Ke, K.; Liu, Z.-Y.; Yang, M.-B.; Yang, W. Boosting Solar Steam Generation in Dynamically Tunable Polymer Porous Architectures. *Polymer (Guildf)* **2021**, *226*, 123811.
(530) Ge, C.; Song, Z.; Yuan, Y.; Song, B.; Ren, S.; Wei, W.; Zhao, H.; Sun, B.; Fang, J. Solar Steam Generation by Porous Conducting Polymer Hydrogel. *Solar Energy* **2022**, *240*, 237–245.
(531) Razaqpur, A. G.; Wang, Y.; Liao, X.; Liao, Y.; Wang, R. Progress of Photothermal Membrane Distillation for Decentralized Desalination: A Review. *Water Res* **2021**, *201*, 117299. https://doi.org/https://doi.org/10.1016/j.watres.2021.117299.
(532) Margeson, M. J.; Atwood, M.; Monfared, Y. E.; Dasog, M. Plasmonic Group 4 Transition Metal Carbide Interfaces for Solar-Driven Desalination. *Aggregate* **2024**, *n/a* (n/a), e531. https://doi.org/https://doi.org/10.1002/agt2.531.

(533) Ihsanullah, I. Potential of MXenes in Water Desalination: Current Status and Perspectives. *Nanomicro Lett* **2020**, *12* (1), 72. https://doi.org/10.1007/s40820-020-0411-9.
(534) Finnerty, C. T. K.; Menon, A. K.; Conway, K. M.; Lee, D.; Nelson, M.; Urban, J. J.; Sedlak, D.; Mi, B. Interfacial Solar Evaporation by a 3D Graphene Oxide Stalk for Highly Concentrated Brine Treatment. *Environ Sci Technol* **2021**, *55* (22), 15435–15445. https://doi.org/10.1021/acs.est.1c04010.
(535) Naghdi, B.; Heshmati, F. Z.; Mahjoub, F.; Arabpour Roghabadi, F.; Ahmadi, V.; Luo, Y.; Wang, Z.; Sadrameli, S. M. Salt Precipitation Challenge in Floating Interfacial Solar Water Desalination Systems. *Desalination* **2023**, *565*, 116868. https://doi.org/https://doi.org/10.1016/j.desal.2023.116868.
(536) Zhu, F.; Wang, L.; Demir, B.; An, M.; Wu, Z. L.; Yin, J.; Xiao, R.; Zheng, Q.; Qian, J. Accelerating Solar Desalination in Brine through Ion Activated Hierarchically Porous Polyion Complex Hydrogels. *Mater. Horiz.* **2020**, *7* (12), 3187–3195. https://doi.org/10.1039/D0MH01259A.
(537) Xu, R.; Wei, N.; Li, Z.; Song, X.; Li, Q.; Sun, K.; Yang, E.; Gong, L.; Sui, Y.; Tian, J.; Wang, X.; Zhao, M.; Cui, H. Construction of Hierarchical 2D/2D Ti3C2/MoS2 Nanocomposites for High-Efficiency Solar Steam Generation. *J Colloid Interface Sci* **2021**, *584*, 125–133. https://doi.org/https://doi.org/10.1016/j.jcis.2020.09.052.
(538) Fan, X.; Yang, Y.; Shi, X.; Liu, Y.; Li, H.; Liang, J.; Chen, Y. A MXene-Based Hierarchical Design Enabling Highly Efficient and Stable Solar-Water Desalination with Good Salt Resistance. *Adv Funct Mater* **2020**, *30* (52), 2007110. https://doi.org/https://doi.org/10.1002/adfm.202007110.
(539) Xu, J.; Wang, Z.; Chang, C.; Fu, B.; Tao, P.; Song, C.; Shang, W.; Deng, T. Solar-Driven Interfacial Desalination for Simultaneous Freshwater and Salt Generation. *Desalination* **2020**, *484*, 114423. https://doi.org/https://doi.org/10.1016/j.desal.2020.114423.
(540) Liu, Y.; Tian, J.; Xu, L.; Wang, Y.; Fei, X.; Li, Y. Multilayer Graphite Nano-Sheet Composite Hydrogel for Solar Desalination Systems with Floatability and Recyclability. *New J. Chem.* **2020**, *44* (46), 20181–20191. https://doi.org/10.1039/D0NJ04409A.
(541) Raihananda, F. A.; Philander, E.; Lauvandy, A. F.; Soelaiman, T. A. F.; Budiman, B. A.; Juangsa, F. B.; Sambegoro, P. Low-Cost Floating Solar Still for Developing Countries: Prototyping and Heat-Mass Transfer Analysis. *Results in Engineering* **2021**, *12*, 100300. https://doi.org/https://doi.org/10.1016/j.rineng.2021.100300.
(542) Liu, Z.; Song, H.; Ji, D.; Li, C.; Cheney, A.; Liu, Y.; Zhang, N.; Zeng, X.; Chen, B.; Gao, J.; Li, Y.; Liu, X.; Aga, D.; Jiang, S.; Yu, Z.; Gan, Q. Extremely Cost-Effective and Efficient Solar Vapor Generation under Nonconcentrated Illumination Using Thermally Isolated Black Paper. *Global Challenges* **2017**, *1* (2), 1600003. https://doi.org/https://doi.org/10.1002/gch2.201600003.
(543) Chen, S.; Zhao, P.; Xie, G.; Wei, Y.; Lyu, Y.; Zhang, Y.; Yan, T.; Zhang, T. A Floating Solar Still Inspired by Continuous Root Water Intake. *Desalination* **2021**, *512*, 115133. https://doi.org/https://doi.org/10.1016/j.desal.2021.115133.
(544) Mohsenzadeh, M.; Aye, L.; Christopher, P. Development and Experimental Analysis of an Innovative Self-Cleaning Low Vacuum Hemispherical Floating Solar Still for Low-Cost Desalination. *Energy Convers Manag* **2022**, *251*, 114902. https://doi.org/https://doi.org/10.1016/j.enconman.2021.114902.
(545) Sun, Y.; Zhao, Z.; Zhao, G.; Yang, Y.; Liu, X.; Wang, L.; Jia, D.; Wang, X.; Qiu, J. Solar-Driven Simultaneous Desalination and Power Generation Enabled by Graphene

Oxide Nanoribbon Papers. *J Mater Chem A Mater* **2022**, *10* (16), 9184–9194. https://doi.org/10.1039/D2TA00375A.
(546) Shoeibi, S.; Saemian, M.; Parsa, S. M.; Khiadani, M.; Mirjalily, S. A. A.; Kargarsharifabad, H. A Novel Solar Desalination System Equipped with Thermoelectric Generator, Reflectors and Low-Cost Sensible Energy-Storage for Co-Production of Power and Drinking Water. *Desalination* **2023**, *567*, 116955. https://doi.org/https://doi.org/10.1016/j.desal.2023.116955.
(547) Ren, J.; Chen, L.; Gong, J.; Qu, J.; Niu, R. Hofmeister Effect Mediated Hydrogel Evaporator for Simultaneous Solar Evaporation and Thermoelectric Power Generation. *Chemical Engineering Journal* **2023**, *458*, 141511. https://doi.org/https://doi.org/10.1016/j.cej.2023.141511.
(548) Han, W.; Han, D.; Chen, H. Pyrolysis of Waste Tires: A Review. *Polymers (Basel)* **2023**, *15* (7). https://doi.org/10.3390/polym15071604.
(549) Vang, Ó. K. ATP Measurements for Monitoring Microbial Drinking Water Quality. **2013**.
(550) Sanserwal, M.; Kumar Singh, A.; Singh, P. Impact of Materials and Economic Analysis of Single Slope Single Basin Passive Solar Still: A Review. *Mater Today Proc* **2020**, *21*, 1643–1652. https://doi.org/https://doi.org/10.1016/j.matpr.2019.11.289.
(551) Bait, O. Exergy, Environ–Economic and Economic Analyses of a Tubular Solar Water Heater Assisted Solar Still. *J Clean Prod* **2019**, *212*, 630–646. https://doi.org/https://doi.org/10.1016/j.jclepro.2018.12.015.
(552) Jaziri, N.; Boughamoura, A.; Müller, J.; Mezghani, B.; Tounsi, F.; Ismail, M. A Comprehensive Review of Thermoelectric Generators: Technologies and Common Applications. *Energy Reports* **2020**, *6*, 264–287. https://doi.org/https://doi.org/10.1016/j.egyr.2019.12.011.
(553) Saleque, A. M.; Thakur, A. K.; Saidur, R.; Hossain, M. I.; Qarony, W.; Ahamed, M. S.; Lynch, I.; Ma, Y.; Tsang, Y. H. RGO Coated Cotton Fabric and Thermoelectric Module Arrays for Efficient Solar Desalination and Electricity Generation. *J Mater Chem A Mater* **2024**, *12* (1), 405–418. https://doi.org/10.1039/D3TA04715F.
(554) Kospa, D. A.; Gebreil, A.; El-Hakam, S. A.; Ahmed, A. I.; Ibrahim, A. A. Multifunctional Plasmonic Ag–Cu Alloy Nanoparticles Immobilized on Reduced Graphene Oxide for Simultaneous Solar-Driven Steam, Wastewater Purification, and Electricity Generation. *Journal of Materials Research and Technology* **2023**, *23*, 2924–2939. https://doi.org/https://doi.org/10.1016/j.jmrt.2023.01.141.
(555) Weinberger, C. R.; Thompson, G. B. Review of Phase Stability in the Group IVB and VB Transition-metal Carbides. *Journal of the American Ceramic Society* **2018**, *101* (10), 4401–4424.
(556) Storms, E. K.; McNeal, R. J. THE VANADIUM-VANADIUM CARBIDE SYSTEM1. *J Phys Chem* **1962**, *66* (8), 1401–1408.
(557) Storms, E. K.; Krikorian, N. H. THE NIOBIUM—NIOBIUM CARBIDE SYSTEM1. *J Phys Chem* **1960**, *64* (10), 1471–1477.
(558) Smith, C. J.; Weinberger, C. R.; Thompson, G. B. Phase Stability and Microstructural Formations in the Niobium Carbides. *J Eur Ceram Soc* **2018**, *38* (15), 4850–4866.
(559) Yu, X.-X.; Weinberger, C. R.; Thompson, G. B. Ab Initio Investigations of the Phase Stability in Tantalum Carbides. *Acta Mater* **2014**, *80*, 341–349.
(560) Ghasali, E.; Pakseresht, A. H.; Alizadeh, M.; Shirvanimoghaddam, K.; Ebadzadeh, T. Vanadium Carbide Reinforced Aluminum Matrix Composite Prepared by Conventional, Microwave and Spark Plasma Sintering. *J Alloys Compd* **2016**, *688*, 527–533.

(561) Satya Prasad, V. V; Baligidad, R. G.; Gokhale, A. A. Niobium and Other High Temperature Refractory Metals for Aerospace Applications. *Aerospace Materials and Material Technologies: Volume 1: Aerospace Materials* **2017**, 267–288.
(562) Palomar, F. E.; Zambrano, P. C.; Gomez, M. I.; Colas, R.; Guerrero, M. P.; Castillo, A. Coatings Made of Tungsten Carbide and Tantalum Carbide for Machining Tools. *Vacuum* **2010**, *84* (10), 1236–1239.
(563) Peng, X.; Hu, L.; Wang, L.; Zhang, X.; Fu, J.; Huo, K.; Lee, L. Y. S.; Wong, K.-Y.; Chu, P. K. Vanadium Carbide Nanoparticles Encapsulated in Graphitic Carbon Network Nanosheets: A High-Efficiency Electrocatalyst for Hydrogen Evolution Reaction. *Nano Energy* **2016**, *26*, 603–609.
(564) Peng, X.; Huang, C.; Zhang, B.; Liu, Y. Vanadium Carbide Nanodots Anchored on N Doped Carbon Nanosheets Fabricated by Spatially Confined Synthesis as a High-Efficient Electrocatalyst for Hydrogen Evolution Reaction. *J Power Sources* **2021**, *490*, 229551.
(565) Bak, S.; Qiao, R.; Yang, W.; Lee, S.; Yu, X.; Anasori, B.; Lee, H.; Gogotsi, Y.; Yang, X. Na-ion Intercalation and Charge Storage Mechanism in 2D Vanadium Carbide. *Adv Energy Mater* **2017**, *7* (20), 1700959.
(566) Tang, W.; Zhong, W.; Wu, Y.; Qi, Y.; Guo, B.; Liu, D.; Bao, S.-J.; Xu, M. Vanadium Carbide Nanoparticles Incorporation in Carbon Nanofibers for Room-Temperature Sodium Sulfur Batteries: Confining, Trapping, and Catalyzing. *Chemical Engineering Journal* **2020**, *395*, 124978.
(567) Dall'Agnese, Y.; Taberna, P.-L.; Gogotsi, Y.; Simon, P. Two-Dimensional Vanadium Carbide (MXene) as Positive Electrode for Sodium-Ion Capacitors. *J Phys Chem Lett* **2015**, *6* (12), 2305–2309.
(568) Zbasnik, J.; Toth, L. E. Electronic Structure of Vanadium Carbide. *Phys Rev B* **1973**, *8* (2), 452.
(569) Dai, D.; Roszak, S.; Balasubramanian, K. Electronic Structures of Niobium Carbides: NbC n (N= 3− 8). *J Phys Chem A* **2000**, *104* (43), 9760–9769.
(570) Kalemos, A.; Dunning, T. H.; Mavridis, A. The Electronic Structure of Vanadium Carbide, VC. *J Chem Phys* **2005**, *123* (1).
(571) Kondaiah, P.; Niranjan, K.; John, S.; Barshilia, H. C. Tantalum Carbide Based Spectrally Selective Coatings for Solar Thermal Absorber Applications. *Solar Energy Materials and Solar Cells* **2019**, *198*, 26–34. https://doi.org/https://doi.org/10.1016/j.solmat.2019.04.016.
(572) Pflüger, J.; Fink, J.; Weber, W.; Bohnen, K.-P.; Crecelius, G. Dielectric Properties of ZrN, NbC, and NbN as Determined by Electron-Energy-Loss Spectroscopy. *Phys Rev B* **1985**, *31* (3), 1244–1247. https://doi.org/10.1103/PhysRevB.31.1244.
(573) Mahar, N.; Al-Ahmed, A.; Al-Saadi, A. A. Synthesis of Vanadium Carbide MXene with Improved Inter-Layer Spacing for SERS-Based Quantification of Anti-Cancer Drugs. *Appl Surf Sci* **2023**, *607*, 155034. https://doi.org/https://doi.org/10.1016/j.apsusc.2022.155034.
(574) Lan, L.; Fan, X.; Yu, S.; Gao, J.; Zhao, C.; Hao, Q.; Qiu, T. Flexible Two-Dimensional Vanadium Carbide MXene-Based Membranes with Ultra-Rapid Molecular Enrichment for Surface-Enhanced Raman Scattering. *ACS Appl Mater Interfaces* **2022**, *14* (35), 40427–40436. https://doi.org/10.1021/acsami.2c10800.
(575) Shevchuk, K.; Sarycheva, A.; Gogotsi, Y. Evaluation of Two-Dimensional Transition-Metal Carbides and Carbonitrides (MXenes) for SERS Substrates. *MRS Bull* **2022**, *47* (6), 545–554.

(576) Wang, Y.; Wang, Y.; Chen, K.; Qi, K.; Xue, T.; Zhang, H.; He, J.; Xiao, S. Niobium Carbide MXenes with Broad-Band Nonlinear Optical Response and Ultrafast Carrier Dynamics. *ACS Nano* **2020**, *14* (8), 10492–10502. https://doi.org/10.1021/acsnano.0c04390.
(577) Lan, L.; Fan, X.; Gao, Y.; Li, G.; Hao, Q.; Qiu, T. Plasmonic Metal Carbide SERS Chips. *J Mater Chem C Mater* **2020**, *8* (41), 14523–14530.
(578) Rafieerad, A.; Yan, W.; Alagarsamy, K. N.; Srivastava, A.; Sareen, N.; Arora, R. C.; Dhingra, S. Fabrication of Smart Tantalum Carbide MXene Quantum Dots with Intrinsic Immunomodulatory Properties for Treatment of Allograft Vasculopathy. *Adv Funct Mater* **2021**, *31* (46), 2106786. https://doi.org/https://doi.org/10.1002/adfm.202106786.
(579) Mahar, N.; Al-Ahmed, A.; Al-Saadi, A. A. Synthesis of Vanadium Carbide MXene with Improved Inter-Layer Spacing for SERS-Based Quantification of Anti-Cancer Drugs. *Appl Surf Sci* **2023**, *607*, 155034.
(580) Wu, Z.; Li, C.; Li, Z.; Feng, K.; Cai, M.; Zhang, D.; Wang, S.; Chu, M.; Zhang, C.; Shen, J.; Huang, Z.; Xiao, Y.; Ozin, G. A.; Zhang, X.; He, L. Niobium and Titanium Carbides (MXenes) as Superior Photothermal Supports for CO2 Photocatalysis. *ACS Nano* **2021**, *15* (3), 5696–5705. https://doi.org/10.1021/acsnano.1c00990.
(581) Dai, C.; Chen, Y.; Jing, X.; Xiang, L.; Yang, D.; Lin, H.; Liu, Z.; Han, X.; Wu, R. Two-Dimensional Tantalum Carbide (MXenes) Composite Nanosheets for Multiple Imaging-Guided Photothermal Tumor Ablation. *ACS Nano* **2017**, *11* (12), 12696–12712. https://doi.org/10.1021/acsnano.7b07241.
(582) Liu, Z.; Lin, H.; Zhao, M.; Dai, C.; Zhang, S.; Peng, W.; Chen, Y. 2D Superparamagnetic Tantalum Carbide Composite MXenes for Efficient Breast-Cancer Theranostics. *Theranostics* **2018**, *8* (6), 1648–1664. https://doi.org/10.7150/thno.23369.
(583) Alhowity, S.; Balogun, K.; Ganesan, A.; Lund, C. J.; Omolere, O.; Adesope, Q.; Chukwunenye, P.; Amagbor, S. C.; Anwar, F.; Altafi, M. K. Niobium Carbide and Tantalum Carbide as Nitrogen Reduction Electrocatalysts: Catalytic Activity, Carbophilicity, and the Importance of Intermediate Oxidation States. *ACS Appl Mater Interfaces* **2024**, *16* (2), 2180–2192.
(584) Wu, Z.; Shen, J.; Li, C.; Zhang, C.; Wu, C.; Li, Z.; An, X.; He, L. Niche Applications of MXene Materials in Photothermal Catalysis. *Chemistry (Easton)* **2023**, *5* (1), 492–510.
(585) Zhang, F.; Zhang, X.; Hu, S.; Hu, H.; Ye, J.; Wang, D. Selective Photothermal Reduction of CO2 to CH4 via the Synergistic Effect of Ni-Nanoparticle@ NiO-Nanosheet/V2C-MXene Catalyst. *Mater Today Energy* **2024**, *39*, 101470.
(586) Farahmandjou, M.; Abaeiyan, N. Chemical Synthesis of Vanadium Oxide (V2O5) Nanoparticles Prepared by Sodium Metavanadate. *J Nanomed Res* **2017**, *5* (1), 00103.
(587) Gupta, A.; Mittal, M.; Singh, M. K.; Suib, S. L.; Pandey, O. P. Low Temperature Synthesis of NbC/C Nano-Composites as Visible Light Photoactive Catalyst. *Sci Rep* **2018**, *8* (1), 13597. https://doi.org/10.1038/s41598-018-31989-z.
(588) Carvajal-Campos, Y.; Ceballos-Mendivil, L.; Baldenebro-López, F.; Pérez-Rábago, C.; Estrada, C. A. Synthesis and Characterization of Tantalum Carbide Nanoparticles Using Concentrated Solar Energy. *Advanced Powder Technology* **2019**, *30* (11), 2574–2579. https://doi.org/https://doi.org/10.1016/j.apt.2019.08.004.
(589) Tan, Y.; Jiang, T.; Chen, G. Z. Mechanisms and Product Options of Magnesiothermic Reduction of Silica to Silicon for Lithium-Ion Battery Applications. *Front Energy Res* **2021**, *9*.

(590) Feng, L.; Fahrenholtz, W. G.; Hilmas, G. E.; Zhou, Y. Synthesis of Single-Phase High-Entropy Carbide Powders. *Scr Mater* **2019**, *162*, 90–93. https://doi.org/https://doi.org/10.1016/j.scriptamat.2018.10.049.
(591) Cao, J.; Sun, T.; Grattan, K. T. V. Gold Nanorod-Based Localized Surface Plasmon Resonance Biosensors: A Review. *Sens Actuators B Chem* **2014**, *195*, 332–351.
(592) Martin-Carrasco, F.; Garrote, L.; Iglesias, A.; Mediero, L. Diagnosing Causes of Water Scarcity in Complex Water Resources Systems and Identifying Risk Management Actions. *Water Resources Manag* **2013**, *27* (6), 1693–1705. https://doi.org/10.1007/s11269-012-0081-6.
(593) Perks, C.; Mudd, G. Titanium, Zirconium Resources and Production: A State of the Art Literature Review. *Ore Geol Rev* **2019**, *107*, 629–646.
(594) Sverdrup, H. U.; Sverdrup, A. E. An Assessment of the Global Supply, Recycling, Stocks in Use and Market Price for Titanium Using the WORLD7 Model. *Sustainable Horizons* **2023**, *7*, 100067.
(595) Gambogi, J. Hafnium (Hf). *Metal Prices in the United States Through 2010* 63.
(596) Oezaslan, M.; Hasché, F.; Strasser, P. In Situ Observation of Bimetallic Alloy Nanoparticle Formation and Growth Using High-Temperature XRD. *Chemistry of Materials* **2011**, *23* (8), 2159–2165.
(597) Sun, Y.; Ren, Y. In Situ Synchrotron X-Ray Techniques for Real-Time Probing of Colloidal Nanoparticle Synthesis. *Particle & Particle Systems Characterization* **2013**, *30* (5), 399–419.
(598) Prinsi, C. B.; Kulluri, R.; Motta, G.; Perrone, G. Combined Optical Water Quality Monitoring and Sanitization System. In *Optical Fibers and Sensors for Medical Diagnostics, Treatment and Environmental Applications XXIII*; SPIE, 2023; Vol. 12372, pp 110–115.
(599) Lu, K. Sintering of Nanoceramics. *International Materials Reviews* **2008**, *53* (1), 21–38.
(600) Chen, T.; Cai, J.; Gong, D.; Liu, C.; Liu, P.; Cheng, X.; Zhang, D. Facile Fabrication of 3D Biochar Absorbers Dual-Loaded with Fe3O4 Nanoparticles for Enhanced Microwave Absorption. *J Alloys Compd* **2023**, *935*, 168085.
(601) Ma, Y.; Guan, G.; Hao, X.; Cao, J.; Abudula, A. Molybdenum Carbide as Alternative Catalyst for Hydrogen Production–A Review. *Renewable and Sustainable Energy Reviews* **2017**, *75*, 1101–1129.
(602) Xu, K.; Sun, B.; Lin, J.; Wen, W.; Pei, Y.; Yan, S.; Qiao, M.; Zhang, X.; Zong, B. ε-Iron Carbide as a Low-Temperature Fischer–Tropsch Synthesis Catalyst. *Nat Commun* **2014**, *5* (1), 5783.
(603) Castle, E.; Csanádi, T.; Grasso, S.; Dusza, J.; Reece, M. Processing and Properties of High-Entropy Ultra-High Temperature Carbides. *Sci Rep* **2018**, *8* (1), 8609.
(604) Calzolari, A.; Oses, C.; Toher, C.; Esters, M.; Campilongo, X.; Stepanoff, S. P.; Wolfe, D. E.; Curtarolo, S. Plasmonic High-Entropy Carbides. *Nat Commun* **2022**, *13* (1), 5993.
(605) Madhumitha, A.; Preethi, V.; Kanmani, S. Photocatalytic Hydrogen Production Using TiO2 Coated Iron-Oxide Core Shell Particles. *Int J Hydrogen Energy* **2018**, *43* (8), 3946–3956.
(606) Armelles, G.; Cebollada, A.; García-Martín, A.; González, M. U. Magnetoplasmonics: Combining Magnetic and Plasmonic Functionalities. *Adv Opt Mater* **2013**, *1* (1), 10–35.
(607) Kitsou, I.; Panagopoulos, P.; Maggos, T.; Arkas, M.; Tsetsekou, A. Development of SiO2@ TiO2 Core-Shell Nanospheres for Catalytic Applications. *Appl Surf Sci* **2018**, *441*, 223–231.

(608) Aslam, M.; Qamar, M. T.; Ahmed, I.; Rehman, A. U.; Ali, S.; Ismail, I. M. I.; Hameed, A. The Suitability of Silicon Carbide for Photocatalytic Water Oxidation. *Appl Nanosci* **2018**, *8* (5), 987–999. https://doi.org/10.1007/s13204-018-0772-2.
(609) Wang, T.; Wang, H.-J.; Lin, J.-S.; Yang, J.-L.; Zhang, F.-L.; Lin, X.-M.; Zhang, Y.-J.; Jin, S.; Li, J.-F. Plasmonic Photocatalysis: Mechanism, Applications and Perspectives. *Chinese Journal of Structural Chemistry* **2023**, 100066.
(610) Yaqub, M.; Lee, W. Zero-Liquid Discharge (ZLD) Technology for Resource Recovery from Wastewater: A Review. *Science of the total environment* **2019**, *681*, 551–563.
(611) Kashyap, V.; Ghasemi, H. Solar Heat Localization: Concept and Emerging Applications. *J Mater Chem A Mater* **2020**, *8* (15), 7035–7065. https://doi.org/10.1039/D0TA01004A.
(612) Tamura, H.; Nagahama, H.; Tokura, S. Preparation of Chitin Hydrogel under Mild Conditions. *Cellulose* **2006**, *13*, 357–364.
(613) Zainal, S. H.; Mohd, N. H.; Suhaili, N.; Anuar, F. H.; Lazim, A. M.; Othaman, R. Preparation of Cellulose-Based Hydrogel: A Review. *Journal of Materials Research and Technology* **2021**, *10*, 935–952.
(614) Ahmad, S.; Ahmad, M.; Manzoor, K.; Purwar, R.; Ikram, S. A Review on Latest Innovations in Natural Gums Based Hydrogels: Preparations & Applications. *Int J Biol Macromol* **2019**, *136*, 870–890.
(615) Aboabboud, M.; Mink, G.; Kudish, A. Condensation Heat Recycle in Solar Stills. In *Proceedings of the World Congress on Engineering*; 2009; Vol. 2.
(616) Sharon, H.; Reddy, K. S.; Gorjian, S. Parametric Investigation and Year Round Performance of a Novel Passive Multi-Chamber Vertical Solar Diffusion Still: Energy, Exergy and Enviro-Economic Aspects. *Solar Energy* **2020**, *211*, 831–846.
(617) Chen, H.; Wu, S.-L.; Wang, H.-L.; Wu, Q.-Y.; Yang, H.-C. Photothermal Devices for Sustainable Uses Beyond Desalination. *Advanced Energy and Sustainability Research* **2021**, *2* (3), 2000056. https://doi.org/https://doi.org/10.1002/aesr.202000056.
(618) Lin, Y.; Shao, K.; Li, S.; Li, N.; Wang, S.; Wu, X.; Guo, C.; Yu, L.; Murto, P.; Xu, X. Hygroscopic and Photothermal All-Polymer Foams for Efficient Atmospheric Water Harvesting, Passive Humidity Management, and Protective Packaging. *ACS Appl Mater Interfaces* **2023**, *15* (7), 10084–10097. https://doi.org/10.1021/acsami.3c00302.
(619) Chang, J.; Shi, Y.; Wu, M.; Li, R.; Shi, L.; Jin, Y.; Qing, W.; Tang, C.; Wang, P. Solar-Assisted Fast Cleanup of Heavy Oil Spills Using a Photothermal Sponge. *J Mater Chem A Mater* **2018**, *6* (19), 9192–9199. https://doi.org/10.1039/C8TA00779A.
(620) Wu, Y.; Dong, L.; Shu, X.; Yang, Y.; Feng, P.; Ran, Q. Recent Advancements in Photothermal Anti-Icing/Deicing Materials. *Chemical Engineering Journal* **2023**, *469*, 143924. https://doi.org/https://doi.org/10.1016/j.cej.2023.143924.
(621) Noureen, L.; Zaman, S.; Ali Shah, W.; Wang, Q.; Humayun, M.; Xu, Q.; Wang, X. Bifunctional Photothermal Membrane for High-Temperature Interfacial Solar Steam Generation and off-Grid Sterilization. *Chemical Engineering Journal* **2023**, *473*, 145122. https://doi.org/https://doi.org/10.1016/j.cej.2023.145122.
(622) Geng, Z.; Yu, Y.; Liu, J. Broadband Plasmonic Photocatalysis Enhanced by Photothermal Light Absorbers. *The Journal of Physical Chemistry C* **2023**, *127* (36), 17723–17731. https://doi.org/10.1021/acs.jpcc.3c03639.
(623) Ghoussoub, M.; Xia, M.; Duchesne, P. N.; Segal, D.; Ozin, G. Principles of Photothermal Gas-Phase Heterogeneous CO2 Catalysis. *Energy Environ Sci* **2019**, *12* (4), 1122–1142. https://doi.org/10.1039/C8EE02790K.

(624) Zhang, J.; Chen, H.; Duan, X.; Sun, H.; Wang, S. Photothermal Catalysis: From Fundamentals to Practical Applications. *Materials Today* **2023**, *68*, 234–253. https://doi.org/https://doi.org/10.1016/j.mattod.2023.06.017.
(625) Mascaretti, L.; Naldoni, A. Hot Electron and Thermal Effects in Plasmonic Photocatalysis. *J Appl Phys* **2020**, *128* (4).
(626) Adleman, J. R.; Boyd, D. A.; Goodwin, D. G.; Psaltis, D. Heterogenous Catalysis Mediated by Plasmon Heating. *Nano Lett* **2009**, *9* (12), 4417–4423. https://doi.org/10.1021/nl902711n.
(627) Sivan, Y.; Baraban, J. H.; Dubi, Y. Experimental Practices Required to Isolate Thermal Effects in Plasmonic Photo-Catalysis: Lessons from Recent Experiments. *OSA Contin* **2020**, *3* (3), 483–497. https://doi.org/10.1364/OSAC.376809.
(628) Li, J.; Ye, Y.; Ye, L.; Su, F.; Ma, Z.; Huang, J.; Xie, H.; Doronkin, D. E.; Zimina, A.; Grunwaldt, J.-D.; Zhou, Y. Sunlight Induced Photo-Thermal Synergistic Catalytic CO2 Conversion via Localized Surface Plasmon Resonance of MoO3−x. *J Mater Chem A Mater* **2019**, *7* (6), 2821–2830. https://doi.org/10.1039/C8TA10922B.
(629) Galuska, A. A.; Uht, J. C.; Marquez, N. Reactive and Nonreactive Ion Mixing of Ti Films on Carbon Substrates. *Journal of Vacuum Science & Technology A: Vacuum, Surfaces, and Films* **1988**, *6* (1), 110–122.
(630) Ahmed, B.; Anjum, D. H.; Hedhili, M. N.; Gogotsi, Y.; Alshareef, H. N. H 2 O 2 Assisted Room Temperature Oxidation of Ti 2 C MXene for Li-Ion Battery Anodes. *Nanoscale* **2016**, *8* (14), 7580–7587.
(631) Aas, N.; Pringle, T. J.; Bowker, M. Adsorption and Decomposition of Methanol on TiO2, SrTiO3 and SrO. *Journal of the Chemical Society, Faraday Transactions* **1994**, *90* (7), 1015–1022.
(632) Kaufmann, R.; Klewe-Nebenius, H.; Moers, H.; Pfennig, G.; Jenett, H.; Ache, H. J. XPS Studies of the Thermal Behaviour of Passivated Zircaloy-4 Surfaces. *Surface and interface analysis* **1988**, *11* (10), 502–509.
(633) Hauser, D.; Auer, A.; Kunze-Liebhäuser, J.; Schwarz, S.; Bernardi, J.; Penner, S. Hybrid Synthesis of Zirconium Oxycarbide Nanopowders with Defined and Controlled Composition. *RSC Adv* **2019**, *9* (6), 3151–3156.
(634) Harel, S.; Mariot, J.-M.; Hague, C. F. Electronic Structure at Zirconia-Nickel and Zirconia-Nickel Oxide Interfaces. *Surf Sci* **1992**, *269*, 1167–1172.
(635) Ramqvist, L.; Hamrin, K.; Johansson, G.; Fahlman, A.; Nordling, C. Charge Transfer in Transition Metal Carbides and Related Compounds Studied by ESCA. *Journal of Physics and Chemistry of Solids* **1969**, *30* (7), 1835–1847.
(636) Yang, Y.; Qian, L.; Tang, J.; Liu, L.; Fan, S. A Low-Vacuum Ionization Gauge with HfC-Modified Carbon Nanotube Field Emitters. *Appl Phys Lett* **2008**, *92* (15).
(637) Morant, C.; Galan, L.; Sanz, J. M. An XPS Study of the Initial Stages of Oxidation of Hafnium. *Surface and interface Analysis* **1990**, *16* (1-12), 304–308.

APPENDIX

A.1 Raw Data and Figures

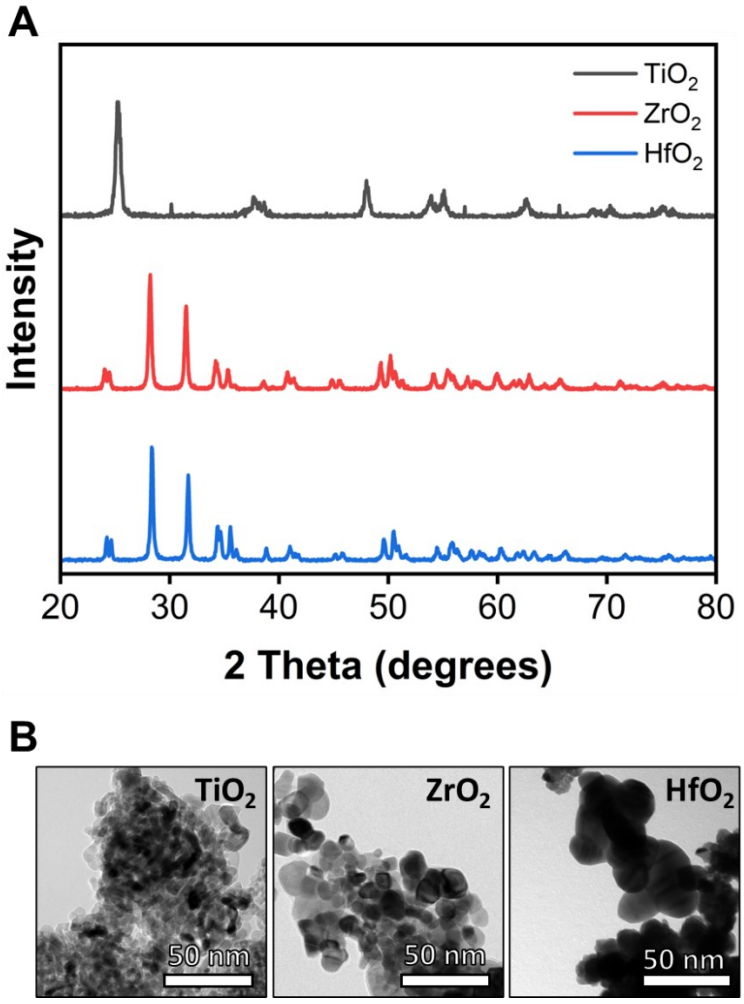

Figure A.1. (A) PXRD spectrum and (B) TEM images of TiO_2, ZrO_2, and HfO_2 precursors.

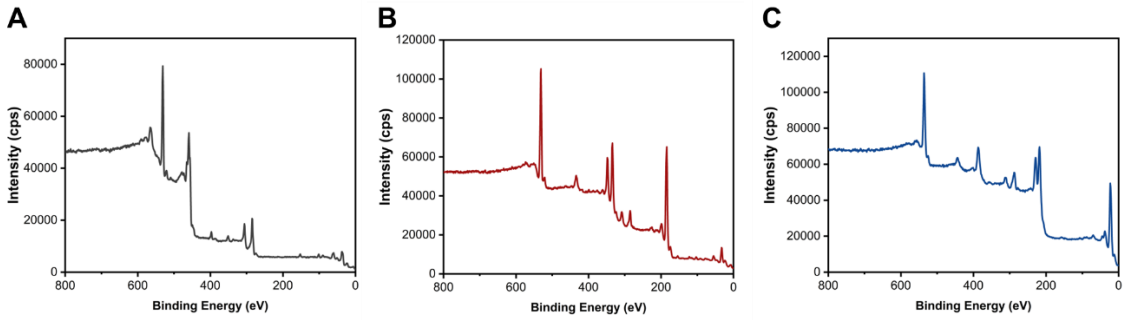

Figure A.2. XPS survey scans for (A) TiC, (B) ZrC, (C) HfC.

Table A1. Fitted binding energies for spectra in Figure 3.5 with literature binding energies for comparison.

Spectrum	Peak Identity	Binding Energy (eV)	Reference
C 1s (TiC)	TiC 1s	281.8	281.7 eV[629]
Ti 2p (TiC)	TiC $2p_{3/2}$	455.1	454.9 eV[629]
Ti 2p (TiC)	TiO_xC_y $2p_{3/2}$	456.7	456.9 eV[630]
Ti 2p (TiC)	TiO_2 $2p_{3/2}$	459.1	458.5 eV[631]
C 1s (ZrC)	ZrC C1s	282.1	282.1 eV[632]
Zr 2p (ZrC)	ZrC $3d_{5/2}$	180.2	179.6 eV[632]
Zr 2p (ZrC)	ZrO_xC_y $3d_{5/2}$	182.1	181.7 eV[633]
Zr 2p (ZrC)	ZrO_2 $3d_{5/2}$	183.8	183.2 eV[634]
C 1s (HfC)	HfC 1s	280.9	280.8 eV[635]
Hf 2p (HfC)	HfC $4f_{7/2}$	15.8	14.7 eV[636]
Hf 2p (HfC)	HfO_xC_y $4f_{7/2}$	17.5	17.1 eV[636]
Hf 2p (HfC)	HfO_2 $4f_{7/2}$	19.4	19.6 eV[637]

Figure A.3. Images of prepared waste product powders prior to pyrolysis.

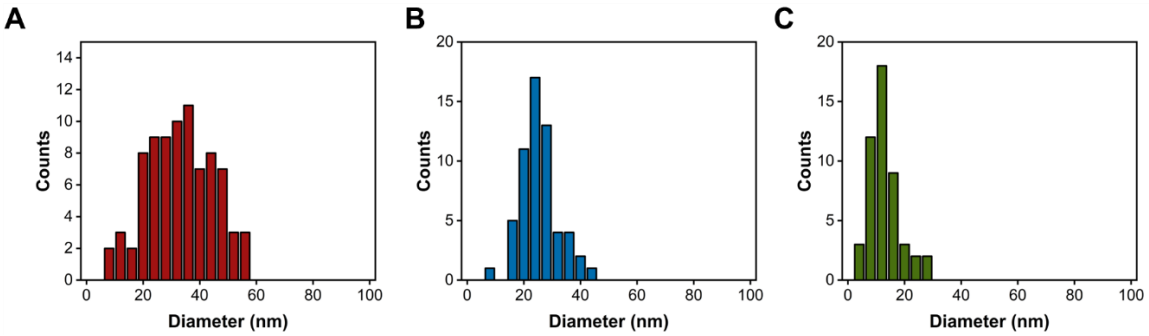

Figure A.4. Size dispersion histograms of TiC NPs prepared using (A) KW, (B) CG, and (C) TR char.

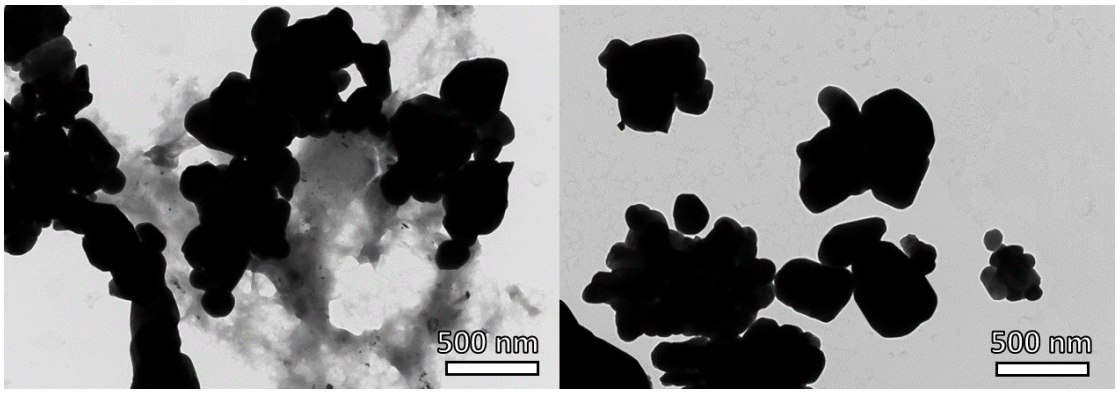

Figure A.5. TEM images of prepared V_2O_5 NPs.

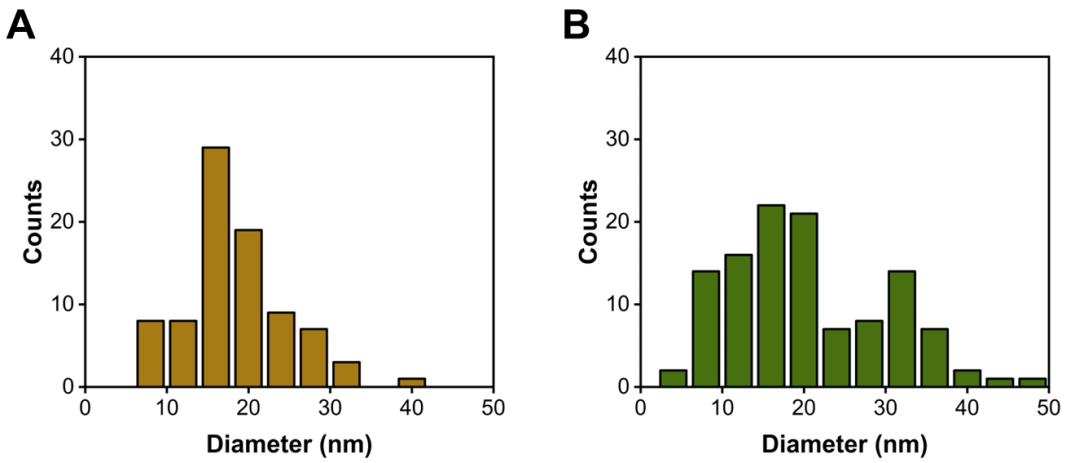

Figure A.6. Size dispersion histograms of (A) VC, and (B) NbC NPs.

A.2 Copyright Permission

Copyright permission for Figure 2.1

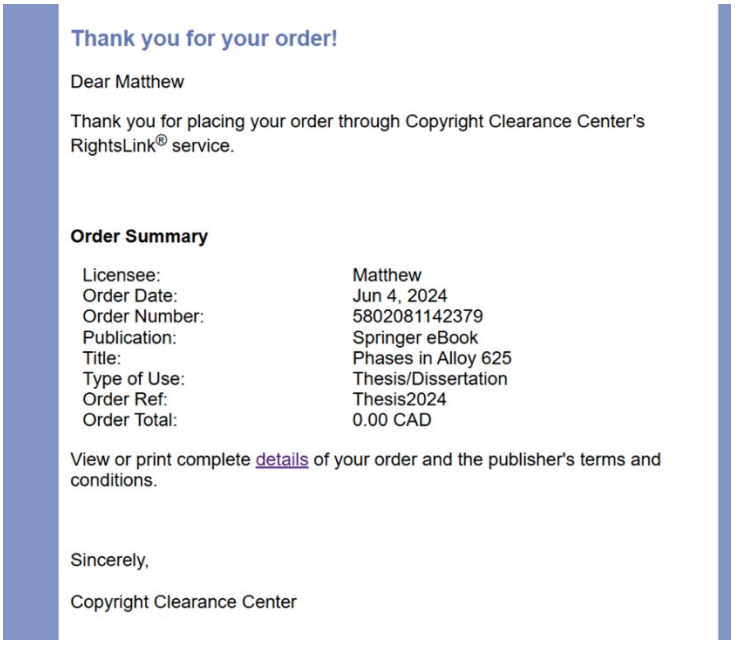

Thank you for your order!

Dear Matthew

Thank you for placing your order through Copyright Clearance Center's RightsLink® service.

Order Summary

Licensee:	Matthew
Order Date:	Jun 4, 2024
Order Number:	5802081142379
Publication:	Springer eBook
Title:	Phases in Alloy 625
Type of Use:	Thesis/Dissertation
Order Ref:	Thesis2024
Order Total:	0.00 CAD

View or print complete details of your order and the publisher's terms and conditions.

Sincerely,

Copyright Clearance Center

A.2 Photothermal Efficiency Derivation

The energy balance of the system consisting of the plasmonic NP solution within a quartz container irradiated by a light source can be given using:

$$\sum_i m_i C_{p,i} \frac{dT}{dt} = Q_I + Q_0 - Q_{ext} \tag{A.1}$$

where m and C_p are the mass and heat capacity of each component of the sample cell, respectively. T is the sample cell temperature, Q_I is the photothermal energy input by the NPs, Q_0 is the baseline energy input by the sample cell, and Q_{ext} is heat transferred to the surrounding. With the light source off, Q_{ext} is represented by:

$$Q_{ext} = hS(T - T_{amb}) \tag{A.2}$$

where T_{amb} is the ambient temperature, h is the heat transfer coefficient, and S is the surface area of the illumination. The thermal and cooling cycle has an exponential time dependence and therefore a thermal time constant τ can be expressed by:

$$\tau = \frac{\sum_i m_i C_{p,i}}{hS} \tag{A.3}$$

The heat transfer coefficient, h, can be determined by equation A.2 using either the heating or the cooling data. Once h is determined, the amount of heat energy accumulated or lost from the sample cell can be calculated. When the sample cell reaches an equilibrium temperature, the power flowing into the sample cell (Q_I and Q_0) is equivalent to the power outflow as shown by:

$$Q_1 + Q_0 = hS(T_{max} - T_{amb}) \tag{A.4}$$

The Q_I can be represented as the heat dissipated by electron-phonon relaxation when the NPs are induced by irradiation, as expressed by:

$$Q_I = I(1 - 10^{-A_\lambda})\eta_T \tag{A.5}$$

where I is the incident light intensity, η_T is the photothermal transduction efficiency, A_λ is the optical density of the sample solution at the excitation wavelength. By substituting equation A.5 into equation A.4, the photothermal transduction efficiency can be expressed by equation 2.6:

$$\eta_T = \frac{hS(T_{max} - T_{min}) - Q_0}{I(1 - 10^{-A_\lambda})} \tag{2.6}$$